MINISTÉRIO DA EDUCAÇÃO
UNIVERSIDADE FEDERAL DO RIO GRANDE DO SUL
PROGRAMA DE PÓS-GRADUAÇÃO EM ENGENHARIA MECÂNICA

NON DEGENERATE ANISOTROPIC GREEN'S FUNCTION FOR 3D MAGNETO-ELECTRO-ELASTICITY AND BEM SHAPE SENSITIVITY FRAMEWORK FOR 3D CONTACT IN ANISOTROPIC ELASTICITY

por

Cristiano João Brizzi Ubessi

Tese para obtenção do Título de
Doutor em Engenharia

Porto Alegre, Setembro de 2019

NON DEGENERATE ANISOTROPIC GREEN'S FUNCTION FOR 3D MAGNETO-ELECTRO-ELASTICITY AND BEM SHAPE SENSITIVITY FRAMEWORK FOR 3D CONTACT IN ANISOTROPIC ELASTICITY

por

Cristiano João Brizzi Ubessi
Ms. Engenheiro Mecânico

Tese submetida ao Corpo Docente do Programa de Pós-Graduação em Engenharia Mecânica, PROMEC, da Escola de Engenharia da Universidade Federal do Rio Grande do Sul, como parte dos requisitos necessários para a obtenção do Título de

Doutor em Engenharia

Área de Concentração: Mecânica dos Sólidos

Orientador: Prof. Dr. Rogério José Marczak
Co-Orientador: Prof. Dr. Federico Buroni - Universidad de Sevilla (ES)

Aprovada por:

Prof. Dr. Éder Lima de Albuquerque ..... PCMEC / UnB

Prof. Dr. Eduardo Bittencourt ..... PPGEC / UFRGS

Prof. Dr. Ignacio Iturrioz ..... PROMEC / UFRGS

Prof. Dr. Fernando Marcelo Pereira
Coordenador do PROMEC

Porto Alegre, 26 de Setembro de 2019

AGRADECIMENTOS

Primeiramente agradeço ao Professor Rogério pela sua dedicação, disponibilidade, confiança, paciência na orientação deste trabalho. A sua paixão pela Engenharia muitas vezes serviu de inspiração na realização desta tese. Agradeço ao Professor Federico pela confiança em ter aceito me receber na Universidade de Sevilha, pela sua receptividade, e pela sua orientação que foi importante não somente para o melhor proveito do período de Doutorado Sanduíche, como também após o meu retorno. Agradeço também pela oportunidade de colaborar no desenvolvimento das soluções fundamentais MEE.

Agradeço aos membros da banca de avaliação, Professores Éder, Eduardo e Ignácio, e também aos que participaram apenas do exame de qualificação, Otávio, Bardo e Daniel, cujas contribuições, sugestões e correções impactaram na qualidade deste trabalho.

Agradeço a todos os camaradas do GMAp que, cada um à sua maneira, deram incontáveis contribuições a este trabalho nas mais diversas discussões e cafés tomados no laboratório. Reservo um agradecimento especial ao Filipe pela sua prestatividade na revisão do texto.

Agradeco ao CNPQ pela bolsa de Doutoramento e à CAPES pela bolsa do Programa de Doutorado Sanduíche no Exterior (PDSE).

Agradeço aos meus pais Sandra e Gilmei, pelo apoio ao meu interesse pela Engenharia, e pelo subsídio fornecido ao longo deste período, aos meus avós Alzira, Ancila e Antônio, pelo apoio e paciência, e à minha irmã Fernanda.

Finalmente, e em especial, agradeço imensamente à minha esposa Caroline, sem a qual nada disso teria se concretizado. Ao longo destes anos, seu amor incondicional e companheirismo foram como raios de sol nesta caminhada. Sua paciência e perseverança me adjudaram a superar cada uma das dificuldades que nos foram impostas ao longo desta jornada, e sua inteligência extraordinária e sagacidade foram cruciais para superar os problemas mais aleatórios. Neste sentido, sou grato ao universo por ter me proporcionado a alegria diária de ter ao meu lado um ser humano que transparece o que há de melhor e mais bonito na natureza, servindo de inspiração para eu também ser uma pessoa melhor que ontem a cada dia.

RESUMO

A primeira parte da tese apresenta uma nova expressão para a solução fundamental Magneto-Eletro-Elástica explícita em termos de autovalores de Stroh, bem definida para autovalores repetidos, e exata. Em seguida, uma série de Fourier dupla é utilizada como uma forma rápida e robusta para avaliar a solução fundamental e as suas derivadas. As expressões recém-desenvolvidas permitem calcular os coeficientes de Fourier para qualquer simetria ou anisotropia de material, o que é feito apenas uma vez para um dado material. Diversos resultados são apresentados para materiais elásticos, piezoelétricos e magneto-eletro-elásticos. A segunda parte desta tese apresenta uma formulação completa para análise de sensibilidade em estruturas elasticas anisotrópicas baseada nestas funções de Green recém apresentadas, incluindo condições de contato. A sensibilidade à parâmetros é avaliada utilizando o método do incremento complexo, método extremamente robusto, similar a diferenciação finita (FD), mas independente do tamanho do incremento. Problemas de contato de Hertz e não Hertzianos foram resolvidos, assim como um estudo de aplicação de uma palheta de turbinas a gás. Foi avaliada a sensibilidade à variação de forma das tensões de contato, tensões cisalhantes máximas e também nas tensões equivalentes de Von Mises, em diferentes materiais anisotrópicos. Os resultados mostraram boa correlação com soluções analíticas assim como em outros trabalhos da literatura. Quando comparado com FD, que não obteve convergência em um dos exemplos, o método CS demonstrou excelente estabilidade e precisão para uma larga faixa de tamanhos de incremento.

Palavras-chave: Elasticidade anisotrópica; Magneto-Eletro-Elasticidade; Funções de Green; Método dos Elementos de Contorno; Sensibilidade de Forma; Método do Incremento Complexo; Contato com Atrito.

ABSTRACT

The first part of the thesis presents a new expression for the magneto electro elastic (MEE) fundamental solution which is explicit in terms of the Stroh's eigenvalues, remains well-defined for repeated Stroh's eigenvalues and is exact. We then define a fast and robust numerical scheme to evaluate the function and its derivatives based on a double Fourier series representation. These newly developed expressions allow to compute the Fourier coefficients for any material symmetry or anisotropy, and is done only once for a given material. One evaluates the Green's function and its derivatives through simple trigonometric formulas. Several results are presented for elastic, piezoelectric/piezomagnetic and magneto-eletro-elastic materials. The second part of the thesis provides a BEM-based formulation for shape sensitivity analysis of anisotropic elastic media, also including contact conditions, and based on the newly presented Green's functions. The parameter sensitivity is evaluated using the complex step (CS) method: An approach similar to finite differentiation (FD), with the advantage of being step-size independent, therefore an extremely robust method. A convergence study on shape sensitivity is provided, proving the efficiency of the CS-BEM approach. We solve Hertz and non-Hertzian type contact problems as well as an application example of a dovetail joint found in gas turbines. We analyzed several parmeter sensitivities to shape variation, such as contact pressure, shear stress, as well as Von Mises stress, for both isotropic and anisotropic materials. The results showed good agreement with analytical solutions, as well as other works from the literature. In comparison with FD, which did not converged for an example case, the CS method showed excellent stability and precision for a broad range of step sizes.

Keywords: Shape Sensitivity; Anisotropic Elasticity; Magneto-Electro-Elasticity; Green's function; Boundary Element Method; Complex Step Method; Frictional Contact.

INDEX

LIST OF FIGURES

LIST OF TABLES

LIST OF ACRONYMS AND ABBREVIATIONS

ACA	adaptive cross approximation
BEM	boundary element method
BIE	boundary integral equations
BVP	boundary value problem
CAD	computer aided design
CPV	Cauchy principal value
CS	complex step
CS-BEM	boundary element method with complex step
DOF	degrees of freedom
FD	finite differentiation
FEM	finite element method
FMM	fast multipole method
FRP	fiber reinforced plastic
GNMls	generalized Newton method with line search
GMRES	generalized minimum residual
ID	implicit differentiation
LHS	left-hand side
LS	level set
MADV	material derivative-adjoint variable
MEE	magneto electro elastic
MMA	method of moving asymptotes
NSE	nonlinear system of equations
NURBS	non-uniform rational B-spline
PE	piezo electric
PM	piezo magnetic
RHS	right-hand side
SIMP	Solid Isotropic Material with Penalization
SLE	system of linear equations
XFEM	extended finite element method

LIST OF SYMBOLS

Roman Letters

$\mathbf{a}_i$	Eigenvector in the context of the Stroh's formalism
$\mathbf{b}_i$	Eigenvector in the context of the Stroh's formalism
b_i	Body forces vector N/m^3
$\mathbf{b}$	Right hand side vector of the boundary element method
c_{ijkl}	Elastic stiffness tensor $\left[\frac{N}{m^2}\right]$
C_{iJKl}	Extended MEE constants matrix $\left[\frac{N}{m^2}\right]$
$\hat{\mathbf{e}}$	Direction coordinate versor ($\|\hat{\mathbf{e}}\| \equiv 1$)
e_{ijk}	Piezoeletric Constants $\left[\frac{C}{m^2}\right]$
E	Longitudinal elastic modulus N/m^2
E_i	Longitudinal elastic modulus for region i N/m^2
G	Galerkin vector modulus
G_l	Galerkin vector, for a load applied in direction l
$\mathbf{G}^{ij}$	Single layer potential matrix,Equation 3.37b
$\mathbf{H}$	Second Barnett-Lothe tensor
$\hat{\mathbf{H}}^{ij}$	Double layer potential matrix without consideration of the free term, Equation 3.37a
$\mathbf{H}^{ij}$	Double layer potential matrix for source node i and collocation at node j
i	Point of application of force i
i	Arbitrary index, integer varying from 1 to some value
$\mathfrak{i}$	Unit imaginary part of a complex number $\mathfrak{i} = \sqrt{-1}$
$\mathbf{I}$	Identity matrix (δ_{ij})
j	Integer index
k	Integer index
l	Integer index
m	Integer index
n	Integer index
n_i	Outward normal vector (component $i \| i = 1:3$)
nel	Number of nodes

nn	Number of nodes
N	Fundamental elasticity matrix
$\mathbf{N}_i$	Fundamental elasticity matrix constituents, $i = \{1, 3\}$ Equation 2.53
p	boundary traction vector on global coordinate system
p_α	Stroh's eigenvalue $\alpha = 1 : d$ (elastic: $d = 3$, PE/PM: $d = 4$, MEE: $d = 5$)
q_n	Constant from polynomial decomposition of the adjoint Christoffel tensor $\hat{\mathbf{\Gamma}}(p)$, Equation 2.90
q_{ijk}	Piezomagnetic Constants $\left[\frac{N}{A\,m}\right]$
Q	Fundamental elasticity matrix
R	Fundamental elasticity matrix
T	Fundamental elasticity matrix
T	Fundamental elasticity matrix
S	Boundary of the unit circle used in the Stroh's formalism
u	Displacement
T_{ij}	Green's function for traction at **x** in direction j, for a unit force application at origin in direction i [m]
U_{ij}	Green's function for displacements at **x** in direction j, for a unit force application at origin in direction i [m]
u	boundary displacement vector on global coordinate system
u_k^*	boundary displacement vector on global coordinate system
x_i	First direction of cartesian coordinate system, or Component of position vector **x**
x	Position vector
y	Parameter vector for the Fourier transform, Equation 2.67
z_i	Position vector on plane 12, in the context of the Stroh's formalism in two dimensions Equation 2.38

Greek Letters

α	Arbitrary index, integer
δ_{ij}	Kronecker's delta
$\delta(\boldsymbol{x_i})$	Dirac's delta at **x**, in direction x_i
$\Delta\gamma$	Perturbation performed in design variable γ

Δx Perturbation performed in x

$\Delta \mathbf{g}_t$ Definition in Equation 5.10, Page 99

$\Delta \tau$ Definition in Equation 5.11, Page 99

ε Radius of the hemisphere considered on the limit performed in the Somigliana identity. Depicted in Figure 3.1, Page 77

ε_{ij} Linear or small deformations tensor, defined in Equation 2.5, Page 22

ϕ Angle between x_3 axis and vector $\mathbf{x}$ [rad]

Γ A surface under consideration

Γ_ε Surface of the hemisphere depicted in Figure 3.1, Page 77

$\mathbf{\Gamma}(p)$ Christoffel tensor, Equation 2.75, Page 37

$\hat{\mathbf{\Gamma}}(p)$ Adjoint christoffel tensor, Equation 2.80, Page 38

Ω A domain under consideration

Γ The boundary of a domain Ω

$\boldsymbol{\lambda}_i$ Contact traction vector for a node pair, defined in their local coordinate system, Equation 5.30

λ_i Contact traction component for a single node

λ_{ij} Magneto-electric coefficients $\left[10^{-9}\frac{N\,s}{A\,m}\right]$

$\lambda_{ij}^{(m,n)}$ Fourier series coefficients

Λ Vector containing all the nodal contact traction vectors $\boldsymbol{\lambda}_i$ for the current equation system

μ Coefficient of friction [-]

μ Lamé constant, shear modulus [Pascal]

$\prod$ Product symbol

ϵ_{ij} Dielectric permeability coefficients $\left[10^{-9}\frac{C}{Vm}\right]$

$\boldsymbol{\xi}$ Element local coordinate system

μ_{ij} Magnetic permeability coefficients $\left[10^{-6}\frac{Ns^2}{C^2}\right]$

ν Poisson's ratio [-]

Ω Domain under consideration

$\mathbf{\Phi}$ Shape function

$\bar{\mathbf{\Phi}}$ Discontinuous interpolation function

θ Angle between x_1 axis and projection at plane x_{12} of vector $\mathbf{x}$ [rad]

Ψ A scalar norm for the residual $\mathbf{\Theta}$ for a system of equations, defined

ρ	Parameter for the Fourier series, integer
$\rho_{\mathbf{mat}}$	Density of material 'mat' kg/m^3
σ_{ij}	Cauchy stress component, $\{i, j\} = [1 \dots 3]$ [Pa]
σ_{IJ}	Extended MEE stress component, $\{I, J\} = [1 \dots 5]$ [dependent on the component direction]

1 INTRODUCTION

This chapter presents the motivation, objectives, and related literature supporting the development of this work. To provide some insights on the current engineering applications, in Section 1.1.1, we address some recurring industrial examples.

1.1 Motivation

Contact problems occur often in engineering. While some of them may be simplified or even assumed to be irrelevant, there exist cases where they are the reason for the existence of that particular engineering problem. With the fast growth on the use of advanced and high-performance materials in engineering, raises the need for highly accurate numerical software for life-cycle prediction, where the contact stresses are a crucial parameter. Tear, wear, fretting, among others, are all phenomena which could arise by the occurrence of contact. The optimal design of contact shape in engineering structures can increase the fatigue life of components and also reduce the need for corrective maintenance.

As stress smoothness in the contact zone has a direct influence on fatigue life and sliding and friction-related wear [Collins and Dooner, 2003], the optimal shape between contacting structures is a recurring subject of research. Haslinger et al., 1988, for instance, treated this theme on a unilateral contact problem, with and without friction, to reduce a preexisting stress concentration. In their work, the total potential energy was used as a cost function to obtain contact shape without stress concentration. The authors concluded that the minimization of this energy, in fact, leads to a constant distribution of flux on the contact surface. In Haslinger, 1991, and Klarbring and Haslinger, 1993, the same principles were applied to obtain a constant distribution of contact pressure through shape optimization. In Haslinger and Klarbring, 1993, the authors proposed a different cost functional, which resulted in constant contact traction. Fancello et al., 1995, compared the two cost functions from Haslinger et al., 1988, and Haslinger and Klarbring, 1993, with considerable differences in the resulting contact traction distribution. Haslinger, 1999, demonstrated that the functionals on contact shape optimization are only directionally differentiable. Furthermore, their derivatives result in another quadratic programming problem. Vondrák et al., 2010, performed contact shape optimization for 3D FEM prob-

lems using a domain decomposition method designed for parallel implementation. Wei et al., 2017, proposed a new shape derivative methodology based on the adjoint variable method, for nonlinear structures subject to contact without friction. Zhang and Niu, 2018, formulated a relaxation model to avoid null sensitivities on the free parts of the boundary, aiming to perform shape optimization in constrained contact force problems. The authors consider plane-strain and axisymmetric examples using the finite element method (FEM) and the globally convergent method of moving asymptotes (MMA).

It is also possible to find works combining shape and topology optimization, under the influence contact conditions, or to find a better contact stress smoothness. One may notice that gradient-based methods, in particular, the Solid Isotropic Material with Penalization (SIMP) and level set (LS) methods, are the most efficient, and very often are preferred over their alternatives [Niu et al., 2019].

Fancello, 2006, performed topology optimization considering contact and local failure constraints for multiple load cases, using SIMP. Luo et al., 2016, employed the adjoint variable method on the topology optimization of hyperelastic structures under sliding contact supports by a mathematical programming algorithm. Strömberg and Klarbring, 2010, minimized the compliance under a volume constraint, considering unilateral contact for a 3D support. Jeong et al., 2018, obtained considerable different topologies for bonded and contact type interfaces. The authors minimized structural compliance while satisfying a volume constraint. Sensitivity was calculated using the adjoint method. Strömberg, 2018, is one of the few works considering contact and anisotropic materials. One of the latest papers using SIMP, Niu et al., 2019, provides an extensive literature review of topological optimization methodologies including contact conditions. The authors employed the adjoint method for the shape sensitivity derivation and estimated the contact pressure sensitivity to the design variables with an additional FEM analysis.

Among the works which use the LS method is possible to list: Myśliński, 2008, proposed a LS algorithm for shape and topology optimization, for the case of a body in contact with a rigid foundation. For the minimization of normal contact stress, the authors employed the material derivative-adjoint variable (MADV) for the shape derivative; Liu et al., 2016, using the extended finite element method (XFEM), considered cohesive interface effects in the topology and shape optimization. The authors employed a multi-phase material and calculate the objective function sensitivities using the adjoint

method; Maury et al., 2017, used the LS method along with various objective functions to optimise the topology and shape other than the contact boundaries. The authors used two approaches (i) minimize volume under a compliance constraint and (ii) optimize the contact pressure with a volume constraint. Shape derivatives were calculated using the MADV. A considerable number of plane optimization examples were solved and a few similar cases with 3D geometry. Although the shape profiles obtained in 3D are similar to the ones in 2D, they have considerable differences along the third dimension, which is motivation to employ 3D formulations for real use-cases. Also, different friction laws or frictionless contact seem to influence the optimal shape considerably; Lawry and Maute, 2018, developed a shape and topology optimization based on the LS considering two different components or phases. The formulation considers finite strains and adopts XFEM. That work enforces the contact restrictions with a method similar to the augmented Lagrangian.

Among the works above, one finds two main characteristics crucial to the optimization performance and quality:

(i) Sensitivity accuracy: Fancello, 2006, for instance, has developed integral forms for the sensitivity, based on boundary only integrals, but a volume integration scheme was adopted due to poor FEM boundary results; Lawry and Maute, 2018, analyzed several problems to determine the sensitivity accuracy and investigates the semi-analytic method comparing it with direct finite differentiation (FD); Zhang and Niu, 2018, also employed the traditional semi-analytic sensitivity scheme differentiating the structural response with the design variable.

(ii) Contact solution quality: Although the FEM is the base of these works, Liu et al., 2016, adopted the XFEM, which allows representing the contacting parts of the problem with greater accuracy; Lawry and Maute, 2018, used the XFEM enrichment for both the finite strain assumption and for the contact problem using a surface-to-surface integration.

What is found in the aforementioned works, is that the consideration of 3D problems showed significant influence on the optimal shapes and topologies. In many of these, dealing with topological optimization only, the contact shape is not allowed to change. Most works focus on stiffness maximization subjected to a volume constraint. Although one can consider a variety of objective functions, Calvo and Gracia, 2001, showed that

the vast majority of them result in a boundary-only integral formulation in which the boundary element method (BEM) offers many advantages. Nevertheless, achieving a uniform distribution of contact pressure is still a challenging issue in structural optimization of continuum structures [Niu et al., 2019]. Ostanin et al., 2017, presented the BEM as a powerful method to be used on structural optimization, due to its sensitivity precision, the possibility of boundary only representation, allied with the scalability and speed of the fast multipole method (FMM).

Sensitivity analysis is a critical task for all the gradient-based shape or topological optimization algorithms aforementioned. Even tough Strömberg, 2018, shows that for orthotropic media, different material orientation results in entirely different material distributions, however, neither of these works studied the influence or considered the effects of material anisotropy in the optimal contact shape of these structures. Due to this scenario, the development of fast and reliable sensitivity algorithms is an utmost necessity. Therefore, without an efficient and reliable contact stress prediction, there are no possible means for this achievement.

The objective of this work is to provide a framework for sensitivity analysis of 3D anisotropic structures based on the BEM, including contact type boundary conditions, which, to the best of our knowledge, one can not find in the literature.

The motivation for the development of these procedures is related to the advantages of BEM, including its contact stress accuracy, and the reduction of the problem's dimension, i.e., the boundary only representation, which provides simpler meshing and modification, among many other advantages (see Ostanin et al., 2017, for instance).

1.1.1 Engineering application

According to Langston, 2015, and also reported by Koff, 1989, single crystal blades have been the answer for combined increases in military engine thrust, creep resistance, and their subsequent fatigue life. Over the years, these blades migrated to civil aircraft engines to provide fuel economy, and to dedicated power generation turbines, with blades four to five times the size of the aircraft ones [Langston, 2015]. The addition of a steam turbine to the cycle due to this increase in output temperature can yield over 60% net energy efficiency to the combined cycle [Vandervort et al., 2016].

According to Lee et al., 2011, more than 80% of the CO_2 emissions are due to the

energy production industry. Also, fossil fuel engines' emissions play a crucial role in the increase in mean global temperature, and they are expected to continue increasing along the years [Macmillan, 2010]. Power plants based on gas-turbines are among the best solutions in terms of reducing this environmental impact, since their environmentally harmful gas emissions, including NO_x, are much lower than any other heat engine [Lee et al., 2011]. Also, due to their higher thermal efficiency and fuel flexibility, these systems have been increasingly applied over the last years. Their fuel flexibility allows utilization of biomass, which has a lower economic cost ($/GJ) than natural gas and can sustain near null CO_2 emissions [Moharamian et al., 2017].

The key aspect in the construction of these engines is mechanical contact: the assembly mechanism of the hundreds of blades which provide air compression and transform heat in mechanical energy is through contact couplings such as fir-tree and dovetail types (Figure 1.1), being a recurrent motivation as well as direct subject of research [Arakere and Swanson, 2000; Arakere et al., 2006; Xue et al., 2014; Bagault, 2013; Bharatish et al., 2018].

Although these blades suffer corrosion due to their operating conditions, a failure mode frequently found in the literature is in their connections [Ruiz and Nowell, 2000], and generally occurs due to fretting fatigue [Carter, 2005; Shi et al., 2016; Barella et al., 2011; Yang et al., 2017; Rani et al., 2017], caused by the combination between fretting and cyclic tangential loading [Arakere and Swanson, 2000]. Therefore, the development of numerical methods for their design optimization must provide excellent contact stress accuracy, where the BEM lies as a strong candidate [Reyhani et al., 2013; Brandão et al., 2016].

Another application example of highly anisotropic materials which commonly finds contact conditions are fiber reinforced plastic (FRP) composites. Their usage is in constant rise due to their lightness and toughness. The easiness of manufacturing intricate shapes without expensive machinery and tooling is another advantage over metallic structures [Jones, 1999].

Although these structures are usually designed to carry large loads per unit weight, they are not as resistant to the compression loads generally occurring in contact interfaces and are known to have a lower bearing strength than the traditional metallic and ceramic materials. Many FRP parts must provide metallic inserts [Jones, 1999; Camanho

and Matthews, 2000] to allow their assembly and alignment by conventional fasteners or pins, which can cause a negative influence in their weight, stiffness, and durability. Henceforth, the development of numerical software capable of correctly reproducing their elastic behavior and failure is key to their engineering analysis and design [Camanho and Matthews, 1999; Tserpes et al., 2002; Warren et al., 2016].

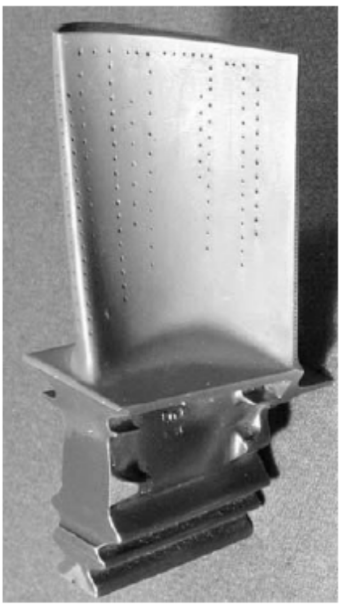

Figure 1.1 – Single crystal HPT blade for CF6-80E engine (General Electric). [Adapted from: Walston et al., 2005]

1.2 A review of BEM applications in structural optimization, shape sensitivity considering anisotropic elasticity and contact problems

In the last decades, BEM has appeared as a popular alternative to FEM, particularly in situations where it does not perform well. The characteristics that makes BEM attractive to its application in engineering problems come from its mathematical foundation: Contrary to the FEM, which comes from a weak formulation, the BEM comes from the integral form of the inverse governing problem. The weighting functions employed (fundamental solutions) have the same continuity requirements from the analytical solution, which gives to the method an exceptional precision [Beer et al., 2008; Brebbia et al., 2012].

One of the most relevant BEM characteristics is that it just requires the boundary information. Besides greatly simplifying tasks such as mesh generation, this BEM charac-

teristic allows a more straightforward computer aided design (CAD) integration because it is closer to the geometric definition. Beyond that, unlike FEM's stiffness matrix which is defined node-to-node, needing an explicit connection between the elements to transfer the volume load, BEM does not need this connection, allowing for local mesh refinements, an attractive characteristic for contact problems, where small fractions of the geometry may need a more detailed discretization than the rest.

In BEM displacement and traction are primal variables, an attractive characteristic to solve contact problems, leading to better accuracy, also it is easier to treat bonded contact problems by a simple introduction of the compatibility conditions at the contact interface. Moreover, since the contact is a boundary-only non-linearity, there is no need to rewrite the boundary integral equations (BIE).

Fast matrix-vector product approximation schemes such as the adaptive cross approximation (ACA) [Bebendorf and Rjasanow, 2003], and the FMM [Rokhlin, 1985; Liu, 2009], which reduce the method's computational cost has been proven to increase performance while maintaining solution quality [Ostanin et al., 2017]. Therefore, they allow large-scale simulations with BEM, which would otherwise require a computer cluster, in desktop computers. It also reduces considerably the method's computational cost, which, allied with the excellent precision and easiness of re-meshing, brings a diversity of advantages during the product conception. The isogeometric shape definition is another feature which increases the attention to BEM [Li and Qian, 2011], as the boundary meshing can be superseded by the CAD definition itself, cutting analysis preprocessing time which, depending on the geometry and simplicity of the analysis tool available, can be not only time-consuming but also tediously empirical. Campos et al., 2017, provide a considerable review on this topic.

1.2.1 3D contact solution with BEM

Most of the works considering contact with BEM throughout the years were plane or axisymmetric [Andersson, 1981; Man et al., 1993; Blázquez et al., 1998]. Blázquez et al., 2006, is one of the first considering anisotropic elasticity.

Until recently, 3D BEM challenged the available computational power, meaning high computation time, or limited to relatively small problems. Many methodologies have arisen to manage this problem and were superseded by FMM and ACA methods.

In one of the first 3D contact applications, París et al., 1992, used constant triangles to solve 3D contact problems without friction to overcome the difficulties involved with memory requirements. As the constant element have only one central collocation point, it has a total of three degrees of freedom (DOF) per element. Also, due to its unitary interpolation function, the integration can be performed analytically for most kernels, resulting in a fast assembly and solution. That work used the well-known iterative procedure to find a compatible contact solution. Although the high contact traction gradients are challenging to interpolate, the constant boundary element is not found to increase the problem's stiffness [París et al., 1992]. Besides using fewer elements within the contact area, the obtained results were in good agreement with finer meshes using 2D BEM and FEM.

Frictionless contact problems only need to fulfill the simple unilateral contact condition, i.e., the non-negative distance between the bodies and non-positive surface tractions. Ghaderi-Panah and Fenner, 1998, propose a similar approach to the one found in Katsikadelis and Kokkinos, 1993: An iterative procedure tries to guess the initial contact state, and iterates until it fulfills all possible contact restrictions. The algorithm checks are of interpenetration outside the contact zone or the existence of tensile stress. The authors included the matrix forms of the generated system of linear equations (SLE), using node to node contact. In one of the examples (a flat punch on an elastic foundation), the authors compared their results with the ones seen in París et al., 1992. While Segond and Tafreshi, 1998, used linear triangles, Leahy and Becker, 1999, used the 8-node quadratic rectangular element, both 3D contact formulations performed iterative checking of tensile stress and interpenetration at each incremental loading step. Espinosa and Mediavilla, 2012, presented a purely iterative process to solve thermoelastic contact problems without friction. Comparing the obtained solutions with 2D and 3D algorithms the authors concluded that the 3D solution provides better results on the coupling's thermal resistance. Sfantos and Aliabadi, 2007, developed a wear modeling solution using BEM, with a simplification that does not consider friction, taking the material loss into account via geometry updates. The authors validated the BEM procedure against analytical solutions, experimental data, and FEM results.

The iterative-incremental technique was also successfully applied in frictional problems, such as Sahli et al., 2008, which suggested two approaches for non-conforming fric-

tional contact using 3D BEM. The contact state solution is iterative, with an incremental loading procedure. Examples considered were of a flat punch and a cylinder-flat indentation. Yu et al., 2005, applied the FMM to accelerate the 3D BEM on the solution of frictional contact. The authors used a point to surface non-conforming coupling algorithm by interpolation of the target point at the secondary body. The contact conditions were applied using a mathematical programming approach, while a GMRES(m) algorithm was employed to solve the contact problem iteratively in a two-step approach, similar to the Uzawa method. As an example, the authors solved a flat punch problem. Chen et al., 2010 also used the mathematical programming approach and the FMM, now based on Taylor series, using a node to surface coupling scheme, for frictional contact problems.

The Penalty and Lagrange multiplier methods are well-known regularization approaches to deal with the inequalities arising in contact problems, and they are also found in algorithms using BEM. Yamazaki et al., 1994b, solved 3D contact using the penalty parameter formulation from a previous work Yamazaki and Mori, 1989,. The problems analyzed were of the Hertzian kind, and most meshes presented very distorted elements, which does not seem to hinder the results. Weber et al., 2011, used the penalty method to consider frictional contact on the analysis of crack closure problems in fatigue simulation.

González et al., 2008, and Rodríguez-Tembleque et al., 2008, treated the contact coupling between FEM and BEM problems using the notion of localized Lagrange multipliers. These works propose a coupling method which interpolates the displacements and does the traction-force transformation and interpolation in an intermediary surface, called the contact frame. Rodríguez-Tembleque and Abascal, 2010, motivated by these previous works, used the same Augmented Lagrangian formulation based on Alart and Curnier, 1991, which circumvents some weaknesses existing on the Lagrangian multiplier and penalty methods. The contact restrictions are imposed using projection functions, resulting in a robust framework for both FEM and BEM frictional contact analysis. By taking advantage of the traction and gap normal complementarity, the authors reduced the DOF needed for the system solution. As these functions result in a non-linear system of equations, the authors use the generalized Newton method with line search (GNMls). The GNMls is a generalization of the standard Newton's method to B-differentiable functions[1], with an unconstrained optimization (line search) between each iteration to accelerate its

[1]See, e.g., Pang, 1990.

convergence. Rodríguez-Tembleque et al., 2010, studied wear in rolling contact problems, while Rodríguez-Tembleque and Abascal, 2010, use this method to solve rolling contact problems coupling FEM and BEM. In these works, the tangential slip velocity also plays a role in the system of equations and contact restrictions.

1.2.2 Anisotropic BEM and Contact

Since the 1970s, applying BEM in 3D anisotropic elasticity was a matter of much interest. However, methods for numerically evaluating fundamental solutions, in this case, resulted in elevated relative computational cost, Vogel and Rizzo, 1973, for instance, have not solved any numerical example, but presented the formulation to compute the needed fundamental solutions in detail. The references for these functions were the works of John, 1955, Synge and Rheinboldt, 1957.

Wilson and Cruse, 1978, discussed the heavy dependence of the anisotropic 3D BEM on efficient methods for evaluating the fundamental solutions and proposed an approximation method using cubic interpolation and precomputation of tabulated values on a sphere. Wilson and Cruse evaluated the line integrals numerically, using Simpson's rule, and forms a database of modulation functions, which are the material and position-dependent part of the fundamental solutions (the second Barnett-Lothe tensor). This methodology is often called as the Wilson-Cruse approach.

Sales and Gray, 1998, developed a formulation based on residue calculus [Sveshnikov and Tikhonov, 1971] and found it to be four times faster than the Wilson-Cruse approach, which, according to the authors, was not very practical due to the pre-calculated tables storage cost. Also, the cubic interpolation could lead to errors in materials with mechanical behavior more than moderately anisotropic. This solution is not stable for the degenerate case, and more recently, Phan et al., 2005, provided a solution for this problem with some algebraic enhancements to reduce its computation time. Ting and Lee, 1997, appear in the literature as the first complete fundamental solution for general anisotropic elasticity in explicit form in terms of the Stroh's eigenvalues [Stroh, 1958] also valid when these are equal, a key feature on the implementation of a general BEM code.

Over the years, many anisotropic BEM related works focus on fracture mechanics. Pan and Yuan, 2000b, studied stress concentration in cracked transversely isotropic solids using 3D BEM and fundamental solutions from Pan and Chou, 1976.

Tonon et al., 2001, presented a complete 3D BEM implementation for anisotropic elasticity, including internal stress. The authors approximate complicated parts of the second-order derivative by a Lagrange polynomial, an approach proposed by Pan and Tonon, 2000, for piezoelectric solids.

Wang and Denda, 2007, performed analytical integration of the triangular boundary element, using the fundamental solution in integral form. This way, one can obtain boundary element matrices by performing a line integral over a semi-circle. The authors present numerical examples considering a cube and a spherical cavity for some anisotropic materials like aluminum crystal and sapphire.

Benedetti et al., 2009, developed a fast large-scale Dual BEM for the analysis of cracked anisotropic solids using the Wilson-Cruse approach, with ACA acceleration algorithm. They investigate optimum preconditioning schemes by performing many comparisons on the solution speed, and also the influence of the modulation function approximation on the final solution accuracy.

Approximated fundamental solutions are also found in Shiah et al., 2012, using a Fourier series approach. Tan et al., 2013, presented a simplified and real-valued formulation for these, implemented in a BEM code. Later, these functions were applied by Rodríguez et al., 2014, along with the ACA on large scale problems. These approximated modulation functions are much faster to compute than their analytic counterparts and are also more general due to their dependence on pre-computed coefficients only.

Távara et al., 2008, presented real-valued equations for the particular case of transversely isotropic solids in their unique explicit form. Távara et al., 2012, presented a formulation for the second-order derivative of the Green's function in the same fashion as their previous work, to evaluate internal stress through the hypersingular integral identity.

Buroni et al., 2011 and Buroni and Sáez, 2013, used the Stroh's formalism and residue calculus to obtain the Green's function and its first-order derivative for general anisotropy. These functions are explicit in terms of the Stroh's eigenvalues, and the residue theorem provided an alternative formulation to deal with degeneracies appearing when eigenvalues are close to each other. Buroni and Sáez, 2010, provided these functions for fully coupled magneto electro elastic (MEE) materials.

One of the first anisotropic 3D BEM application in contact problems is due to Rodríguez-Tembleque et al., 2011, where the augmented Lagrangian provided the contact

restrictions using projection functions. The fundamental solutions employed were the formulation from Buroni et al., 2011. The authors obtained excellent agreement with analytic solutions using relatively coarse BEM meshes in comparison with the works of Alart and Lebon, 1998, Peillex et al., 2008, Lovell, 1998, and Arakere et al., 2006, for instance, where the FEM mesh refinement is extreme. Rodríguez-Tembleque et al., 2013a, and Rodríguez-Tembleque et al., 2013b, focused their studies in the 3D contact between polymer composites, using similar formulations as their previous work. As the frictional contact restrictions result in a non-linear system of equations, solved the problem with two different methods: GNMls, and the iterative (Uzawa) approach. Both procedures are due to Alart and Curnier, 1991.

The general approach used in these works, based on the augmented Lagrangian with projection functions, is also found in several other works [González et al., 2008; Rodríguez-Tembleque and Abascal, 2013; Rodríguez-Tembleque et al., 2016; Cavalcante et al., 2017; Rodríguez-Tembleque et al., 2019], proving its reliability and efficiency.

1.2.3 Shape optimization and sensitivity

Dostál et al., 1996, stated that BEM is more adequate than FEM in shape optimization, as the domain remeshing hinders the accuracy of the shape derivatives in the latter. Zhang and Niu, 2018, for instance, had to apply a Laplacian smoothing technique on the interior nodes to avoid mesh distortion. Also, it needed a considerably fine mesh in the contact area, which hinders its application for 3D problems, due to the high computational cost.

Since the 80s, the well-known advantages of BEM in shape optimization and its subsequent application in these problems has motivated shape sensitivity development with the method [Barone and Yang, 1988, 1989]. For instance, Soares et al., 1984, optimized shaft cross-sections for maximum torsional stiffness and Mota Soares et al., 1984, optimized the shape of plane structures for minimum compliance.

Barone and Yang, 1989, one of the first works to deal with 3D shape sensitivities, performed an error analysis, showing that the general sensitivity results were extremely accurate. According to Kočandrle and Koška, 1996, there are two basic methods for deriving shape sensitivities: MADV and implicit differentiation (ID). Although these methods rely on numerical integration, they are often called analytical methods. Bonnet, 1997, per-

formed a profound analysis, concluding that the implicit differentiation approach remains valid under the assumption of regularized BIE from Guiggiani et al., 1992, Guiggiani et al., 1992, such that the resulting sensitivities possess the same level of singularity as the governing BIE. The author based his proof on the context of the spherical limiting process on the Somigliana's identity, i.e., proving that boundary perturbations do not alter the free term arising from the limit. Yamazaki et al., 1994a, performed shape optimization of 3D isotropic structures using a mathematical programming approach using ID.

Erman and Fenner, 1997, proposed the evaluation of the sensitivity to the normal outward direction at the design variable point, reducing the computational time by a factor of three. The resulting sensitivities must be obtained through hypersingular integration, which was performed via element subdivision and with the rigid body translation technique. Sensitivities were calculated for simple examples comparing it with FD.

Shape sensitivity also has been used for the computation of stress intensity factors [Matsumto et al., 2000] and for more general fracture analysis, related to crack shape sensitivity [Bonnet, 2001]. Tafreshi, 2015, used an ID shape sensitivity approach for calculating the J_2 integral. Tafreshi, 2016, performed a similar analysis on bi-material problems. Morse et al., 2019, analyzed the mechanical reliability of structures for creep with a viscoelastic material consideration on *plane-stress* problems. The analysis employed a high-order shape sensitivity formulation, obtained with ID.

The MADV was the method used in Burczyński et al., 1995 and Burczyński et al., 1997, that compared it with the ID method, and next by Kočandrle and Koška, 1996, which performed shape optimization of 3D structures using the design sensitivity methodologies from Choi, 1987 and Choi and Kwak, 1988. Calvo and Gracia, 2001, investigated the MADV shape sensitivity approach in functional form, similar to that Fancello, 2006, in FEM. This treatment is useful in the context of BEM, as, in general, all shape derivatives result in boundary-only integrals. Notice also that, according to Rus and Gallego, 2007, the ID technique requires significantly less discretization density than the MADV approach developed by Burczyński et al., 1995.

Tai and Fenner, 1996, optimized the position of holes in a bracket for two cases: (i) minimizing the maximum equivalent stress and (ii) to equalize the force between them. The authors suggested a coordinate transformation that reduces the singularity of the

shape derivative kernels, simplifying their integration. The displacement and traction shape derivative kernels are integrated using Gauss quadrature and rigid body displacements, respectively.

Li and Qian, 2011, for instance, optimized the shape of 2D and 3D structures using non-uniform rational B-spline (NURBS) based isogeometric BEM and gradient based shape optimization (MMA). The authors solved two examples based on minimizing the volume under maximum stress constraints. The first problem solved was a 3D fillet on a shaft under axial stress, while the second problem is the optimization of several shape variables of a connecting rod.

Kita and Tanie, 1997, used BEM along with genetic algorithms to find the shape of a 2D beam under uniform pressure. The authors adopted minimum mass objective function and maximum stress restrictions. Although this kind of algorithm avoids sensitivity calculation, it resulted in a high computational cost: The beam example took 100 iterations to converge, each considering 50 analyses. The gradient-based algorithm used in Li and Qian, 2011, appears to be more efficient than the one used by Kita and Tanie, 1997, with reduced iterations and fewer design variables than the equivalent genetic populations. Nevertheless, no work in the literature directly compared these two methodologies under similar conditions.

Rus and Gallego, 2005, employed shape sensitivity on inverse elastodynamic problems to find the position of defects in non-destructive testing. Later, Rus and Gallego, 2007, investigated the semi-analytic shape sensitivity performance.

The BEM has been successfully applied in LS methods for structural optimization based on shape sensitivity analysis on plane problems [Ullah and Trevelyan, 2016] and also in 3D ones [Ullah et al., 2015].

Lian et al., 2016, use the regularized isogeometric BEM for shape optimization of plane problems. The advantage of this regularized BIE, is that it yields the same singularity for sensitivity as in the original problem.

Ostanin et al., 2017, proposed a shape and topology optimization procedure based on a scalable implementation of the kernel independent fast multipole method. That work is practically an extension to three dimensions of çthe hard-kill material removal method from Marczak, 2008, using cubic voxels.

Sfantos and Aliabadi, 2006, one of the few works considering contact sensitivity,

performed ID of the boundary integral equations. The authors solved a cylinder-block contact problem, in which they compared the sensitivity results with FD, and finds that ID is more reliable and more precise than direct FD.

One of the few works considering anisotropy influence on the optimal shape, Tafreshi, 2005, performed shape optimization of composite structures under ***plane-stress*** conditions. The author minimized the elastic compliance under stress, volume, and dimensional constraints. Tafreshi, 2006, performed shape sensitivity and optimized the positioning of holes and cutouts on *plane* composite structures. Tafreshi, 2009, estimated shape sensitivity of composites under contact conditions using ID.

The FD scheme is a well-known method for approximating derivatives and is applied for numerous reasons, mainly for its simplicity. One can get the shape derivatives simply by solving the problem a second time with a small perturbation in the design variable. In optimization problems, direct FD can be computationally more expensive due to the number of design variables and iterations, and choosing the appropriate step size can be time-consuming. Therefore, the semi-analytic method is often preferred.

To avoid the strongly- and hyper-singular integration of the fundamental solutions derivatives, Saigal et al., 1989, use the semi-analytical method, employing FD to obtain the required partial derivatives of the BEM matrices. The approach uses the same triangular factorization from the original system solution, which can save some computational time. Aithal et al., 1991, evaluated shape sensitivities for 3D problems using multiple regions and semi-analytic method, based on FD. Although the semi-analytical method depends on the correct step size selection, the authors found the ID only slightly faster and more accurate.

Recently, the complex step (CS) method is being increasingly employed as an automatic differentiation tool [Martins et al., 2003; Mundstock and Marczak, 2009], and an alternative to FD. The CS method was accidentally discovered by Lyness and Moler, 1967, which employed the Cauchy-Riemann equations to obtain numerical derivatives of functions using complex variables. Many years later, Squire and Trapp, 1998, demonstrated that if one evaluates a function with an *imaginary increment*, the resulting imaginary part approximates its derivative. In comparison with FD, one avoids computing the function two times. As this method does not involve a difference, there is no cancellation error, rendering a numerically exact derivative, once the step size gets small enough, which is

a huge benefit, in comparison with FD, as the method is much more reliable. Martins et al., 2001, for instance, showed the application of the CS on an aero-structural solver, in which the CS method provides excellent results for any step size chosen, while the best converged FD error is orders of magnitude worse.

The first BEM application of the CS method was done by Gao et al., 2002, to compute the internal stress on a non-linear formulation, which would otherwise require the domain integration of the traction fundamental solution derivative (hyper-singular). The non-linear formulation added even more complexity to the internal stress computation, which was also avoided using the CS method.

On inverse analysis, which is an optimization problem, Gao and He, 2005, also used the CS method for shape sensitivity. That work treats plane heat conduction problems for the identification of internal features with fixed boundary values. A low number of iterations were needed to find the solutions, which shows the performance of this method in comparison with others listed in this review.

Mundstock and Marczak, 2009, applied the CS method into a plane BEM implementation to evaluate shape sensitivities in elastic isotropic problems. The CS was used to obtain sensitivity of the beam bending and of a thick tube under internal pressure with respect to design variables in analytic form to provide a comparison case. Then, the authors solved these two problems with the CS-BEM implementation. The results using CS-BEM were more accurate than both ID and the MADV from Burczyński et al., 1997.

Although most approaches listed so far employed ID and MADV, they are troublesome and one has to deal with higher singularity integrals (or to regularize them), these methods were the popular choice for sensitivity analysis with BEM. In this context, the CS method is a powerful tool which enables one to obtain numerous sensitivities without dealing with hypersingular integration, and is less prone to mathematical and numerical errors found on the ID or the FD, be it direct or semi-analytical.

To the best of the authors' knowledge, there is no 3D BEM using the CS method — either isotropic or anisotropic, nor contact, or any combination of these problems. Therefore, this work fills an interesting and promising research field, which is the investigation of the CS method quality and performance in these problems. One can also apply the CS method in a semi-analytic fashion for higher performance on optimization algorithms, and combine it with other acceleration approaches.

1.3 Objectives

In the current literature, there are only a handful of works dealing with three-dimensional contact with anisotropic BEM formulation. Contact shape sensitivity was studied only for plane problems, which is an easier problem in the context of the BEM formulation. None of them, to the best of author's knowledge, evaluates sensitivities on 3D anisotropic elasticity.

The main objective of this work is to develop a BEM based numerical tool for the shape sensitivity analysis in three-dimensional contact problems involving anisotropic materials.

The main idea behind the methodology is to use the CS method to provide the shape sensitivity automatically. The main building block for this sensitivity analysis framework is a 3D BEM considering anisotropic elasticity. As it is well-known, fundamental solutions for this problem are the recurrent subject of research. To be able to apply the CS method, we employed a real-valued fundamental solution based on a Fourier series approximation. This strategy also provides a more efficient BEM computational implementation, as the same function is valid for any material configuration. Also, this 3D fundamental solution is faster than the integral and the Stroh's formalism.

The specific objectives to be accomplished in this work are the implementation of:

- 3D anisotropic fundamental solution based on Fourier series, which is real-valued, allowing the application of the CS method.
- The CS method.
- Perfectly bonded contact (subregion);
- Frictional contact coupling and a Non-linear solution strategy;

We perform the validation of the proposed methodologies through the solution of problems with known analytic solutions, as well as problems previously solved in other works from the literature.

1.4 Contributions

First and foremost, one contribution of this work is to improve the Fourier series approach for 3D fundamental solutions for general anisotropic elasticity, extending it for

MEE materials. Also, taking advantage of the Barnett-Lothe tensor period, we redefine the Fourier series in a manner that halves the terms needed and its computational cost.

These solutions, based on the non-degenerate factorization of the Stroh's eigenvalues, enable a seamless usage of anisotropic properties, without the problems involved with previous degenerate formulations.

Also, the Fourier series approximation of the Green's function derivatives is much more straightforward than their direct computation, contributing to the easiness of implementation. The Green's function computation methodology can be used in the integration of the Fourier coefficients, meaning that other researches, which already have a slower method implemented, can benefit from our findings.

The second part of this work provides an anisotropic 3D BEM for elastic materials, based on the Fourier series approximated Green's function, which one can readily extend to MEE materials. For that purpose, there are only a few practical modifications to the code (e.g., treatment of boundary conditions) preventing us from analyzing fully coupled MEE materials with BEM.

The third part of this work, an additional contribution, is to apply the CS method to evaluate contact shape sensitivities in anisotropic materials. The single analysis of 3D shape sensitivity considering anisotropic materials with the BEM is another contribution of this work. The analysis of 3D shape sensitivity considering anisotropic materials, performed at the end of Chapter 4 is another contribution of this work, as it is the first time 3D anisotropic BEM performs this task.

The sensitivity evaluation opens a new field of investigation, which allows us to take advantage of existing shape optimization implementations to study the optimal shape of contacting structures with anisotropic materials using the BEM. Nevertheless, one can study the optimal shape of so-called smart structures by taking advantage of the MEE solutions we developed alongside this work.

1.5 Work organization

This work is structured in 7 chapters.

On Chapter 2 the Green's functions are derived for elastic and MEE materials (including piezo electric (PE) or piezo magnetic (PM)). Numerical results are presented for these materials along with an anisotropy index study on the Fourier series precision.

Chapter 3 presents the BIE and its discretization with the BEM.

On Chapter 4 we present the CS method, its integration with the BEM, and perform a convergence analysis of the method for a 3D elasticity problem.

Chapter 5 describes the contact formulation and its numerical treatment for BEM formulation. Also, it shows the non-linear system solution method.

On Chapter 6 we present numerical results on example problems, comparing with analytical and numerical solutions. Sensitivity results using the CS-BEM in comparison with analytical Hertz solution derivative or finite differentiation.

Chapter 7 closes this work with discussion and conclusions on the results and performance of our proposed methodologies. Also, we include considerations concerning the continuity of this work.

2 GREEN'S FUNCTION FOR GENERAL ANISOTROPIC ELASTICITY, AND MAGNETO-ELECTRO-ELASTICITY

This chapter is divided into the following topics:

- Section 2.1, basic elasticity equations are presented, providing a theoretical foundation to the following part where Kelvin's solution is shown, i.e., the isotropic Green's function.

- In Section 2.2, we present the classes of symmetries encountered in the elastic constitutive tensor.

- Section 2.3, Green's function for elastic anisotropy, presents the theoretical foundation and some existing solutions for computing the Green's function in anisotropic elasticity.

- Section 2.4 presents the formulation of the coupled MEE problem necessary to obtain the MEE Green's function, which is accomplished by a formulation similar to the elastic one.

  Furthermore, this section presents a new formulation for MEE materials in which the degeneracies appearing from close to or repeated Stroh's eigenvalues are avoided, based on simple factorization. This approach, developed alongside this work, is the basis for a new and general procedure for the computation of Green's functions using a fast non-degenerate Fourier series framework, proposed in Section 2.5. Finally, the non-degenerate MEE Green function smoothness in a near-degenerate case is demonstrated, including also previous degenerate solution to provide a comparison case.

- Section 2.5, we propose an enhanced Fourier Series approach for numerical computation of Green's function and its derivatives, for Elastic, PM/PE, and MEE Anisotropic materials. We improve a previous formulation reducing by half the terms needed for the function evaluation by taking advantage of the periodic nature of Green's function.

- In Section 2.6, numerical results are presented for the proposed Fourier series solution and compared with previous solutions from the literature. The coefficient

integration is studied, analyzing the numerical integration of the Fourier coefficients for the following types of materials: Elastic with cubic symmetry, Piezoelectric with transversely isotropic symmetry, uncoupled transversely isotropic MEE material (PE+ME), and finally a fully coupled anisotropic MEE material. Furthermore, we present the solution convergence through plotting the error as a function of the number of terms added in the solution for these materials. This analysis also includes the error considering the equivalent to the previous solutions from literature to show the efficiency gains in the convergence of this new solution. Finally, a parametric study is performed to analyze the influence of the material anisotropy on the Fourier series approximation error.

2.1 Isotropic Elastic Fundamental Solutions

Basic Linear Elasticity One of the main objectives of elasticity studies in engineering are the internal forces resulting from the loads present on structures. The equilibrium equations governing the static elasticity theory derive from the analysis of the stresses acting at a point inside of a continuous body. Let us represent the stress state at this point by an infinitely small cube, as illustrated in Figure 2.1.

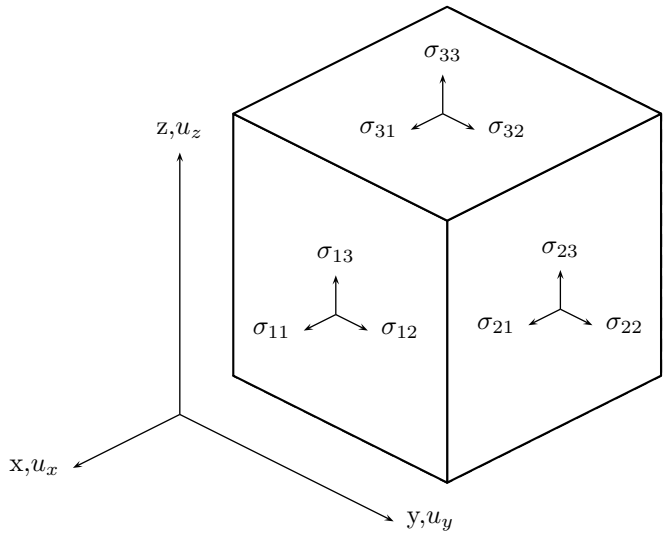

Figure 2.1 – Definition of stress on the infinitesimal cube.

Notice that components of equal magnitude and contrary directions equilibrate the

ones depicted in Figure 2.1. This way, the Cauchy stress tensor is defined as

$$\boldsymbol{\sigma} = \begin{bmatrix} \sigma_{11} & \sigma_{12} & \sigma_{13} \\ \sigma_{21} & \sigma_{22} & \sigma_{23} \\ \sigma_{31} & \sigma_{32} & \sigma_{33} \end{bmatrix}. \tag{2.1}$$

In order to respect the equilibrium of moments around all the coordinate system axes the following conditions must be met

$$\sigma_{21} = \sigma_{12}, \qquad \sigma_{31} = \sigma_{13}, \qquad \sigma_{32} = \sigma_{23}. \tag{2.2}$$

The static equilibrium of forces in the directions x_1, x_2 and x_3 results in the following equilibrium equations

$$\begin{aligned} &\frac{\partial \sigma_{11}}{\partial x_1} + \frac{\partial \sigma_{12}}{\partial x_2} + \frac{\partial \sigma_{13}}{\partial x_3} + b_1 = 0, \\ &\frac{\partial \sigma_{21}}{\partial x_1} + \frac{\partial \sigma_{22}}{\partial x_2} + \frac{\partial \sigma_{23}}{\partial x_3} + b_2 = 0, \qquad \text{in } \Omega, \\ &\frac{\partial \sigma_{31}}{\partial x_1} + \frac{\partial \sigma_{32}}{\partial x_2} + \frac{\partial \sigma_{33}}{\partial x_3} + b_3 = 0, \end{aligned} \tag{2.3}$$

where b_i are the body forces acting in the domain. Equation 2.3 is the general static elasticity equilibrium equations. These equations can be represented in a more compact mode,

$$\sigma_{kj,j} + b_k = 0, \qquad \text{in } \Omega, \tag{2.4}$$

where comma denotes differentiation, and repeated indices imply summation.

The infinitesimal strain tensor or linear deformations are calculated as a function of the displacements as

$$\varepsilon_{ij} = \frac{1}{2}\left(\frac{\partial u_i}{\partial x_j} + \frac{\partial u_j}{\partial x_i}\right). \tag{2.5}$$

The stress-strain or constitutive relation for an isotropic material is defined by

$$\sigma_{ij} = \lambda \delta_{ij} \varepsilon_{kk} + 2\mu \varepsilon_{ij}, \tag{2.6}$$

where ε_{kk} is the trace of the infinitesimal strain tensor, δ_{ij} is the Kronecker delta (or identity matrix). The Lamé constants λ and μ relate with the longitudinal elastic modulus

E, and Poisson Coefficient ν, through the following relations,

$$\mu = \frac{E}{2\,(1+\nu)}, \qquad \lambda = \frac{E\nu}{(1+\nu)\,(1-2\nu)}. \tag{2.7}$$

Isotropic Fundamental Solutions

According to Brebbia et al., 2012, a well-known form to obtain the displacement, U_{lk}, and traction, T_{lk}, fundamental solutions begins by writing the elasticity equilibrium equations in terms of displacements. Replacing the isotropic stress-strain relation Equation 2.6, on Equation 2.4, and then in Equation 2.5, which relates displacements and strains, the Navier's equation is obtained

$$\left(\frac{1}{1-2\nu}\right) u_{j,jk} + u_{k,jj} + \frac{1}{\mu} b_k = 0 \qquad \text{in}\,\Omega. \tag{2.8}$$

Kelvin's solution for displacements is obtained from Equation 2.8 by applying a Dirac delta $\delta(\mathbf{x}-\mathbf{x}')$ at the source point $\mathbf{x}'$ on direction e_l, so that

$$b_l = \delta(\mathbf{x}-\mathbf{x}')e_l, \tag{2.9}$$

and representing the displacements in terms of the Galerkin vector G,

$$u_j = G_{j,mm} - \frac{1}{2(1-\nu)} G_{m,jm}. \tag{2.10}$$

Therefore, replacing Equations 2.9 and 2.10 on Equation 2.8, results in

$$G_{l,mmjj} - \frac{1}{\mu}\delta(\mathbf{x}-\mathbf{x}')e_l = 0, \tag{2.11}$$

or,

$$\nabla^2(\nabla^2 G_l) - \frac{1}{\mu}\delta(\mathbf{x}-\mathbf{x}')e_l = 0, \tag{2.12}$$

which could be also written as

$$\nabla^2(F_l) - \frac{1}{\mu}\delta(\mathbf{x}-\mathbf{x}')e_l = 0, \tag{2.13}$$

where

$$F_l = \nabla^2 G_l. \tag{2.14}$$

The solution of Equation 2.13 for three-dimensional problems is

$$F_l = \frac{1}{4\pi r\mu} e_l, \tag{2.15}$$

where

$$r = \|\mathbf{x} - \mathbf{x}'\| \tag{2.16}$$

is the distance between point $\mathbf{x}'$, where the Dirac delta is being applied, and the field point $\mathbf{x}$, the observation point, or field point. Replacing Equation 2.15 on Equation 2.13 generates

$$\nabla^2 G_l = \frac{1}{4\pi\mu r} e_l. \tag{2.17}$$

The solution for Equation 2.17 is

$$G_l = G\, e_l, \tag{2.18}$$

where

$$G = \frac{1}{8\pi\mu} r. \tag{2.19}$$

Taking each load independently, one can define G_{lk}, the k-th component of the Galerkin vector at a point $\mathbf{x}$, where an unit load is applied on direction e_l at $\mathbf{x}'$,

$$G_{lk} = G\delta_{lk}. \tag{2.20}$$

Analogously, U_{lk} represents the displacement at $\mathbf{x}$ on direction e_k, when a unit load is applied at $\mathbf{x}'$ on direction e_l,

$$u_k = U_{lk} e_l. \tag{2.21}$$

In agreement with Equation 2.10, the displacements could be written as

$$U_{lk} = G_{lk,mm} - \frac{1}{2(1-\nu)} G_{lm,km}. \tag{2.22}$$

Replacing Equations 2.20 and 2.21 in Equation 2.22, one finally obtains

$$U_{lk} = \frac{1}{16\pi\mu(1-\nu)r} \left((3-4\nu)\,\delta_{lk} + r_{,l} r_{,k} \right), \tag{2.23}$$

which is the Kelvin's solution for the displacement at point $\mathbf{x}$ in the direction e_k, resulting from a unit load at point $\mathbf{x}'$ in the direction e_l.

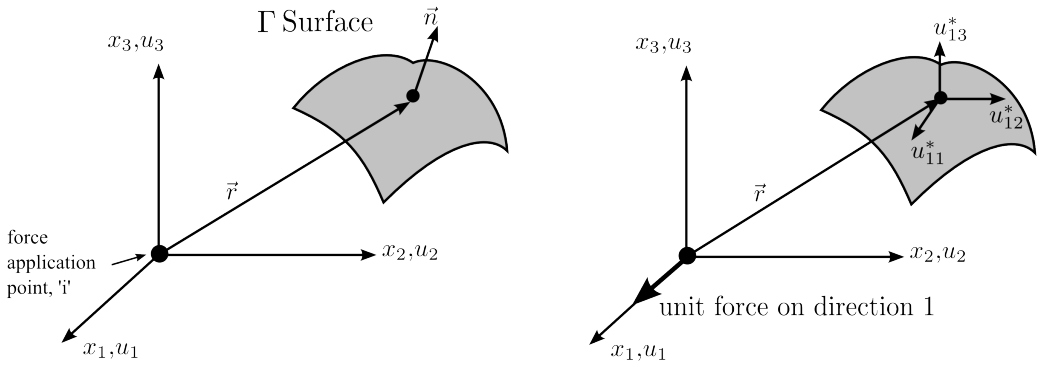

Figure 2.2 – (a) Graphical illustration of the fundamental solution point system and (b) example considering force at direction x_1, and the solution components U_{1l} for this case.

The traction vector at the surface Γ (Figure 2.2) can be written as

$$p_k = T_{lk} e_l, \tag{2.24}$$

taking the fundamental solution for a traction on the direction k when a unit load is applied on point $\mathbf{x}'$ at the direction l

$$T_{lk} = \frac{-1}{8\pi(1-\nu)r^2}\left\{\frac{\partial r}{\partial n}\left[(1-2\nu)\delta_{lk} + 3r_{,l}r_{,k}\right] - (1-2\nu)(r_{,l}n_k - r_{,k}n_l)\right\}, \tag{2.25}$$

where n_l is the component on the direction e_l of the outward normal vector of surface Γ at the point $\mathbf{x}$. $\partial r/\partial n$ is the derivative of r relative to the outward normal vector n [Brebbia et al., 2012].

2.2 Elastic stiffness tensor symmetries

Let σ_{ij} be the Cauchy stress tensor, and ε_{ij} the linear small strain tensor, and let the generalized Hooke's law be

$$\sigma_{ij} = c_{ijkl}\varepsilon_{kl}, \tag{2.26}$$

where c_{ijkl} is the fourth-order stiffness tensor.

The Voigt notation, or reduced notation, as described by Chadwick et al., 2001, is

$$11 \to 1 \quad 22 \to 2 \quad 11 \to 3 \quad 23 \to 4 \quad 13 \to 5 \quad 12 \to 6, \tag{2.27}$$

thus the fourth order stiffness tensor is reduced to a $[6 \times 6]$ matrix, e.g., $c_{1123} = c_{14}$, $c_{3112} = c_{56}$. In that fashion, the stress and strain tensors can also be written as vectors,

i.e.,

$$\sigma_i = c_{ij}\varepsilon_j. \tag{2.28}$$

Let m be the number of independent elastic constants on the elastic tensor. One can classify elastic materials by the number of crystallographic symmetry planes. According to Chadwick et al., 2001, this classification can be reduced to eight basic elastic symmetries:

(i) The isotropic, being the simplest one, has infinite symmetry planes and, therefore, only two independent elastic constants. Its structure is:

$$C = \begin{bmatrix} c_{11} & c_{12} & c_{12} & 0 & 0 & 0 \\ & c_{11} & c_{12} & 0 & 0 & 0 \\ & & c_{11} & 0 & 0 & 0 \\ & & & \otimes & 0 & 0 \\ & & & & \otimes & 0 \\ & & & & & \otimes \end{bmatrix}, \quad \otimes = \frac{(c_{11} - c_{12})}{2}, \quad m = 2, \tag{2.29}$$

According to Head, 1979, the isotropic symmetry is not found naturally in monolithic crystalline structures, and the simplest crystal is the Hexagonal, followed by the Cubic crystal.

(ii) The hexagonal crystal has infinite planes of symmetry. It is also known as the transversely isotropic material, although this is a consequence of having an axis of symmetry, rather than a direct property as in the isotropic case, and due to this axis of symmetry, it has five (5) independent elastic constants. A transversely isotropic material with symmetry axis at x_3, behaves isotropically at the plane x_1x_2, i.e., the following stiffness tensor arises,

$$C = \begin{bmatrix} c_{11} & c_{12} & c_{13} & 0 & 0 & 0 \\ & c_{11} & c_{13} & 0 & 0 & 0 \\ & & c_{33} & 0 & 0 & 0 \\ & & & c_{44} & 0 & 0 \\ & & & & c_{44} & 0 \\ & & & & & \frac{(c_{11}-c_{12})}{2} \end{bmatrix}, \quad m = 5, \tag{2.30}$$

where c_{11}, c_{12}, c_{13}, c_{33}, and c_{44} are the only independent elastic constants.

(iii) The cubic crystal, differently to the hexagonal one, has a finite number of symme-

try planes (nine) but has only three (3) independent elastic constants. The lesser amount of planes causes the cubic to be worse than the hexagonal (for obtaining the Green's function), although it appears to be less complicated for having less independent constants. Considering the cubic material with its principal axes aligned with the coordinate system, it has the following stiffness tensor,

$$C = \begin{bmatrix} c_{11} & c_{12} & c_{12} & 0 & 0 & 0 \\ & c_{11} & c_{12} & 0 & 0 & 0 \\ & & c_{11} & 0 & 0 & 0 \\ & & & c_{44} & 0 & 0 \\ & & & & c_{44} & 0 \\ & & & & & c_{44} \end{bmatrix}, \quad m = 5, \tag{2.31}$$

where c_{11}, c_{12}, and c_{44} are the only independent elastic constants, and defining $A = 2c_{44}/(c_{11} - c_{12})$, is the Zener's anisotropic index which, for $A \neq 1$, the material is not isotropic.

(iv) Next in the anisotropy level is the Tetragonal, which has five (5) planes of symmetry and six (6) independent elastic constants. This material has a stiffness tensor similar to the transversely isotropic one, but with the shear modulus being independent to the other constants (similarly to the cubic crystal).

(v) The orthotropic (also known as Rhombic) material has three orthogonal planes of symmetry (the coordinate planes $\theta = 0$, $\theta = \pi/2$ and $\phi = 0$) and has 9 independent elastic constants. Laminated fiber-reinforced composites present this symmetry at the macro scale, [Lempriere, 1968; Ayorinde and Gibson, 1993; Frederiksen, 1997]. Its elastic tensor for this symmetry has the following configuration

$$C = \begin{bmatrix} c_{11} & c_{12} & c_{13} & 0 & 0 & 0 \\ & c_{22} & c_{23} & 0 & 0 & 0 \\ & & c_{33} & 0 & 0 & 0 \\ & & & c_{44} & 0 & 0 \\ & & & & c_{55} & 0 \\ & & & & & c_{66} \end{bmatrix}, \quad m = 9. \tag{2.32}$$

(vi) The first to present coupling between the shear and the normal constants — the

Trigonal has only three planes of symmetry (at $\theta = 0$ and $\theta = \pm\pi/3$). Although it has only six (6) independent elastic constants, the stiffness matrix is more populated than the Transversely isotropic because some constants are repeated. The in-plane shear modulus depends on the normal stiffness components as in transversely isotropic materials, e.g., $c_{44} = (c_{11} - c_{12})/2$, i.e.,

$$C = \begin{bmatrix} c_{11} & c_{12} & c_{13} & c_{14} & 0 & 0 \\ & c_{11} & c_{13} & -c_{14} & 0 & 0 \\ & & c_{33} & 0 & 0 & 0 \\ & & & c_{44} & 0 & 0 \\ & & & & c_{44} & c_{14} \\ & & & & & \frac{(c_{11}-c_{12})}{2} \end{bmatrix}, \quad m = 6, \tag{2.33}$$

where c_{11}, c_{12}, c_{13}, c_{33}, c_{44} and c_{34} are the essential elastic constants. Quartz is an example of such material configuration [see Heyliger et al., 2003].

(vii) The last material configuration which does not possess 21 unique elastic constants is the Monoclinic. It has only one symmetry plane, which, when aligned with the coordinate axis, e.g, x_1, produces coupling between its shear module, $c_{56} \neq 0$, and coupling between the shear and longitudinal modules from all three directions, i.e., $c_{41} \neq c_{42} \neq c_{43} \neq 0$. This situation results in 13 independent elastic constants, which, considering the symmetry plane is x_2x_3 at $x_1 = 0$, Ting, 1996,

$$C = \begin{bmatrix} c_{11} & c_{12} & c_{13} & c_{14} & 0 & 0 \\ & c_{22} & c_{23} & c_{24} & 0 & 0 \\ & & c_{33} & c_{34} & 0 & 0 \\ & & & c_{44} & 0 & 0 \\ & & & & c_{55} & c_{56} \\ & & & & & c_{66} \end{bmatrix}, \quad m = 13. \tag{2.34}$$

(viii) The triclinic crystal has no symmetry planes and all 21 independent elastic constants.

2.3 Green's function for General Anisotropic Elasticity

The fundamental solutions brought in Section 2.1, are the basis for the BEM precision, and for many of the mathematical barriers which are yet objective of advanced research. One can select these functions matching the problem under consideration, and, in the case of 3D linear elasticity, it corresponds to the infinite space Green's function for displacements (and its derivatives). That function is the particular solution of the governing differential equations for the displacement resultant at an observation point $\mathbf{x}$, for a point load (Dirac delta) at a source point $\mathbf{x}'$.

One of the assumptions which simplifies the solution of the Green's function is that the domain under consideration has constant and homogeneous elastic properties throughout the space. Although it is a dual point function, due to such assumption, the source point $\mathbf{x}'$ can be considered as the origin of the coordinate system without loss of generality, and $U = f(\mathbf{x}, \mathbf{x}')$ becomes $U = f(\mathbf{x})$.

In the procedure presented in Section 2.1, which results in Equation 2.23, the isotropic stress-strain law (Equation 2.6) was directly applied in the equilibrium equations resulting in the Navier's equation of equilibrium, which is written explicitly in terms of the displacements. That procedure resulted in a simpler set of partial differential equations to be solved. The formulations for anisotropic elasticity provide the Navier's equation in a general form, without any material assumption. A solution for such a problem is more difficult (and cumbersome) to obtain than Kelvin's. Lifshitz and Rozentsveig, 1947, demonstrated that it is possible to obtain this solution explicitly in terms of the roots of a sixth-order characteristic equation for the general anisotropic case. Those roots were later called the Stroh's eigenvalues, named after A.N. Stroh, which published many essential works in the field, such as Stroh, 1958, Stroh, 1962. In those works, the author devised a procedure that would be later called the formalism of Stroh. The virtue of this approach is that, for plane problems, any solution can be written as a sum of arbitrary functions.

When solving for the three-dimensional Green's function, one has to perform a one-dimensional integration of some sort, which has many forms of being surpassed: The simplest one is the integral formalism, which performs the contour integral at the oblique plane to the position vector. This form is the one presented by Barnett, 1972, employing a Fourier transform method to solve the anisotropic Navier's equation. This was performed to clarify its extension to alternative methods for calculating Green's function derivatives.

In Lifshitz and Rozentsveig, 1947, the authors perform the integration at the oblique plane through residue calculus. This approach leads to a finite sum over the poles of the function, which are shown to be the roots of a sixth-order polynomial in terms of the position vector and the material constants. As it is known for many years since Head, 1979, the roots of the generalized sixth-order polynomial, which arises on general anisotropic elasticity, are not solvable in closed form.

Although in some specific cases the cubic symmetry is solvable, in the general case the author states "for general directions and elastic constants, is impossible to express the roots of the sextic as a formula of finite length containing only arithmetic operations, radicals, rational numbers and the symbols denoting the elastic constants and the direction in the crystal."[Head, 1979]. Although it is possible to obtain these solutions explicitly for the general case, the process always has to rely on numerical schemes to evaluate the Stroh eigenvalues or the roots of the sixth.

Another crystal symmetry mentioned by Head, 1979, are the ones in which the characteristic equation reduces to a third-degree polynomial in p^2. In this case, the Green's function can be obtained explicitly in terms of the position and the material constants. That is also true for points at the symmetry plane of the monoclinic material [Ting and Lee, 1997]. For the transversely isotropic, which is a particular case of the monoclinic, this is true for any plane which contains the axis of symmetry. This property is demonstrated by Ting and Lee, 1997, for the monoclinic material and extended for a transversely isotropic material. The solution is obtained first for a point at the $x_2 = 0$ plane and then generalized using rotation matrices for points where $x_2 \neq 0$, obtaining then a closed form solution for any point $\mathbf{x}$. This approach is the one used in Távara et al., 2008, for instance.

As is briefly demonstrated in this chapter, there are many forms to obtain and present Green's function for the general anisotropic case. Xie et al., 2016, compared three of the most common Green's function formulations for three-dimensional elasticity, among them, their own previously proposed solution. In this work, it is possible to observe the high computational cost of these functions. Nevertheless, the authors do not present any comparison on the evaluation of the first-order derivative, necessary in all the BEM variants.

Another method commonly found in the literature to obtain Green's functions with

simplicity is the Radon transform. In Wang and Achenbach, 1995, this transform is used to obtain the Green's function for the elastodynamic problem, considering anisotropic elasticity. As the authors assemble the solution in a convolution scheme, the explicit solution still possesses the time integration as expected. Wang, 1997, presented a similar solution for elastostatics integrating with residue calculus.

Although Ting, 1996, presented a formalism to obtain fundamental solutions through the Lekhnitskii formalism, which starts with the equilibrated stress functions followed by compatibility equations, this chapters limits itself to the presentation of the *Stroh's formalism*. This theorem begins with the compatible displacements followed by the equilibrium equations [Hwu, 2010].

2.3.1 The sextic Stroh's formalism in two dimensions

Although the Stroh's formalism was not entirely devised by himself, as it bases in the work of Eshelby et al., 1953, it set a common ground for many other works [Ting, 1996]. The works which laid the foundation for this formalism were Stroh, 1958, Stroh, 1962. We present the following sections according to Ting, 1996, and the references therein.

As already stated, the Stroh's formalism in two dimensions starts from the equilibrium equations 2.4, in terms of the displacements. Let define the generalized Hooke's law Equation 2.26, in terms of the displacements as

$$\sigma_{ij} = c_{ijkl} \frac{1}{2} \left(u_{k,l} + u_{l,k} \right). \tag{2.35}$$

Replacing Equation 2.35 in Equation 2.4, results in the equilibrium equations of Navier,

$$c_{ijkl} u_{k,li} = 0. \tag{2.36}$$

Considering two-dimensional deformations, in which u_i depends on x_1 and x_2 only, Equation 2.36 is an homogeneous second-order differential equation consisting of two independent variables. A general solution for u_i can be written, without loss of generality, as

$$u_i = a_i f(z), \tag{2.37}$$

where

$$z = x_1 + p\, x_2, \tag{2.38}$$

and $f(z)$ is an arbitrary function of z, whether p and a_i are unknown constants to be determined [Ting, 1996].

Differentiating Equation 2.37 with respect to x_s gives

$$u_{k,s} = (\delta_{s1} + p\delta_{s2})a_k f'(z), \tag{2.39}$$

in which prime denotes differentiation with respect to the argument z and δ_{si} is the Kronecker delta. Differentiating Equation 2.39 with respect to x_j, the differential equation will be satisfied with non-trivial solutions if

$$c_{ijkl}(\delta_{j1} + p\delta_{j2})(\delta_{l1} + p\delta_{l2})a_k = 0 \tag{2.40}$$

or

$$\left\{c_{i1k1} + p(c_{i1k2} + c_{i2k1}) + p^2 c_{i2k2}\right\} a_k = 0. \tag{2.41}$$

Equation 2.41 can be written in terms of some well-known identities, $\mathbf{Q}$, $\mathbf{R}$, $\mathbf{T}$, defined in two-dimensional problem as

$$Q_{ik} = c_{i1k1}, \quad R_{ik} = c_{i1k2}, \quad T_{ik} = c_{i2k2}, \tag{2.42}$$

which results in the classic matrix notation,

$$\left\{\mathbf{Q} + p(\mathbf{R} + \mathbf{R}^T) + p^2\mathbf{T}\right\} \mathbf{a} = 0, \tag{2.43}$$

which for a non-trivial solution of $\mathbf{a}$, one must have

$$\left|\mathbf{Q} + p(\mathbf{R} + \mathbf{R}^T) + p^2\mathbf{T}\right| = 0, \tag{2.44}$$

which gives six roots for the eigenvalue p [Ting, 1996].

The stress formulation is an important relation obtained from the Stroh's formalism. Applying Equation 2.39 in the stress-strain law Equation 2.35 gives

$$\begin{aligned} \sigma_{i1} &= (Q_{ik} + pR_{ik})a_k f'(z), \\ \sigma_{i2} &= (R_{ki} + pT_{ik})a_k f'(z). \end{aligned} \tag{2.45}$$

Equation 2.45 can be rewritten as

$$\sigma_{i1} = -p\, b_i\, f'(z), \tag{2.46}$$

$$\sigma_{i2} = \quad b_i\, f'(z), \tag{2.47}$$

where, vectors $\mathbf{a}$ and $\mathbf{b}$ are related by

$$\mathbf{b} = (\mathbf{R}^T + p\mathbf{T})\mathbf{a} = -\frac{1}{p}(\mathbf{Q} + p\mathbf{R})\mathbf{a}, \tag{2.48}$$

which follows from Equation 2.43. It is possible to assemble these two equations in the following form

$$\begin{bmatrix} -\mathbf{Q} & 0 \\ -\mathbf{R}^T & \mathbf{I} \end{bmatrix} \begin{bmatrix} \mathbf{a} \\ \mathbf{b} \end{bmatrix} = p \begin{bmatrix} \mathbf{R} & \mathbf{I} \\ \mathbf{T} & 0 \end{bmatrix} \begin{bmatrix} \mathbf{a} \\ \mathbf{b} \end{bmatrix}, \tag{2.49}$$

being $\mathbf{I}$ the identity matrix. According to Ting, 1996, $\mathbf{Q}$ and $\mathbf{T}$ are symmetric and positive definite, therefore, one can pre-multiply both sides of Equation 2.49, by

$$\begin{bmatrix} \mathbf{0} & \mathbf{T}^{-1} \\ \mathbf{I} & -\mathbf{R}\mathbf{T}^{-1} \end{bmatrix}, \tag{2.50}$$

so the former system, Equation 2.49, can be reduced to the following standard eigenrelation,

$$\mathbf{N} \begin{bmatrix} \mathbf{a} \\ \mathbf{b} \end{bmatrix} = p \begin{bmatrix} \mathbf{a} \\ \mathbf{b} \end{bmatrix} \tag{2.51}$$

where,

$$\mathbf{N} = \begin{bmatrix} \mathbf{N}_1 & \mathbf{N}_2 \\ \mathbf{N}_3 & \mathbf{N}_1^T \end{bmatrix}, \tag{2.52}$$

and

$$\mathbf{N}_1 = -\mathbf{T}^{-1}\mathbf{R}^T, \quad \mathbf{N}_2 = \mathbf{T}^{-1}, \quad \mathbf{N}_3 = \mathbf{R}\mathbf{T}^{-1}\mathbf{R}^T - \mathbf{Q}. \tag{2.53}$$

The $[6 \times 6]$ matrix $\mathbf{N}$ is the *fundamental elasticity matrix*, and it is used to obtain the Stroh's eigenvalues.

The following stress function is introduced to obtain stress and displacement,

$$\varphi_i^{\mathrm{S}} = b_i f(z), \tag{2.54}$$

such that one can write the stress tensor from Equation 2.46 as

$$\sigma_{i1} = \varphi_{i,2}^{\mathrm{S}}, \quad \sigma_{i2} = \varphi_{i,1}^{\mathrm{S}}. \tag{2.55}$$

The general stress function solution $\boldsymbol{\varphi}^{\mathrm{S}}$ is obtained by superposing six solutions in the form of Equation 2.54 associated with the six eigenvalues p_α, $(\alpha = [1, 6])$ [Ting, 1996].

These solutions for displacement and stress are expressed in the following form,

$$\mathbf{u} = \sum_{\alpha=1}^{3} \left\{ \mathbf{a}_\alpha f_\alpha(z_\alpha) + \bar{\mathbf{a}}_\alpha f_{\alpha+3}(\bar{z}_\alpha) \right\}, \tag{2.56}$$

$$\boldsymbol{\varphi}^{\mathrm{S}} = \sum_{\alpha=1}^{3} \left\{ \mathbf{b}_\alpha f_\alpha(z_\alpha) + \bar{\mathbf{b}}_\alpha f_{\alpha+3}(\bar{z}_\alpha) \right\}, \tag{2.57}$$

where $\bar{\cdot}$ stands for complex conjugate, vectors $\mathbf{a}_\alpha$ and $\mathbf{b}_\alpha$ are the Stroh eigenvectors, and $z_\alpha = x_1 + p_\alpha x_2$, and Equations 2.56 and 2.57 are the sextic formalism of Stroh.

Notice that from Equations 2.48 and 2.49, the following matrices arise, composed by the eigenvectors $\mathbf{a}$ and $\mathbf{b}$,

$$\mathbf{A} = [\mathbf{a}_1, \mathbf{a}_2, \mathbf{a}_3], \tag{2.58}$$

$$\mathbf{B} = [\mathbf{b}_1, \mathbf{b}_2, \mathbf{b}_3], \tag{2.59}$$

which, through some algebraic manipulation of previous relations, is possible to write the so-called Barnett-Lothe tensors, $\mathbf{S}$, $\mathbf{H}$, $\mathbf{L}$,

$$\mathbf{S} = 2\mathrm{i}\mathbf{B}\mathbf{B}^T, \tag{2.60}$$

$$\mathbf{H} = 2\mathrm{i}\mathbf{A}\mathbf{A}^T, \tag{2.61}$$

$$\mathbf{L} = \mathrm{i}\left(\mathbf{A}\mathbf{B}^T - I\right). \tag{2.62}$$

It is worth mentioning that $\mathbf{H}$ is the second Barnett-Lothe tensor, as is shown later on, it is the modulatory part of Green's function.

One should notice that the columns of $\mathbf{A}$ and $\mathbf{B}$ are linearly independent as in Equation 2.58, they are formed by the Stroh's eigenvectors, thus their product must be purely imaginary [Hwu, 2010].

Although Equation 2.61 would be useful to compute the (second) Barnett-Lothe tensor $\mathbf{H}$, it requires the computation of the eigenvectors $\mathbf{A}$ (and $\mathbf{B}$), which have higher computational cost than the alternatives presented in the literature based on numerical integration or which require only the eigenvalues.

2.3.2 Stroh's eigenrelation for an oblique plane

Although the Stroh's formalism was initially devised in two dimensions, it can be generalized to three-dimensional space if one considers an oblique plane normal to the

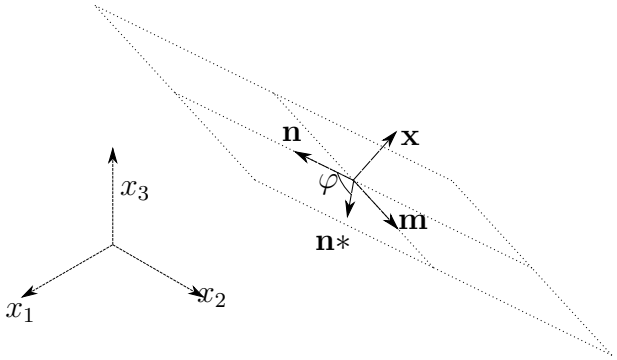

Figure 2.3 – The oblique plane and the right-handed triad $[\mathbf{n}, \mathbf{m}, \mathbf{x}]$, the $\mathbf{n}*$ vector, and ψ, its angle with $\mathbf{n}$.

position vector in this space, instead of the x_1, x_2 plane in Equation 2.41. The precursor of this extension is the work of Barnett and Lothe, 1975. Let us define the oblique plane by a right-handed triad $[\mathbf{n}, \mathbf{m}, \mathbf{k}]$, where $[\mathbf{n}, \mathbf{m}]$ are tangent vectors and $\mathbf{k}$ is the outward normal vector, as illustrated in Figure 2.3. If $\mathbf{m}$ and $\mathbf{n}$ are set as the new x_1 and x_2 axes, tensors $\mathbf{Q}$, $\mathbf{R}$, $\mathbf{T}$ also can be redefined at this new 3D framework,

$$Q_{ik} = c_{ijks} n_j n_s, \quad R_{ik} = c_{ijks} n_j m_s, \quad T_{ik} = c_{ijks} m_j m_s. \tag{2.63}$$

One can easily see that they reduce to their 2D versions when $\mathbf{n}$ and $\mathbf{m}$ coincide with x_1 and x_2. In order to provide some physical meaning to these tensors, Ting, 1996, points out that Q_{ik} is the *acoustic tensor* for waves propagating in the direction of $\mathbf{n}$. Analogously, this also holds for the pair T_{ik} and $\mathbf{m}$. Tensor R_{ik} does not relate to any physical meaning in the literature.

The standard Stroh's eigenrelation, Equation 2.52 remains valid in the same fashion, and the newly introduced 3D notation does not change it by any means with the consideration of Equation 2.63.

2.3.3 Elastic Green's function for the infinite space

The fundamental solution applied as weight function in the BEM formulation is the Green's function for the infinite space (and its first spatial derivative). According to Ting, 1996, it can be expressed in terms of the three Barnett-Lothe tensors $\mathbf{S}$, $\mathbf{H}$, $\mathbf{L}$, at the oblique plane. The main difference to the two-dimensional deformations considered previously is that the 3D equilibrium equations are written such that the displacements

and deformations depend on all x_i, $(i = [1, 3])$. If Navier's equilibrium equations are written considering a concentrated force $\mathbf{f}$ is considered at the origin $\mathbf{x} = \mathbf{0}$, the right-hand side of Equation 2.36 including this force is

$$c_{ijks}u_{k,sj} = -\delta(x_1)\delta(x_2)\delta(x_3)f_i, \tag{2.64}$$

where $\delta(x)$ is the Dirac delta function. The solution of Equation 2.64 proposed by Lifshitz and Rozentsveig, 1947 is performed through a Fourier transform with respect to x_1, x_2, x_3, which is

$$c_{ijks}y_j y_s \tilde{u}_{k,sj} = f_i \tag{2.65}$$

where y_i are the transform parameters and

$$\tilde{u}_k = \iiint u_k(x_1, x_2, x_3)e^{(\mathbf{i}\mathbf{y}\cdot\mathbf{x})}dx_1dx_2dx_3, \tag{2.66}$$

while vector $\mathbf{y}$ in the integrand is

$$\mathbf{y}^T = [y_1, y_2, y_3]. \tag{2.67}$$

Solving $\tilde{u}_k$ from Equation 2.65, and performing the inverse transforms, leads to

$$\mathbf{u} = \frac{1}{2\pi^3}\iiint \mathbf{Q}^{-1}\,\mathbf{f}\,e^{-(\mathbf{i}\mathbf{y}\cdot\mathbf{x})}dy_1dy_2dy_3 \tag{2.68}$$

where

$$Q_{ik}(\mathbf{y}) = c_{ijks}y_j y_s. \tag{2.69}$$

A recurrent reference for the reduction of the integral in Equation 2.68 is the work of Lifshitz and Rozentsveig, 1947, which has shown that it is reducible to

$$\mathbf{u} = \frac{1}{8\pi^2 r}\int_S \mathbf{Q}^{-1}(\mathbf{y})\mathbf{f}ds, \tag{2.70}$$

where $r = |\mathbf{x}|$ and the integral is performed around the unit circle S, with $|\mathbf{y}| = 1$ on the oblique plane normal to $\mathbf{x}$ [Ting, 1996].

To further reduce the integral in Equation 2.70, let define a unit vector $\mathbf{n}^*$ on the oblique plane,

$$\mathbf{n}^* = \mathbf{n}\cos\psi + \mathbf{m}\sin\psi, \tag{2.71}$$

where ψ is an arbitrary parameter, $\mathbf{m}$ and $\mathbf{n}$ are any mutually orthogonal unit vectors on

an oblique plane whose normal is $\mathbf{x}$ (Figure 2.3). Hence, Equation 2.69 is rewritten as

$$Q_{ik}(\psi) = c_{ikjs}(n_j \cos\psi + m_j \sin\psi)(n_s \cos\psi + m_s \sin\psi), \tag{2.72}$$

which reduces to Equation 2.63, when $\psi = 0$. Also, $Q_{ik}(\psi)$ is periodic in ψ with period π, as is possible to confirm in Equation 2.72.

Writing Equation 2.70 as $\mathbf{u} = \mathbf{U}(\mathbf{x})\mathbf{f}$, and applying Equation 2.72 in $\mathbf{U}(\mathbf{x})$, results in

$$\mathbf{U}(\mathbf{x}) = \frac{1}{4\pi^2 r}\int_{-\pi/2}^{\pi/2} \mathbf{Q}^{-1}(\psi)d\psi, \tag{2.73}$$

where the integration is performed only in half the unit circle, as $Q_{ik}(\psi)$ is periodic in ψ with period π [Ting and Lee, 1997].

Equations 2.70 and 2.73 represent the Green's function for the displacements $\mathbf{u}$ resulting from a point load $\mathbf{f}$. Although this solution is simple to implement, it is of limited practical usage in BEM due to the line integral, which can be cumbersome and has to be numerically calculated.

Also, notice that it requires the inversion of the acoustic tensor $\mathbf{Q}$ at each independent position vector. Nevertheless, Equation 2.73 is a straightforward manner for numerically evaluating the three-dimensional Green's function.

To avoid the integration of Equation 2.73, since Q_{ik}, R_{ik}, and T_{ik}, are independent of ψ, it is possible to rewrite Equation 2.72, as

$$\mathbf{Q}(\psi) = \mathbf{Q}\cos^2\psi + (\mathbf{R} + \mathbf{R}^T)\cos\psi\sin\psi + \mathbf{T}\sin^2\psi = \cos^{\frac{1}{2}}\boldsymbol{\Gamma}(p), \tag{2.74}$$

where $p = \tan\psi$, and the Christoffel tensor $\Gamma_{ij}(p)$ is defined as

$$\boldsymbol{\Gamma}(p) = \mathbf{Q} + p(\mathbf{R} + \mathbf{R}^T) + p^2\mathbf{T}. \tag{2.75}$$

Notice that, as is known from the Stroh's formalism, the determinant of $\Gamma_{ij}(p)$ is null,

$$|\boldsymbol{\Gamma}(p)| = 0, \tag{2.76}$$

which leads to the sixth-order equation in p, i.e., Equations 2.44 and 2.51.

Equation 2.73 can be written in terms of the second Barnett-Lothe tensor as

$$\mathbf{U}(\mathbf{x}) = \frac{1}{4\pi r}\mathbf{H}(\hat{\mathbf{e}}), \tag{2.77}$$

where,

$$\mathbf{H}(\hat{\mathbf{e}}) = \frac{1}{\pi}\int_{-\pi/2}^{\pi/2} \mathbf{Q}^{-1}(\psi)d\psi. \tag{2.78}$$

If Equation 2.74 and the identity $p = \tan\psi$ are applied in Equation 2.78, it can be rewritten as

$$\mathbf{H}(\hat{\mathbf{e}}) = \frac{1}{\pi}\int_{-\infty}^{\infty} \mathbf{\Gamma}^{-1}(p)dp. \tag{2.79}$$

To avoid a matrix inversion $\hat{\mathbf{\Gamma}}(p)$, the adjoint of $\mathbf{\Gamma}(p)$, also mentioned in the literature as the co-factor matrix, is considered and is defined as

$$\mathbf{\Gamma}(p)\hat{\mathbf{\Gamma}}(p) = \left|\hat{\mathbf{\Gamma}}(p)\right|\mathbf{I}, \tag{2.80}$$

applying Equation 2.80 in Equation 2.79 one rewrites it as

$$\mathbf{H}(\hat{\mathbf{e}}) = \frac{1}{\pi}\int_{-\infty}^{\infty} \frac{\hat{\Gamma}_{ij}(p)}{|\mathbf{\Gamma}(p)|}dp. \tag{2.81}$$

Let p_v $(v = 1, 2, 3)$ be the roots of the positive imaginary part. Using Cauchy residue theory, one can replace the integral by a contour one over the upper half of the complex plane p (See e.g. Sveshnikov and Tikhonov, 1971, Chapter 5), obtaining

$$\mathbf{H}(\hat{\mathbf{e}}) = 2\mathrm{i}\sum_{v=1}^{3} \frac{\hat{\Gamma}_{ij}(p_v)}{|\mathbf{\Gamma}(p_v)|'}, \tag{2.82}$$

where $|\Gamma_{ij}(p_v)|' = d(|\Gamma_{ij}(p_v)|)/dp$. Equation 2.82 is mathematically equal to the one obtained by Lifshitz and Rozentsveig, 1947. With Equation 2.82 presented, it clears the need of the identity in Equation 2.80: It enables one to apply the Cauchy residue theory, transforming the integral in a simple sum of the residues. The integral over p from $-\infty$ to ∞ can be replaced by the sum of the function residues at the poles p_v. It is worthwhile to mention that, the function must be complex analytic in the upper half-plane (in the sense of a holomorphic function) to eliminate this integral.

Is possible to write $|\mathbf{\Gamma}(p_v)|'$ explicitly in terms of the Stroh eigenvalues from Equation 2.75 as

$$|\mathbf{\Gamma}(p_v)| = |\mathbf{T}|\, f(p), \tag{2.83}$$

$$f(p) = (p - p_1)(p - \bar{p}_1)(p - p_2)(p - \bar{p}_2)(p - p_3)(p - \bar{p}_3), \tag{2.84}$$

so Equation 2.82 resumes to

$$\mathbf{H}(\hat{\mathbf{e}}) = \frac{2\mathrm{i}}{|\mathbf{T}|}\sum_{v=1}^{3} \frac{\hat{\Gamma}(p_v)}{f'(p)}, \tag{2.85}$$

where $f'(p) = df(p)/dp$, which is exemplified by Ting and Lee, 1997 with $f'(p_1)$ being

$$f'(p_1) = (p - \bar{p}_1)(p_1 - p_2)(p_1 - \bar{p}_2)(p_1 - p_3)(p_1 - \bar{p}_3), \tag{2.86}$$

and expressions for $f'(p_2)$ and $f'(p_3)$ also can easily be obtained. Equation 2.85 is not valid for degenerate cases (repeated eigenvalues). Moreover, it does not show that $H(\hat{\mathbf{e}})$ is real as expected. In the next section, an alternative expression for this solution, proposed by Ting and Lee, 1997, is presented.

2.3.4 Ting and Lee's polynomial decomposition

An alternative expression for Equation 2.85 was proposed by Ting and Lee, 1997, which is valid for non-degenerate cases and also has a clearly real-valued result. For that purpose it must be defined that the eigenvalues p_v are arbitrary complex variables defined as

$$p_v = \alpha_v + \mathbf{i}\beta_v, \quad \beta_v > 0 (v = 1, 2, 3). \tag{2.87}$$

The formulation proposed by Ting is based on the fact that the co-factor matrix $\hat{\Gamma}(p)$ is a fourth degree polynomial in p. It can be written in the following manner

$$\hat{\Gamma}(p) = \sum_{n=0}^{4} p^n \hat{\Gamma}^{(n)}, \tag{2.88}$$

where the real matrices $\hat{\Gamma}^{(n)}$ $(n = 0, 1, 2, 3, 4)$ are independent of p. Following Ting and Lee, 1997, Equation 2.85 can be written as

$$\mathbf{H}(\hat{\mathbf{e}}) = \frac{2\mathbf{i}}{|\mathbf{T}|} \sum_{n=0}^{4} q^{(n)} \hat{\Gamma}^{(n)}, \tag{2.89}$$

where

$$q^{(n)} = \left\{ \frac{p_1^n}{\beta_1 (p_1 - p_2)(p_1 - \bar{p}_2)(p_1 - p_3)(p_1 - \bar{p}_3)} + \dots \right\}. \tag{2.90}$$

By means of Equation 2.90 is not clear if Equation 2.89 is valid for degenerate cases. As can be seen in Equation 2.75, $\hat{\Gamma}$ depends on the material properties and the oblique vectors $\mathbf{m}$, $\mathbf{n}$. The final expression for $q^{(n)}$ is found in Ting and Lee, 1997, while the ones for each term of the co-factor matrix $\hat{\Gamma}^{(n)}$ are found in Shiah et al., 2012, which are included here for completeness

$$\hat{\Gamma}_{ij}^{(n)} = \tilde{\Gamma}_{(i+1)(j+1)(i+2)(j+2)}^{(n)} - \tilde{\Gamma}_{(i+1)(j+2)(i+2)(j+1)}^{(n)}, \qquad (i, j = 1, 2, 3) \tag{2.91}$$

where

$$\begin{aligned}
\tilde{\Gamma}^{(4)}_{pqrs} &= T_{pq}T_{rs},\\
\tilde{\Gamma}^{(3)}_{pqrs} &= V_{pq}T_{rs} + T_{pq}V_{rs},\\
\tilde{\Gamma}^{(2)}_{pqrs} &= T_{pq}Q_{rs} + Q_{pq}T_{rs}, + V_{pq}V_{rs},\\
\tilde{\Gamma}^{(1)}_{pqrs} &= V_{pq}Q_{rs} + Q_{pq}V_{rs},\\
\tilde{\Gamma}^{(0)}_{pqrs} &= Q_{pq}Q_{rs},
\end{aligned}$$

where matrices Q, R, T, are the acoustic tensors previously defined in Equation 2.63, and $V_{pq} = R_{pq} + R_{qp}$.

2.3.5 Multiple pole residue approach from Buroni et al., 2011

The solution proposed by Buroni et al., 2011 deals with material degeneracy by the application of different formulations for each combination of the Stroh's eigenvalues. It is also valid for cases where these values are different but too close in magnitude to each other which causes near-degeneracy. The most extreme case of degeneracy is the isotropic symmetry which all the eigenvalues are constant and only imaginary, $p_1 = p_2 = p_3 = \mathrm{i}$ [Ting and Lee, 1997]. The solution generates 3 cases:

(i) Three different eigenvalues $p_1 \neq p_2 \neq p_3$: For this case **Equation 2.85** is used since this case is not degenerate. This representation is also *cheaper* computationally than Equation 2.89. The final version presented by Buroni and Sáez, 2010, has a more compact form than the one presented by Ting,

$$H_{jk} = \frac{1}{|\mathbf{T}|}\sum_{\alpha=1}^{3}\frac{\hat{\Gamma}_{jk}(p_\alpha)}{\beta_\alpha \prod_{\substack{\xi=1\\ \xi\neq\alpha}}^{3}(p_\alpha - p_\xi)(p_\alpha - \bar{p}_\xi)}, \tag{2.92}$$

where the symbol $\prod_{a=1}^{n}(p_a)$ represents a product with indices varying from $a = 1$ to $a = n$. The denominator in Equation 2.92 is mathematically the same as Equation 2.84.

(ii) Two repeated eigenvalues $p_1 = p_2 \neq p_3$ For the case when two eigenvalues are equal $p_1 = p_2 = p_0$, and a third one is different, $p_3 \neq p_0$, the Barnett-Lothe tensor is

evaluated as follows

$$H_{jk}(\hat{\mathbf{e}}) = \frac{1}{|\mathbf{T}|}\left[\frac{2\mathbf{i}}{-4\beta_0^2(p_0-p_3)(p_0-\bar{p}_3)}\right.$$
$$\left.\left\{\hat{\Gamma}'_{jk}(p_0) - \hat{\Gamma}_{jk}(p_0)\left(\frac{1}{p_0-p_3}+\frac{1}{p_0-\bar{p}_3}+\frac{1}{\mathbf{i}\beta_0}\right)\right\}\frac{\hat{\Gamma}_{jk}(p_3)}{\beta_3(p_3-p_0)^2(p_3-\bar{p}_0)^2}\right]. \quad (2.93)$$

(iii) Finally, when the three eigenvalues are equal, $p_1 = p_2 = p_3 = p_0$, the formulation used is

$$H_{jk}(\hat{\mathbf{e}}) = \frac{3\hat{\Gamma}_{jk}(p_0) - \beta_0\left(3\mathbf{i}\hat{\Gamma}'_{jk}(p_0) + \beta_0\hat{\Gamma}''_{jk}(p_0)\right)}{4\,|\mathbf{T}|\,\beta_0^5}. \quad (2.94)$$

Notice that, throughout this chapter, we do not present the free-space Green's function first- or second-order derivatives. For instance, Ting and Lee, 1997, proposes a finite differentiation scheme, which may have some penalty on the precision of the derivative computation. Buroni et al., 2011, presents explicit formulations for the first-order derivatives of the Green's function.

2.4 Green's function for general anisotropic Magneto-electro-elasticity

According to Buroni and Sáez, 2010, the study and application of Magneto-Electro-Elastic (MEE) composite materials have been receiving enormous efforts, due to their enhanced ability to convert energy among the mechanical, electric, and magnetic fields. In an extensive review performed by Nan et al., 2008, it is shown that the magneto-electric effect is more pronounced in composites layered by combinations of piezomagnetic (PM) and piezoelectric (PE) phases together. These composites can produce electromagnetic coupling, which are several orders of magnitude higher than the single-phase materials readily found in nature.

2.4.1 Basic equations of linear magneto-electro-elasticity

Let x_i be a Cartesian coordinate system in three-dimensions, $i = 1 \ldots 3$, the governing equilibrium equations for the Elastic, Electric and Magnetic problems are written

as

$$\sigma_{ij,j} + f_i = 0, \tag{2.95}$$

$$D_{i,i} = f^e = 0, \tag{2.96}$$

$$B_{i,i} = f^m = 0, \tag{2.97}$$

where σ_{ij} is the Cauchy stress tensor, D_i is the electric displacement vector, and B_i is the *magnetic induction* vector. f_i are the body forces vector, f^e is the *electric charge* density, and f^m is the *electric current* density. The infinitesimal strain tensor ε_{ij}, the electric field E_i, and the magnetic field H_i are defined as:

$$\varepsilon_{ij} = \frac{1}{2}(u_{i,j} + u_{j,i}) \tag{2.98}$$

$$E_i = -\varphi_{,i} \tag{2.99}$$

$$H_i = -\vartheta_{,i} \tag{2.100}$$

where u_i denotes the components of the elastic displacement field, φ and ϑ are the electric and magnetic potentials. Equations 2.95 to 2.100 are coupled through a linear constitutive law according to Buroni and Sáez, 2010 and Soh et al., 2005,

$$\sigma_{ij} = C_{ijkl}\varepsilon_{kl} - e_{lij}E_l - q_{lij}H_l, \tag{2.101}$$

$$D_i = e_{ikl}\varepsilon_{kl} - \epsilon_{il}E_l - \lambda_{il}H_l, \tag{2.102}$$

$$B_i = q_{ikl}\varepsilon_{kl} - \lambda_{il}E_l - \mu_{il}H_l, \tag{2.103}$$

where C_{ijkl}, ϵ_{il} and μ_{il} are the elastic stiffness, dielectric permittivity and magnetic permeability tensors, respectively, which represent the uncoupled part, i.e., the individual phenomena, whilst e, q, and λ are piezoelectric, piezomagnetic and magneto-electric coupling tensors, which account for the interaction mechanism between these different potentials. The coefficient tensors present the following symmetries

$$\begin{gathered} C_{ijkl} = C_{jikl} = C_{ijlk} = C_{klij}, \quad e_{kij} = e_{kji}, \quad q_{kij} = q_{kji}, \\ \epsilon_{kl} = \epsilon_{lk}, \quad \lambda_{kl} = \lambda_{lk}, \quad \mu_{kl} = \mu_{lk}, \end{gathered} \tag{2.104}$$

and the elastic, dielectric and magnetic tensors, must be positive definite, i.e., as in elasticity the strain energy is always positive, as well as the respective energies for the

electric and magnetic fluxes

$$\begin{aligned} &C_{ijkl}\varepsilon_{ij}\varepsilon_{kl} > 0, \quad \epsilon_{ij}E_iE_j > 0 \quad \text{and} \quad \mu_{ij}H_iH_j > 0, \\ &\forall \varepsilon_{ij}, E_i, H_i \in \mathbb{R}; \quad \text{and} \quad \varepsilon_{ij} = \varepsilon_{ji} \neq 0, \quad E_i \neq 0, \quad H_i \neq 0. \end{aligned} \tag{2.105}$$

Equation 2.105 is known as the *strong convexity condition* [Ting, 1996]. The potentials in Equations 2.98 to 2.100 could be combined in an extended potential fashion such as developed by Barnett and Lothe, 1975, for PE materials, and is commonly found in the MEE literature [Alshits and Lothe, 1992; Buroni and Sáez, 2010; Buroni et al., 2019]. The extended potential field vector is written as

$$u_J = \begin{cases} u_j & J \leq 3, \\ \varphi & J = 4, \\ \vartheta & J = 5. \end{cases} \tag{2.106}$$

By defining an *extended MEE stiffness matrix* with the following components [Alshits and Lothe, 1992],

$$C_{iJKm} = \begin{cases} C_{ijkm} & J, K \leq 3, \\ e_{mij} & J \leq 3, K = 4, \\ q_{mij} & J \leq 3, K = 5, \\ e_{ikm} & J = 4, K \leq 3, \\ -\lambda_{im} & J = 4, K = 5; \quad J = 5, K = 4, \\ -\epsilon_{im} & J, K = 4, \\ q_{ikm} & J = 5, K \leq 3, \\ -\mu_{im} & J = 5, K = 5, \end{cases} \tag{2.107}$$

where C_{ijkm} are components of the elastic stiffness tensor, at constant electric and magnetic fields, ϵ_{im} is the dielectric permittivity tensor at constant strains and magnetic fields, and μ_{im} is the magnetic permeability at constant stress and electric displacements. ϵ_{im} is the PE coupling coefficients at constant magnetic field, q_{ijk} is the PM coupling at constant electric fields and λ_{im} is the ME coupling coefficients at constant strains and electric fields. This definition is also found in Buroni and Sáez, 2010. The influence of thermal effects is not contemplated, i.e., these coefficients are considered under isothermal conditions.

The extended MEE stiffness matrix has only the symmetry $C_{iJKm} = C_{mKJi}$. As pointed out by Fan, 2009, for piezoelectricity, these matrix representations are not tensors, so one has to be careful when changing coordinates systems.

Taking advantage of the extended coefficient matrix, Equations 2.101 to 2.103 can be recast in a single extended stress tensor, which combines the Cauchy stress, electric displacement and magnetic induction, as

$$\sigma_{iJ} = \begin{cases} \sigma_{ij} & J \leq 3, \\ D_i & J = 4, \\ B_i & J = 5. \end{cases} \tag{2.108}$$

With Equation 2.108 it is possible to recast Equations 2.101 to 2.103, in an extended stress-strain law, in terms of the extended potential vector derivative,

$$\sigma_{iJ} = C_{iJMl}\, u_{M,l}\,. \tag{2.109}$$

With the introduced matrix representation, the elliptic differential equations of equilibrium for the elastic, electric, and magnetic problems in terms of the extended displacements can be recast similarly to the Navier's equation for elasticity as

$$C_{iJKm} u_{K,mi} + f_J = 0, \tag{2.110}$$

where f_J is the extended body force vector, defined as

$$f_J = \begin{cases} f_j & J \leq 3 \\ -f^e & J = 4 \\ -f^m & J = 5, \end{cases}, \tag{2.111}$$

being f_i, f^e, and f^m the three components of body forces, the electric charge density and the electric current density, respectively, and comma denotes differentiation. Notice that uncoupled problems, i.e., purely elastic, electric and/or magnetic, can be considered by setting the corresponding coefficient e_{ijk}, q_{ijk}, or λ_{il} to zero.

2.4.2 Three-dimensional Green's function for anisotropic MEE solids

Let consider a homogeneous and infinite medium in the three-dimensional space Re, and let $\delta(\mathbf{x})$ be the Dirac delta function centered at the origin of a fixed Cartesian coordinate system x_i and δ_{JK} the five-dimensional Kronecker delta. The Green function is a second-order tensor which satisfies the Navier's extended equilibrium equations

$$C_{iJKm} U_{KP,mi}(\mathbf{x}) - \delta_{JP}\delta(\mathbf{x}) = 0, \tag{2.112}$$

where the generalized force corresponds to a point load at the origin $f_J = \delta_{JP}\delta(\mathbf{x})$. The physical description of $U_{JK}(\mathbf{x})$ [Buroni and Sáez, 2010], is the extended potentials at the field point $\mathbf{x}$, due to the application of an extended force f_J at the source point (which in this case is the origin), i.e.,

- the elastic displacement at $\mathbf{x}$ in the x_K direction, $K \leq 3$,
- the electric potential at $\mathbf{x}$, $K = 4$,
- the magnetic potential at $\mathbf{x}$, $K = 5$,

resultant from the application of

- a mechanical force at $\mathbf{x}'$ in x_J direction, $J \leq 3$;
- a point electric charge at $\mathbf{x}'$, $J = 4$;
- a point electric current at $\mathbf{x}'$, $J = 5$.

Extended fundamental solution for tractions As mentioned in Section 2.1 the isotropic fundamental solution for traction Equation 2.25 is always written in closed form, directly from the Kelvin's solution and it represents the direction j of the generalized traction vector on a surface with normal n_i, for a generalized point force in direction k. It is the result from the application of the Cauchy formula, i.e.,

$$T_{KJ} = (\sigma^*_{iJ})_K n_i, \tag{2.113}$$

where $(\sigma^*_{iJ})_K$ represents a fundamental solution for the extended stress tensor Equation 2.108 at the field point $\mathbf{x}$ when an extended point force is applied at the source point in direction x_K. To write this tensor in terms of the displacements, one has to recur to the stress strain law, i.e.,

$$\sigma_{iJ} = C_{iJMl}\, u_{M,l}\,, \tag{2.114}$$

which, in terms of the fundamental solution is written as

$$(\sigma^*_{iJ})_K = C_{iJMl}(\varepsilon^*_{lM})_K, \tag{2.115}$$

where,

$$(\varepsilon^*_{mL})_K = \frac{1}{2}(U_{KM,l} + U_{KL,m}), \tag{2.116}$$

is the fundamental Strain tensor at the observation point y when a point load is applied in the source point x on direction x_k. Finally, one write the fundamental solution for traction as a combination of stress-strain law Equation 2.109 and Cauchy theorem, as a function of the displacement Green's function derivative,

$$T_{KJ} = C_{iJMl} U_{MK,l} n_i, \tag{2.117}$$

where $U_{MK,l}$ denotes the derivative of U_{MK} with respect to direction l. Notice that due to the tensor's symmetries, the extended strain tensor is simplified to $U_{mk,l}$ in this equation, and there is no need to use Equation 2.116.

Note on implementation Notice that the index k of the derivative is the one which is carried over to the tensor as this direction is the point force application. This index is essential in the context of BEM due to the lack of symmetry of the fundamental solution for traction. In that sense, it should be mentioned that the choice of this index position is not standardized and not always adopted among the literature (see Table 2.1). It should be emphasized that the extended notation during this passage can mean a point force in direction $K = [1, 3]$, a point charge, $K = 4$, or a point current, $K = 5$.

Table 2.1 – Index referring to the source and field points for the Green tensor commonly found in BEM literature.

Source point is the first direction	Source point is the second direction
Brebbia et al., 2012 Beer et al., 2008	Katsikadelis and Kokkinos, 1993 Banerjee and Butterfield, 1981

2.4.3 MEE Green's function from Buroni and Sáez, 2010

The first explicit formula for MEE Green's function is due to Pan and Tonon, 2000, which was derived using a methodology found in their previous work for PE materials: Pan and Yuan, 2000a. Both works are based on the formulation used by Wang, 1997, to obtain the elastic Green's function, the main difference to the more commonly referenced one Ting and Lee, 1997, is that the solution of the partial differential equation is performed with a Radon transform. Although a different approach is employed in the derivation, the final expression for the Green's function presented by Pan and Tonon, 2000, has

the same form of Equation 2.92, with the difference being the number of the Stroh's eigenvalues (which is 10), as it results from the extended MEE fundamental matrix $\mathbf{N}^{\text{MEE}}$, thus, being valid only for non-degenerate cases. Pan and Tonon, suggested introducing a perturbation in the elastic constants to avoid repeated eigenvalues, and claim the solution will not lose precision by such trick. Another argument is found in Shiah et al., 2012, which advocates perturbing the elastic constants to avoid repeated eigenvalues: "*with mechanical properties of materials typically given with only up to 3 or 4 significant figures in accuracy, the percentage errors (...) are clearly more than acceptable for engineering analysis*". Although this is true in the context of the Green's function alone, it cannot be directly translated to BEM code without a sensitivity analysis, compromising the reliability of the final solution. The integration process in BEM is already accuracy compromised by the use of less than desirable Gauss integration points due to Green's function complexity and singularities.

In Buroni and Sáez, 2010, an alternative formulation for MEE materials is found which mitigates the numerical instabilities caused by the proximity of the Stroh's eigenvalues. The initial process for obtaining the Green's function is firstly carried out via the Radon transform, as in Wang and Achenbach, 1995, but the integral representation is then further simplified using the same process as in Ting and Lee, 1997, based on the Christoffel tensor, the modulation function of the Green function, $\mathbf{H}$, the second Barnett-Lothe tensor, is obtained by

$$H_{JK}(\hat{\mathbf{e}}) = \frac{1}{\pi}\int_{-\infty}^{\infty} \frac{\hat{\Gamma}_{JK}(p)}{|\mathbf{\Gamma}(p)|}dp. \tag{2.118}$$

Equation 2.118 has exactly the same format as Equation 2.81, where the extended Christoffel tensor for the MEE problem is

$$\Gamma_{JK}(p) = Q_{JK} + p(R_{JK} + R_{KJ}) + p^2 T_{JK}, \tag{2.119}$$

where the tensors Q_{JK}, R_{JK}, T_{JK} are computed at the oblique plane from the extended MEE stiffness matrix, C_{iJKl}, and n_i, m_i vectors,

$$Q_{JK} = C_{iJKl}n_i n_l, \quad R_{ik} = C_{iJKl}n_i m_l, \quad T_{ik} = C_{iJKl}m_i m_l. \tag{2.120}$$

Following the formulation from Buroni and Sáez, 2010, the kernel in Equation 2.118, is a single-valued holomorphic function in the upper complex half-plane except at five complex poles with positive imaginary part and their conjugates that corresponds to the roots

of the tenth-order polynomial equation

$$|\mathbf{\Gamma}(p)| = 0. \tag{2.121}$$

This determinant in Equation 2.121 can be factorized as

$$|\mathbf{\Gamma}(p)| = |\mathbf{T}| \prod_{\xi=1}^{5} (p - p_\xi)(p - \bar{p}_\xi), \tag{2.122}$$

where p_ξ are known as the Stroh's eigenvalues and the bar over p_ξ denotes complex conjugate and $\mathbf{T}$ as defined in Equation 2.120. Therefore, assuming that all Stroh's eigenvalues are different, the integration in Equation 2.118 can be done by the Cauchy's residue theory to yield

$$H_{JK} = \frac{2\mathrm{i}}{|\mathbf{T}|} \sum_{\alpha=1}^{5} \frac{\hat{\Gamma}_{JK}(p_\alpha)}{(p_\alpha - \bar{p}_\alpha) \prod\limits_{\substack{\xi=1 \\ \xi \neq \alpha}}^{5} (p_\alpha - p_\xi)(p_\alpha - \bar{p}_\xi)}. \tag{2.123}$$

Equation 2.123 is similar to its elastic counterpart, Equation 2.82, and is the same as presented by Pan, 2002. As can be seen in the numerator of Equation 2.123, it is not numerically stable when the eigenvalues assume values close to each other.

For points where repeated eigenvalues are found, an alternative representation, such as the ones presented in Equations 2.93 and 2.94, is proposed by Buroni and Sáez, 2010, also based in residue calculus, e.g.: Sveshnikov and Tikhonov, 1971. Let a function $f(p)$, and let p_0 be a pole of order m of f. The residue of $f(p)$ is given by

$$Res(p_0) = \frac{1}{(m-1)!} \lim_{p \to p_0} \frac{d^{m-1}}{dp^{m-1}} [(p - p_0)^m f(p)], \tag{2.124}$$

which applied on Equation 2.123, results in [Buroni and Sáez, 2010]

$$H_{JK}(\hat{\mathbf{e}}) = \frac{2\mathrm{i}}{|\mathbf{T}|} \sum_{\alpha=1}^{N} \frac{1}{(m_\alpha - 1)!} \times \left[\frac{d^{m_\alpha - 1}}{dp^{m_\alpha - 1}} \left\{ \frac{\hat{\Gamma}_{JK}(p)}{(p - \bar{p}_\alpha)^{m_\alpha} \prod_{\substack{\xi=1 \\ \xi \neq \alpha}}^{N} [(p - p_\xi)(p - \bar{p}_\xi)]^{m_\xi}} \right\} \right]. \tag{2.125}$$

The main difficulty in evaluating Equation 2.125, is that the high possibility of repeated eigenvalues and is uncertain when each case will happen, so the implementation to be general and automatized must include many conditions to avoid the occurrence of degeneracy. Also, there are many combinations of repeated eigenvalues to be included in these conditions. Nevertheless, it is important to emphasize that this methodology is still

more efficient than the numerical integration of Equation 2.118.

2.4.4 Non-degenerate displacement MEE Green's function

A non-degenerate displacement Green's function can be obtained using the same idea of Ting and Lee, 1997, to derive an explicit function in the same fashion as Equation 2.89, i.e., parting from Equation 2.123. Recall that, per Equation 2.119, the extended MEE Christoffel tensor Γ_{JK} is polynomial in p. Furthermore, the adjoint matrix, $\hat{\Gamma}_{JK}(p)$, defined in Equation 2.80 as being the tensor for which the following relation applies, $\mathbf{\Gamma}(p)\hat{\mathbf{\Gamma}}(p) = |\mathbf{\Gamma}(p)|\,\mathbf{I}$, is a polynomial of degree eight in p, written as

$$\hat{\Gamma}_{JK}(p) = \sum_{n=0}^{8} p^n \hat{\Gamma}_{JK}^{(n)}, \quad J, K = \{1, 5\} \tag{2.126}$$

where $\hat{\Gamma}_{JK}^{(n)}$ are constant real matrices depending only on the material properties C_{iJKl} and the position vector $\hat{\mathbf{e}}$.

By this decomposition it is possible to write the *extended MEE Barnett-Lothe tensor* $H_{JK}(\hat{\mathbf{e}})$ similarly to Equation 2.89, adjusting the sum for the polynomial order of the adjoint Christoffel tensor,

$$\mathbf{H}(\hat{\mathbf{e}}) = \frac{2\,\mathrm{i}}{|\mathbf{T}|} \sum_{n=0}^{8} q_n \hat{\mathbf{\Gamma}}^{(n)}, \tag{2.127}$$

where q_n are constants depending only on the Stroh's eigenvalues, and are written as

$$q_n = \sum_{\alpha=1}^{5} \frac{2\,\mathrm{i}\,p_\alpha^n}{(p_\alpha - \bar{p}_\alpha) \prod\limits_{\substack{\xi=1 \\ \xi\neq\alpha}}^{5} (p_\alpha - p_\xi)(p_\alpha - \bar{p}_\xi)}. \tag{2.128}$$

In order to completely remove the indeterminate condition caused when $p_\alpha - p_\xi = 0$ in Equation 2.128, a careful factorization must be carried out, such that a common denominator for all q_n be made equal to $\prod_{\alpha=1}^{5}\prod_{\xi=1}^{5}(p_\alpha - \bar{p}_\xi)$, i.e.,

$$\frac{q_n^{\mathrm{Num}}}{\prod_{\alpha=1}^{5}\prod_{\xi=1}^{5}(p_\alpha - \bar{p}_\xi)} = \sum_{\alpha=1}^{5} \frac{2\,\mathrm{i}\,p_\alpha^n}{(p_\alpha - \bar{p}_\alpha) \prod\limits_{\substack{\xi=1 \\ \xi\neq\alpha}}^{5} (p_\alpha - p_\xi)(p_\alpha - \bar{p}_\xi)}, \tag{2.129}$$

where q_n^{Num} is obtained by factorization. The denominator is never null because the subtractions are performed between conjugated complex numbers — even when there are

repeated eigenvalues and the real part becomes zero, the imaginary part is never null. The resulting expression for q_n^{Num} the numerator of q_n can be obtained straightforwardly using symbolic mathematical software, but are quite large to be included in this work, as is implied by the number of possible combinations of terms in Equation 2.129.

The final expression for the non-degenerate MEE Barnett-Lothe tensor is recast for completeness:

$$H_{JK}(\hat{\mathbf{e}}) = \frac{2\,\mathbf{i}}{|\mathbf{T}| \prod_{\alpha=1}^{5} \prod_{\xi=1}^{5} (p_\alpha - \bar{p}_\xi)} \sum_{n=0}^{8} q_n^{\text{Num}} \hat{\mathbf{\Gamma}}^{(n)}, \tag{2.130}$$

To illustrate this non-degenerate solution in a near-degenerate case, let us consider a transversely isotropic piezoelectric material, with elastic and electric properties found Appendix I at Table I.1. For this material configuration when the position vector $\mathbf{r} = \mathbf{x} - \mathbf{x}'$ coincides with x_3 axis, all the four Stroh's eigenvalues related to the piezoelectric potentials become equal, $\{p_j = 0 + 1\mathbf{i} \,|\, j = [1, 4]\}$. Figure 2.4 shows the degenerate solution (Equation 2.123) is unstable, even when further away from the x_3 axis, while the non-degenerate Green's function is smooth and well-defined in all the domain. Also, the degenerate solution is not defined when $\mathbf{r}$ coincides with the x_3 axis for this material configuration.

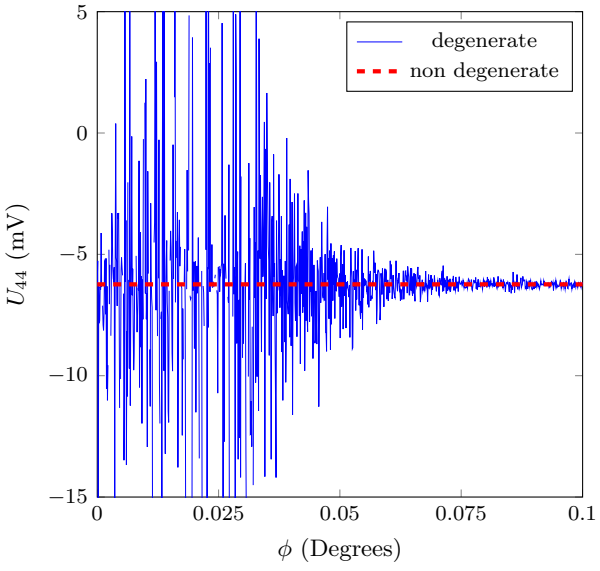

Figure 2.4 – Degenerate and non-degenerate approach for the Green functions close to the x_3 axis. Piezoelectric Material A.

In Table 2.2, results for the non-degenerate Green's function for MEE materials at $\mathbf{x} = (1, 1, -1)$ are shown for *Material B*. Equation 2.92 was used to compute the solution, which should yield the same value. A numerical difference appears between the proposed solution and the reference one, that could be attributed to the high number of sums involved in the computation of q_n^{Num}, Equation 2.129, and could be easily overcome by the application of a Kahan's sum algorithm (see Goldberg, 1991, for instance).

Table 2.2 – Green's function U_{JK} for magneto-electro-elastic Material B at $\mathbf{x} = (1, 1, -1)$.

(JK)	Buroni and Sáez, 2010	present work (non-degenerate)	relative difference
11	$7.7141369757490015 \times 10^{-4}$	$7.7141366651463308 \times 10^{-4}$	4.0264×10^{-8}
12	$1.2027080088980113 \times 10^{-4}$	$1.2027080690932257 \times 10^{-4}$	5.0050×10^{-8}
13	$-1.2945920760425760 \times 10^{-4}$	$-1.2945919822994514 \times 10^{-4}$	7.2411×10^{-8}
14	$-1.0347227658113671 \times 10^{-4}$	$-1.0347226896648796 \times 10^{-4}$	7.3591×10^{-8}
15	$4.2667071176276332 \times 10^{-6}$	$4.2667067164579118 \times 10^{-6}$	9.4023×10^{-8}
22	$7.7141369757490015 \times 10^{-4}$	$7.7141366651463308 \times 10^{-4}$	4.0264×10^{-8}
23	$-1.2945920760425762 \times 10^{-4}$	$-1.2945919822994529 \times 10^{-4}$	7.2411×10^{-8}
24	$-1.0347227658113787 \times 10^{-4}$	$-1.0347226896648809 \times 10^{-4}$	7.3591×10^{-8}
25	$4.2667071176276350 \times 10^{-6}$	$4.2667067164579153 \times 10^{-6}$	9.4023×10^{-8}
33	$4.8476833195420852 \times 10^{-4}$	$4.8476831665570996 \times 10^{-4}$	3.1558×10^{-8}
34	$5.0073977011499986 \times 10^{-4}$	$5.0073975331344647 \times 10^{-4}$	3.3553×10^{-8}
35	$2.4195754528575155 \times 10^{-5}$	$2.4195754183322036 \times 10^{-5}$	1.4269×10^{-8}
44	$-3.4041791147399341 \times 10^{-3}$	$-3.4041790013154500 \times 10^{-3}$	3.3319×10^{-8}
45	$2.9749048777373694 \times 10^{-5}$	$2.9749048155802629 \times 10^{-5}$	2.0894×10^{-8}
55	$-4.1918947944612555 \times 10^{-6}$	$-4.1918946641014401 \times 10^{-6}$	3.1098×10^{-8}
avg			5.1688×10^{-8}

As is pointed out in Buroni et al., 2019, an interesting work by Xie et al., 2018, has proposed an alternative unified formula for the fundamental solution and its first-derivative, which considers only piezoelectric anisotropic materials, but a similar formulation could be used for MEE materials, similarly as the one presented in this work. In that work, after an algebraic rearrangement and the usage of recursive relations, the integral coefficients (equivalent to q_n before integration) are calculated by Cauchy residue theorem. The resulting expressions in explicit-form seem to be more compact than the ones presented here, however, more labor-intensive to implement. As occurs in the extension from elasticity to piezoelectricity, the extension to MEE materials demands an even more cumbersome algebra. In any case, the underlying principle that allows removing the mathematical degeneracy is the factorization of the denominator in Equation 2.128, since this comes from the mathematical structure and not from physical arguments.

Provided these properties, one can propose many alternative factorization schemes to promote a faster numerical algorithm. However, to ensure an efficient integration

scheme in BEM methodologies, we propose an approximation approach in the next section.

2.5 Fourier Series representation of the Green's function and its derivatives for Elastic, Electric, Magnetic and multifield MEE materials

The nondegenerate solution Equation 2.130 is employed to obtain the series coefficients for a given material. The Green's function is then approximated using those coefficients, which are also used to approximate the first- (and second) order derivatives.

With a general non-degenerate solution able to calculate the displacement Green's function, it is now possible to create a general framework allowing its application in BEM, with the aid of the double Fourier series for its approximation.

By this approach, the end user is allowed to virtually apply any material symmetry or configuration, without the need to worry about the problems associated with degeneracies or regarding specific knowledge of Green's function, as the base function which generates the coefficients is trouble-free.

Therefore, the resulting BEM code can be significantly generalized, with a single routine capable of evaluating the fundamental solutions for any of the three *phenomena or material* depending only on the previously calculated Fourier coefficients. Moreover, their computation has significantly less cost than BEM's assembly and solution routines for a reasonably sized problem. If a reasonable integration rule is used to compute the series coefficients, it takes comparable effort to integrate a few boundary elements, should take a neglectable fraction of the total analysis time. For the magneto electro elastic (MEE) problem, in comparison with the Stroh Formalism approach, i,e., Equation 2.123, one avoids a 10^{th}-order eigenvalue problem for each integration point.

Also, it is worth to emphasize that the computation of the first and second derivatives through the Fourier Series is much simpler with the Fourier approximation than with the explicit approach. It is dependent on the same constants as the original function, as will be shown in this section. Consequently, speedup can be gained from the Fourier series representation — The computation of the fundamental solution for traction is orders of magnitude less costly than the explicit solution.

Another feature of the series approach is that the user can define the accuracy on the solution approximation through the number of terms selected, allowing to prioritize performance, which can be useful during preliminary analysis stages. From the algorithm

point of view, it has the advantage of being composed of large amounts of parallel work and very few sequential steps, which can benefit from modern computational architectures such as graphics processing units commonly found in engineering workstations to manage computer aided design (CAD) workloads.

In this section the formulation from Shiah et al., 2012, Tan et al., 2013, is extended to MEE materials. An efficiency improvement to the previous approaches on the Fourier series is proposed, based on the Green's function period in the spherical coordinate system.

As already mentioned at Sections 2.3 and 2.4, the displacement Green's function $U_{JK}(\mathbf{x})$, $J, K = [1, 5]$ is the product of a singular term $f(|\mathbf{x}|^{-1})$ (which depends only on the modulus of $\mathbf{x}$, i.e., the radial distance r) with a modulation function $\mathbf{H}(\hat{\mathbf{e}})$, which is the second Barnett-Lothe tensor [Ting, 1996], that depends only on the vector $\hat{\mathbf{e}}$, the direction of $\mathbf{x}$. Such tensor can be fully represented at the spherical coordinate system, i.e., $\mathbf{H}(\hat{\mathbf{e}}) = \mathbf{H}(\hat{\mathbf{e}}(\theta, \phi))$, so

$$\mathbf{U}(\mathbf{x}) = \mathbf{U}(r, \theta, \phi) = \frac{1}{4\,\pi\,r}\mathbf{H}(\theta, \phi). \tag{2.131}$$

To clarify the many existent notations for a spherical coordinate system in the literature, the vector $\hat{\mathbf{e}}$ is expressed in terms of the following spherical coordinates θ and ϕ as

$$\hat{\mathbf{e}} = (\sin\phi\cos\theta, \sin\phi\sin\phi, \cos\phi), \tag{2.132}$$

where ϕ is chosen to be the $\hat{e} \angle e_3$ angle , and θ is the $x_{12} \angle e_1$ angle, where $x_{12} = (x_1, x_2)$ is the projection of $\mathbf{x}$ on the plane e_1, e_2. Therefore, those angles are defined in the following intervals, $(-\pi \leq \theta < \pi,\ 0 \leq \phi < \pi)$, and the inverse transformation is brought here for completeness [Shiah et al., 2012],

$$\theta = \tan^{-1}(x_2/x_1), \qquad -\pi \leq \theta < \pi, \tag{2.133}$$

$$\phi = \cos^{-1}(x_3/r), \qquad 0 \leq \phi < \pi. \tag{2.134}$$

It is important to point out that from the numerical implementation standpoint, the function $\tan^{-1}$ must be evaluated using a four-quadrant inverse tangent to determine the position of θ relative to the $\mathbf{x}$ coordinate system (otherwise it will not satisfy Equation 2.133).

In Shiah et al., 2012, the tensor $H_{jk}(\theta, \phi)$ is assumed to be 2π periodic in both (θ, ϕ), although ϕ is defined as $\phi = [0, \pi]$. It admits a double Fourier series representation

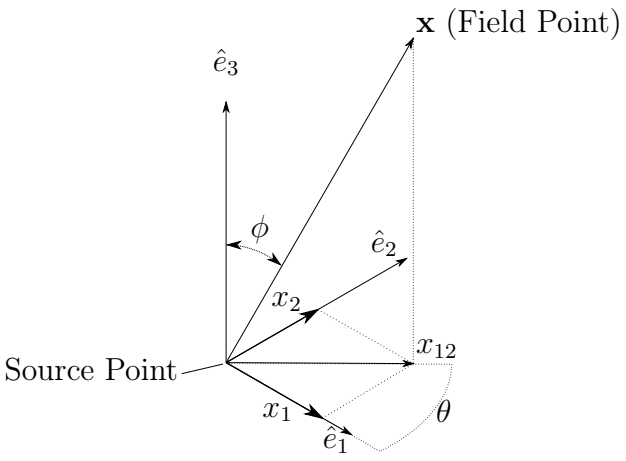

Figure 2.5 – The spherical coordinate system adopted in this work.

which is firstly presented in terms of the complex exponential as

$$H_{jk}(\theta,\phi) = \sum_{m=-\infty}^{\infty}\sum_{n=-\infty}^{\infty} \lambda_{jk}^{(m,n)} \mathrm{e}^{\mathrm{i}(m\theta+n\phi)}, \tag{2.135}$$

being the Fourier expansion coefficients given by

$$\lambda_{jk}^{(m,n)} = \frac{1}{4\pi^2}\int_{-\pi}^{\pi}\int_{-\pi}^{\pi} H_{JK}(\theta,\phi)\mathrm{e}^{-\mathrm{i}(m\theta+n\phi)}\mathrm{d}\theta\mathrm{d}\phi. \tag{2.136}$$

Notice that the double Fourier series representation (2.135) for the displacement solution $H_{jk}(\theta,\phi)$ converges absolutely and uniformly since $\frac{\partial^2 H_{jk}}{\partial\theta\partial\phi}$ exists and is continuous.

Then, one can approximate $H_{jk}(\theta,\phi)$ by truncating the infinite series Equation 2.135 in a sufficiently large number of terms α to yield results as accurate as required, so

$$H_{jk}(\theta,\phi) = \sum_{m=-\alpha}^{\alpha}\sum_{n=-\alpha}^{\alpha} \lambda_{jk}^{(m,n)} \mathrm{e}^{\mathrm{i}(m\theta+n\phi)}. \tag{2.137}$$

Although Tan et al., 2013 presents a simplified and real-valued version of these approximations, it is previously given attention to a simple analysis of the Barnett-Lothe tensor periodicity, which will result in an efficiency increase and a reduction in the computational effort to compute the function and its coefficients.

2.5.1 Periodicity analysis and series improvement

Due to the characteristics of Equation 2.73, the second Barnett-Lothe tensor, the modulation function $H_{JK}(\mathbf{x})$ depends on the direction of x but not on its modulus, so

$H_{JK}(\mathbf{x}) = H_{JK}(\hat{\mathbf{e}})$. Also, it is known in context of the Stroh formalism Ting, 1996, as being one of the three extended Barnett-Lothe tensors, which is symmetric, $H_{JK} = H_{KJ}$, and $H_{JK}(\hat{\mathbf{e}}) = H_{JK}(-\hat{\mathbf{e}})$. Hence, the Green's function $U(\mathbf{x})$ is also symmetric and the following properties

$$U_{JK}(\mathbf{x}) = U_{JK}(-\mathbf{x}), \tag{2.138}$$

the first-order derivative,

$$U_{JK,l}(\mathbf{x}) = -U_{JK,l}(-\mathbf{x}), \tag{2.139}$$

and the second-order derivative,

$$U_{JK,lm}(\mathbf{x}) = U_{JK,lm}(-\mathbf{x}), \tag{2.140}$$

are respectively satisfied. Another consequence of Equation 2.73, is that H_{JK} is periodic in θ and ϕ, i.e.,

$$\mathbf{H}(\theta, \phi) = \mathbf{H}(\theta + L_\theta, \phi) = \mathbf{H}(\theta, \phi + L_\phi). \tag{2.141}$$

Let $\theta' = \theta + L_\theta$, $\phi' = \phi + L_\phi$ and $(\theta', \phi') < 2\pi$. Using properties Equation 2.132 in Equation 2.138, where θ' and ϕ' are the corresponding spherical coordinates at $-\hat{\mathbf{e}}$, the following system of equations arise,

$$\cos\theta \sin\phi = -\cos\theta' \sin\phi', \tag{2.142}$$

$$\sin\theta \sin\phi = -\sin\theta' \sin\phi', \tag{2.143}$$

$$\cos\phi = -\cos\phi' \tag{2.144}$$

which, by the last statement, Equation 2.144 results in

$$\phi' = \phi + \pi. \tag{2.145}$$

Applying Equation 2.145 in the right-hand side of Equations 2.142 and 2.143 results in

$$\cos\theta \sin(\phi) = -\cos\theta' \sin(\phi + \pi), \tag{2.146}$$

$$\sin\theta \sin(\phi) = -\sin\theta' \sin(\phi + \pi), \tag{2.147}$$

which, by the property $\sin(\phi) = -\sin(\phi + \pi)$, is the same as writing

$$\cos\theta = \cos\theta', \tag{2.148}$$

$$\sin\theta = \sin\theta', \tag{2.149}$$

which is only satisfied if $\theta' = \theta + 2\pi$, resulting in the following period for application in the Fourier Series.

$$\mathbf{H}(\theta, \phi) = \mathbf{H}(\theta + 2\pi, \phi) = \mathbf{H}(\theta, \phi + \pi), \tag{2.150}$$

which allows one to write the Fourier series provided by Shiah et al., 2012, in a more efficient manner with respect to the variable ϕ.

To demonstrate the behavior described in Equation 2.150, one component of the tensor, $H_{44}(\theta, \phi)$, is plotted for the ranges defined in Equation 2.150, considering the properties of a fully anisotropic and coupled material C. The plots for each one of the 15 remaining components of the full tensor are also included in Appendix B (Figures B.1 to B.4).

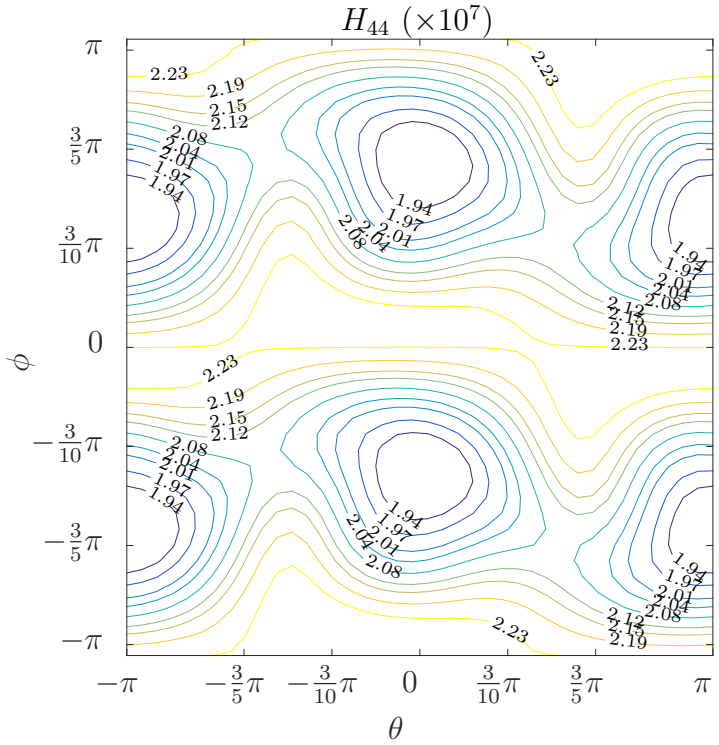

Figure 2.6 – The Barnett-Lothe tensor, H_{44} for the *Material C - MEE*, in spherical coordinates.

The Barnett-Lothe tensor $H_{jk}(\theta, \phi)$ should present period $L = \pi$, due to the property $\mathbf{H}(\hat{\mathbf{e}}) = \mathbf{H}(-\hat{\mathbf{e}})$. It is clear that if the transformation Equations 2.133 and 2.134 is employed, the tensor presents a periodicity of π in θ, in the plane (x_1, x_2), $\phi = \pi/2$, i.e.,

$$H_{44}(\theta, \frac{\pi}{2}) = H_{44}(\theta + \pi, \frac{\pi}{2}), \tag{2.151}$$

but not outside of this plane, due to the definition of ϕ in Equation 2.134. This fact can be seen in Figure 2.6, also in the figures included in the Appendix B, as in the following example,

$$H_{44}(\theta, \phi) = H_{44}(\theta + \pi, \phi). \tag{2.152}$$

Unfortunately, even though the function is fully defined in the semi-sphere $\theta = [0, \pi]$, $\phi = [0, \pi]$, no linear transformation of coordinates can maintain the spherical symmetry, as the functions becomes anti-symmetric in θ, for which the tensor exhibits a period $L = \pi$ in both ϕ and θ, as expected.

2.5.2 Review of the Fourier series considering the new period

The double Fourier series for a periodic function such as $\mathbf{H}(\theta, \phi)$ with periods equal to L_θ and L_ϕ, respectively, is written as

$$H_{jk}(\theta, \phi) = \sum_{m,n=-\infty}^{m,n=\infty} \lambda_{jk}^{mn} \, \mathrm{e}^{\mathrm{i}(m\theta/L_\theta + m\phi/L_\phi)} \tag{2.153}$$

where the constant coefficients λ_{jk}^{mn}, are defined through the following integral

$$\lambda_{jk}^{mn} = \frac{1}{L_\phi L_\theta} \int_{\Omega_\phi} \int_{\Omega_\theta} H_{jk}(\theta, \phi) \mathrm{e}^{-\mathrm{i}(\mathrm{m}\theta\pi/\mathrm{L}_\theta + \mathrm{m}\phi\pi/\mathrm{L}_\phi)} \mathrm{d}\theta \mathrm{d}\phi, \tag{2.154}$$

where Ω_ϕ and Ω_θ are the respective domains of definition of these functions, which for the Green's function, one may refer to Equations 2.133 and 2.134. The generalized integral can be rewritten for a case where $L_\phi = \pi$, defining $L'_\phi = L_\phi/\rho$, such that

$$\lambda_{jk}^{mn} = \frac{\rho}{4\pi^2} \int_0^{\frac{2\pi}{\rho}} \int_{-\pi}^{\pi} H_{jk}(\theta, \phi) \mathrm{e}^{-\mathrm{i}(\mathrm{m}\theta + \rho \mathrm{n}\phi)} \mathrm{d}\theta \mathrm{d}\phi. \tag{2.155}$$

Variable ρ indicate $L = 2\pi$ in θ when $\rho = 1$ and $L = \pi$ when $\rho = 2$. Writing Equation 2.155 using the trigonometric form of the complex exponential, one has

$$\lambda_{jk}^{(m,n)} = \frac{\rho}{4\pi^2} \int_0^{\frac{2\pi}{\rho}} \int_{-\pi}^{\pi} H_{jk}(\theta, \phi) \left[\cos(m\theta + \rho n\phi) - \mathfrak{i} \sin(m\theta + \rho n\phi)\right] d\theta d\phi, \tag{2.156}$$

which may be referred as

$$\lambda_{jk}^{(m,n)} = \mathbf{R}^{(m,n)} + \mathfrak{i}\mathbf{I}^{(m,n)}. \tag{2.157}$$

Due to trigonometric properties

$$\cos(a+b) = \cos(a)\cos(b) - \sin(a)\sin(b) \tag{2.158}$$

$$-\sin(a+b) = -\sin(a)\cos(b) - \cos(a)\sin(b), \tag{2.159}$$

is possible to expand Equation 2.156, resulting in

$$\boldsymbol{\lambda_{R1}}^{(m,n)} = \frac{\rho\kappa_m\kappa_n}{4\pi^2}\int_0^{\frac{2\pi}{\rho}}\int_{-\pi}^{\pi} H_{jk}(\theta,\phi)\cos(m\theta)\cos(\rho n\phi)d\theta d\phi, \tag{2.160}$$

$$\boldsymbol{\lambda_{R2}}^{(m,n)} = -\frac{\rho\kappa_m\kappa_n}{4\pi^2}\int_0^{\frac{2\pi}{\rho}}\int_{-\pi}^{\pi} H_{jk}(\theta,\phi)\sin(m\theta)\sin(\rho n\phi)d\theta d\phi, \tag{2.161}$$

$$\boldsymbol{\lambda_{I1}}^{(m,n)} = -\frac{\rho\kappa_m\kappa_n}{4\pi^2}\int_0^{\frac{2\pi}{\rho}}\int_{-\pi}^{\pi} H_{jk}(\theta,\phi)\cos(m\theta)\sin(\rho n\phi)d\theta d\phi, \tag{2.162}$$

$$\boldsymbol{\lambda_{I2}}^{(m,n)} = -\frac{\rho\kappa_m\kappa_n}{4\pi^2}\int_0^{\frac{2\pi}{\rho}}\int_{-\pi}^{\pi} H_{jk}(\theta,\phi)\sin(m\theta)\cos(\rho n\phi)d\theta d\phi, \tag{2.163}$$

where a scaling factor κ_l is introduced, whose purpose will be addressed further on. The aforementioned coefficient matrices are unique in the sense that they all hold orthogonality to each other as expected.

Using relations Equations 2.158 and 2.159 in Equation 2.153, and taking advantage of symmetry with respect to positive and negative values of (m,n) of Equations 2.160 to 2.163, i.e., $\boldsymbol{\lambda_{I2}}^{(m,n)} = \boldsymbol{\lambda_{I2}}^{(-m,n)} = \boldsymbol{\lambda_{I2}}^{(m,-n)}$, it is possible to write Equation 2.153 in the following form

$$\mathbf{H} = \sum_{m,n=0}^{\alpha}\left[\boldsymbol{\Lambda}^{(m,n)}(\theta,\phi)\right], \tag{2.164}$$

where matrix $\boldsymbol{\Lambda}^{(m,n)}(\theta,\phi)$ is evaluated as

$$\boldsymbol{\Lambda}^{(m,n)}(\theta,\phi) = \overset{\frown}{\Gamma}_{jk}^{(m,n)}(\theta)\cos\rho n\phi - \overset{\smile}{\Gamma}_{jk}^{(m,n)}(\theta)\sin\rho n\phi, \tag{2.165}$$

and the terms dependent only on θ are written as

$$\overset{\frown}{\Gamma}_{jk}^{(m,n)}(\theta) = \boldsymbol{\lambda_{R2}}^{(m,n)}\cos m\theta - \boldsymbol{\lambda_{I1}}^{(m,n)}\sin m\theta, \tag{2.166}$$

$$\overset{\smile}{\Gamma}_{jk}^{(m,n)}(\theta) = \boldsymbol{\lambda_{R1}}^{(m,n)}\sin m\theta + \boldsymbol{\lambda_{I2}}^{(m,n)}\cos m\theta. \tag{2.167}$$

As the complete passage from Equation 2.154 to Equation 2.164 consists of algebraic manipulation, it is included in Appendix A for reference. Notice that when used to approximate the actual function, the coefficients multiply different trigonometric functions then the ones used to obtain them — this is due to the negative imaginary term which

appears in Equation 2.155, causing a rotation at the complex plane. With coefficient matrices written in the above format is much clear why one only needs the positive indices in the reproduction of the Fourier series. As only the positive m and n are being used, one has to double the coefficients with $(m, n) \neq 0$, therefore, the scaling factor κ_l, introduced in Equations 2.160 to 2.163, assumes the follwing values

$$\kappa_l = \begin{cases} 1 & l = 0, \\ 2 & l \neq 0. \end{cases} \tag{2.168}$$

Notice that when the constants m or n is zero, only $\boldsymbol{\lambda}_{R1} \neq 0$. To maintain a compact form of Equation 2.165, they are not excluded from the sum in the formulation presented. As is known from the Fourier series properties these coefficients must decrease consistently as the series terms m, n increase — the Barnett-Lothe tensor is infinitely differentiable (analytic) at all points of its domain. The work multiplying and adding these null terms can be avoided using numerical schemes which also avoid the spurious non-null values arising from the numerical integration, which can be several orders of magnitude smaller than the maximum coefficients. A user-defined threshold can control the series precision by using only the most significant elements of the coefficient matrices in Equations 2.160 to 2.163, further demonstrated in Section 2.6.

For clarity, the final formula for the Green's function approximation at an observation point $\mathbf{x}$ is

$$\mathbf{U}(\mathbf{x}) = \mathbf{U}(r, \theta, \phi) = \frac{1}{4\,\pi\,r} \sum_{m,n=0\ldots\alpha} \left[\boldsymbol{\Lambda}^{(m,n)}(\theta, \phi) \right]. \tag{2.169}$$

First order derivative of the Green's function

The first-order derivative can also be expressed as a singular part by a modulation function which only depends on $\hat{\mathbf{e}}$ as

$$U_{jk,l}(\mathbf{x}) = \frac{1}{4\pi r^2} \tilde{U}_{jkl}(\hat{\mathbf{e}}) \tag{2.170}$$

being the modulation function given by

$$\tilde{U}_{jkl}(\hat{\mathbf{e}}) = -\hat{\mathrm{e}}_l H_{jk} + \frac{\mathrm{m}_l}{\sin\phi} \frac{\partial H_{jk}}{\partial \theta} + \mathrm{n}_l \frac{\partial H_{jk}}{\partial \phi} \tag{2.171}$$

where $\hat{\mathrm{e}}_l$, n_l and m_l are the components of the right-hand triad mentioned in Equation 2.63 and in Figure 2.3 which are defined as

$$\hat{\mathbf{e}} = (\sin\phi\cos\theta, \sin\phi\sin\theta, \cos\phi) \tag{2.172}$$

$$\mathbf{n} = (\cos\phi\cos\theta, \cos\phi\sin\theta, -\sin\phi), \tag{2.173}$$

$$\mathbf{m} = (-\sin\theta, \cos\theta, 0) \tag{2.174}$$

Performing the derivatives appearing in Equation 2.171, results in the following

$$\begin{aligned}\tilde{U}_{jkl}(\theta,\phi) = &- \hat{\mathrm{e}}_l \sum_{m,n=0}^{\alpha} \left[\mathbf{\Lambda}^{(m,n)}(\theta,\phi)\right] + \\ &- \frac{\mathrm{m}_l}{\sin\phi} \sum_{m,n=0}^{\alpha} m \left[\tilde{\Gamma}_{jk}^{(m,n)}(\theta)\cos\rho n\phi - \hat{\Gamma}_{jk}^{(m,n)}(\theta)\sin\rho n\phi\right] + \\ &- \mathrm{n}_l \sum_{m,n=0}^{\alpha} \rho n \left[\widehat{\Gamma}_{jk}^{(m,n)}(\theta)\sin\rho n\phi - \breve{\Gamma}_{jk}^{(m,n)}(\theta)\cos\rho n\phi\right],\end{aligned} \tag{2.175}$$

where, from the derivative with respect to θ in Equation 2.171, the following terms arise

$$\begin{aligned}\tilde{\Gamma}_{jk}^{(m,n)}(\theta) &= \left[\boldsymbol{\lambda}_{\mathbf{R2}}{}^{(m,n)}\sin m\theta + \boldsymbol{\lambda}_{\mathbf{I1}}{}^{(m,n)}\cos m\theta\right], \\ \hat{\Gamma}_{jk}^{(m,n)}(\theta) &= \left[\boldsymbol{\lambda}_{\mathbf{R1}}{}^{(m,n)}\cos m\theta - \boldsymbol{\lambda}_{\mathbf{I2}}{}^{(m,n)}\sin m\theta\right].\end{aligned} \tag{2.176}$$

Second-order derivative of the Green's function

The Green's function second-order derivative can be written in terms of Equation 2.170 using chain rule as

$$U_{jk,ml}(\mathbf{x}) = \frac{\partial U_{jk,m}}{\partial r}\frac{\partial r}{\partial x_l} + \frac{\partial U_{jk,m}}{\partial \theta}\frac{\partial \theta}{\partial x_l} + \frac{\partial U_{jk,m}}{\partial \phi}\frac{\partial \phi}{\partial x_l}. \tag{2.177}$$

After carrying out this derivation, the result can also be separated as the product of a singular part and a modulation function,

$$U_{jk,lm}(\mathbf{x}) = \frac{1}{2\pi r^3}\tilde{U}_{jklm}. \tag{2.178}$$

,

The second-order derivative of the modulation function $\tilde{U}_{jklm}$ is computed as

$$\begin{aligned}
\tilde{U}_{jklm}(\theta,\phi) = &- \Omega^{(1)}_{lm} \sum_{m,n=0}^{\alpha} \left[\tilde{\Lambda}^{(m,n)}_{jk}(\theta,\phi)\right] + \\
&- \Omega^{(2)}_{lm} \sum_{m,n=0}^{\alpha} m \left[\tilde{\Gamma}^{(m,n)}_{jk}(\theta)\cos\rho n\phi - \hat{\Gamma}^{(m,n)}_{jk}(\theta)\sin\rho n\phi\right] + \\
&- \Omega^{(3)}_{lm} \sum_{m,n=0}^{\alpha} \rho n \left[\widehat{\Gamma}^{(m,n)}_{jk}(\theta)\sin\rho n\phi - \breve{\Gamma}^{(m,n)}_{jk}(\theta)\cos\rho n\phi\right] + \\
&+ \Omega^{(4)}_{lm} \sum_{m,n=0}^{\alpha} m\rho n \left[\tilde{\Gamma}^{(m,n)}_{jk}(\theta)\sin\rho n\phi - \hat{\Gamma}^{(m,n)}_{jk}(\theta)\cos\rho n\phi\right] + \\
&+ \Omega^{(5)}_{lm} \sum_{m,n=0}^{\alpha} m^2 \tilde{\Lambda}^{(m,n)}_{jk}(\theta,\phi) + \\
&+ \Omega^{(6)}_{lm} \sum_{m,n=0}^{\alpha} (\rho n)^2 \tilde{\Lambda}^{(m,n)}_{jk}(\theta,\phi),
\end{aligned} \tag{2.179}$$

where $\Omega^{([1\ldots6])}_{ml}$ are symmetric matrices which result from the spatial derivatives appearing in Equation 2.177 listed in Table 2.3. Without loss of generality, the sums range is considered as $m = [0, \alpha]$ and $n = [0, \alpha]$, even when is clearly seen that many summands will be null. By this approach it is possible to be clarified which of the terms can be reused or rearranged numerically, without the need to explicitly type the non-zero terms.

Table 2.3 – Partial derivatives from the spherical coordinate system used in the computation of the Green's function second derivative.

$\{i,j\}$	$\Omega^1_{\{i,j\}}$	$\Omega^2_{\{i,j\}}$	$\Omega^3_{\{i,j\}}$
$1,1$	$1.5(1-\cos 2\phi)\cos^2\theta - 1$	$-\sin 2\theta(1+1/\sin^2\phi)$	$2\cos^2\theta\sin 2\phi - \sin^2\theta\cot\phi$
$1,2$	$1.5\sin 2\theta\sin^2\phi$	$\cos 2\theta(1+1/\sin^2\phi)$	$\sin 2\theta(0.5\cot\phi + \sin 2\phi)$
$1,3$	$1.5\cos\theta\sin 2\phi$	$-\sin\theta\cot\phi$	$2\cos\theta\cos 2\phi$
$2,2$	$1.5(1-\cos 2\phi)\sin^2\theta - 1$	$\sin 2\theta(1+1/\sin^2\phi)$	$2\sin^2\theta\sin 2\phi - \cos^2\theta\cot\phi$
$2,3$	$1.5\sin\theta\sin 2\phi$	$\cos\theta\cot\phi$	$2\sin\theta\sin 2\phi$
$3,3$	$1.5\cos 2\phi + 0.5$	0	$-2\sin 2\phi$
$\{i,j\}$	$\Omega^4_{\{i,j\}}$	$\Omega^5_{\{i,j\}}$	$\Omega^6_{\{i,j\}}$
$1,1$	$-\sin 2\theta\cot\phi$	$-\sin^2\theta/\sin^2\phi$	$-\cos^2\theta\cos^2\phi$
$1,2$	$\cos 2\theta\cot\phi$	$0.5\sin 2\theta/\sin^2\phi$	$-0.5\sin 2\theta\cos^2\phi$
$1,3$	$\sin\theta$	0	$0.5\cos\theta\sin 2\phi$
$2,2$	$\sin 2\theta\cot\phi$	$-\cos^2\theta/\sin^2\phi$	$-\sin^2\theta\cos^2\phi$
$2,3$	$-\cos\theta$	0	$0.5\sin\theta\sin 2\phi$
$3,3$	0	0	$-\sin^2\phi$

Coordinate transformation for avoidance of the indetermination near the x_3 axis

Although the Fourier series is free of singularities, its derivative, from which results the fundamental solution for traction in BEM, Equation 2.117, the second term of Equation 2.175 is indeterminate as $\phi \to 0$, due to the division by $\sin\phi$. To circumvent this problem, Shiah et al., 2012, suggests adding a perturbation to ϕ and set to zero the other angles of the derivative, which cancels out this term.

Although one can accept this solution in some cases, there exist the possibility that an entire line of integration points to be aligned with the x_3 axis during the computation BEM integrals — this can cause the resulting integral to be incorrect. That solution can also cause performance constraints in the underlying BEM implementation, which one should avoid at all costs.

Another manner to deal with this problem is to use a rotation matrix, as suggested in Tan et al., 2013, for the computation of the *second derivative* of the Green's function, hence rotating the coordinate system (x_i), $(i = 1, 2, 3)$ on the x_2 axis by an angle of $\pi/2$ represented by the following proper orthogonal transformation matrix

$$\Omega^{(2)|_{\frac{\pi}{2}}} = \begin{bmatrix} 0 & 0 & -1 \\ 0 & 1 & 0 \\ 1 & 0 & 0 \end{bmatrix}. \tag{2.180}$$

The first- and second-order derivatives of the Green's function are calculated at this rotated coordinate vector $(\hat{\mathbf{e}}^*_{(3)})$, as $\tilde{U}^*_{ABc}$ and $\tilde{U}^*_{ABcd}$, then rotated to the original coordinate axis through relations

$$\tilde{U}_{IKj}(\hat{\mathbf{e}}_{(3)}) = \Omega^{(2)|_{\frac{\pi}{2}}}_{AI}\, \Omega^{(2)|_{\frac{\pi}{2}}}_{BK}\, \Omega^{(2)|_{\frac{\pi}{2}}}_{cj}\, \tilde{U}^*_{ABc}(\hat{\mathbf{e}}^*_{(3)}) \tag{2.181}$$

and

$$\tilde{U}_{IKjl}(\hat{\mathbf{e}}_{(3)}) = \Omega^{(2)|_{\frac{\pi}{2}}}_{AI}\, \Omega^{(2)|_{\frac{\pi}{2}}}_{BK}\, \Omega^{(2)|_{\frac{\pi}{2}}}_{cj}\, \Omega^{(2)|_{\frac{\pi}{2}}}_{dl}\, \tilde{U}^*_{ABcd}(\hat{\mathbf{e}}^*_{(3)}). \tag{2.182}$$

As this rotation is not necessarily a material symmetry operation nor it is a reflection, a new set of coefficients (Equation 2.156) must also be evaluated at the newly

rotated coordinate system. The rotated stiffness tensors are written as

$$\begin{aligned} C^*_{ijkm} &= \Omega^{(2)|_{\frac{\pi}{2}}}_{ia}\Omega^{(2)|_{\frac{\pi}{2}}}_{jb}\Omega^{(2)|_{\frac{\pi}{2}}}_{kc}\Omega^{(2)|_{\frac{\pi}{2}}}_{md}\, C_{abcd}, \\ e^*_{ijk} &= \Omega^{(2)|_{\frac{\pi}{2}}}_{ia}\Omega^{(2)|_{\frac{\pi}{2}}}_{jb}\Omega^{(2)|_{\frac{\pi}{2}}}_{kc}\, e_{abc}, \\ q^*_{ijk} &= \Omega^{(2)|_{\frac{\pi}{2}}}_{ia}\Omega^{(2)|_{\frac{\pi}{2}}}_{jb}\Omega^{(2)|_{\frac{\pi}{2}}}_{kc}\, q_{abc}, \\ \epsilon^*_{ij} &= \Omega^{(2)|_{\frac{\pi}{2}}}_{ia}\Omega^{(2)|_{\frac{\pi}{2}}}_{jb}\, \epsilon_{ij}, \\ \lambda^*_{ij} &= \Omega^{(2)|_{\frac{\pi}{2}}}_{ia}\Omega^{(2)|_{\frac{\pi}{2}}}_{jb}\, \lambda_{ab}, \\ \mu^*_{ij} &= \Omega^{(2)|_{\frac{\pi}{2}}}_{ia}\Omega^{(2)|_{\frac{\pi}{2}}}_{jb}\, \mu_{ab}. \end{aligned} \tag{2.183}$$

Efficient integration of Fourier Series coefficients of the Barnett-Lothe tensor

The integration of the Fourier coefficients, Equations 2.160 to 2.163, are of the kind

$$\int_0^{\frac{2\pi}{\rho}} \int_0^{2\pi} f(\hat{e}(\theta,\phi))d\theta d\phi, \tag{2.184}$$

in fact if $f(\hat{e})$ is constant, the integral results in the surface area of the sphere times the function value. Applying the Gaussian quadrature to compute this integral results in

$$\frac{1}{4}\sum_{k_1}\sum_{k_2} f(\theta_{k_1},\phi_{k_2})w_{k_1}w_{k_2}, \tag{2.185}$$

where θ_{k_1}, ϕ_{k_2} are the Gauss abscissas in both directions k_1, k_2, i.e., $\theta_k = \pi p_k$ $\phi_k = \frac{1}{2}\pi p_k$, scaled by the integration domain, and $\frac{1}{4}$ is the corresponding Jacobian. p_k is the vector containing the Gauss integration points.

One assumes that all coefficients are computed using the same quadrature rule; Therefore, function f can be evaluated only one time for each Gauss abscissa, then, multiplied by the weights vector which is organized in the following fashion

$$\mathbf{w}_{\mathrm{K}} = \frac{1}{4}\begin{bmatrix} w_1w_1 & w_1w_2 & \dots & w_1w_{k_2} & w_2w_1 & \dots & w_2w_{k_2} & \dots & w_{k_1}w_{k_2} \end{bmatrix}^T. \tag{2.186}$$

The matrix having function f may contain 6 (Elastic), 10 (PE or ME) or 15 (MEE) components of the Barnett-Lothe tensor evaluated at each one of the $\mathrm{K} = [1, k_1k_2]$ Gauss abscissas. Therefore, one can premultiply it by the weights vector resulting in

$$\mathbf{H^w}_{K\mathrm{v}} = \mathbf{H}_{K\mathrm{v}}\mathbf{w}_K \qquad \text{(no implicit sum)}, \tag{2.187}$$

where v stands for the Voigt vector representation of the symmetric tensor H_{JK}, $J, K =$

$[1, ndof]$. The cosine and sine for all Gauss points can be also stated in matrix form, such as

$$\begin{aligned} \mathbf{c}^{\theta}_{K\mathrm{m}} &= \cos(\mathrm{m}\theta_{\mathrm{K}}) \quad \mathbf{s}^{\theta}_{K\mathrm{m}} = \sin(\mathrm{m}\theta_{\mathrm{K}}) \\ \mathbf{c}^{\phi}_{K\mathrm{n}} &= \cos(\rho\mathrm{n}\phi_{\mathrm{K}}) \quad \mathbf{s}^{\phi}_{K\mathrm{n}} = \sin(\rho\mathrm{n}\phi_{\mathrm{K}}) \end{aligned} \tag{2.188}$$

The numerical integration of the coefficients can be then performed by the following sum over the K Gauss point (implied over the repeated index in the matrix multiplication)

$$\lambda_{R1(\mathrm{vmn})} = \mathbf{H}^{\mathbf{w}}{}_{K\mathrm{v}}\mathbf{c}^{\theta}_{K\mathrm{m}}\mathbf{c}^{\phi}_{K\mathrm{n}} \tag{2.189}$$

$$\lambda_{R2(\mathrm{vmn})} = \mathbf{H}^{\mathbf{w}}{}_{K\mathrm{v}}\mathbf{s}^{\theta}_{K\mathrm{m}}\mathbf{s}^{\phi}_{K\mathrm{n}} \tag{2.190}$$

$$\lambda_{I1(\mathrm{vmn})} = \mathbf{H}^{\mathbf{w}}{}_{K\mathrm{v}}\mathbf{c}^{\theta}_{K\mathrm{m}}\mathbf{s}^{\phi}_{K\mathrm{n}} \tag{2.191}$$

$$\lambda_{I2(\mathrm{vmn})} = \mathbf{H}^{\mathbf{w}}{}_{K\mathrm{v}}\mathbf{s}^{\theta}_{K\mathrm{m}}\mathbf{c}^{\phi}_{K\mathrm{n}} \tag{2.192}$$

After this computation, the terms can be properly scaled by the constants appearing in Equations 2.160 to 2.163, i.e.,

$$\lambda_{(\cdot)(\mathrm{vmn})} = \frac{\rho\kappa_m\kappa_n}{4\pi^2}\lambda_{(\cdot)(\mathrm{vmn})}, \qquad \text{(no implicit sum)}. \tag{2.193}$$

It is necessary to point out that, as K, m and n, the cosine and sine matrices should be computed preferably inside a loop for each Gauss point to avoid their storage, otherwise, the arrays of size $[K \times m]$ and $[K \times n]$ may not fit in memory. As the high-order terms of the series must decrease in magnitude (or converge to zero) due to properties of Green's function, using the same quadrature for the computation of all terms can be beneficial as it ensures greater precision on the low-order terms. At the same time, it also ensures that the high-order terms are not under-sampled, i.e., a low-order polynomial, e.g., a 10 point Gaussian quadrature cannot approximate the quick variation of the high-order terms (e.g., $\cos(15\,\phi)$). This effect is verified in the next section.

2.6 Results for the Fourier series coefficients and solution evaluation

In this section, the various aspects of the fundamental solution represented using the Fourier Series are explored and verified. One has to evaluate a considerable number of materials, due to the dependence of the approximation method on the properties and the numerous symmetries of the materials being represented. The most commonly found applications in engineering are isotropic at the macro-scale (poly-crystalline materials), transversely isotropic or orthotropic (fiber reinforced plastic composites) and layered ge-

ological materials. Also, since the 1980 decade, Nickel alloys solidified as a monolithic crystal with cubic symmetry are being used in the first stage blades of jet engines to avoid creep at near-melting temperatures. As there are many elastic materials to consider, in the author's experience, the most difficult of these materials regarding convergence of integration and the solution reproduction, was the cubic symmetry. The number of non-zero coefficients after the integration was high, and the convergence was the slowest. A selection of MEE and PE materials was also done, and they are listed as follows.

This analysis was carried out for the following materials:

- Cubic elastic material (Nickel) with principal planes aligned with the coordinate system, found in Table 4.1 (Figure 2.7a);
- Piezoelectric material PZT4 (Figure 2.7b);
- Piezoelectric + Piezomagnetic material, without Magneto-Electric coupling (Figure 2.7c). It is a transversely isotropic material with the elastic and piezoelectric properties of $BaTiO_3$ and the piezomagnetic coefficients of $CoFe_2O_4$, but no electromagnetic coupling, due to Pan, 2002, which were taken from the work of Huang and Kuo, 1997;
- Fully coupled Maneto-Electro-Elastic composite, namely $BaTiO_3$—$CoFe_2O_4$, using a volume fraction v = 0.50, whose properties are due to Buroni and Sáez, 2010 (Figure 2.7d).

The first aspect covered is the integration convergence of the Fourier series coefficients Equations 2.160 to 2.163, presented in Figure 2.7 and Figure 2.8. Since analytical values for these terms are not possible to be explicitly obtained for the materials analyzed, let us propose the following mean error rule

$$e_{\text{int}}^{(K,\alpha)}\left[\lambda_{uv}^{K(m,n)}\right] = \frac{\sum_{u,v=1}^{\text{ndof}}\left[\sum_{m,n=-\alpha}^{\alpha}\left|\lambda_{uv}^{K(m,n)} - \lambda_{uv}^{\text{ref}\,(m,n)}\right|\right]}{(2\alpha)^2(\text{ndof}^2)\max\left(\left|\lambda_{uv}^{\text{ref}\,(m,n)}\right|\right)} \tag{2.194}$$

where $\lambda_{uv}^{R(m,n)}$ is a reference coefficient matrix evaluated with a high number of Gauss abscissas, and $\lambda_{uv}^{K(m,n)}$ is the matrix being evaluated with an order K rule.

Although both figures present mainly the same information, in Figure 2.7 is possible to analyze how a specific set of coefficients respond to the increase in the number of

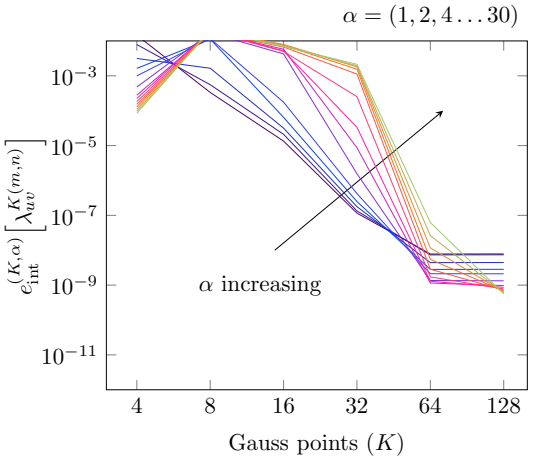

(a) Cubic Ni

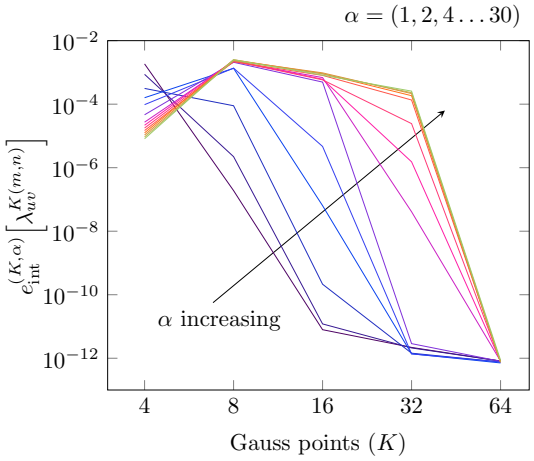

(b) PE *Material A*

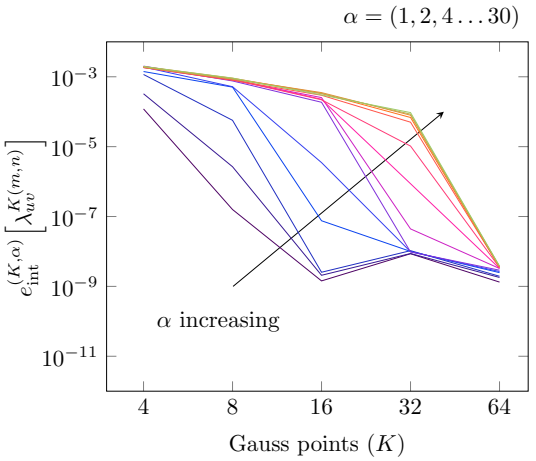

(c) PE+PM *Material B*

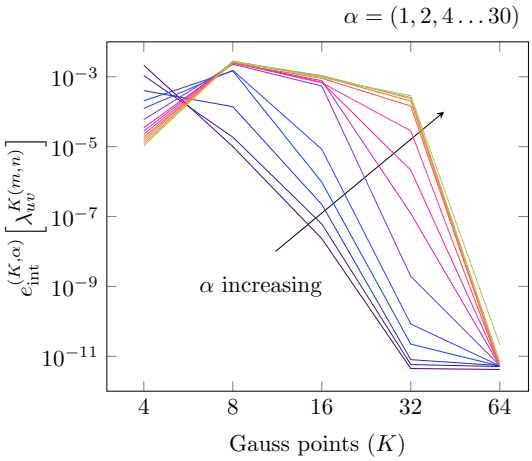

(d) MEE *Material C*

Figure 2.7 – Mean relative difference on the coefficient integration, Equation 2.194, as a function of the integration rule $K = \{4, 8, 16, 32, 64, 128\}$, for a fixed cofficient matrix size, $m = n = \alpha$, with $\alpha = [1, 30]$.

integration points. In Figure 2.8 is possible to verify the correspondence to each integration rule to the increase in the number of terms. This second plotting method is useful to establish the maximum number of terms a quadrature rule can integrate with reasonable accuracy for a given material.

As could be noticed in the presented plots, Gaussian quadrature rules increasing from $K = 4$ to $K = 128$ in each direction were selected for this analysis. The range of

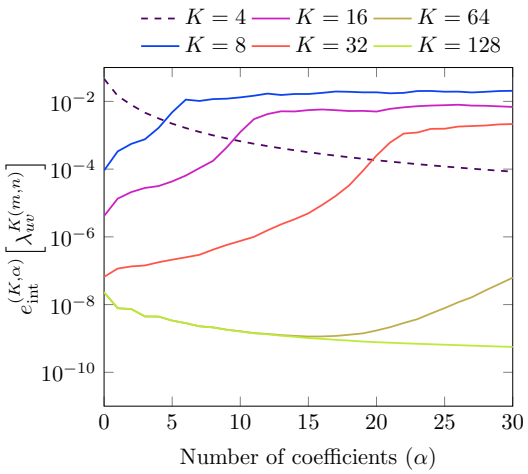

(a) Nickel

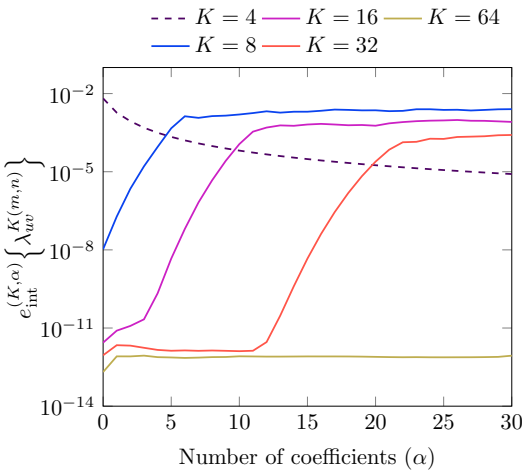

(b) PE *Material A*

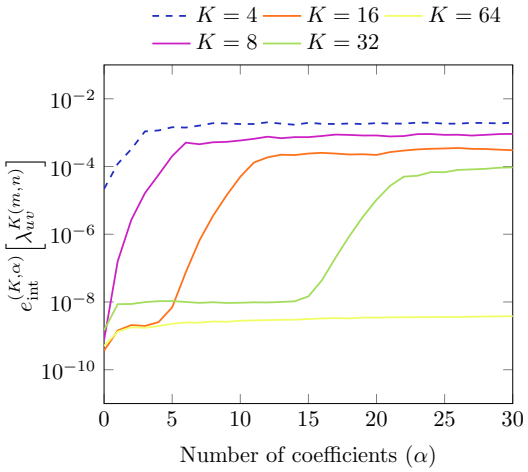

(c) PE+PM *Material B*

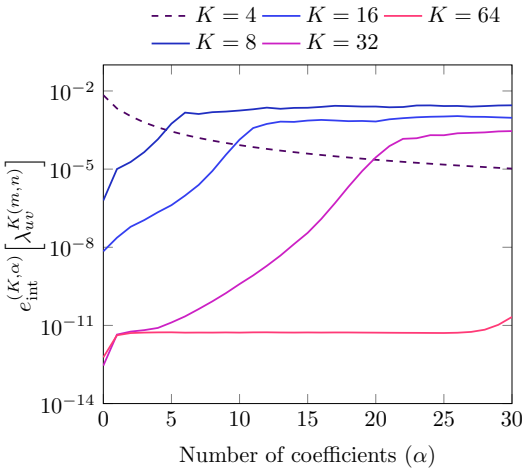

(d) MEE *Material C*

Figure 2.8 – Mean relative difference on the coefficient integration, Equation 2.194, as a function of the number of coefficients, $m = n = \alpha$, with $\alpha = [1, 30]$, for a set of fixed integration rules $K = \{4, 8, 16, 32, 64\}$.

terms considered for the coefficient matrices was $\alpha = [1, 30]$.

Convergence of the Fourier Green's function and its derivatives

In Figure 2.9a, the Fourier series solution using the already converged coefficients was evaluated against the function used to compute the coefficients Equations 2.160 to 2.163. The error norm e_{S_1} is evaluated over the surface of a unit sphere using the

following scheme

$$\mathrm{e}_{S_1}[U_{ij}] = \frac{\left\|U_{ij} - U_{ij}^{\mathrm{ref}}\right\|_{S_1}}{\left\|U_{ij}^{\mathrm{ref}}\right\|_{S_1}}, \tag{2.195}$$

where, $\|\cdot\|_{S_1} = \int_{S_1} |\cdot| dS$ and S_1 is a unit sphere. The convergence of the Fourier series solution is presented in Figure 2.9a. For this example Equation 2.195 was evaluated using $n = 16$ quadrature rule.

As was pointed out earlier in this work, the Barnett-Lothe tensor is an analytic and holomorphic function, i.e., it presents no discontinuities or abrupt changes and it is smooth throughout its entire domain; It is a periodic function, which implies it is also smooth and continuous at the boundaries. As the terms of the Fourier series of this function are integrated, the progressively increasing number of wave numbers will result in decaying values for an increase in the coefficient order. The result is that a *finite* number of terms should be necessary for its reproduction considering finite precision (floating point). Although this holds for any material configuration, it is only possible to be demonstrated with closed-form solutions, as those can be analytically integrated, revealing which terms of the series are not null.

As an analytical solution to compare the Green function from Buroni et al., 2019, is available, it is possible to analyze the convergence of the Fourier series effectively. Nevertheless, instead of probing the error of the Fourier series at a single point, the relative error is evaluated at the sphere surface domain. This relative error is then numerically integrated, a useful measure once this function is never evaluated at a single point, instead it is integrated throughout the elements on the assembly of the BEM equation system.

A $K = 128$ rule in each direction was considered for this example to ensure the high-order coefficients were correctly integrated. For all practical purposes, a 64 point rule is sufficient for integrating up to 20 terms with an accurate reproduction of the base function.

Tables Tables 2.4 to 2.6 sample the proposed Fourier series approximation for the Green's function and its derivatives at the point $\mathbf{x} = [1, 1, -1]$.

2.6.1 Influence of equivalent anisotropy index

The possibility and existence of a wide range of material symmetries as well as numerous levels of anisotropy requires one to investigate the influence of the anisotropic

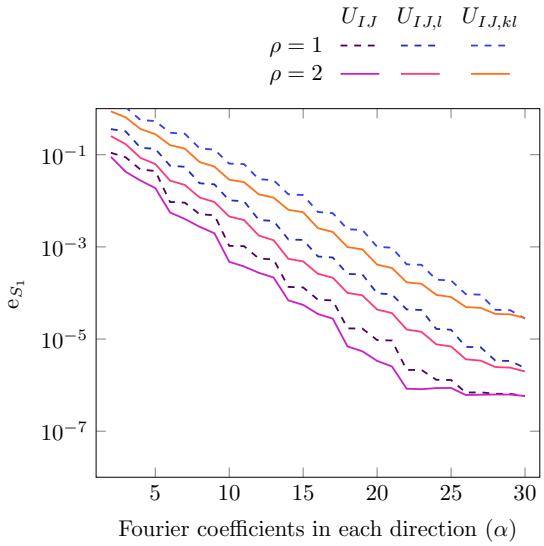

(a) Nickel

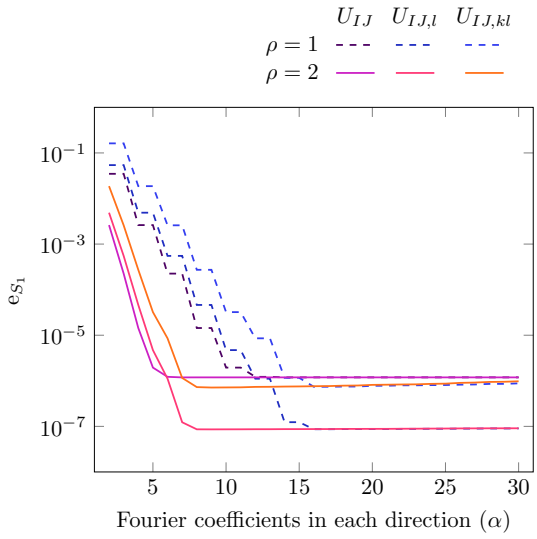

(b) PE *material A*: PZT-4

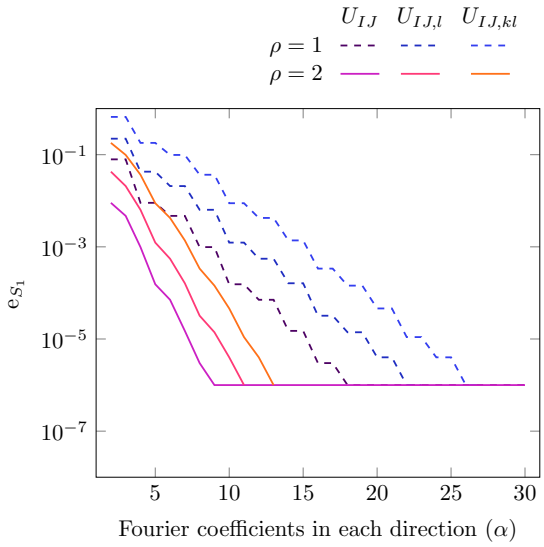

(c) PE+PM *material B*: PZT4 - CoFe2O4

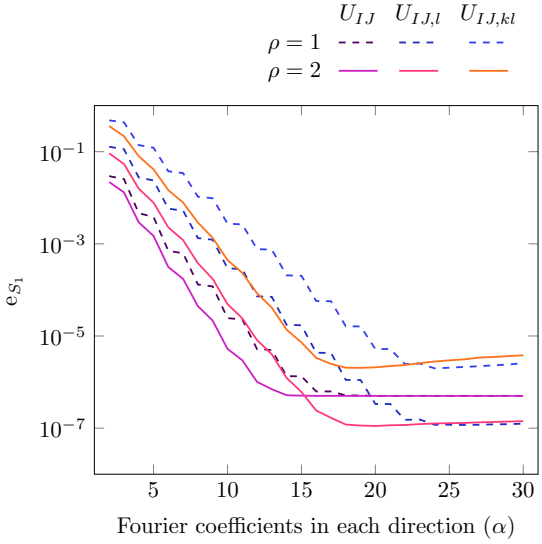

(d) MEE *material C*: BaTiO3-CoFe2O4

Figure 2.9 – Error integral over the unit sphere e_{S_1} for the MEE Green's function and its derivatives considering Shiah et al., 2012, formulation, $\rho = 1$ (dashed lines) and the present work formulation, $\rho = 2$ (continuous lines).

index on the accuracy of the Fourier series Green's function for these materials. Also, as pointed out by Gaul et al., 2013: "The piezoelectric effect does not appear in all crystals, but only in those that lack a centre of symmetry. As a consequence, piezoelectric materials are always anisotropic." MEE materials with efficient magneto-electric coupling

Table 2.4 – Green's function U_{JK} for MEE Material C.

$\{jk\}$	Buroni and Sáez, 2010	present work (non-degenerate)	present work (Fourier $\rho = 2$)
11	$8{,}7225398002742391 \times 10^{-4}$	$8{,}7225391529708176 \times 10^{-4}$	$8{,}7225391143385966 \times 10^{-4}$
12	$6{,}4154620180000892 \times 10^{-5}$	$6{,}4154633546640012 \times 10^{-5}$	$6{,}4154635388780994 \times 10^{-5}$
13	$3{,}1446825949164037 \times 10^{-4}$	$3{,}1446823384049725 \times 10^{-4}$	$3{,}1446823020702950 \times 10^{-4}$
14	$-1{,}2680519416303164 \times 10^{-3}$	$-1{,}2680518422761380 \times 10^{-3}$	$-1{,}2680518331308015 \times 10^{-3}$
15	$-5{,}1231568254934725 \times 10^{-7}$	$-5{,}1231566218975244 \times 10^{-7}$	$-5{,}1231566172255558 \times 10^{-7}$
22	$7{,}6090426614139801 \times 10^{-4}$	$7{,}6090421241993020 \times 10^{-4}$	$7{,}6090420962374212 \times 10^{-4}$
23	$4{,}9374127465890965 \times 10^{-5}$	$4{,}9374116000788879 \times 10^{-5}$	$4{,}9374114832466072 \times 10^{-5}$
24	$4{,}5315107542192896 \times 10^{-4}$	$4{,}5315103712122884 \times 10^{-4}$	$4{,}5315103438906013 \times 10^{-4}$
25	$2{,}8343787079494569 \times 10^{-7}$	$2{,}8343785605411864 \times 10^{-7}$	$2{,}8343785543437576 \times 10^{-7}$
33	$1{,}0440331060742933 \times 10^{-3}$	$1{,}0440330705104972 \times 10^{-3}$	$1{,}0440330649497012 \times 10^{-3}$
34	$-1{,}8426611715379502 \times 10^{-3}$	$-1{,}8426611016083994 \times 10^{-3}$	$-1{,}8426610912217531 \times 10^{-3}$
35	$-6{,}5916283018091271 \times 10^{-7}$	$-6{,}5916280287229014 \times 10^{-7}$	$-6{,}5916280074504749 \times 10^{-7}$
44	$1{,}2157849166703620 \times 10^{-2}$	$1{,}2157848479829412 \times 10^{-2}$	$1{,}2157848421365205 \times 10^{-2}$
45	$1{,}8466901349619211 \times 10^{-6}$	$1{,}8466900615535804 \times 10^{-6}$	$1{,}8466900594546791 \times 10^{-6}$
55	$2{,}5182299673182738 \times 10^{-7}$	$2{,}5182298256559097 \times 10^{-7}$	$2{,}5182298226958415 \times 10^{-7}$

Table 2.5 – Derivative of Green's function $U_{JK,3}$ for MEE Material C.

$\{jk, l\}$	Finite differences	Buroni and Sáez, 2010	present work
11, 3	$-3{,}675\,418\,036\,705\,983 \times 10^{-13}$	$-3{,}675\,418\,038\,147\,529 \times 10^{-13}$	$-3{,}675\,415\,184\,885\,964\,0 \times 10^{-13}$
12, 3	$-1{,}022\,473\,809\,428\,751 \times 10^{-13}$	$-1{,}022\,473\,811\,350\,401 \times 10^{-13}$	$-1{,}022\,471\,681\,140\,282\,5 \times 10^{-13}$
13, 3	$-1{,}130\,914\,219\,850\,401 \times 10^{-14}$	$-1{,}130\,914\,522\,684\,852 \times 10^{-14}$	$-1{,}130\,916\,308\,353\,429\,9 \times 10^{-14}$
14, 3	$3{,}207\,066\,889\,615\,237 \times 10^{-4}$	$3{,}207\,067\,004\,117\,469 \times 10^{-4}$	$3{,}207\,074\,366\,896\,354\,2 \times 10^{-4}$
15, 3	$2{,}240\,137\,639\,332\,812 \times 10^{-7}$	$2{,}240\,137\,681\,772\,090 \times 10^{-7}$	$2{,}240\,348\,281\,547\,726\,9 \times 10^{-7}$
22, 3	$-3{,}482\,702\,552\,773\,726 \times 10^{-13}$	$-3{,}482\,702\,562\,831\,942 \times 10^{-13}$	$-3{,}482\,711\,709\,887\,898\,8 \times 10^{-13}$
23, 3	$2{,}457\,210\,719\,924\,869 \times 10^{-15}$	$2{,}457\,208\,785\,075\,626 \times 10^{-15}$	$2{,}457\,898\,647\,735\,611\,1 \times 10^{-15}$
24, 3	$-1{,}386\,199\,675\,011\,690 \times 10^{-4}$	$-1{,}386\,199\,583\,437\,589 \times 10^{-4}$	$-1{,}386\,224\,660\,320\,099\,8 \times 10^{-4}$
25, 3	$-1{,}123\,708\,543\,004\,768 \times 10^{-7}$	$-1{,}123\,708\,508\,292\,927 \times 10^{-7}$	$-1{,}123\,638\,542\,164\,919\,5 \times 10^{-7}$
33, 3	$-8{,}404\,303\,395\,022\,170 \times 10^{-14}$	$-8{,}404\,303\,328\,191\,928 \times 10^{-14}$	$-8{,}404\,340\,451\,696\,422\,0 \times 10^{-14}$
34, 3	$1{,}966\,253\,560\,794\,704 \times 10^{-4}$	$1{,}966\,253\,482\,908\,411 \times 10^{-4}$	$1{,}966\,268\,142\,258\,674\,7 \times 10^{-4}$
35, 3	$1{,}850\,871\,822\,783\,363 \times 10^{-7}$	$1{,}850\,871\,866\,296\,891 \times 10^{-7}$	$1{,}850\,690\,508\,534\,595\,3 \times 10^{-7}$
44, 3	$-3{,}346\,553\,299\,576\,044 \times 10^{6}$	$-3{,}346\,553\,312\,754\,738 \times 10^{6}$	$-3{,}346\,559\,638\,224\,575\,9 \times 10^{6}$
45, 3	$-7{,}696\,119\,549\,791\,547 \times 10^{2}$	$-7{,}696\,119\,653\,866\,651 \times 10^{2}$	$-7{,}696\,075\,707\,465\,677\,6 \times 10^{2}$
55, 3	$-1{,}323\,349\,050\,039\,724 \times 10^{2}$	$-1{,}323\,349\,045\,127\,773 \times 10^{2}$	$-1{,}323\,334\,126\,068\,789\,6 \times 10^{2}$

Table 2.6 – Second derivative of Green's function $U_{JK,ls}$ for the MEE Material C.

$\{jk, ls\}$	Finite differences (Buroni and Sáez, 2010)	present work
11, 11	$-2.1980595058120835 \times 10^{-4}$	$-2.1978899449576415 \times 10^{-4}$
12, 11	$1.9687625791783847 \times 10^{-4}$	$1.9687288627287911 \times 10^{-4}$
13, 11	$2.0689019605574925 \times 10^{-4}$	$2.0687790498394083 \times 10^{-4}$
14, 11	$1.2939342436055212 \times 10^{-4}$	$1.2939411002126129 \times 10^{-4}$
15, 11	$4.9919418072938075 \times 10^{-4}$	$4.9919589319171225 \times 10^{-4}$
22, 11	$2.8999238991037073 \times 10^{-5}$	$2.9007574036204438 \times 10^{-5}$
23, 11	$-1.5980459863788832 \times 10^{-4}$	$-1.5980472435096293 \times 10^{-4}$
24, 11	$8.2646416647196368 \times 10^{-5}$	$8.2646486728975450 \times 10^{-5}$
25, 11	$4.9176303315383834 \times 10^{-5}$	$4.9176515955750446 \times 10^{-5}$
33, 11	$-2.1532552044162658 \times 10^{-4}$	$-2.1532570098457580 \times 10^{-4}$
34, 11	$8.4475529653002539 \times 10^{-5}$	$8.4475777310801128 \times 10^{-5}$
35, 11	$7.0842975461045929 \times 10^{-5}$	$7.0842038016214879 \times 10^{-5}$
44, 11	$-2.4896882218204035 \times 10^{-4}$	$-2.4896293517520753 \times 10^{-4}$
45, 11	$2.0394690732235263 \times 10^{-4}$	$2.0394549294444864 \times 10^{-4}$
55, 11	$1.2754151363068311 \times 10^{-4}$	$1.2753740393729069 \times 10^{-4}$

are usually produced by layering different phases of PE and ME materials.

This configuration inherently presents levels of anisotropy, be it on their elastic,

magnetic, electric, or at the coupling between these fields [Espinosa-Almeyda et al., 2011].

As an anisotropy index for MEE materials is yet to be defined and as the Zener and Siegel, 1949, anisotropy index is valid for Cubic materials, let us use the Universal anisotropic index from Ranganathan and Ostoja-Starzewski, 2008, which also provides an equivalent anisotropy index that enabling direct comparison with the Zener index. For cubic materials, Zener and Siegel, 1949, introduced a measure to quantify the anisotropy, known as the Zener anisotropic index, is defined by

$$A = \frac{2C_{44}}{C_{11} - C_{12}}. \tag{2.196}$$

For more general materials, another anisotropy index exist, such as Chung and Buessem, 1967, Ledbetter and Migliori, 2006, and others. The Universal anisotropy index, is due to Ranganathan and Ostoja-Starzewski, 2008, and is

$$A^U = 5(\frac{G_v}{G_r}) + (\frac{K_v}{K_r}) - 6 \tag{2.197}$$

where G_v and K_v are the Voigt average shear and bulk modulus, and G_r and K_r are the Reuss average shear and bulk modulus. Voigt and Reuss defined these modules as

$$\begin{aligned}
9K_V &= (C_{11} + C_{22} + C_{33}) + 2\,(C_{12} + C_{23} + C_{31})\,, \\
15G_V &= (C_{11} + C_{22} + C_{33}) - (C_{12} + C_{23} + C_{31}) + 3\,(C_{44} + C_{55} + C_{66})\,, \\
1/K_R &= (s_{11} + s_{22} + s_{33}) + 2\,(s_{12} + s_{23} + s_{31})\,, \\
15/G_R &= 4\,(s_{11} + s_{22} + s_{33}) - 4\,(s_{12} + s_{23} + s_{31}) + 3\,(s_{44} + s_{55} + s_{66})\,.
\end{aligned}$$

Where $s_{ij} = C_{ij}^{-1}$. To enable direct comparison with Zener's, the authors proposed an *equivalent anisotropic index*,

$$A^{eq} = \left(1 + \frac{5}{12}A^U\right) + \sqrt{\left(1 + \frac{5}{12}A^U\right)^2 - 1}. \tag{2.198}$$

Through the use of these concepts we propose a rule for the variation of *material B*, in which A^{eq} could vary from an isotropic to highly anisotropic.

In the particular case of piezoelectric and MEE materials, to the best of the author's knowledge, there is not available in the literature an anisotropy index for these materials. Although it seems to be useful to formulate an extended anisotropic index for MEE materials, it is out of the scope of this work, and therefore, simple rules which cause

anisotropy of both the electric and the magnetic constants are defined. The coupling constants are not altered being maintained the same as the *reference material B*.

As it was observed previously, the derivatives of this function seems to maintain a fixed precision offset relative to the function, characteristic to the approximation, so the anisotropy effect is studied only on the displacement Green's function.

To obtain the properties of an isotropic material, $A^{eq} = 1$, C_{1111} and C_{2233} are maintained as in *material B*, and a new stiffness tensor, C_{iJKl}, is obtained modifying the following set of properties,

$$\begin{aligned} \tilde{C}_{3333} &= \tilde{C}_{2222} = C_{1111}, \\ \tilde{C}_{1122} &= \tilde{C}_{1133} = C_{2233}, \\ \tilde{C}_{2323} &= (C_{1111} - C_{1122})/2, \\ \tilde{C}_{1212} &= \tilde{C}_{1313} = C_{2323}, \\ \tilde{\mu}_{33} = \tilde{\mu}_{22} &= \mu_{11}, \quad \tilde{\epsilon}_{33} = \tilde{\epsilon}_{22} = \epsilon_{11}. \end{aligned} \tag{2.199}$$

To obtain $A^{eq} \neq 1$, the following rule is devised for the update of *material B* stiffness tensor, C_{iJKl}

$$\begin{aligned} \tilde{C}_{2323} &= A^d C_{2323}, \\ \tilde{C}_{1313} &= A^d C_{1313}, \\ \tilde{C}_{1212} &= A^d (C_{1111} - C_{1122})/2, \end{aligned} \tag{2.200}$$

where A^d is the desired anisotropy index. With A^{eq} obtained, the dielectric and magnetic properties are modified accordingly,

$$\tilde{\mu}_{33} = A^{eq}\mu_{11}, \quad \tilde{\epsilon}_{33} = A^{eq}\epsilon_{11}, \tag{2.201}$$

The input values used in Equation 2.200 are brought in Table 2.7. The resultant A^{eq} from the devised rules are close to the desired ones A^d. Notice that the measure of anisotropy A^{eq} is performed only on the elastic part of the extended MEE tensor.

Table 2.7 – Resulting A^{eq} for the elastic part of the extended MEE stiffness tensor, for A^d used as input variable.

A^d	1,000	1,467	2,154	3,162	4,641	6,812	10,00
A^{eq}	1,000	1,471	2,157	3,165	4,645	6,817	10,00

Figure 2.10 depicts the results for this analysis. Although the isotropic configuration presents a lower error, the precision is not directly dependent on the level of anisotropy. As the number of terms is increased above $\alpha = 16$, it is found that the highest differences occurr for the configurations with $A^{eq} = 2{,}157$ and $3{,}165$.

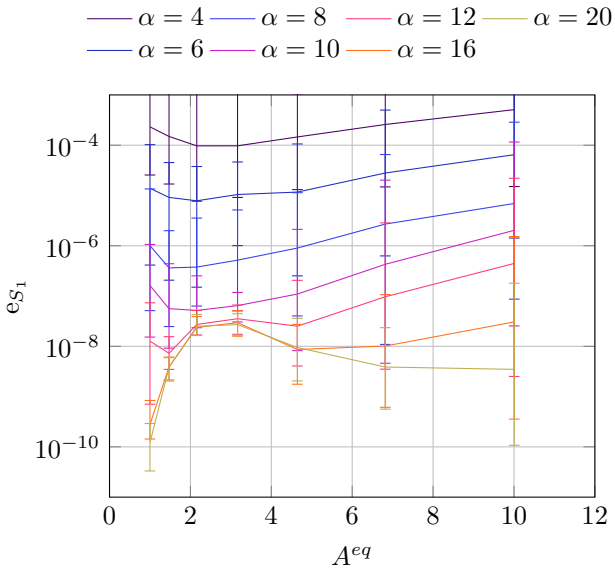

Figure 2.10 – Integral of the relative error over the unit sphere ($e_{s1}(U_{ij})$), on the approximation of the Green's function for anisotropic indices varying from 1 (isotropic) to 10 (highly anisotropic).

3 BOUNDARY INTEGRAL EQUATIONS AND THE BOUNDARY ELEMENT METHOD

This chapter presents the integral equations which the boundary element method (BEM) derives from, as shown by Brebbia et al., 2012, and also in Beer et al., 2008.

3.1 Boundary integral equations

One can attribute the BEM as a computational technique to Jawson, 1963 and Symm, 1963. These works used its original designation as *Boundary Integral Equation Method*. Rizzo, 1967, applied the method for plane elasticity, and in Cruse, 1969, is presented the first relevant work with BEM for three-dimensional elasticity.

The BEM is based on the integral representation of the Maxwell-Betti theorem, which can be obtained through the application of weighted residuals in the elasticity equilibrium equations, [Brebbia et al., 2012], i.e.,

$$\int_{\Omega} \left(\sigma_{kj,j} + b_k\right) u_k^* d\Omega = 0\,, \tag{3.1}$$

where the integral Equation 3.1 is the residue, and u_k^* is known as trial or weight function. Integrating by parts the first term of Equation 3.1 and grouping the domain integrals to the left-hand side of the equality one obtains

$$-\int_{\Omega} \sigma_{kj} u_{k,j}^* d\Omega + \int_{\Omega} b_k u_k^* d\Omega = -\int_{\Gamma} p_k u_k^* d\Gamma. \tag{3.2}$$

Integrating by parts again the first term of Equation 3.2 results in

$$\int_{\Omega} \sigma_{kj,j}^* u_k d\Omega + \int_{\Omega} b_k u_k^* d\Omega = -\int_{\Gamma} p_k u_k^* d\Gamma + \int_{\Gamma} p_k^* u_k d\Gamma, \tag{3.3}$$

which corresponds to the Maxwell-Betti reciprocal theorem[1] [Brebbia et al., 2012].

Equation 3.1 must satisfy the following boundary conditions

$$\begin{aligned} u_k &= \bar{u}_k \qquad \text{in} \quad \Gamma_1, \\ p_k &= \bar{p}_k \qquad \text{in} \quad \Gamma_2, \end{aligned} \tag{3.4}$$

[1] This theorem enforces linear reciprocity between stress and strains. On the other hand, its strong-form is robust as it states that the work of the internal forces is equal to the work of external forces. In that sense, one writes the boundary integral equations (BIE) in terms of the total energy of the system.

where $\bar{(\cdot)}$ represents known values of displacement and traction at the boundary. Separating the boundary Γ in the regions where the boundary conditions are set, Γ_1 and Γ_2, results in

$$\int_\Omega \sigma^*_{kj,j} u_k d\Omega + \int_\Omega b_k u^*_k d\Omega = -\int_{\Gamma_1} p_k u^*_k d\Gamma - \int_{\Gamma_2} \bar{p}_k u^*_k d\Gamma + \int_{\Gamma_1} \bar{u}_k p^*_k d\Gamma + \int_{\Gamma_2} u_k p^*_k d\Gamma. \quad (3.5)$$

Integrating by parts the first term on the left-hand side (LHS) of Equation 3.5 two more times, one obtains the following relation

$$\int_\Omega (\sigma_{kj,j} + b_k)\, u^*_k d\Omega = \int_{\Gamma_2} (p_k - \bar{p}_k) u^*_k d\Gamma + \int_{\Gamma_1} (\bar{u}_k - u_k) p^*_k d\Gamma. \quad (3.6)$$

Equation 3.6 is a generalized theorem which can also be used as a starting point to obtain the BIE, equivalent to Equation 3.1. According to Brebbia et al., 2012, $(p_k - \bar{p}_k)$ and $(\bar{u}_k - u_k)$ are also residuals being orthogonalized by the weighting functions.

One can return to Equation 3.5 by having this relations established, and proceed from it applying as weighting functions the fundamental solutions for a point force (Dirac delta) $b_l = \delta^i e_l$, along the direction of the unitary vector e_l. The first domain integral on the LHS of Equation 3.5 simplifies to

$$\int_\Omega \sigma^*_{lj,j} u_l d\Omega = -\int_\Omega \delta^i u_l e_l d\Omega = -u^i_l e_l, \quad (3.7)$$

where u^i_l represents the l component of the displacement at the load application point i.

Equation 3.5 can be written to represent the three components of displacement at i, if one writes the starred displacements and tractions as $u^*_l = U_{lk}\, e_l$, and $p^*_l = T_{lk}\, e_l$. With respect to Chapter 2, U_{lk} and T_{lk} are the Green's function for displacement, Equation 2.73, and the fundamental solution for traction, Equation 2.117. Writing each direction e_l independently results in

$$u^i_l + \int_{\Gamma_1} T_{lk} \bar{u}_k d\Gamma + \int_{\Gamma_2} T_{lk} u_k d\Gamma = \int_{\Gamma_1} U_{lk} p_k d\Gamma + \int_{\Gamma_2} U_{lk} \bar{p}_k d\Gamma + \int_\Omega U_{lk} b_k d\Omega, \quad (3.8)$$

which can be written in a more compact form without splitting the unknowns and the boundary conditions as

$$u^i_l = \int_\Gamma U_{lk} p_k d\Gamma - \int_\Gamma T_{lk} u_k d\Gamma + \int_\Omega U_{lk} b_k d\Omega. \quad (3.9)$$

Equation 3.9 is the well-known Somigliana Identity and is valid for any force applied at a point $\mathbf{x}'$ inside the domain Ω. Through this identity, it is possible to obtain displacements at any internal point as a function of the boundary values, the domain forces, and the fundamental solutions.

Evaluating Equation 3.9 when point i is at the boundary causes a singularity which needs to be separately analyzed. Considering a hemisphere of radius ε around the singularity, on a surface Γ_ε, as in Figure 3.1, the limit is taken in all integrals in Equation 3.9, remaining the following non-null term [Brebbia et al., 2012]

$$\int_\Gamma T_{lk} u_k d\Gamma = \lim_{\varepsilon \to 0} \left\{ \int_{\Gamma - \Gamma_\varepsilon} T_{lk} u_k d\Gamma \right\} + \lim_{\varepsilon \to 0} \left\{ \int_{\Gamma_\varepsilon} T_{lk} u_k d\Gamma \right\}, \tag{3.10}$$

in which the second term on the right-hand side (RHS) of Equation 3.10 can be written as

$$\lim_{\varepsilon \to 0} \left\{ \int_{\Gamma_\varepsilon} T_{lk} u_k d\Gamma \right\} = u_k^i \lim_{\varepsilon \to 0} \left\{ \int_{\Gamma_\varepsilon} T_{lk} d\Gamma \right\}. \tag{3.11}$$

Integral Equation 3.11 does not vanish when $\varepsilon \to 0$ but produces a free term. At smooth boundary points, one finds

$$\lim_{\varepsilon \to 0} \left\{ \int_{\Gamma_\varepsilon} T_{lk} d\Gamma \right\} = -\frac{1}{2} \delta_{lk}, \tag{3.12}$$

and all other integrals in Equation 3.9 vanishes. Therefore, Equation 3.10 can be written in the limit as

$$\cancel{\int_\Gamma} T_{lk} u_k d\Gamma - \frac{1}{2} \delta_{lk} u_k^i = \cancel{\int_\Gamma} T_{lk} u_k d\Gamma - \frac{1}{2} u_l^i, \tag{3.13}$$

where $\cancel{\int}(\cdot)$ denotes the Cauchy Principal Value of the integral $\int(\cdot)$.

Naming the free term $\frac{1}{2}\delta_{lk} = c_{lk}$, resulting from the limit, Equation 3.13, the resulting identity for boundary points is

$$c_{lk}^i u_k^i + \cancel{\int_\Gamma} T_{lk} u_k d\Gamma = \int_\Gamma U_{lk} p_k d\Gamma + \int_\Omega U_{lk} b_k d\Omega. \tag{3.14}$$

Formulations for free terms c_{lk}, for nodes not contained on a smooth surface, can be found in Mantic, 1993.

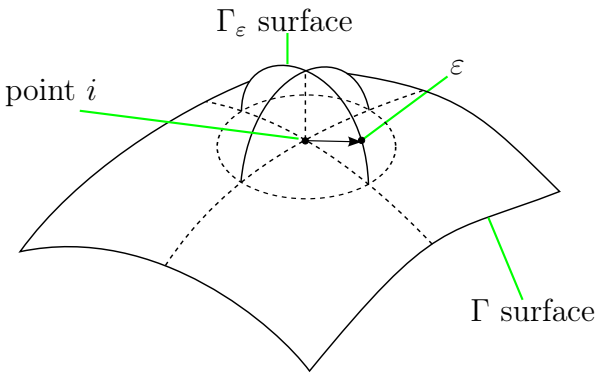

Figure 3.1 – Limit evaluated by Equation 3.10.

3.2 Numerical implementation

This section describes the transformation from the continuous integral formulation to the discrete one (splitting the boundary Γ into parametric elements), which can be solved by an algebraic formulation. By the consideration of discontinuous elements, one treats the geometric and boundary value problem (BVP) variables differently. This well-known approach is possible due to the collocation nature of the BEM procedure, i.e., each source node generates a set of equations obtained by collocation at all field nodes.

The geometry is discretized using quadrilateral elements, allowing one to use standard mesh generation routines, the same as the ones used in FEM — The geometry comes from a 3D surface-only mesh. To simplify the implementation, the *collocation nodes*, are automatically generated during the mesh loading process and are positioned at a fixed offset to the *geometric nodes*. In some particular cases, it is essential to have nodes in corners; Those are possible to be obtained using a null offset in some elements when necessary.

This type of element simplifies the matrix assembly process due to: (i) the free-term, is constant and equals to $\frac{1}{2}$; (ii) there is no need to perform the nodal superposition, thereby, it is possible to use non-conforming meshes (there is no necessity of nodal coincidence between neighboring elements throughout the mesh, e.g., see Rüberg and Schanz, 2009).

3.2.1 Geometry interpolation

Let us consider rectangular elements with a normalized local coordinate system (ξ_1, ξ_2) varying from $[-1, 1]$ (Figure 3.2).

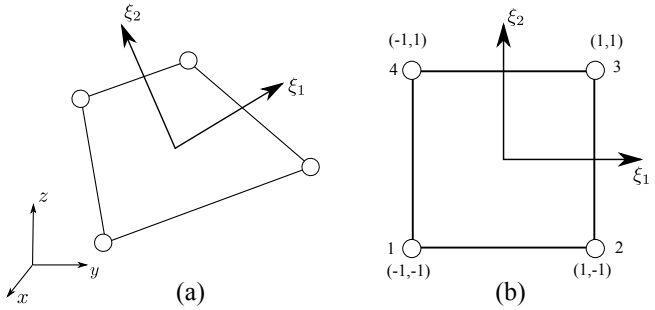

Figure 3.2 – Rectangular Element at: (a) General coordinates and (b) local coordinates.

Let $\boldsymbol{\xi}$ be a point with local coordinates $\boldsymbol{\xi} = (\xi_1, \xi_2)$, on an element j. One calculates the Cartesian coordinates vector, $\mathbf{x}$, for this point through the following relation

$$\mathbf{x} = \sum_{n=1}^{\mathrm{nn}^j} \phi_n^j(\xi_1, \xi_2)\mathbf{x}_n^j, \tag{3.15}$$

where nn is the number of nodes of the element j, ϕ_n is the n-th interpolation function value of the element at (ξ_1, ξ_2). x_n^j is the coordinate of the n-th node of that element. This sum is resumed in matrix notation as

$$\mathbf{x} = \mathbf{x}^j_{[3\times \mathrm{nn}]}\boldsymbol{\Phi}_{[\mathrm{nn}\times 1]}, \tag{3.16}$$

where $\boldsymbol{\Phi}$ is the interpolation functions vector at $\boldsymbol{\xi} = (\xi_1, \xi_2)$, and $\mathbf{x}^j$ is the matrix containing the coordinates $\mathbf{x}$ for each geometric node of element j, with size $[3 \times \mathrm{nn}]$.

The interpolation functions for the linear element are described by the following equation

$$\phi_n = \frac{1}{2}(1 + \xi_1^n\xi_1)\frac{1}{2}(1 + \xi_2^n\xi_2), \tag{3.17}$$

where ξ_d^n are the n-th node position as in Figure 3.2 (e.g.: $\xi_1^3 = -1, \xi_2^3 = 1$). Adding intermediate nodes at the elements edges, between the existent ones, one gets the well

known quadratic *serendipity* element.

$$\begin{aligned}
\phi_1 &= \frac{1}{4}(1-\xi_1)(1-\xi_2)(-\xi_1-\xi_2-1), & \phi_5 &= \frac{1}{2}(1-\xi_1^2)(1-\xi_2),\\
\phi_2 &= \frac{1}{4}(1+\xi_1)(1-\xi_2)(\xi_1-\xi_2-1), & \phi_6 &= \frac{1}{2}(1+\xi_1)(1-\xi_2^2),\\
\phi_3 &= \frac{1}{4}(1+\xi_1)(1+\xi_2)(\xi_1+\xi_2-1), & \phi_7 &= \frac{1}{2}(1-\xi_1^2)(1+\xi_2),\\
\phi_4 &= \frac{1}{4}(1-\xi_1)(1+\xi_2)(-\xi_1+\xi_2-1), & \phi_8 &= \frac{1}{2}(1-\xi_1)(1-\xi_2^2).
\end{aligned} \tag{3.18}$$

An internal middle node known as the bubble node may also be added. However, its advantages are not so significant in the BEM as reported in finite element method (FEM). The local coordinates of the quadratic element and the ones shared with the linear one are listed in Table 3.1.

Table 3.1 – Local coordinates of the linear element (nodes 1-4) and quadratic (nodes 1-8).

n	ξ_1	ξ_2
1	-1.0	-1.0
2	1.0	-1.0
3	1.0	1.0
4	-1.0	1.0
5	0.0	-1.0
6	1.0	0.0
7	0.0	1.0
8	-1.0	0.0

3.2.2 Discretization of unknowns and loads

The discontinuous elements offer extra flexibility in BEM, and can always be simplified to the continuous version when the offset is null. The first use of this element type is from the works of Patterson and Sheikh, 1981, 1984. The collocation nodes are offset from the geometric nodes towards the center of the element as in Figure 3.3.

The functions for those elements can be obtained multiplying the continuous ones by transformation matrices, however, is also possible to parametrize them as a function

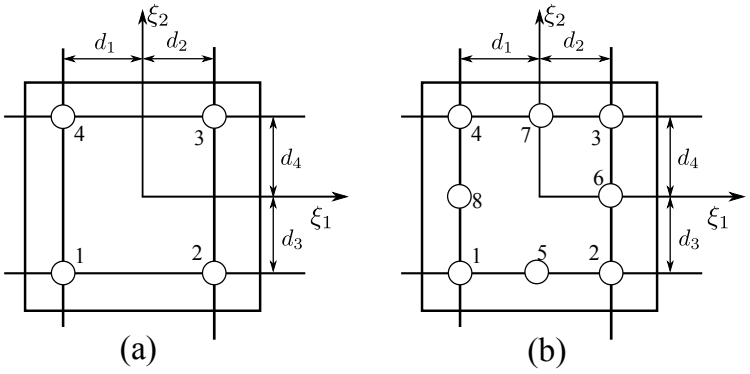

Figure 3.3 – Discontinuous elements (a) Linear and (b) Quadratic.

of the offset, as shown in Beer et al., 2008. The resulting linear functions are then

$$\begin{aligned}
\bar{\phi}_1 &= \frac{1}{c}(d_1 - \xi_1)(d_3 - \xi_2), \quad \bar{\phi}_2 = \frac{1}{c}(d_2 + \xi_1)(d_3 - \xi_2), \\
\bar{\phi}_3 &= \frac{1}{c}(d_2 + \xi_1)(d_4 + \xi_2), \quad \bar{\phi}_4 = \frac{1}{c}(d_1 - \xi_1)(d_4 + \xi_2), \\
c &= (d_1 + d_2)(d_3 + d_4),
\end{aligned} \tag{3.19}$$

where $d_1, \ldots, d_4$ are the distances from the element center to the nodes, as shown on Figure 3.3. The resulting quadratic functions can be written as

$$\begin{aligned}
\bar{\phi}_1 &= \frac{1}{c}(d_1 - \xi_1)(d_3 - \xi_2)(-1 - \frac{\xi_1}{d_2} - \frac{\xi_2}{d_4}), \\
\bar{\phi}_2 &= \frac{1}{c}(d_2 + \xi_1)(d_3 - \xi_2)(-1 - \frac{\xi_1}{d_1} - \frac{\xi_2}{d_4}), \\
\bar{\phi}_3 &= \frac{1}{c}(d_2 + \xi_1)(d_4 + \xi_2)(-1 - \frac{\xi_1}{d_1} - \frac{\xi_2}{d_3}), \\
\bar{\phi}_4 &= \frac{1}{c}(d_1 - \xi_1)(d_4 + \xi_2)(-1 - \frac{\xi_1}{d_2} - \frac{\xi_2}{d_3}), \\
\bar{\phi}_5 &= \frac{(d_1 - \xi_1)(d_2 - \xi_1)(d_3 - \xi_2)}{d_1 d_2 (d_3 + d_4)}, \\
\bar{\phi}_6 &= \frac{(d_2 - \xi_1)(d_3 + \xi_1)(d_4 - \xi_2)}{d_3 d_4 (d_1 + d_2)}, \\
\bar{\phi}_7 &= \frac{(d_1 - \xi_1)(d_2 - \xi_1)(d_4 + \xi_2)}{d_1 d_2 (d_3 + d_4)}, \\
\bar{\phi}_8 &= \frac{(d_1 - \xi_1)(d_3 - \xi_2)(d_4 - \xi_2)}{d_3 d_4 (d_1 + d_2)}.
\end{aligned} \tag{3.20}$$

Returning to continuous shape functions is straightforward and only needs that the distances d_i are all set as 1.

To simplify the computational code it is defined that those distances are equal for all the physical nodes of the same element and the outer distance, called offset, is used instead of the inner one, d

$$d = d_1 \equiv d_2 \equiv d_3 \equiv d_4, \tag{3.21}$$

$$\mathit{offset} = (1 - d). \tag{3.22}$$

One can interpolate displacement $\mathbf{u}$ and traction $\mathbf{t}$ at element j as a function of its nodal values $\mathbf{u}^j$, $\mathbf{p}^j$, trough

$$\mathbf{u} = \bar{\mathbf{\Phi}}\mathbf{u}^j, \tag{3.23a}$$

$$\mathbf{p} = \bar{\mathbf{\Phi}}\mathbf{p}^j, \tag{3.23b}$$

where the vectors $\mathbf{u}$ and $\mathbf{p}$ are the displacement and traction at an arbitrary boundary Γ point and are written as

$$\mathbf{u} = \begin{Bmatrix} u_1 & u_2 & u_3 \end{Bmatrix}^T, \tag{3.24a}$$

$$\mathbf{p} = \begin{Bmatrix} p_1 & p_2 & p_3 \end{Bmatrix}^T, \tag{3.24b}$$

and the nodal displacement and traction matrices for the element j take the following form

$$\mathbf{u}^j = \begin{bmatrix} u_1^1 & u_1^2 & & u_1^{nnos} \\ u_2^1 & u_2^2 & \cdots & u_2^{nnos} \\ u_3^1 & u_3^2 & & u_3^{nnos} \end{bmatrix}, \tag{3.25}$$

$$\mathbf{p}^j = \begin{bmatrix} p_1^1 & p_1^2 & & p_1^{nnos} \\ p_2^1 & p_2^2 & \cdots & p_2^{nnos} \\ p_3^1 & p_3^2 & & p_3^{nnos} \end{bmatrix}. \tag{3.26}$$

The $\bar{\mathbf{\Phi}}$ and $\mathbf{\Phi}$ matrices store the interpolation functions of the element physical and geometrical partition, for each of the element node. They take the form

$$\bar{\mathbf{\Phi}} = \begin{Bmatrix} \bar{\varphi}^1 & \bar{\varphi}^2 & \cdots & \bar{\varphi}^{nnos} \end{Bmatrix}^T, \tag{3.27a}$$

$$\mathbf{\Phi} = \begin{Bmatrix} \varphi^1 & \varphi^2 & \cdots & \varphi^{nnos} \end{Bmatrix}^T, \tag{3.27b}$$

where $\bar{\boldsymbol{\varphi}}^j$ e $\boldsymbol{\varphi}^j$, are defined in index notation as

$$\bar{\varphi}^j_{ab} = \bar{\phi}_j \delta_{ab}, \tag{3.28a}$$

$$\varphi^j_{ab} = \phi_j \delta_{ab}, \tag{3.28b}$$

where δ_{ab} is the Kronecker delta, and $\bar{\phi}_j$ and ϕ_j are the interpolation function corresponding to the j-th element node.

3.2.2.1 Coordinate transformation

Due to the global-local coordinate system transformation, the Jacobian must be calculated, which in the 3D case, Beer et al., 2008, define as being the real area of an unitary segment at the local coordinate system. Firstly, one must define the element directional vectors v_1 and v_2 as

$$v_{1i} = \frac{\partial \xi_1}{\partial x_i}, \qquad v_{2i} = \frac{\partial \xi_2}{\partial x_i}. \tag{3.29}$$

With those vectors, the normal vector to the element surface can be obtained by cross product

$$v_3 = v_1 \times v_2, \tag{3.30}$$

and finally the Jacobian is defined through the following norm

$$J = \|v_3\| . \tag{3.31}$$

3.2.3 Discretization of the integral equations

As already stated on the start of Section 3.2, the continuous integral formulation must be discretized to allow an algebraic computational solution, process which leads to the method known as BEM. Equation 3.14 is rewritten in matrix notation as

$$c^i \mathbf{u}^i + \oint_\Gamma \mathbf{T}\mathbf{u}^i d\Gamma = \int_\Gamma \mathbf{U}\mathbf{p}^i d\Gamma + \int_\Omega \mathbf{U}\mathbf{b}^i d\Omega, \tag{3.32}$$

where $c^i = \frac{1}{2}\mathbf{I}$, according to Brebbia et al., 2012, and the fundamental solutions are expressed in the following form

$$\mathbf{U} = \begin{bmatrix} U_{11} & U_{12} & U_{13} \\ U_{21} & U_{22} & U_{23} \\ U_{31} & U_{32} & U_{33} \end{bmatrix}, \quad \mathbf{T} = \begin{bmatrix} T_{11} & T_{12} & T_{13} \\ T_{21} & T_{22} & T_{23} \\ T_{31} & T_{32} & T_{33} \end{bmatrix}. \tag{3.33}$$

Applying the element discretization including the interpolation functions, i.e., Equation 3.27 in Equation 3.32, the former boundary integrals become a sum over each element integral which, considering the i-th source node, results in

$$c^i\mathbf{u}^i + \sum_{j=1}^{\text{nel}} \left\{ \int_{\Gamma_j} \mathbf{T}\mathbf{\Phi} d\Gamma \right\} \mathbf{u}^j = \sum_{j=1}^{\text{NE}} \left\{ \int_{\Gamma_j} \mathbf{U}\mathbf{\Phi} d\Gamma \right\} \mathbf{p}^j + \sum_{s=1}^{M} \left\{ \int_{\Omega_s} \mathbf{U}\mathbf{b} d\Omega \right\}, \tag{3.34}$$

where nel denotes the total number of boundary elements, Γ_j is the element's j surface, and $\mathbf{u^j}$ and $\mathbf{p^j}$ are the nodal displacement and traction for the j-th element. Finally, the local coordinates are applied in the integration so $d\Gamma_x = Jd\Gamma_\xi$ and $d\Omega_x = J_\Omega d\Omega_\xi$. Therefore, Equation 3.34 is rewritten as

$$c^i\mathbf{u}^i + \sum_{1}^{\text{NE}} \left\{ \int_{\Gamma_\xi} \mathbf{T}\mathbf{\Phi} J d\Gamma_\xi \right\} \mathbf{u}^j = \sum_{1}^{\text{NE}} \left\{ \int_{\Gamma_\xi} \mathbf{U}\mathbf{\Phi} J d\Gamma_\xi \right\} \mathbf{p}^j + \sum_{s=1}^{\text{M}} \left\{ \int_{\Omega_\xi} \mathbf{U}\mathbf{b} J_\Omega d\Omega_\xi \right\}. \tag{3.35}$$

Instead of referring to each element, it is more interesting to assemble it as function of the collocation nodes $j = \{1, \text{NN}\}$ in the following manner

$$c^i\mathbf{u}^i + \sum_{j=1}^{\text{NN}} \hat{\mathbf{H}}^{ij}\mathbf{u}^j = \sum_{j=1}^{\text{NN}} \mathbf{G}^{ij}\mathbf{p}^j + \sum_{s=1}^{\text{M}} \mathbf{f}^{is}, \tag{3.36}$$

where

$$\hat{\mathbf{H}}^{ij} = \int_{\Gamma_\xi} \mathbf{T}\bar{\phi}_{n(j)}\, J\, d\Gamma_\xi \tag{3.37a}$$

$$\mathbf{G}^{ij} = \int_{\Gamma_\xi} \mathbf{U}\bar{\phi}_{n(j)}\, J\, d\Gamma_\xi \tag{3.37b}$$

$$\mathbf{f}^{is} = \int_{\Omega_\xi} \mathbf{U}\mathbf{b} J_\Omega d\Omega_\xi. \tag{3.37c}$$

The discontinuous function $\bar{\phi}_{n(j)}$ Index $n(j)$ denotes for which local node n of the field

element the global index j corresponds to. So, calling

$$\mathbf{H}^{ij} = \begin{cases} \hat{\mathbf{H}}^{ij}, & \text{if } i \neq j, \\ \hat{\mathbf{H}}^{ij} + \mathbf{c}^{\mathbf{i}}, & \text{if } i = j, \end{cases} \tag{3.38}$$

simplifies Equation 3.36 in:

$$\sum_{j=1}^{\mathrm{NN}} \mathbf{H}^{ij}\mathbf{u}^{j} = \sum_{j=1}^{\mathrm{NN}} \mathbf{G}^{ij}\mathbf{p}^{j} + \sum_{s=1}^{M} \mathbf{f}^{is}. \tag{3.39}$$

Notice that, in this notation, matrices $\mathbf{H}$ and $\mathbf{G}$ for a source node i, and field node j, has the same form as the fundamental solutions Section 3.2.3, $s_{\mathbf{H}} = s_{\mathbf{G}} = [3, 3]$, while the body force vector $\mathbf{f}^{i}$ for a source node i has size $s_{\mathbf{f}} = [3]$.

Assembling the sub matrices for all the source nodes i, forms the BEM system of linear equations (SLE) for boundary

$$\mathbf{Hu} = \mathbf{Gp} + \mathbf{f}. \tag{3.40}$$

3.2.4 System Solution

In the general case, the SLE Equation 3.40 contains mixed unknowns and boundary conditions in both vectors u and p, so one has to rearrange it to form a standard SLE. Multiplying the boundary conditions, $\bar{t}_j$ and $\bar{u}_j$, by the corresponding columns of the coefficient matrices, $\mathbf{G}$ and $\mathbf{H}$ and adding the resultant domain forces vector $\mathbf{f}$, one forms the following RHS vector $\mathbf{b}$, whose components can be written in index notation as

$$b_i = G_{il}\bar{p}_l - H_{ik}\bar{u}_k + \mathrm{f}_i. \tag{3.41}$$

where indices l and k corresponds to nodal directions where traction and displacement is imposed, respectively, and $l \cup k = \{1, \mathrm{NN}\}, l \cap u = \emptyset$.

In the same fashion, one can compose the solution vector $\mathbf{x}$ with the remaining unknowns of the problem, assembling the coefficient matrix $\mathbf{A}$ with the corresponding columns of $\mathbf{G}$ and $\mathbf{H}$ as

$$\mathrm{A}_{ij}\mathrm{x}_j \equiv \mathrm{H}_{il}\mathrm{u}_l - \mathrm{G}_{ik}\mathrm{p}_k, \tag{3.42}$$

where u_l and p_l denotes the unknown boundary displacement and traction, respectively. The indices l and k have direct correspondence to the ones in Equation 3.41, which finally

forms the SLE

$$\mathbf{Ax} = \mathbf{b}. \tag{3.43}$$

3.2.5 Numerical Integration of G and H matrices

In the assembly of **G** and **H** matrices, the non-singular integrals (not written in the Cauchy principal value (CPV) sense) are evaluated using standard Gauss quadrature. Equations 3.37a and 3.37b simplifies to

$$\mathbf{G}^{ij} = \sum_{k_1=1}^{K_1} \sum_{k_2=1}^{K_2} \mathbf{U}(p^i, q^j_{\mathbf{k}}(\boldsymbol{\xi}))\, \phi_{n(j)}(\boldsymbol{\xi})\, J(q^j_{\mathbf{k}}(\boldsymbol{\xi}))\, w_{k_1} w_{k_2} \tag{3.44a}$$

$$\mathbf{H}^{ij} = \sum_{k_1=1}^{K_1} \sum_{k_2=1}^{K_2} \mathbf{T}(p^i, q^j_{\mathbf{k}}(\boldsymbol{\xi}))\, \phi_{n(j)}(\boldsymbol{\xi})\, J(q^j_{\mathbf{k}}(\boldsymbol{\xi}))\, w_{k_1} w_{k_2} \tag{3.44b}$$

where $\mathbf{k} = (k_1, k_2)$, K_1 and K_2 are the number of abscissas of the quadrature for each direction of the element coordinate system $\boldsymbol{\xi} = (\xi_1, \xi_2)$. The local coordinates $\boldsymbol{\xi}$ are defined by the Gauss quadrature for each abscissae pair k_1, k_2.

p^i is the source point i, and $q_{\mathbf{k}}(\boldsymbol{\xi})$ is the $\mathbf{k}$-th integration point along the corresponding element (field point), and w_{k_1} and w_{k_2} are vectors containing the quadrature weights corresponding to each direction.

The discontinuous interpolation function $\phi_{n(j)}$ corresponds to the n-th local element node, the j-th collocation node, i.e., one of the linear functions Equation 3.20, or the quadratic Equation 3.19.

To correctly approximate the integrals, one must select an adequate number of abscissas: The fundamental solutions may lead to several quasi-singularities arising from the element closeness, due to the asymptotic behavior of $\mathrm{O}(1/\mathrm{r})$ and $\mathrm{O}(1/\mathrm{r}^2)$, element distortion, among others reported in the literature. According to Eberwien et al., 2005, the non-singular integration can be performed with controlled accuracy and more efficiently by following the rules listed in Table 3.2.

To maintain the routines simplicity we compute the **G** submatrices using the same integration rules as needed for the **H**, i.e., using the second column rules of Table 3.2. Because they are calculated for the same coordinates, with this approach, we can reuse the Barnett-Lothe tensor in the first-order derivative as observed in Section 2.5.2, Equation 2.171.

Due to the incorporation of the anisotropic fundamental solutions, it is not only

Table 3.2 – Maximum normalized distance r/L for a 0.1% error bound integrating $f(r) = 1/r$ and $f(r) = 1/r^2$ over a 1-dimensional element due to Eberwien et al., 2005.

	$f(r)$	
	r^{-1}	r^{-2}
n	r/L	
3	1.40257	4.10299
4	0.79263	1.67767
6	0.39947	1.01772
8	0.33302	0.54183
10	0.25652	0.34371
12	0.19612	0.24490
14	0.17697	0.21964
16	0.16789	0.19524

difficult but also not in the scope of this work to develop asymptotic expansions allowing their direct integration, as it was performed previously by the authors in Ubessi, 2014. The authors expect to develop these direct integration procedures as needed in the continuation of this work. Thereby, the remaining CPV integrals which arise when source and field nodes coincide are evaluated trough the concept of rigid-body displacement, as in [Brebbia et al., 2012]. Thus, one can obtain the diagonal terms of the H matrix indirectly as

$$\mathbf{H}^{ii} = -\sum_{j=1\,(j\neq i)}^{\mathrm{NN}} \mathbf{H}^{ij} - \mathbb{I}_{\infty}, \tag{3.45}$$

where $\mathbb{I}_{\infty}$ corresponds to the negative azimuthal integral [Beer et al., 2008], which depends on the kind of boundary under consideration, i.e.,

$$\mathbb{I}_{\infty} = \begin{cases} 0 \quad \text{for internal/finite problems (bounded domain),} \\ -\frac{1}{2}\mathbf{I} \quad \text{for semi-infinite problems (truncated half-space),} \\ -\mathbf{I} \quad \text{for infinite problems (unbounded domain).} \end{cases} \tag{3.46}$$

It is worth mentioning that these values were presented by Beer et al., 2008, considering the isotropic fundamental solution for tractions, Equation 2.25. One may assume these values are still valid for anisotropic elasticity. In any case, it is recommended to compute the azimuthal integral for the corresponding anisotropic material, as it is needed only once,

$$\mathbb{I}_{\infty} = \int_{S_R} \mathbf{T}(P,Q)\, dS, \tag{3.47}$$

where S_R is the surface of a semi-infinite or infinite sphere. Beer et al., 2008 has shown this integral is independent of the radius, thus, the sphere can be considered to be unitary.

The diagonal terms of the matrix $\mathbf{G}$ can be computed by Gaussian quadrature, with the aid of the third-degree polynomial transformation from Telles and Oliveira, 1994. For the cases when i and j belong to the same element but $i \neq j$, the integrals of matrices $\mathbf{H}^{ij}$ and $\mathbf{G}^{ij}$ are not singular, as the fundamental solution singularity $T_{jk} = O(r^{-2})$ cancels out with the interpolation function $\bar{\phi} \equiv 0$ at the point j [Beer et al., 2008]. Therefore, they are also computed using the Telles and Oliveira, 1994 transformation, as they are weakly singular at most.

4 SHAPE SENSITIVITY

In this chapter we present the theoretical background for the complex step (CS) method and its applications in shape sensitivity. The CS method is introduced from the finite differentiation (FD) standpoint. We also present a convergence analysis for a simple trigonometric function which demonstrates the FD schemes and the CS method behavior for a wide range of increment sizes.

The boundary integral equations are rewritten introducing the CS to illustrate the relation between the standard boundary element method (BEM) and the boundary element method with complex step (CS-BEM) formulation. As an application example to validate the CS-BEM approach, we evaluate the error convergence of displacement and its shape derivative for a classical case of a cantilever beam under bending load.

4.1 Theoretical foundation and finite differentiation

Let us define $f'(x)$ as the derivative of the function $f(x)$ through the concept of differentiation, introduced by Isaac Newton (1642–1727) and Gottfried Leibniz (1646–1716),

$$f'(x) = \lim_{\Delta x \to 0} \frac{f(x + \Delta x) - f(x)}{\Delta x}. \tag{4.1}$$

Similarly to Equation 4.1, it is possible to get $f'(x)$ from the Taylor series of $f(x)$,

$$f(x) = f(a) + \frac{f'(x)}{1!}(x - a) + \frac{f''(x)}{2!}(x - a)^2 + \dots , \tag{4.2}$$

by setting $a = x + \Delta x$ and reordering Equation 4.2, it resembles Equation 4.1,

$$f'(x) = \frac{f(x + \Delta x) - f(x)}{\Delta x} + \mathcal{O}(\Delta x). \tag{4.3}$$

Equation 4.3 is the well-known Finite Differentiation (FD) expression for the first-order derivative. The approximation error residue $\mathcal{O}(\Delta x)$ corresponds to neglected terms which are in the order of Δx. Notice that this is the *forward finite differentiation*. The *backward finite differentiation* can also be written analogously by choosing $a = x - \Delta x$. More significant in many numerical applications is the *central finite differetiation*, which is obtained performing the increment in both directions, i.e.,

$$f'(x) = \frac{f(x + \Delta x) - f(x - \Delta x)}{2\Delta x} + \mathcal{O}(\Delta x^2). \tag{4.4}$$

Notice that this scheme presents a lower error bound, within the order of Δx^2.

From the comparison of Equations 4.1 and 4.3 one observes that the limit on $\Delta x \to 0$ imposes the accuracy on the finite differentiation technique, i.e., the approximation accuracy depends on how close to zero one can set Δx. The remainder in Equations 4.3 and 4.4 is obtained through the *truncation* of the Taylor series, and it is called the *truncation error*. In the FD scheme, this error is always present, and one can only attenuate it to some extent. Truncation determines the approximation accuracy of a FD scheme. The single-step schemes, i.e., the forward and backward FD schemes, are first-order accurate, while the central FD scheme Equation 4.4 is of second-order accuracy. According to Abreu et al., 2013, one can obtain fourth-order accuracy by performing one more layer of increments, like in the central approach.

An error of computational nature appears in the quest for the lowest possible increment: *Cancellation error*. This error arises from the subtraction operation of nearby values, [see Goldberg, 1991], and is inherent to floating-point arithmetic. As it depends on the relation of the numerator in Equations 4.1 and 4.3, and on the number of significant digits available at the floating-point implementation, it is difficult to predict, and, in many cases, requires an empiric approach. The general starting point found in many bibliographies is $\Delta x \approx \sqrt{\varepsilon}$, where $\varepsilon = (\beta/2)\beta^{-p}$ is the *machine epsilon*, the lowest possible difference between two consecutive floating point real numbers. The IEEE-754 standard requires for binary representatoin $\beta = 2$ and $p = 24$ for *single precision* results in $\varepsilon^{\mathrm{S}} = 2^{-24} = 5.960464478 \times 10^{-8}$ and $\Delta x^{\mathrm{S}} \approx \sqrt{2^{-24}} = 2{,}4 \times 10^{-4}$; For *double precision*, $p = 53$, results in $\varepsilon^{\mathrm{D}} = 2^{-53} = 1.110223025 \times 10^{-16}$ and $\Delta x^{\mathrm{S}} \approx \sqrt{2^{-53}} = 1 \times 10^{-8}$.

The combination of these two error types narrows the usable range of Δx which the resulting error is low. Moreover, other sources of imprecision which can significantly reduce this range may arise in general algorithms, such as error accumulation, limiting the precision of the FD scheme. A common alternative for this problem usually is to use central FD, due to its second-order accuracy. On the other hand, it needs two function incrementations (twice as the forward or backward approaches).

4.2 The complex step method

Lyness and Moler, 1967, used complex variables to compute derivatives of functions through the Cauchy-Riemann theorem. Based on these ideas, Squire and Trapp, 1998,

proposed the complex-step (CS) method and it is well-known for its simplicity to obtain numerically exact derivatives for any real-valued function. Let us define $\mathfrak{i} \equiv \sqrt{-1} | \mathfrak{i} \in \mathbb{C}$, and Δx to be a real number. One can formulate the CS method exactly as done previously in Equation 4.2, i.e., using a Taylor series expansion of $f(x + \mathfrak{i}\Delta x)$,

$$\begin{aligned} f(x + \mathfrak{i}\Delta x) &= f(x) + \mathfrak{i}\Delta x\, f'(x) + \frac{(\mathfrak{i}\Delta x)^2}{2!} f''(x) + \frac{(\mathfrak{i}\Delta x)^2}{3!} f'''(x) + \dots \\ &= \sum_{n=0}^{\infty} \frac{(\mathfrak{i}\Delta x)^n}{n!} f^n(x). \end{aligned} \tag{4.5}$$

Reordering Equation 4.5 to isolate $\mathfrak{i}f'(x)$ to the left-hand side and taking the imaginary part in both sides, results in

$$f'(x) = \frac{\mathrm{Im}\left[f(x + \mathfrak{i}\Delta x)\right]}{\Delta x} + \mathcal{O}(\Delta x^2), \tag{4.6}$$

which is the expression for the derivative found by Squire and Trapp, 1998. Notice that, when is taken the imaginary part in both sides of Equation 4.2, the first term, $f(x)$ vanishes as $\mathrm{Im}[f(x)] \equiv 0$. Thus, this is a requirement for the method application: $\mathrm{Im}[f(x)] \equiv 0$, in other words, $f(x) : \mathbb{R} \to \mathbb{R}$.

Equation 4.6 means only one function evaluation is needed. As the step size Δx can be lower than ε^D, the term $O(h^2)$ tends to vanish, which results in a numerically exact derivative.

Figure 4.1 shows the convergence of the aforementioned methods for the function $\sin(x)/x$ for $x = \pi/2$, a function appearing in the Fourier kernels, Equations 2.164 and 2.175. Notice that although the usable range is indeed wider for the central FD, it is only due to its second-order accuracy. For smaller step sizes, it presents the same error as the forward FD, which means that a wrongly chosen increment size can lead to the same accuracy as the cheaper forward FD scheme. Notice also that for $\Delta x \lesssim \sqrt{\epsilon^D}$ the CS scheme becomes numerically exact, as expected, and stable down to $\Delta x \approx 1 \times 10^{-308}$, the minimum representable in *double precision* floating-point.

4.3 Boundary integral equations considering the complex step method

Let us present the boundary integral equations (BIE) considering the effect of an imaginary increment to demonstrate the simplicity and advantages of this approach. For that purpose, let us perform the perturbation Δx at the imaginary part of some design

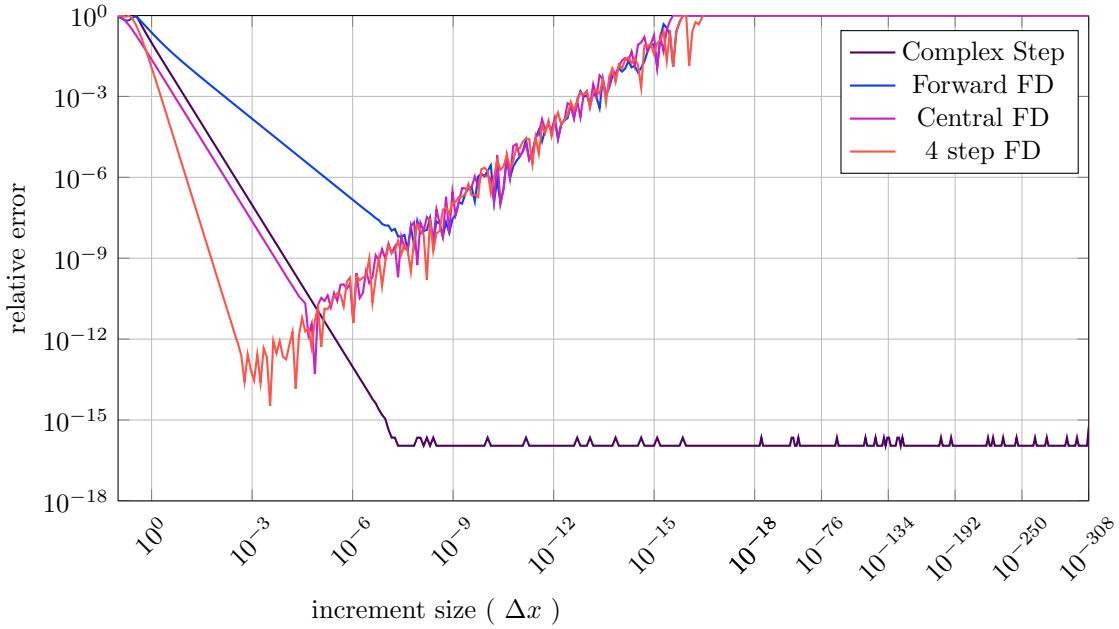

Figure 4.1 – Convergence of $f'(x)$ for the function $f(x) = \sin(x)/x$ at $x = \pi/2$ for the methods in question.

variable γ, which defines the boundary Γ coordinates. One can write the CS version of the displacement BIE as

$$\mathbf{C}\mathbf{u} + \fint_{\Gamma} \mathbf{T}(\mathbf{x} + \mathrm{i}\Delta\mathbf{x})\,\mathbf{u}\,\mathrm{d}\Gamma = \int_{\Gamma} \mathbf{U}(\mathbf{x} + \mathrm{i}\Delta\mathbf{x})\,\mathbf{t}\,\mathrm{d}\Gamma + \int_{\Omega} \mathbf{U}(\mathbf{x} + \mathrm{i}\Delta\mathbf{x})\,\mathbf{b}\,\mathrm{d}\Omega, \tag{4.7}$$

where $f(\mathbf{x} + \mathrm{i}\Delta\mathbf{x})$ implies source and field points to be complex. Notice that there is no difference between Equation 4.7 and Equation 3.14, its real-valued counterpart. Matrices $\mathbf{T}$ and $\mathbf{U}$ are the traction and displacement fundamental solutions, addressed in Chapter 2. $\fint(\cdot)\mathrm{d}\Gamma$ denotes the Cauchy Principal Value of integral $\int(\cdot)\mathrm{d}\Gamma$.

After the element discretization of Γ, Equation 4.7 for a source point i is divided into the following sums for each element,

$$\mathbf{C}^i\mathbf{u}^i + \sum_{e=1}^{N} \tilde{\mathbf{H}}^{ie}\mathbf{u}^e = \sum_{e=1}^{N} \mathbf{G}^{ie}\mathbf{p}^e, \tag{4.8}$$

where the matrices $\tilde{\mathbf{H}}_i^e$ and $\mathbf{G}_i^e$ are are obtained for each element e through

$$\tilde{\mathbf{H}}^{ie} = \fint_{\Gamma^e} \mathbf{T}(\mathbf{x} + \mathrm{i}\Delta\mathbf{x})\,\bar{\phi}\,d\Gamma^e\,, \quad \mathbf{G}^{ie} = \int_{\Gamma^e} \mathbf{U}(\mathbf{x} + \mathrm{i}\Delta\mathbf{x})\,\bar{\phi}\,d\Gamma^e\,. \tag{4.9}$$

Equation 4.8 and Equation 3.36 are also equivalent. Assembly of Equation 4.8 through

the collocation process over all the nodes result in

$$\mathbf{H}(\mathbf{x}+\mathrm{i}\Delta\mathbf{x})\mathbf{u} = \mathbf{G}(\mathbf{x}+\mathrm{i}\Delta\mathbf{x})\mathbf{p}. \tag{4.10}$$

Notice that vectors $\mathbf{u}$ and $\mathbf{p}$ may contain unknowns or boundary conditions. The system of linear equations $\mathbf{Az} = \mathbf{b}$ is assembled by switching the columns of $\mathbf{H}$ and $\mathbf{G}$, as in Equation 3.43. Multiplying the boundary conditions as is shown in the right-hand side (RHS) of Equation 3.42 forms the RHS vector $\mathbf{b}$. Both $\mathbf{A}$ and $\mathbf{b}$ are complex, hence, so is the system of linear equations (SLE) solution vector $\mathbf{z}$.

The real part of the solution vector $\mathbf{z}$ corresponds to the usual unknowns, displacement and traction, at the boundary element collocation nodes,

$$\mathbf{u} = \mathrm{Re}[\mathbf{z}^{\mathbf{u}}], \quad \text{and,} \quad \mathbf{p} = \mathrm{Re}[\mathbf{z}^{\mathbf{p}}], \tag{4.11}$$

The displacement and traction sensitivities with respect to the design variable γ are obtained by

$$\frac{\partial \mathbf{u}}{\partial \gamma} = \frac{\mathrm{Im}\left[\mathbf{z}^{\mathbf{u}}\right]}{\Delta\gamma}, \quad \frac{\partial \mathbf{p}}{\partial \gamma} = \frac{\mathrm{Im}\left[\mathbf{z}^{\mathbf{p}}\right]}{\Delta\gamma}. \tag{4.12}$$

In order to reassure the CS method simplicity, it is worth mentioning the above passages apply to both CS-BEM and the conventional BEM, the only differences being the complex variables, due to the complex step performed in the design variable γ. Employing this framework, one obtains both the solution and its sensitivity to γ in a single pass of the BEM routine.

4.4 Shape sensitivity of 3D anisotropic structure

Let us consider a cantilever beam with a tip-load to demonstrate the CS method in a shape sensitivity analysis case. In Figure 4.2 it is shown the problem configuration, whereas the material properties considered for the beam are listed in Table 4.1. The initial mesh used in this analysis has 64 quadratic elements, as shown in Figure 4.3. All the subsequent refinements were performed through the reduction of the element size, while the element aspect ratio is kept constant. This approach leads to the total number of elements being a quadratic function of $\mathrm{nelem}_n = \mathrm{nelem}_0\, n^2$, where n is the number of elements/m^2. The degrees of freedom (DOF) number is equal to $\mathrm{DOF} = 3 \cdot \mathrm{nnos} \cdot \mathrm{nelem}$, as the discontinuous elements DOF are all independent. The initial mesh depicted in

Figure 4.2 have $\text{nelem}_0 = 6{,}4 \times 10^1$ elements whereas the most refined one had $\text{nelem}_5 = 1{,}600 \times 10^3$, resulting in a range from 1.536 to 38.400 DOF, using quadratic elements.

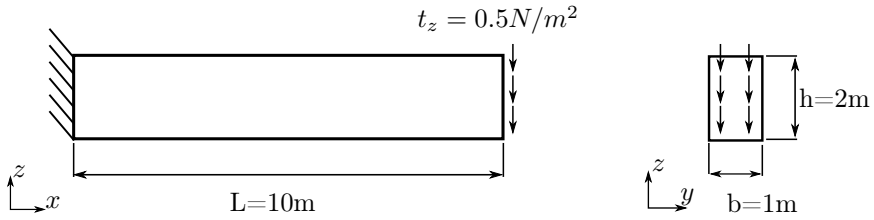

Figure 4.2 – Cantilever beam problem.

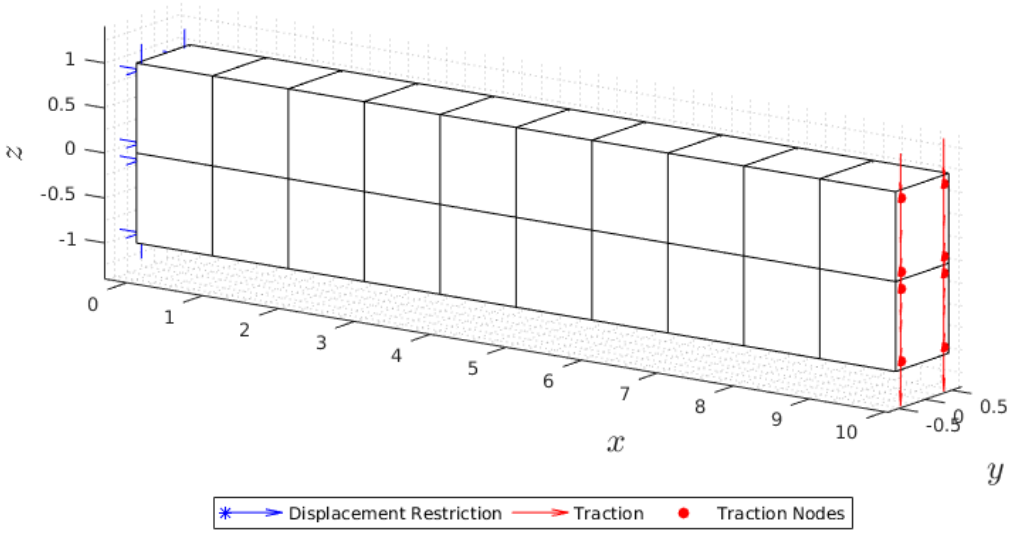

Figure 4.3 – Initial coarser mesh for the beam bending case including boundary conditions.

The Euler-Bernoulli theory for displacement was selected to evaluate the convergence of the methodology. The resulting solution for the force $P = t_z\, h\, b$, which is also dependent on parameter h, is

$$y(x) = -\frac{2(t_z hb)x^2(3L - x)}{(Ebh^3)}. \tag{4.13}$$

The sensitivity to the parameter h is obtained differentiating Equation 4.13 with respect to h,

$$\frac{\partial y(x)}{\partial h} = \frac{4t_z x^2(3L - x)}{Ebh^3}. \tag{4.14}$$

The complex increment size used in those analyses was $\Delta h = 1 \times 10^{-66}$. For this analysis, the routine used includes the increment at the imaginary part of the mesh nodes in z dimension, proportionally to its coordinates in this direction. The resulting position for a node n is $\hat{\mathbf{x}}_n = [x_n \quad y_n \quad z_n]^T + \mathbf{i}[0 \quad 0 \quad \Delta h/z_n]^T$. Moreover, the CS is carried out to the collocation nodes, as the integration procedure it generates them from the mesh nodes.

Table 4.1 – Elastic constitutive properties considered in the examples.

Material	Elastic stiffness properties			
Steel Alloy	Young Modulus	E_{St}	$2{,}00 \times 10^2$	GPa
	Poisson Ratio	ν_{St}	0.3	
Nickel Crystal	(FCC [100])	C_{11}	252	GPa
		C_{12}	152	GPa
		C_{44}	123	GPa

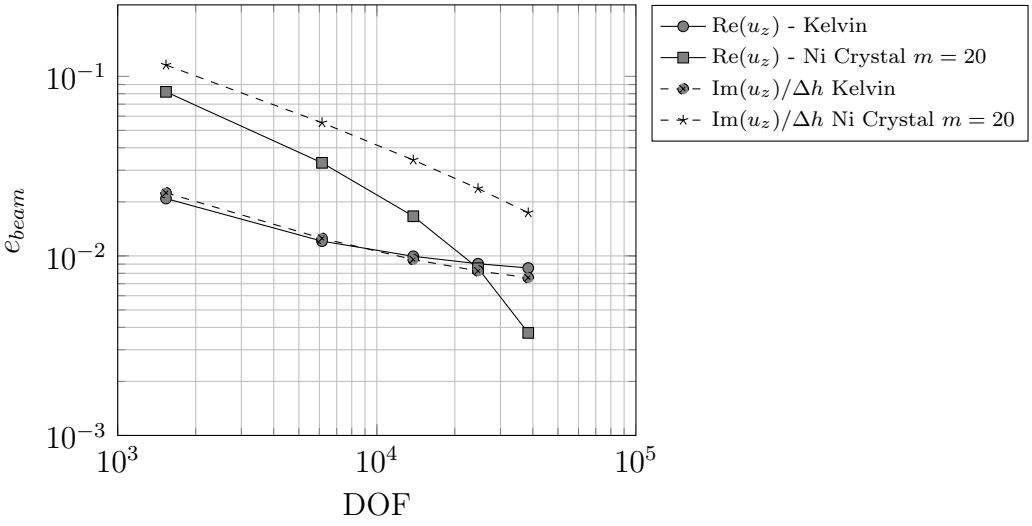

Figure 4.4 – Relative error for the beam tip displacement $\mathrm{Re}(u_z)$ relative to the analytic solution, Equation 4.13, and for the shape derivative $\mathrm{Im}(u_z)/\Delta h$, with respect to the beam height, $\partial u_z/\partial h$, Equation 4.14.

5 ELASTIC CONTACT AND NUMERICAL TREATMENT

This chapter presents the formulation to solve frictional contact with BEM. It starts with the continuum description of the unilateral Coulomb contact law along with its kinematics. We present the augmented Lagrangian of the problem, followed by the contact variables discretization, non-linear system assembly, and solution method.

The main advantage of the penalty method in finite element method (FEM) is that they treat the contact problem using only the displacements, i.e., the penalty factor acts as a zero initial length spring linking the contact nodes. The contact stress is not part of the equations in this method, being proportional to the gap. According to [Bussetta et al., 2012], the problem is that it introduces a residual penetration (and tangential displacement), which cannot be avoided by increasing the penalization as this causes oscillation and prevents convergence. On the other hand, reducing the penalization can cause the solution to have no physical meaning.

Generally, the augmented Lagrangian is avoided in FEM due to the Lagrange multipliers, which are additional variables to the problem. In the boundary element method (BEM), this fact does not apply: As multipliers denote the contact tractions, and as surface tractions are already primal variables, this method closely relates to the BEM. Differently to the penalty methods, due to the augmentation, it exactly fulfills the non-penetration and friction constraints, with finite penalty values, which also results in better conditioning [Simo and Laursen, 1992; Mijar and Arora, 2004]. On the other hand, this duality of BEM variables allows one to implement incremental-iterative methods, which solve the contact problem using incremental-loading and iteratively testing the contact pairs. These methods can be related to the Uzawa's scheme, as a class of predictor-corrector algorithms.

The selection of the augmented Lagrangian is due to the following properties: (i) Finite penalization, fulfilling the contact restrictions accurately; (ii) Avoids trial and error process of the incremental-iterative approach; (iii) The solution can be done by both Newton method or the Uzawa scheme, as shown in Rodríguez-Tembleque and Abascal, 2013. The formulation described in this chapter is due to Rodríguez-Tembleque et al., 2011, and references therein.

As demonstrated in Chapter 4, the complex step (CS) method does not require

any special consideration apart from the ones relative to complex variable specific implementation. The addition of a relatively small imaginary increment is straightforward and does not interfere in the contact problem solution. For that reason, the variables within this chapter are considered to be real-valued. Moreover, it is worth mentioning that finite differentiation is likely to affect the contact state due to the use of larger increments (to avoid numerical cancellation), which can yield incorrect shape sensitivity values.

5.1 The elastic contact problem

Consider the following boundary value problem comprising two elastic bodies, with domains Ω_1 and Ω_2, and boundaries $\Gamma = \Gamma_{\bar{\mathbf{p}}} \cup \Gamma_{\bar{\mathbf{u}}} \cup \Gamma_c$ and $\Gamma_{\bar{\mathbf{p}}} \cap \Gamma_{\bar{\mathbf{u}}} \cap \Gamma_c = 0$ (disjoint set); where $\Gamma_{\bar{\mathbf{p}}}$, $\Gamma_{\bar{\mathbf{u}}}$, Γ_c correspond to the boundary portion with prescribed tractions, displacaments, and the *possible contact region*, as illustrated in Figure 5.1. Prescribed tractions, $\bar{\mathbf{p}}$, or displacements, $\bar{\mathbf{u}}$, are specified along the boundaries, and the complementary variables, $\mathbf{u}$ and $\mathbf{p}$, are the unknowns.

The contact boundary Γ_c have conditions which depend on the contact state, mainly defined by the gap $\mathbf{g}$ between the two regions. Let us consider the case of unilateral non-adhesive contact[1], where the bodies can separate, i.e., if the gap is positive, the surfaces are free to move, and the tractions are null. On the other hand, if this distance is zero, the compatibility ensures the non-penetration conditions: normal tractions can only be positive; Tangential traction is dependent on a Coulomb friction law.

5.2 Contact variables and discretization

The BEM formulation considered herein assumes small strains and displacements. Moreover, a node-to-node contact scheme is adopted. The nodes are positioned in a conforming scheme, as done in Rodríguez-Tembleque et al., 2011, forming pairs, i.e., placing the secondary nodes (Ω^2) as close as possible to the primary nodes (Ω^1), or at least matching the displacement path performed by the contact node pair. Therefore, consider the contact variables relate the reference point P^1 and referenced point P^2, at each contact boundary. These points form a pair, $I \equiv \{P^1, P^2\}$, as depicted in Figure 5.1.

[1] According to [Talon and Curnier, 2003], the inclusion of adhesive effects such as described by Johnson et al., 1971, using the augmented Lagrangian approach is straightforward.

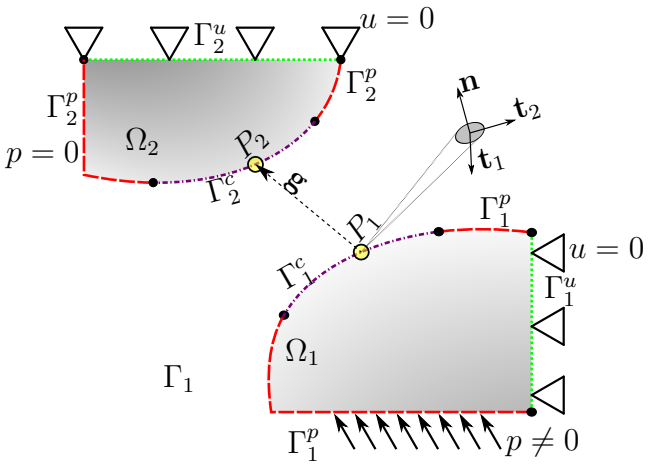

Figure 5.1 – Solids under consideration and its boundary conditions.

The gap $\mathbf{g}$ for any pair of points in this problem is obtained through the following relation

$$\mathbf{g} = \mathbf{B}^T(\mathbf{x}_2 - \mathbf{x}_1) + \mathbf{B}^T(\mathbf{u}_2 - \mathbf{u}_1), \tag{5.1}$$

where $\mathbf{x}_1$ and $\mathbf{x}_2$ are coordinates on boundaries 1 and 2 respectively, while $\mathbf{u}_1$ and $\mathbf{u}_2$ are the displacements of these points, both referring to a global coordinate system. $\mathbf{B}$ is the rotation matrix responsible for transferring the variables to the local coordinate system with origin at $\mathbf{x}_1$, i.e.,

$$\mathbf{B} = \begin{bmatrix} \mathbf{t}_1 & \mathbf{t}_2 & \mathbf{n} \end{bmatrix}, \tag{5.2}$$

where $\mathbf{n}$ is the outward normal vector, while $\mathbf{t}_1$ and $\mathbf{t}_2$ are the tangential vectors, at $\mathbf{x}_1$. Therefore, the gap can be decomposed in its tangential and normal components

$$\mathbf{g} = \begin{bmatrix} \mathrm{g}_{t_1} & \mathrm{g}_{t_2} & \mathrm{g}_n \end{bmatrix}^T. \tag{5.3}$$

In the same manner, one can write the contact traction in terms of their tangential and normal components,

$$\mathbf{t} = \begin{bmatrix} \mathbf{t}_t^T & \mathrm{t}_n \end{bmatrix}^T. \tag{5.4}$$

where the tangential contact traction is $\mathbf{t}_t = [\mathrm{t}_{t_1}\ \mathrm{t}_{t_2}]^T$.

5.3 Kinematics at the contact region

The kinematic laws establish the possible behavior at the region between two bodies which *may* come into contact, which is called the *possible contact region*. Let us further address the laws that describe each condition.

5.3.1 Unilateral contact law

The unilateral contact law avoids the interpenetration between bodies [Rodríguez-Tembleque et al., 2011]. It states the following rules:

- No interpenetration of the regions of domain Ω^α and boundary $\Gamma^\alpha\,(\alpha = 1,2)$: $\Omega^1 \cap \Omega^2 = \emptyset$. The surface of each body may be divided in contact (Γ_c^α), imposed tractions ($\Gamma_{\bar{t}}^\alpha$) and imposed displacements ($\Gamma_{\bar{u}}^\alpha$) regions, so that

$$\Gamma^\alpha = \Gamma_c^\alpha \cup \Gamma_{\bar{t}}^\alpha \cup \Gamma_{\bar{u}}^\alpha \quad and \quad \Gamma_c^\alpha \cap \Gamma_{\bar{t}}^\alpha \cap \Gamma_{\bar{u}}^\alpha = \emptyset. \tag{5.5}$$

- The solids can be separated, i.e.: there is no cohesion on the contact, then for each pair $I \equiv \{P^1, P^2\} \in \Gamma_c : \mathrm{g_n} \geq 0$ and $\mathrm{t_n} \leq 0$, complying with Newton's third law.

- Variables $\mathrm{g_n}$ and $\mathrm{t_n}$ are complementary, i.e.: $\mathrm{g_n t_n} = 0$.

5.3.2 Friction law

The friction law is defined according to a Coulomb model for tangential tractions $\mathbf{p}_t$ and tangential slip velocity, $\dot{\mathbf{g}}_t$. For each pair $I \equiv \{P^1, P^2\} \in \Gamma_c$, the friction law is expressed as

- The tangential contact tractions respect the coulomb friction law:

$$\|\mathbf{t}_t\| \leq \mu\,|t_n|\,, \tag{5.6}$$

  where $|t_n|$ is the absolute normal traction and μ is the friction coefficient.

- The tangential slip velocity and traction follows the maximum energy dissipation principle, $\dot{\mathbf{g}}_t = -\lambda \mathbf{t}_t$, where $\lambda \geq 0$, i.e., a real positive number.

- The remainder of Equation 5.6 ($\|\mathbf{t}_t\| - \mu\,|t_n|$) and the tangential slip velocity module ($\dot{\mathbf{g}}_t$) are complementary,

$$\dot{\mathbf{g}}_t(\|\mathbf{t}_t\| - \mu\,|t_n|) = 0. \tag{5.7}$$

There is no tangential slip velocity if the tangential traction norm does not exceed the normal traction magnitude. On the other hand, if the tangential slip velocity is positive, the tangential traction norm must equals the coefficient of friction times the magnitude of the normal traction.

5.3.3 Summarized unilateral and frictional contact conditions

Grouping the unilateral and frictional laws for any point at the boundary, results in the contact laws for the gap and traction,

$$\begin{cases} \mathrm{t}_n = 0; \quad \mathrm{g}_n \geq 0; \quad \mathbf{t}_t = 0; & \text{Separated,} \\ \mathrm{t}_n \leq 0; \quad \mathrm{g}_n = 0; \quad \|\mathbf{t}_t\| = \mu\,|t_n|\,; \quad \dot{\mathbf{g}}_t \cdot \dot{\mathbf{t}}_t = -\,\|\dot{\mathbf{g}}_t\|\,\left\|\dot{\mathbf{t}}_t\right\|\,; & \text{Contact - Slip,} \\ \mathrm{t}_n \leq 0; \quad \mathrm{g}_n = 0; \quad \dot{\mathbf{g}}_t = 0; & \text{Contact - Stick.} \end{cases} \tag{5.8}$$

The time rate appearing in Equation 5.8 is approximated as in Rodríguez-Tembleque and Abascal, 2010. A finite differentiation (FD) scheme approximates the $\dot{\mathbf{g}}_t$ at time τ_k as follows

$$\dot{\mathbf{g}}_t \simeq \frac{\Delta \mathbf{g}_t}{\Delta \tau} \tag{5.9}$$

with

$$\Delta \mathbf{g}_t = \mathbf{g}_t(\tau_k) - \mathbf{g}_t(\tau_{k-1}) \tag{5.10}$$

and

$$\Delta \tau = \tau_k - \tau_{k-1}. \tag{5.11}$$

5.4 Augmented Lagrangian of the contact problem

Although there are numerous approaches in the literature to solve contact problems with BEM, the method to impose the contact restrictions in this work is the same as in Rodríguez-Tembleque et al., 2011, where it is applied an augmented Lagrangian method, more specifically, is the penalty-duality, or mixed-method due to Alart and Curnier, 1991.

More recently, Mijar and Arora, 2004, proposed a new augmented Lagrangian formulation for contact problems based on a more general variation of the method from

the optimization literature. The main difference, or advantage, is that the augmentation penalty is modified along the solution process, enabling the user not to depend on the empirical choice of parameters. The problem inherent to this method is that it doubles the cost of each Newton iteration, as it finds the contact problem solution and the penalty parameter optimization.

In Equation 5.8, it can be seen that the contact restrictions are a group of equalities and inequalities which results in a constrained optimization problem. Different to the penalty method, the augmented Lagrangian transforms the constrained optimization problem in a sequence of unconstrained ones. This results in the exact satisfaction of the contact restrictions with finite penalization, which results in better conditioning for the nonlinear system of equations (NSE) [Mijar and Arora, 2004].

The augmented Lagrangian formulation from Alart and Curnier, 1991, enforces the frictional contact law using projection operators, i.e., functions which project the contact variables into the admissible solution region [Rodríguez-Tembleque et al., 2011]. As the contact constraints being applied act in different directions, one in the normal other in the tangential, these are firstly separately formulated, and next they are combined to form the complete problem constraint.

5.4.1 Normal projection function

The non-penetration condition law states that the *normal gap* g_n must be no less than zero and that the *normal traction* t_n is never positive (no cohesion or adhesion), and so this two variables are complementary, i.e., one of the two must be always null, which summarizes as

$$\mathrm{t}_n \leq 0\,,\ \mathrm{g}_n \geq 0,\ \ \mathrm{t}_n \mathrm{g}_n = 0. \tag{5.12}$$

To regularize these conditions, the mixed variable t_n^*, denoted as *augmented normal traction*, is defined as

$$t_n^* = t_n + r_n \mathrm{g}_n, \tag{5.13}$$

where r_n is a positive penalization parameter ($r \in \mathbb{R}_+$).

The above inequalities are eliminated using a projection function such as

$$\mathbb{P}_{\mathbb{R}_-}(\cdot) : \mathbb{R} \rightarrow \mathbb{R}_-, \tag{5.14}$$

which projects variable x in $\mathbb{R}$, the admissible region of the contact normal tractions. It is written as

$$\mathbb{P}_{\mathbb{R}_-}(x) = \min(x, 0). \tag{5.15}$$

On rewrites the normal contact restriction as

$$t_n - \mathbb{P}_{\mathbb{R}_-}(t_n^*) = 0. \tag{5.16}$$

5.4.2 Tangential operator

To express the tangential restriction, the augmented tangential traction is defined as

$$\mathbf{t}_t^* = \mathbf{t}_t - r_t \dot{\mathbf{g}}_t, \tag{5.17}$$

where the tangential penalization parameter $r_t \in \mathbb{R}_+$ can differ from the normal one, r_n [Rodríguez-Tembleque et al., 2011]. Introducing the contact tangential projection function, $\mathbb{P}_{\mathbb{C}_g}(\cdot) : \mathbb{R}^2 \to \mathbb{R}^2$, is written as

$$\mathbb{P}_{\mathbb{C}_g}(\mathbf{x}) = \begin{cases} \mathbf{x} & \text{if} \quad \|\mathbf{x}\| < |\mu t_n|\,, \\ |\mu t_n|\,\mathbf{e}_t & \text{if} \quad \|\mathbf{x}\| \geqslant |\mu t_n|\,, \end{cases} \tag{5.18}$$

where $\mathbf{e}_t = \mathbf{x}/\|\mathbf{x}\|$. The tangential projection function $\mathbb{P}_{\mathbb{C}_g}(\mathbf{x})$ ensures that the variable $\mathbf{x} \in \mathbb{R}^2$ to stay inside the Coulomb disk $\mathbb{C}_g$ with radius $g = |\mu t_n|$. Considering a plane defined by the tangential tractions, $t_{t_1} \perp t_{t_2}$, $\mathbb{C}_g$ represents their admissible region for a given normal traction t_n. Therefore, the tangential contact restriction can then be written as

$$\mathbf{t}_t - \mathbb{P}_{\mathbb{C}_g}(\mathbf{t}_t^*) = 0. \tag{5.19}$$

5.4.3 Normal-Tangential operator

To write the relationship between the normal and tangential tractions, one defines the normal-tangential projection function, $\mathbb{P}_{\mathbb{C}_f}$ as

$$\mathbb{P}_{\mathbb{C}_f}(\mathbf{t}^*) = \begin{bmatrix} \mathbb{P}_{\mathbb{C}_g}(\mathbf{t}_t^*) \\ \mathbb{P}_{\mathbb{R}_-}(t_n^*) \end{bmatrix}, \tag{5.20}$$

where the region $\mathbb{C}_f$ is the augmented friction cone, with radius $\left|\mu\mathbb{P}_{\mathbb{R}_-}(t^*{}_n)\right|$ and inclination defined by the coefficient of friction. According to Rodríguez-Tembleque et al., 2011, the constraints of the combined normal-tangential contact problem are

$$\mathbf{t} - \mathbb{P}_{\mathbb{C}_f}(\mathbf{t}^*) = 0. \tag{5.21}$$

5.5 Contact problem discretization

One of the advantages of BEM in contact problems is that the contact traction is already part of the unknowns, therefore, we start to formulate the system of linear equations (SLE) considering a multiple-region system (perfectly bonded interface). In a second part, we exchange the compatibility conditions with the contact laws, resulting in the final NSE.

Let Γ_1^{c} and Γ_2^{c} be the regions where the bodies are bonded, and let Γ_1^{nc} and Γ_2^{nc} the remaining non-contact regions. One writes the displacement compatibility and the third Newton law at Γ_1^{c} and Γ_2^{c}, as

$$\mathbf{u}^{\Gamma_1^{\mathrm{c}}} = \mathbf{u}^{\Gamma_2^{\mathrm{c}}}, \tag{5.22}$$

$$\mathbf{p}^{\Gamma_1^{\mathrm{c}}} = -\mathbf{p}^{\Gamma_2^{\mathrm{c}}}. \tag{5.23}$$

One can directly write Equation 3.40 for each of these two regions, also including Equations 5.22 and 5.23, which results in:

$$\begin{aligned}
\mathbf{H}^{\Gamma_1^{\mathrm{t}}}\mathbf{u}^{\Gamma_1^{\mathrm{t}}} - \mathbf{G}^{\Gamma_1^{\mathrm{nc}}}\mathbf{p}^{\Gamma_1^{\mathrm{nc}}} + \mathbf{H}^{\Gamma_1^{\mathrm{c}}}\mathbf{u}^{\Gamma_1^{\mathrm{c}}} - \mathbf{G}^{\Gamma_1^{\mathrm{c}}}\mathbf{p}^{\Gamma_1^{\mathrm{c}}} &= \bar{\mathbf{G}}^{\Gamma_1^{\mathrm{nc}}}\bar{\mathbf{p}}^{\Gamma_1^{\mathrm{nc}}} - \bar{\mathbf{H}}^{\Gamma_1^{\mathrm{nc}}}\bar{\mathbf{u}}^{\Gamma_1^{\mathrm{nc}}}, \\
\mathbf{H}^{\Gamma_2^{\mathrm{nc}}}\mathbf{u}^{\Gamma_2^{\mathrm{nc}}} - \mathbf{G}^{\Gamma_2^{\mathrm{nc}}}\mathbf{p}^{\Gamma_2^{\mathrm{nc}}} + \mathbf{H}^{\Gamma_2^{\mathrm{c}}}\mathbf{u}^{\Gamma_1^{\mathrm{c}}} + \mathbf{G}^{\Gamma_2^{\mathrm{c}}}\mathbf{p}^{\Gamma_1^{\mathrm{c}}} &= \bar{\mathbf{G}}^{\Gamma_2^{\mathrm{p}}}\bar{\mathbf{p}}^{\Gamma_2^{\mathrm{p}}} - \bar{\mathbf{H}}^{\Gamma_2^{\mathrm{u}}}\bar{\mathbf{u}}^{\Gamma_2^{\mathrm{u}}}.
\end{aligned} \tag{5.24}$$

Equation 5.24 represents a problem where the contact region is purely bonded, i.e., a two region problem.

To introduce contact conditions into the former subregion equations (Equation 5.24), turning the permanently bonded state into a sliding or frictional contact, one introduces two additional sets of equations: the gap-displacement relations, Equation 5.1, and the contact restrictions in the augmented form (Equation 5.21).

To write the first set, one defines relations between the gap and the displacements on the contact regions. The kinematic relations between the position and displacements

between the node pairs are written as

$$\mathbf{k} = \mathbf{C}_g \mathbf{k}_{go} + (\tilde{\mathbf{C}}^2)^T \mathbf{u}^{\Gamma 2c} - (\tilde{\mathbf{C}}^1)^T \mathbf{u}^{\Gamma 1c}, \tag{5.25}$$

where $\mathbf{k}$ is the gap vector, which accounts for all the contact pairs $I = \left[1, \ldots, N^{\mathbb{C}}\right]$, being $N^{\mathbb{C}}$ the number of contact pairs. The vector $\mathbf{k}_{go}$ is the sum of the initial gap and rigid body displacements vectors. The matrices $(\mathbf{C}^\alpha)$, $(\tilde{\mathbf{C}}^\alpha)$, $\alpha = [1, 2]$ and $\mathbf{C}_g$ are defined by

$$\mathbf{C}^\alpha = \sum_{i=1}^{N^\alpha} \sum_{j=1\,(i,j)\equiv I}^{N^f} (\mathcal{L}_i^\alpha)^T \mathbf{B}_j \mathcal{L}_j^f, \tag{5.26}$$

$$\tilde{\mathbf{C}}^\alpha = \sum_{i=1}^{N^f} \sum_{j=1\,(i,j)\equiv I}^{N^f} (\mathcal{L}_i^\alpha)^T \mathbf{B}_j \mathcal{L}_j^f, \tag{5.27}$$

$$\mathbf{C}_g = \sum_{i=1}^{N^f} \sum_{j=1\,(i,j)\equiv I}^{N^f} (\mathcal{L}_i^f)^T \mathcal{L}_j^f, \tag{5.28}$$

where N^α is the number of nodes of body α, while $N^{\mathbb{C}}$ is the number of contact pairs, and the Boolean assembly matrices $\mathcal{L}_i^\alpha$, extracts the displacements $\mathbf{u}_i$ of the corresponding node from body α in the contact pair i, from the solution vector $\mathbf{x}^\alpha$,

$$\mathbf{u}_i^\alpha = \mathcal{L}_i^\alpha \mathbf{x}^\alpha, \tag{5.29}$$

$\mathcal{L}_i^f$, extracts the tractions $\boldsymbol{\lambda}_i^\alpha$ from the multipliers vector $\boldsymbol{\Lambda}$, i.e.,

$$\boldsymbol{\lambda}_i = \mathcal{L}_i^f \boldsymbol{\Lambda} \tag{5.30}$$

and are written in the following manner: Let $\mathcal{I}$ be the matrix which stores the contact node pairs, with dimensions $S_{\mathcal{I}} = [N^{\mathbb{C}} \times 2]$, let $i = [1, \ldots, N^{\mathbb{C}}]$, let $j = [1, \ldots, N^\alpha]$, then, $\mathcal{L}_i^\alpha[3 \times 3N^\alpha]$ is assembled as

$$\mathcal{L}_i^\alpha = \begin{cases} \mathbf{I}_{[3\times 3]} & \text{if} \quad \mathcal{I}_{i\alpha} = j \\ 0 & \text{otherwise.} \end{cases} \tag{5.31}$$

Let $k = [1, \ldots, n^c]$, and $l = [1, \ldots, n^{nodes\,\alpha}]$, then, $\mathcal{L}^f_{[ndofs_\alpha \times ndofs_c]}$ is defined as

$$\mathcal{L}_j^f = \begin{cases} \mathbf{I}_{[3\times 3]} & \text{if} \quad \mathcal{I}_{fj} = l \\ 0 & \text{otherwise.} \end{cases} \tag{5.32}$$

The second set of equations relates the global tractions $\mathbf{p}_c^{\Gamma n}$ and the *contact tractions* vector $\boldsymbol{\Lambda}$. The usual global tractions $\mathbf{p}^{\Gamma \alpha c}$ can be extracted from the reference nodes

coordinate system by the following relations

$$\mathbf{p}^{\Gamma 1c} = \tilde{\mathbf{C}}^{1}\mathbf{\Lambda}, \tag{5.33}$$

$$\mathbf{p}^{\Gamma 2c} = -\tilde{\mathbf{C}}^{2}\mathbf{\Lambda}. \tag{5.34}$$

One can assemble the contact SLE similarly to Equation 5.24, using Equations 5.33 and 5.34 and Equation 5.25 as the traction and displacement compatibility conditions, resulting in

$$\begin{aligned} \mathbf{A}^{\Gamma_1^{nc}}\mathbf{x}^{\Gamma_1^{nc}} + \mathbf{H}^{\Gamma_1^{c}}\mathbf{u}^{\Gamma_1^{c}} - \mathbf{G}^{\Gamma_1^{c}}\tilde{\mathbf{C}}^{1}\mathbf{\Lambda} &= \mathbf{b}^{\Gamma_1}, \\ \mathbf{A}^{\Gamma_2^{nc}}\mathbf{x}^{\Gamma_2^{nc}} + \mathbf{H}^{\Gamma_2^{c}}\mathbf{u}^{\Gamma_2^{c}} + \mathbf{G}^{\Gamma_2^{c}}\tilde{\mathbf{C}}^{2}\mathbf{\Lambda} &= \mathbf{b}^{\Gamma_2}, \\ (\tilde{\mathbf{C}}^{1})^{T}\mathbf{u}^{\Gamma_1^{c}} - (\tilde{\mathbf{C}}^{2})^{T}\mathbf{u}^{\Gamma_2^{c}} + \mathbf{C}_g\mathbf{k} &= \mathbf{C}_g\mathbf{k}_{go}. \end{aligned} \tag{5.35}$$

5.5.1 Detailed assembly of the contact restrictions

As Rodríguez-Tembleque et al., 2008, the discrete contact restrictions can be expressed by writing Equation 5.21 for a single contact pair

$$\boldsymbol{\lambda} - \mathbb{P}_{\mathbb{C}_f}(\boldsymbol{\lambda}^*) = 0, \tag{5.36}$$

which substituting $\lambda^* = \lambda + \mathbf{rk}$,where $\mathbf{r}$ is the penalty parameters vector, returns

$$\boldsymbol{\lambda} - \mathbb{P}_{\mathbb{C}_f}(\boldsymbol{\lambda} + \mathbf{rk}) = 0, \tag{5.37}$$

for the normal direction one writes the restriction as

$$\lambda_n - \min({\lambda_n}^*, 0) = 0, \tag{5.38}$$

which on the free case, where $(\lambda_n^*)^I \geq 0$, returns

$$\lambda_n = 0, \tag{5.39}$$

and by the coulomb friction law, $\lambda_t \leq \mu\lambda_n$ results in

$$\boldsymbol{\lambda_t} = 0. \tag{5.40}$$

Writing the restrictions for the case of contact, for the tangential direction, one needs to write the restrictions separately for stick and slip. On the normal direction, one has $(\lambda_n^*)^I < 0$, so the restriction equation for a node pair I in the normal direction, for

both stick and slip cases, is written as

$$\lambda_n - \min(\,\lambda_n - r_n k_n\,, 0) = 0, \tag{5.41}$$

which results in

$$-\,r_n k_n = 0. \tag{5.42}$$

Notice that this result demonstrates that the normal penalty parameter r_n does not influence the normal contact coupling stiffness.

On the stick case, where $(\lambda_t^*)^I < \mu\,|\lambda_n|$, the tangential restriction results in

$$\boldsymbol{\lambda}_t - \mathbb{P}_{\mathbb{C}_f}(\boldsymbol{\lambda}_t + r_t \mathbf{k}_t) = 0, \tag{5.43}$$

which substituing $\mathbb{P}_{\mathbb{C}_f}(X) = X$, the first case of Equation 5.18, results in

$$r_t \mathbf{k}_t = 0. \tag{5.44}$$

Notice that in the tangential direction the penalty parameter also poses no influence in stiffness, as it would in the case of direct penalty methods.

On the slip case $(\boldsymbol{\lambda}_t^*)^I \geq |\mu\lambda_n|$, therefore the second case of Equation 5.18 implies that $\mathbb{P}_{\mathbb{C}_f}(\boldsymbol{\lambda}_t^*) = |\mu t_n|\,(\mathbf{e}_t^*)$. so the tangential restrictions are written as

$$\lambda_{t_1} + \mu e_{t_1}^* \lambda_n = 0, \tag{5.45}$$

$$\lambda_{t_2} + \mu e_{t_2}^* \lambda_n = 0, \tag{5.46}$$

where

$$\mathbf{e}_t^* = \frac{\boldsymbol{\lambda}_t^*}{\|\boldsymbol{\lambda}_t^*\|}. \tag{5.47}$$

Summarizing all the contact constraints on a single equation system results in

$$\mathbf{P}_\lambda\,\boldsymbol{\lambda} + \mathbf{P}_\mathrm{g}\,\mathbf{k} = \mathbf{0}, \tag{5.48}$$

where $\mathbf{P}_\lambda$ and $\mathbf{P}_\mathrm{g}$ are assembled according to the contact state of each node pair I.

5.5.2 Nonlinear equation system

Grouping the terms of Equation 5.35, the gap kinematic relations, Equation 5.25, the contact restrictions, Equation 5.48, the NSE resultant from the contact problem, $\mathbf{R}(\mathbf{z}) - \mathbf{f} = 0$, is

$$\begin{bmatrix} \mathbf{A}^{\Gamma_1^{\mathrm{nc}}} & \mathbf{H}^{\Gamma_1^{\mathrm{c}}} & \mathbf{0} & \mathbf{0} & -\mathbf{G}^{\Gamma_1^{\mathrm{c}}}\tilde{\mathbf{C}}^{1} & \mathbf{0} \\ \mathbf{0} & \mathbf{0} & \mathbf{A}^{\Gamma_2^{\mathrm{nc}}} & \mathbf{H}^{\Gamma_2^{\mathrm{c}}} & \mathbf{G}^{\Gamma_2^{\mathrm{c}}}\tilde{\mathbf{C}}^{2} & \mathbf{0} \\ \mathbf{0} & (\tilde{\mathbf{C}}^{1})^{T} & \mathbf{0} & -(\tilde{\mathbf{C}}^{2})^{T} & \mathbf{0} & \mathbf{C}_{\mathrm{g}} \\ \mathbf{0} & \mathbf{0} & \mathbf{0} & \mathbf{0} & \mathbf{P}_{\lambda} & \mathbf{P}_{\mathrm{g}} \end{bmatrix} \begin{Bmatrix} \mathbf{x}^{\Gamma_1^{\mathrm{nc}}} \\ \mathbf{u}^{\Gamma_1^{\mathrm{c}}} \\ \mathbf{x}^{\Gamma_2^{\mathrm{nc}}} \\ \mathbf{u}^{\Gamma_2^{\mathrm{c}}} \\ \mathbf{\Lambda} \\ \mathbf{k} \end{Bmatrix} - \begin{Bmatrix} \mathbf{b}^{\Gamma_1} \\ \mathbf{b}^{\Gamma_2} \\ \mathbf{k}_{\mathrm{go}} \\ \mathbf{0} \end{Bmatrix} = 0 \tag{5.49}$$

where $\mathbf{x}^{\Gamma_\alpha^{\mathrm{nc}}}$ are the usual BEM non-contact region unknowns (displacements and tractions) vector for each region α, and $\mathbf{u}^{\Gamma_\alpha^{\mathrm{c}}}$ are the contact nodes displacements for each region α. The vectors $\mathbf{\Lambda}$ and $\mathbf{k}$, are the *contact tractions* and the gap vectors, respectively, which are the normal and tangential contact tractions and gap for the reference node, at the local coordinate system, defined by Equation 5.2. These are assembled in the sequence of the contact pairs. One obtains the secondary nodes traction using Equations 5.33 and 5.34.

The right-hand side (RHS) vector $\mathbf{f}$ vector is composed by the RHS vectors $\mathbf{b}^1$ and $\mathbf{b}^2$ (formed by the boundary conditions and its corresponding BEM matrices, i.e., $\mathbf{b}^\alpha = \bar{\mathbf{G}}^{\boldsymbol{\alpha}}\bar{\mathbf{p}}^{\boldsymbol{\alpha}} - \bar{\mathbf{H}}^{\boldsymbol{\alpha}}\bar{\mathbf{u}}^{\boldsymbol{\alpha}}$) and $\mathbf{C}_{\mathrm{g}}\mathbf{k}_{\mathrm{go}}$ which is the initial gap for each pair. The null lines at the end of the vector correspond to the projection matrices, i.e., the RHS of Equation 5.48.

At $\mathbf{R}$, $\mathbf{A}^{\Gamma_\alpha^{\mathrm{nc}}}$ comes from Equation 5.35 and refer to the independent unknowns (mixed tractions and displacements) for region α. $\mathbf{H}^{\Gamma_\alpha^{\mathrm{c}}}$ refers to the displacement unknowns of the possible contact region. The transformation matrices $\tilde{\mathbf{C}}^{\alpha}$ was defined on Equation 5.33, and appears transposed because it is performing a transformation from the global to local coordinate system, as in Equation 5.25.

The matrices $\mathbf{G}^{\Gamma_\alpha^{\mathrm{c}}}$ correspond to the contact region of each body α. In this case, $\tilde{\mathbf{C}}^{\alpha}$ performs a local to global transformation on the contact tractions $\mathbf{\Lambda}$.

The gap assembly operator is defined as $\mathbf{C}_g = \mathbf{I}$, and $\mathbf{k}_{\mathrm{go}}$ is the initial separation or gap vector, from which the rigid body displacements are not yet excluded.

The projection matrices $\mathbf{P}_\lambda$ and $\mathbf{P}_{\mathrm{g}}$, which comes from Equation 5.48, are assembled for each node pair I and depend on the augmented contact variables $\boldsymbol{\lambda}_I^*$:

- Free: $\lambda^*_{n\,I} \geqslant 0$

$$(\mathbf{P}_\lambda)_I = \begin{bmatrix} 1 & 0 & 0 \\ 0 & 1 & 0 \\ 0 & 0 & 1 \end{bmatrix}_I, (\mathbf{P}_\mathrm{g})_I = \begin{bmatrix} 0 & 0 & 0 \\ 0 & 0 & 0 \\ 0 & 0 & 0 \end{bmatrix}_I . \tag{5.50}$$

- Stick: $\lambda^*_{n\,I} < 0$ and $\|\boldsymbol{\lambda}^*_{t\,I}\| < \mu\,|\lambda^*_{n\,I}|$

$$(\mathbf{P}_\lambda)_I = \begin{bmatrix} 0 & 0 & 0 \\ 0 & 0 & 0 \\ 0 & 0 & 0 \end{bmatrix}_I, (\mathbf{P}_\mathrm{g})_I = \begin{bmatrix} r_t & 0 & 0 \\ 0 & r_t & 0 \\ 0 & 0 & -r_n \end{bmatrix}_I . \tag{5.51}$$

- Slip: $\lambda^*_{n\,I} < 0$ and $\|\boldsymbol{\lambda}^*_{t\,I}\| > \mu\,|\lambda^*_{n\,I}|$

$$(\mathbf{P}_\lambda)_I = \begin{bmatrix} 1 & 0 & \mu\omega^*_{t_1} \\ 0 & 1 & \mu\omega^*_{t_2} \\ 0 & 0 & 0 \end{bmatrix}_I, (\mathbf{P}_\mathrm{g})_I = \begin{bmatrix} 0 & 0 & 0 \\ 0 & 0 & 0 \\ 0 & 0 & -r_n \end{bmatrix}_I , \tag{5.52}$$

where $(\boldsymbol{\omega}^*_t)_I = (\boldsymbol{\lambda}^*_t / \|\boldsymbol{\lambda}^*_t\|)_I$, the slip direction for the pair I.

5.6 Nonlinear system solution: Generalized Newton Method

The contact NSE, Equation 5.49 is not differentiable, but only $\mathcal{B}$-differentiable[1] Rodríguez-Tembleque and Abascal, 2010, and assumes the following form:

$$\boldsymbol{\Theta}(\mathbf{z}) = \mathbf{R}(\mathbf{z}) - \mathbf{f} = 0 \tag{5.53}$$

The solution method adopted in this work is the same as in Rodríguez-Tembleque et al., 2011, the generalized Newton method with line search (GNMls) due to Pang, 1990 and Alart and Curnier, 1991. According to Alart and Curnier, 1991, it is an effective extension of the traditional Newton Method for $\mathcal{B}$-differentiable functions. It can be summarized on the following steps:

GNMls Let $\mathbf{z}^{(o)}$ be an arbitrary initial vector and q, β, σ and ε be positive scalars: $q > 0$, $\beta \in (0, 1)$, $\sigma \in (0, 1/2)$ and $0 < \varepsilon \ll 1$.

[1] A $\mathcal{B}$-differentiable function is a special kind of function which is not Frechet-differentiable, but is continuous and has a generalized Jacobian at some points x [Alart and Curnier, 1991; Alart and Lebon, 1998].

1. Find the search direction for iteration n:

   Given a vector $\mathbf{z}^{(n)}$, the nth solution vector, with $\boldsymbol{\Theta}(\mathbf{z}^{(n)}) \neq \mathbf{0}$, the direction $\boldsymbol{\Delta}\mathbf{z}^{(n)}$ is obtained solving

   $$\boldsymbol{\Theta}(\mathbf{z}^{(n)}) + \mathcal{B}\boldsymbol{\Theta}\left(\mathbf{z}^{(n)}, \Delta\mathbf{z}^{(n)}\right) = \mathbf{0}, \tag{5.54}$$

   where $\mathcal{B}\boldsymbol{\Theta}\left(\mathbf{z}^{(n)}, \Delta\mathbf{z}^{(n)}\right)$ is the $\mathcal{B}$-derivative of the function.

2. Line search:

   Let $\alpha^{(n)} = \beta^{m^{(n)}} q$, $m^{(n)}$ is obtained as the first non negative integer which returns

   $$\Psi\left(\mathbf{z}^{(n)} + \alpha^{(n)}\boldsymbol{\Delta}\mathbf{z}^{(n)}\right) \leq \left(1 - 2\sigma\alpha^{(n)}\right)\Psi(\mathbf{z}^{(n)}), \tag{5.55}$$

   where

   $$\Psi(\mathbf{z}^{(n)}) = \frac{1}{2}\left\|\boldsymbol{\Theta}(\mathbf{z}^{(n)})\right\|^2 \tag{5.56}$$

   is an error function in which the minimum is located at $(\mathbf{z}^{(n)} + \alpha^{(n)}\boldsymbol{\Delta}\mathbf{z}^{(n)})$.

3. Set new solution:

   $$\mathbf{z}^{(n+1)} = \mathbf{z}^{(n)} + \alpha^{(n)}\boldsymbol{\Delta}\mathbf{z}^{(n)} \tag{5.57}$$

4. Check for solution convergence:

   - If $\Psi(\mathbf{z}^{(n)}) \leq \varepsilon_1$: $\rightarrow \mathbf{z}^{(n+1)}$ is the solution.
   - Otherwise, $n + 1 \rightarrow n$ and return to 1;

5.6.1 Search direction: Directional derivatives

The system of equations $\boldsymbol{\Theta}(\mathbf{z}^{(n)})$ can be separated on its linear and nonlinear parts,

$$\boldsymbol{\Theta}(\mathbf{z}^{(n)}) = \boldsymbol{\Theta}_{\mathbf{LD}}(\mathbf{z}^{(n)}) + \boldsymbol{\Theta}_{\mathbf{NLD}}(\mathbf{z}^{(n)}), \tag{5.58}$$

where $\boldsymbol{\Theta}_{\mathbf{LD}}(\mathbf{z}^{(n)})$ is the part of the system which has linear directional derivative, at all points, and $\boldsymbol{\Theta}_{\mathbf{NLD}}(\mathbf{z}^{(n)})$ is the part of the system which has non-linear derivative at some points. The $\mathcal{B}$-derivative $\mathcal{B}\boldsymbol{\Theta}(\mathbf{z}^{(n)}, \Delta\mathbf{z}^{(n)})$ can also be separated in the same manner, as

$$\mathcal{B}\boldsymbol{\Theta}(\mathbf{z}^{(n)}, \Delta\mathbf{z}^{(n)}) = \left(\nabla\boldsymbol{\Theta}_{LD}(\mathbf{z}^{(n)}) + \partial\boldsymbol{\Theta}_{NLD}(\mathbf{z}^{(n)})\right)\boldsymbol{\Delta}\mathbf{z}^{(n)}, \tag{5.59}$$

where $\nabla\boldsymbol{\Theta}_{LD}(\mathbf{z}^{(n)})$ is the linear part of the Jacobian matrix,

$$\nabla\boldsymbol{\Theta}_{LD}(\mathbf{z}^{(n)}) = \begin{bmatrix} \mathbf{A}^{\Gamma 1} & \mathbf{0} & \mathbf{A}_p^1\tilde{\mathbf{C}}^1 & \mathbf{0} \\ \mathbf{0} & \mathbf{A}^{\Gamma 2} & -\mathbf{A}_p^2\tilde{\mathbf{C}}^2 & \mathbf{0} \\ \mathbf{C}^{1\mathrm{T}} & -\mathbf{C}^{2\mathrm{T}} & \mathbf{0} & \mathbf{C}_{\mathrm{g}} \\ \mathbf{0} & \mathbf{0} & \mathbf{0} & \mathbf{0} \end{bmatrix}, \tag{5.60}$$

and $\partial\boldsymbol{\Theta}_{NLD}(\mathbf{z}^{(n)}))\boldsymbol{\Delta}\mathbf{z}^{(n)}$ is the non-linear part of this function. Strömberg, 1997 suggested a linear approximation for this derivative:

$$\partial\boldsymbol{\Theta}_{NLD}(\mathbf{z}^{(n)}) = \begin{bmatrix} \mathbf{0} & \mathbf{0} & \mathbf{0} & \mathbf{0} \\ \mathbf{0} & \mathbf{0} & \mathbf{0} & \mathbf{0} \\ \mathbf{0} & \mathbf{0} & \mathbf{0} & \mathbf{0} \\ \mathbf{0} & \mathbf{0} & \mathbf{J}_\lambda & \mathbf{J}_g \end{bmatrix}^{(n)}, \tag{5.61}$$

where the matrices $\mathbf{J}_\lambda^{(n)}$ and $\mathbf{J}_g^{(n)}$ are written for each contact pair, as the matrices $\mathbf{P}_\lambda$ and $\mathbf{P}_g$, and will depend on the state of the contact augmented variables, i.e., the contact state of each pair

- Separated: $\lambda_{n\,I}^* \geqslant 0$

$$(\mathbf{J}_\lambda)_I = \begin{bmatrix} 1 & 0 & 0 \\ 0 & 1 & 0 \\ 0 & 0 & 1 \end{bmatrix}_I, \quad (\mathbf{J}_{\mathrm{g}})_I = \begin{bmatrix} 0 & 0 & 0 \\ 0 & 0 & 0 \\ 0 & 0 & 0 \end{bmatrix}_I. \tag{5.62}$$

- Stick: $\lambda_{n\,I}^* < 0$ and $\|\lambda_{t\,I}^*\| < \mu\,|\lambda_{n\,I}^*|$

$$(\mathbf{J}_\lambda)_I = \begin{bmatrix} 0 & 0 & 0 \\ 0 & 0 & 0 \\ 0 & 0 & 0 \end{bmatrix}_I, \quad (\mathbf{J}_{\mathrm{g}})_I = \begin{bmatrix} r_t & 0 & 0 \\ 0 & r_t & 0 \\ 0 & 0 & -r_n \end{bmatrix}_I. \tag{5.63}$$

- Slip: $\lambda_{n\,I}^* < 0$ and $\|\lambda_{t\,I}^*\| > \mu\,|\lambda_{n\,I}^*|$

$$(\mathbf{J}_\lambda^{(n)})_I = \begin{bmatrix} \Psi_{11} & \Psi_{12} & \mu\omega_{t_1}^* \\ \Psi_{21} & \Psi_{22} & \mu\omega_{t_2}^* \\ 0 & 0 & 0 \end{bmatrix}_I^{(n)}, \quad (\mathbf{J}_{\mathrm{g}}^{(n)})_I = \begin{bmatrix} -r_t\tilde{\Psi}_{11} & -r_t\tilde{\Psi}_{12} & 0 \\ -r_t\tilde{\Psi}_{21} & -r_t\tilde{\Psi}_{22} & 0 \\ 0 & 0 & -r_n \end{bmatrix}_I^{(n)}, \tag{5.64}$$

where,

$$\boldsymbol{\Psi} = (1+\chi)\mathbf{I} - \zeta\mathbf{L}, \quad \tilde{\boldsymbol{\Psi}} = \boldsymbol{\Psi} - \mathbf{I}, \tag{5.65}$$

and

$$\mathbf{L} = (\boldsymbol{\Lambda}_t^{*(n)})_I \otimes (\boldsymbol{\Lambda}_t^{*(n)})_I, \tag{5.66}$$

and

$$\chi = \frac{\mu(\boldsymbol{\Lambda}_n^{*(n)})_I}{\left\|(\boldsymbol{\Lambda}_t^{*(n)})_I\right\|}, \quad \zeta = \frac{\mu(\boldsymbol{\Lambda}_n^{*(n)})_I}{\left\|(\boldsymbol{\Lambda}_t^{*(n)})_I\right\|^3}. \tag{5.67}$$

5.6.2 Linearized Derivatives

According to Rodríguez-Tembleque and Abascal, 2010, it is possible to simplify the contact NSE, assuming that the nonlinear part of the directional derivatives $(\mathbf{J}_\lambda^{(n)})_I$ and $(\mathbf{J}_g^{(n)})_I$, i.e., Equation 5.64, can be approximated by its linear counterparts $(\mathbf{P}_\lambda)_I$ and $(\mathbf{P}_g)_I$, Equation 5.52. What this assumption means physically is that the slip direction is constant at the Newton iterations and only changes from the initial solution if one divides the boundary conditions, or load application, in various steps.

This simplifies the GNMls Item 1 procedure, which resumes to the solution of

$$\boldsymbol{\Theta}(\mathbf{z}^{(n)}) + \mathbf{R}^{(n)}\boldsymbol{\Delta}\mathbf{z}^{(n)} = 0, \tag{5.68}$$

which is the same as solving the SLE for $\boldsymbol{\Delta}\mathbf{z}^{(n)}$

$$\mathbf{R}^{(n)}(\mathbf{z}^{(n)} + \boldsymbol{\Delta}\mathbf{z}^{(n)}) - \mathbf{f} = 0. \tag{5.69}$$

6 RESULTS

This chapter presents application examples of the methodology shown so far. Problems involving contact shape sensitivity are solved, benchmarks as well as new results which are part of the contribution of this work.

The methodology presented so far is tested through the solution of classical contact problems which have analytical solutions available, allowing an extensive validation of the program in many use-case scenarios. Most cases need the incremental load application to maintain small strains and due to the nonlinearity when the contact area is not constant through the loading.

The problems analyzed are meant to reproduce classic contact solutions such as the Hertz one. Various simplifications are found in numerical contact literature to obtain results closer to analytic solutions. In many works, one of the bodies is considered rigid. Another assumption found in the BEM literature is the consideration of a half-space (semi-infinite) for one region. This assumption leads to a faster solution, and a closer geometry to that one assumed in the closed-form solution. Besides the advantages of the previous assumptions, those representations are numerically simpler to solve, i.e., the half-space needs fewer elements around the region of interest. Moreover, considering a rigid body is closer to prescribing displacements, than to an elastic contact condition, as one knows the contact region displacements a priori. Therefore, the problems analyzed in this work should be viewed not only as benchmarks but also as a more difficult use-case scenario to the contact algorithm. A proportionally small region of the boundary is transferring the load, limiting the contact stress into a few elements.

6.1 Sphere compressed by flat regions

The first problem analyzed is of a sphere being pressed by two elastic regions, with prescribed displacements at the outer faces, Figure 6.1a. Figure 6.1b depicts the mesh used for the sphere and cube, which has 462 and 330 quadratic elements, respectively, totaling 19008 degrees of freedom (DOF). The problem was modeled considering three symmetry planes.

Prescribed displacements u_{0z} were applied on the upper face of the cube while leaving the other directions free. On all elements at the xy, zx and zy plane a symmetry

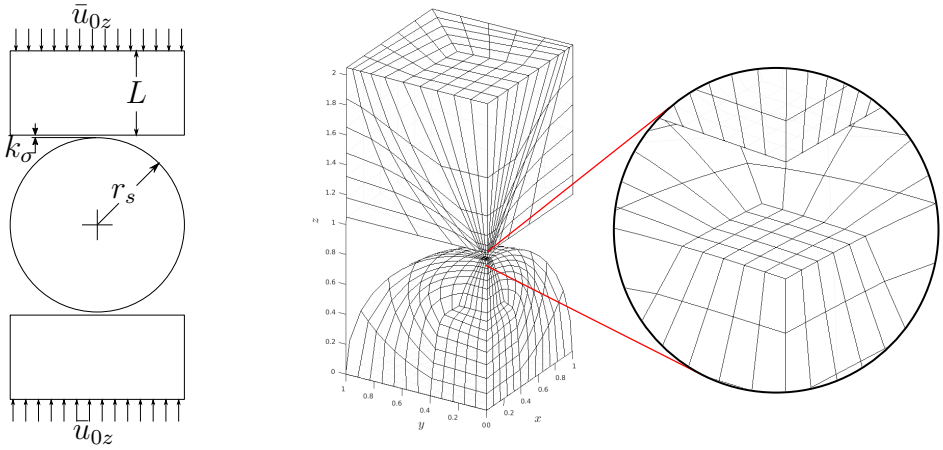

Figure 6.1 – Problem configuration (a) and mesh used (b) on the example.

boundary condition was applied, restricting the displacements only to the outward normal direction and freeing it at their tangential directions. The offset used on the discontinuous elements (Equation 3.22) was $a = 15\%$. In Table 6.1 we list all material and geometrical properties considered in this example. The friction coefficient was set to $\mu = 0$ in this preliminary case, to compare with the solution from Johnson, 1987, which does not consider frictional effects on its formulation.

Table 6.1 – Sphere on Plane contact problem parameters.

E	$1{,}0 \times 10^4$	Pa	Young's Modulus
ν	0.3		Poisson's Ratio
k_0	5×10^{-2}	m	Initial separation
r_s	1.0	m	Sphere radius
L	1.0	m	Cube length
$\bar{u}_{0z}$	$1{,}8 \times 10^{-3}$	m	Displacement applied at the top of the cube
p_0	146.3281	Pa	Contact pressure expected at the center of the contact region
a	$4{,}183\,300 \times 10^{-2}$	m	Contact area radius

The initial parameters used on the generalized Newton method with line search (GNMls) were: $\beta = 0.95$ and $r = 0.80$. Notice that in this problem the tangential penalization has no influence as this is a frictionless case. In an attempt to speed up the solution time, we used the generalized minimum residual (GMRES) iterative solver with an adaptive tolerance scheme. The initial tolerance was 1×10^{-4}, and the following solutions tolerances were set to be always 1×10^{-1} times the last GNMls iteration residual Ψ obtained. Figure 6.2 depicts the residual Ψ, the GMRES tolerance and residual, as well

as the α for each iteration. As can be seen in the diagram, although the solver could not converge to the desired tolerance on the final iterations, the final GNMls residual Ψ was lower than the desired value. This effect is due to the α factor on the line search, which for being lesser than 1, always carry over a small part of the last iteration to the next one. In our experience, the GMRES has not accelerated the computation time, due to the lack of a proper preconditioner, it was much slower than the direct solver from Davis, 2004.

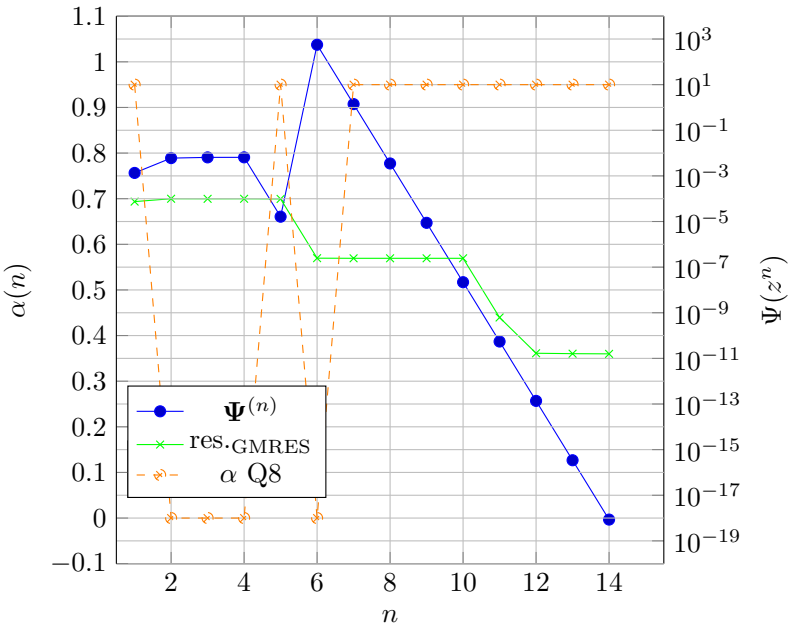

Figure 6.2 – Newton method convergence: Solution residual for each iteration ($\Psi(\boldsymbol{z}^{(n)})$), relative iterative solver residual ($\text{res}_{\text{GMRES}}$), and α obtained on line search.

In Section 6.1, we plot the resulting displacements on the contact region as a function of the radius from the center of the sphere, and the Hertz solution for displacements, both normalized with the prescribed displacements $\bar{u}_{0z}$. As the mesh nodes were disposed on a rectangular grid, so the results are scattered along their relative radius $r = \sqrt{x_i^2 + y_i^2}$.

In Figure 6.4, the obtained normal tractions on the contact region are plotted in the same manner as the displacements, and normalized with the maximum contact pressure p_0 estimated by the closed-form solution. As can be seen in the plots, the displacements and tractions agree with the analytic solution.

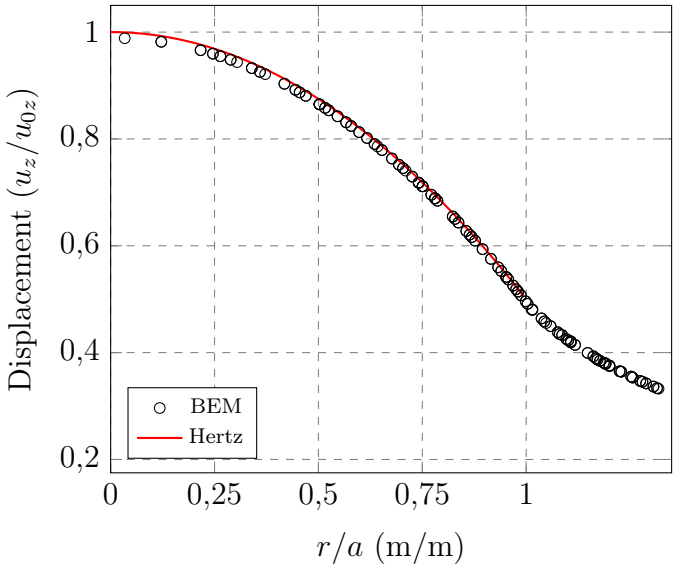

Figure 6.3 – Displacement along the possible contact region selected for the problem.

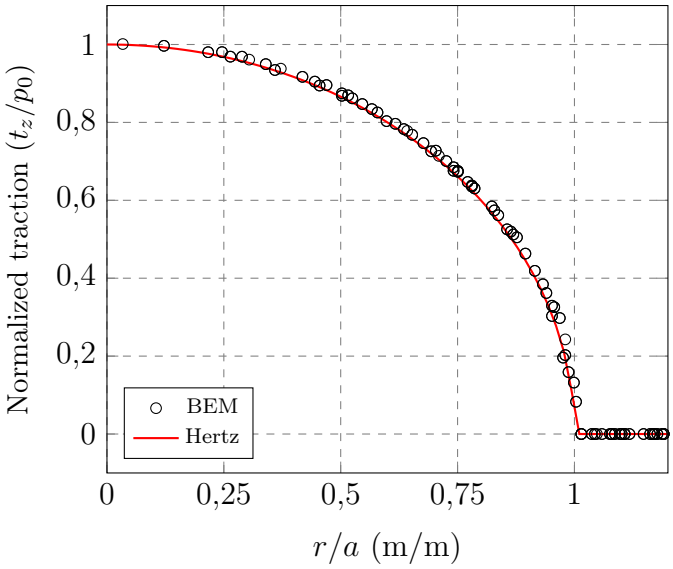

Figure 6.4 – Traction along the possible contact region selected for the problem.

6.2 Sensitivity to material properties - frictional contact between two isotropic spheres

The complex step (CS) verification problem analyzed in this section consists of two spherical bodies in contact (Figure 6.5a), allowing for a direct comparison with the classical Hertz solution. Although the boundary element method (BEM) allows one to model only the contact region considering half-spaces, in this section both solids are entirely considered. Also they are considered with elastic stiffness (many times, in the literature,

one of the bodies is assumed rigid). As in the last problem, we have simplified the mesh by taking advantage of the symmetries (Figure 6.5b). This discretization (considering the complete sphere) allows for the evaluation of the implemented algorithm when a small region of the solid is transferring all the load, resulting in significant stress concentration at a few nodes.

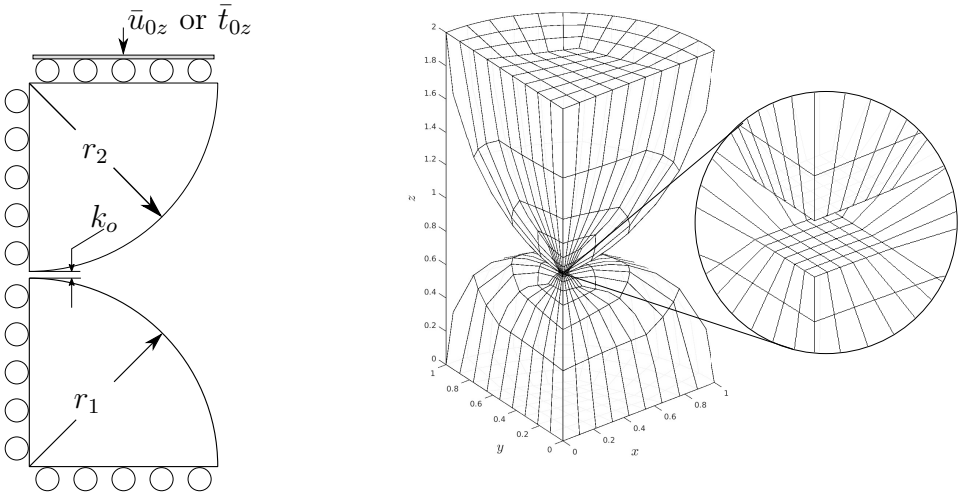

Figure 6.5 – (a) Problem description and (b) mesh used on the Hertzian contact example.

The mesh used for each sphere has 264 quadrilateral elements, as illustrated in Figure 6.5b for quadratic elements. The mesh has a large element size ratio to reduce the overall number of DOF without compromising the solution accuracy. The linear and quadratic elements resulted in 6936 and 14400 DOF, respectively. The kinematic relations and the contact restrictions account for 9 percent of those.

The prescribed displacements $\bar{u}_z$ were applied in the upper face of the half sphere.

We used an offset of 12.5% in all the elements, and in Table 6.2 are listed all material and geometrical properties for this problem. To the best of the authors' knowledge, there is no closed-form solution in the literature for this problem when $\mu \neq 0$. In order to provide a reference solution for the results, the geometrical and material properties selected were the same as in Rodríguez-Tembleque and Abascal, 2010, including the friction coefficient $\mu = 0.1$. Table 6.2 also lists the maximum contact pressure p_0 and the radius of the

contact circle predicted for the prescribed displacements $\bar{u}_z$, from Johnson, 1987.

Table 6.2 – Sphere on Sphere contact problem parameters and results from the hertz solution.

$E_1 = E_2$	$1{,}0 \times 10^4$	Pa	Young's Modulus
ν_1	0.3	-	Sphere 1 Poisson Ratio
ν_2	0.4	-	Sphere 2 Poisson Ratio
μ	0.1	-	Coulomb friction coefficient
r_1, r_2	1.0	m	Sphere radius
k_0	1×10^{-1}	m	Initial separation
$\bar{u}_{0z} - k_0$	8×10^{-4}	m	Prescribed displacements on the top sphere
p_0	145.5131	Pa	Maximum contact pressure (Equation 6.2)
a	0.020	m	Radius of the contact area

A single load step was used to set the boundary conditions, and the initial parameters for the GNMls were $q = 1.0$, $\beta = 0.90$, $r_t = r_n = 0.70$. The residue $\boldsymbol{\Psi}^{(n)}$ and the scaling parameter $\alpha^{(n)}$ during the GNMls iterations are shown in Figure 6.6. The resulting residue during the first few iterations remains almost constant, but, as the algorithm finds an optimal direction, it decreases with logarithmic rate.

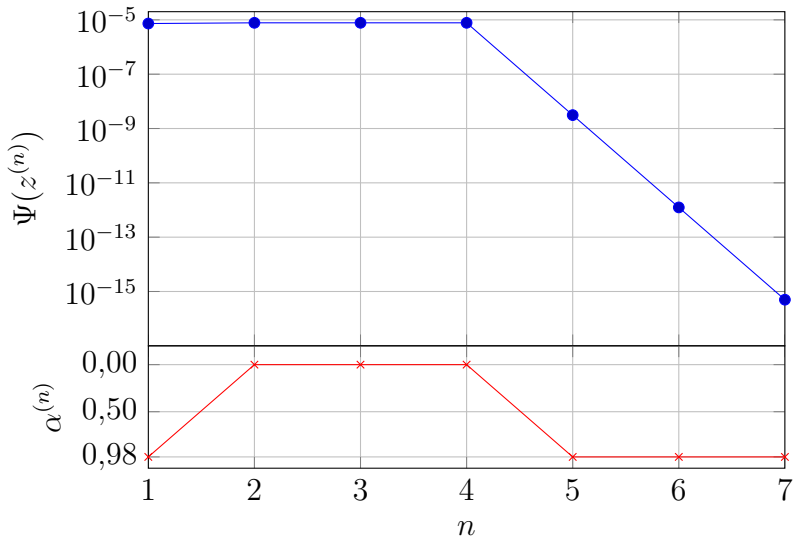

Figure 6.6 – GNMls convergence: Residue ($\boldsymbol{\Psi}$) and scaling parameter (α) obtained by the line search procedure for each iteration n.

The displacements along the contact area are plotted in Figure 6.7, as a function of the coordinates x. These results are from a line of collocation nodes close to the plane of symmetry xz. Both numerical and analytical displacements were normalized with

the prescribed displacements $\bar{u}_z$. In this particular example, the quadratic element (Q8) showed a more significant difference to the Hertz solution for the displacements than the linear one (Q4). The tangential slip obtained for both elements is also depicted in the figure. It is normalized with respect to the maximum slip of the quadratic element. In this case, it is possible to verify the transition from stick to slip states is different in the two cases, due to the lesser nodes in the linear mesh.

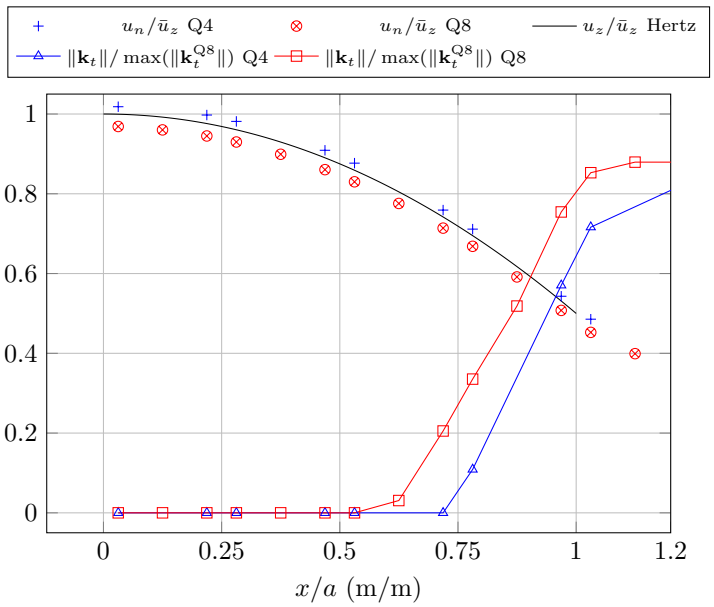

Figure 6.7 – Normalized displacements and tangential slip.

Figure 6.8 shows the normal contact tractions λ_n normalized with the maximum analytic pressure p_0.

The normal displacements and tractions agree well with the reference solution. To verify the fulfillment of the Coulomb friction law, we divide tangential traction norm by the friction coefficient. At approximately 75% of the contact radius, the tangential traction reaches the maximum value predicted by the Coulomb law, precisely where the nodes initiate the slip state. Although the maximum normal traction does not present a pronounced difference between the linear and quadratic elements, in the tangential direction, it is possible to see a larger difference between the two. The quadratic elements also predicted a larger slip region. At this transition region, the normal tractions are in much better agreement with the reference solution, which indicates a better approximation by the quadratic element.

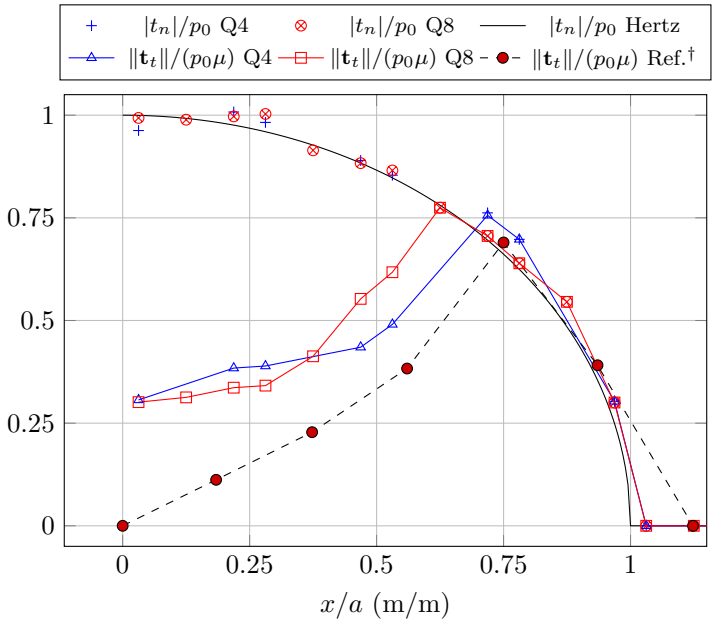

Figure 6.8 – Normalized tractions on the contact region. †Rodríguez-Tembleque and Abascal, 2010.

This effect is also noticed in the results of Rodríguez-Tembleque and Abascal, 2010, as the number of nodes is even more reduced in their mesh. The tangential tractions should have vanished at the symmetry line $x = 0$, but they are producing a residual value. In other numerical experiments, we have found out that if entire meshes are used without the aid of symmetry, correct values are obtained.

6.2.1 Sensitivity to the material properties

The initial analysis for any finite differentiation (FD) scheme should be a verification of step size. However, to show the step size independence of the CS method, we test sizes from 1×10^{-15} to 1×10^{-300}.

The CS was added to the top sphere Young modulus $E_1^* = E_1 + \mathrm{i}\Delta E_1$, and the maximum contact pressure sensitivity was analyzed. The comparison was carried out against the analytical solution, obtained by deriving the Hertz equation for the maximum contact pressure with respect to E_1.

Due to the position of the collocation points in discontinuous elements, there is no node exactly at $x = 0$, so the analytical solution was evaluated at the closest point to the

symmetry plane.

The normal pressure distribution along the contact region is given by Johnson, 1987,

$$p(r) = p_0 \left(1 - \frac{r^2}{a^2}\right), \tag{6.1}$$

where p_o is the maximum pressure and r is the distance from the center of the sphere. p_o is related to the material and geometrical properties by the equation

$$p_0 = \frac{2}{\pi} E^* \sqrt{(u_0/R^*)}, \tag{6.2}$$

where u_0 is the prescribed displacement, $R^* = (1/R_1 + 1/R_2)^{-1}$ and E^* is the equivalent elastic modulus of the pair:

$$E^* = ((1 - \nu_1^2)/E_1 + (1 - \nu_2^2)/E_2)^{-1}. \tag{6.3}$$

Considering $\nu_1 = \nu_2 = \nu$, the result for the derivative of the maximum pressure is

$$\frac{\partial p_o}{\partial E_1} = -\frac{(2/\pi)\sqrt{(\mathrm{u_o/R})}\ ({\nu_1}^2 - 1)}{{E_1}^2 \left(\frac{{\nu_1}^2 - 1}{E_1} + \frac{{\nu_2}^2 - 1}{E_2}\right)^2}. \tag{6.4}$$

The pressure sensitivity is therefore

$$\frac{\partial p}{\partial E_1} = \frac{\partial p_o}{\partial E_1} \left(1 - \frac{r^2}{a^2}\right). \tag{6.5}$$

which, for a radius $r = 6.3 \times 10^{-4}$m, Equation 6.5 results in a sensitivity of $7{,}56 \times 10^{-3}$. Table 6.3 shows the difference obtained by the present approach to the analytical solution for different increment sizes. As can be seen, the relative difference is larger than the variation of the results obtained by the complex step method, which shows the stability of the method for any step size chosen.

Figure 6.9 illustrates the distribution of normal and tangential tractions sensitivities to the Young modulus E_1 over the contact area. The normal contact sensitivity agrees with the analytic solution along the entire contact area.

We do not divided the tangential traction sensitivity by the friction coefficient, differently from Figure 6.8. Therefore, the tangential traction presents a relatively high sensitivity in comparison with the normal component.

$Log(\Delta E_1)$	difference to analytical solution	relative difference
-15	$1{,}736\,641\,581\,748\,989\,83 \times 10^{-4}$	$1{,}6 \times 10^{-2}$
-25	$1{,}736\,641\,581\,752\,129\,68 \times 10^{-4}$	$1{,}6 \times 10^{-2}$
-35	$1{,}736\,641\,581\,754\,003\,18 \times 10^{-4}$	$1{,}6 \times 10^{-2}$
-50	$1{,}736\,641\,581\,749\,284\,74 \times 10^{-4}$	$1{,}6 \times 10^{-2}$
-75	$1{,}736\,641\,581\,750\,672\,51 \times 10^{-4}$	$1{,}6 \times 10^{-2}$
-100	$1{,}736\,641\,581\,748\,105\,12 \times 10^{-4}$	$1{,}6 \times 10^{-2}$
-150	$1{,}736\,641\,581\,753\,465\,42 \times 10^{-4}$	$1{,}6 \times 10^{-2}$
-200	$1{,}736\,641\,581\,746\,006\,11 \times 10^{-4}$	$1{,}6 \times 10^{-2}$
-250	$1{,}736\,641\,581\,746\,734\,69 \times 10^{-4}$	$1{,}6 \times 10^{-2}$
-300	$1{,}736\,641\,580\,409\,436\,36 \times 10^{-4}$	$1{,}6 \times 10^{-2}$

Table 6.3 – Difference of the numerical solution to the analytic values of Equation 6.5 – element Q8.

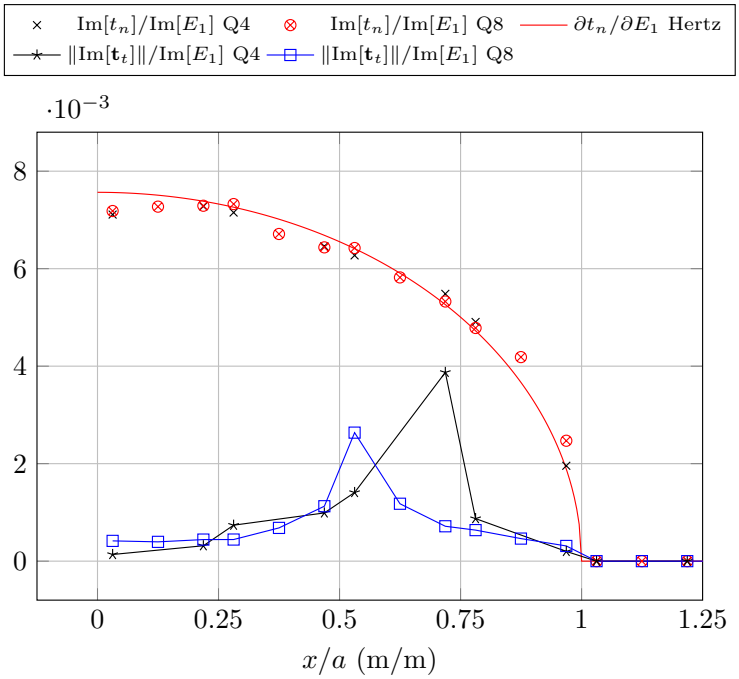

Figure 6.9 – Sensitivity of the normal and tangential contact tractions to the variation of $E_{(1)}$.

6.3 Contact shape sensitivity in anisotropic structures

The example analyzed in this section consists of a flat specimen being indented by a parabolic cylinder with curvature described by $z = x^2$ as depicted in Figure 6.10a. We list the problem dimensions and data in Table 6.4. The material properties for the flat

specimen are considered those of the Nickel crystal at [100] orientation (Table 6.4).

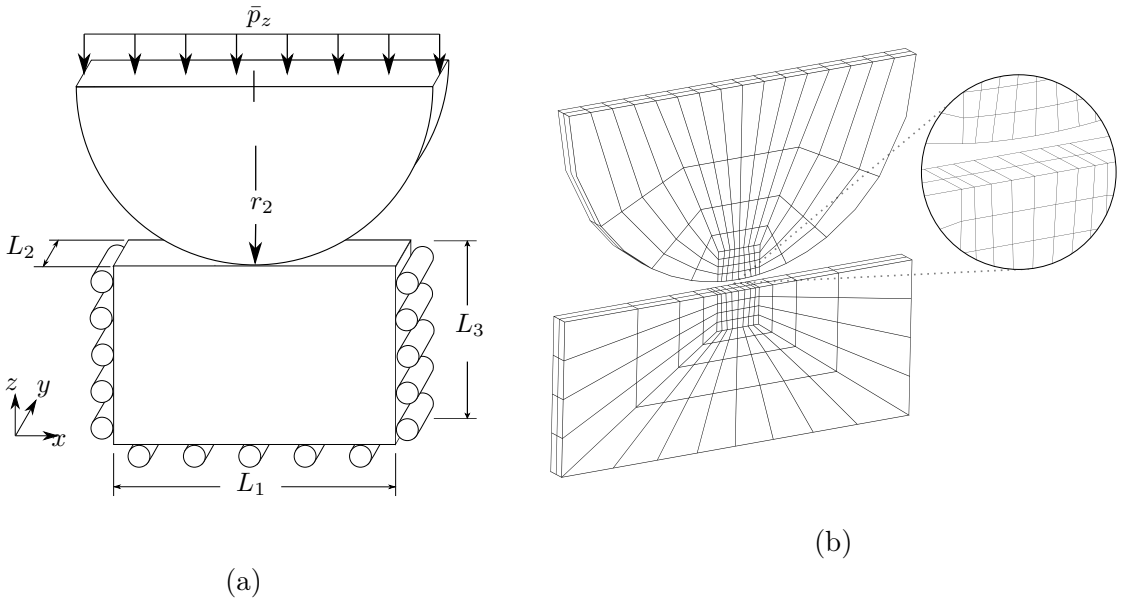

Figure 6.10 – (a) Problem description and (b) mesh used on the flat specimen / cylinder contact example.

The mesh used for the flat region and cylinder has 292 quadratic 8-node elements each and are shown in Figure 6.10b. The contact region semi-width measures 60mm and has five elements. The offset used on the discontinuous elements was $a = 12.5\%$. This discretization results in 7584 DOF, being 576 related to the gap equations and the contact restrictions.

Prescribed tractions $\bar{t}_z$ on the upper face of the half-cylinder were applied. To ensure plane strain conditions on the x_2 direction symmetry boundary conditions were applied. This configuration allows for a comparison with the analytical solution from Hwu and Fan, 1998. This solution is also found in Batra and Jiang, 2008. The friction coefficient used in this example was $\mu = 0.10$.

The boundary conditions were applied on a single load step and the initial parameters used on the line search were $q = 1.10$, $\beta = 0.90$, and $\sigma = 0.20$. The penalization used on the augmented variables was $r_n = r_t = 0.70$.

In Figure 6.11, we show the normal component of the contact tractions λ_n normalized with the maximum Hertz pressure p_0, as well as the norm of tangential tractions divided by the friction coefficient, $\|\boldsymbol{\lambda}_t\|/(p_0\mu)$. These values come from a line of points close to the plane of symmetry xz, with constant y. The normal tractions and the ana-

Table 6.4 – Sphere on Sphere contact problem parameters and results from the hertz solution.

r_1	500	mm	Cylinder radius at $x = 0$
L_1	1000	mm	Flat specimen width
L_2	180	mm	Flat specimen and cylinder depth
L_3	400	mm	
μ	0.10		Coulomb friction
$\bar{t}_z$	$1{,}6 \times 10^{-4}$	Pa	Pressure applied on the top sphere
p_0	$8{,}04 \times 10^{-2}$	Pa	Maximum hertz contact pressure [Hwu and Fan, 1998]
a	50	mm	Contact area semi-width

lytical solution has an excellent agreement.

As the materials in this problem have similar stiffness and Poisson ratio, there are subdued tangential tractions, and almost no slippage occurs at the contact region. This effect is also found in the Nickel-Steel combination. Although the normalization is different, the normal tractions present no noticeable difference. On the other hand, the tangential tractions present noticeable differences in distribution for different materials.

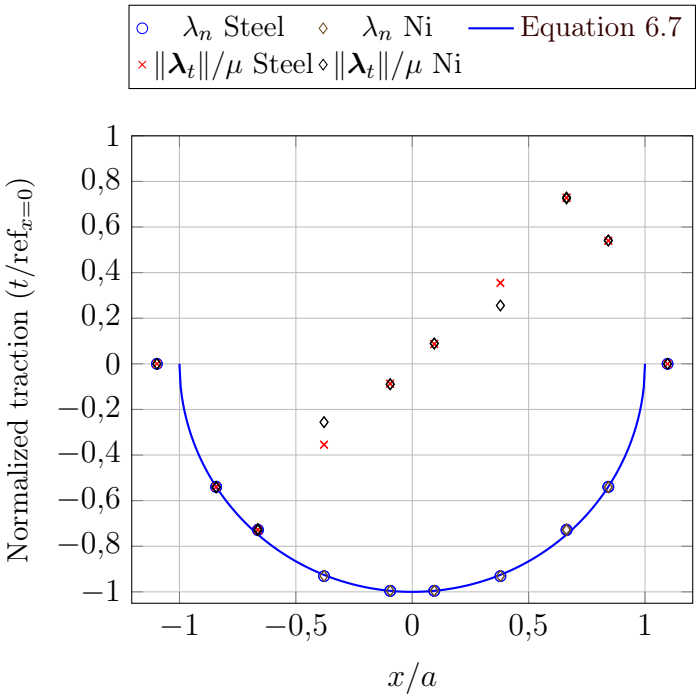

Figure 6.11 – Normal and tangential traction over the possible contact region.

The complex step was appended to the radial position of the nodes, i.e., $\hat{\mathbf{h}} = \mathbf{X}/R \cdot \Delta$, where $\Delta = 1e - 30$. The normal contact traction sensitivity was analyzed. The comparison for the normal traction is done with the analytical solution found in Tafreshi,

2009, which one can obtain by differentiating the pressure solution with respect to the cylinder radius R, resulting in:

$$\frac{\partial p(x)}{\partial R} = \frac{1}{p(x)} \left(\frac{\pi\, x^2 - R\, \mathrm{S}_1\, Y}{\pi\, R^3\, {\mathrm{S}_1}^2} \right), \tag{6.6}$$

where,

$$p(x) = \frac{2Y}{\pi a} \sqrt{1 - \frac{x^2}{a^2}}, \quad a = \sqrt{\frac{2Y\, S_1 R}{\pi}}, \tag{6.7}$$

Y is the total force applied at the cylinder. The material stiffness S_1 for the cubic symmetry, considering plane strain, can be obtained by:

$$S_1 = -\mathrm{Re}\left\{ \frac{b_{22}}{2\mathrm{i}} \left[\frac{1}{\mu_1} - \frac{1}{\bar{\mu}_1} + \frac{1}{\mu_2} - \frac{1}{\bar{\mu}_2} \right] \right\}, \quad b_{22} = \frac{1-\nu^2}{E}, \tag{6.8}$$

and μ_1, μ_2 and its complex conjugates $\bar{\mu}_1, \bar{\mu}_2$, are the characteristic equation complex roots (see, e.g., Chen, 1969, Tafreshi, 2009). Figure 6.12 shows the numerical contact traction shape sensitivity results. The derivative for the normal components agrees with the analytic solution.

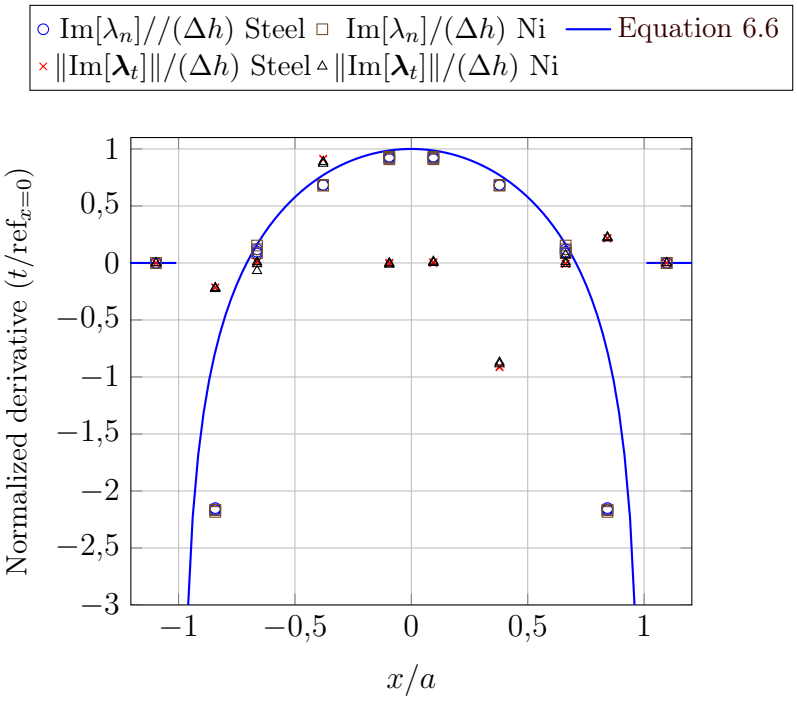

Figure 6.12 – Sensitivity of the contact traction to variation of the cylinder radius R.

Close to the edge of contact is possible to observe a singularity which is well reproduced by the numerical solution. Notice also that the tangential and normal sensitivities approach zero close to the same point. Is also possible to notice the tangential sensitiv-

ities are higher in the stick region, where these tractions can increase their values to a much higher value, whether this is not possible in the slip regions, where their values are already being limited by the Coulomb friction. Notice also that their values has different signs, which means they decrease their magnitude on the slip region, while increasing in the stick part.

6.3.1 Subsurface shear stress and shape sensitivity

Using the same problem configuration of Figure 6.10, we study contact stress behavior in known machine component design problems, resembling tooth contact in gear transmissions or contact paths in ball bearings. Stresses obtained along the symmetry plane of the flat specimen for isotropic and rotated cubic materials (Nickel crystal aligned with the x, y, z axes - and then rotated from 5° to 45° around the y axis.) are plotted in Figure 6.13.

These results show that the depths at which the maximum shear stresses occur are not the same for the different angles of rotation of cubic materials, and their peaks may vary as much as 15%. When the rotated cubic material is analyzed, the maximum shear stress happened much closer to the surface than the other two materials. This effect is particularly important for modern machine component design for the reduction of this order of stress in a fatigue dependent problem may drastically change the component life. The present methodology has potential to explore the optimization of material orientation such that this difference becomes higher, or to investigate how the depth of maximum shear stress can be increased to mitigate the chances of cracks growing towards the contact surface. These results are in good agreement with the ones found in another analytical study from Chen, 1969 for the copper cubic crystal.

Due to its nature, maximum normal stresses always happen on the contact surface and are compressive type [Johnson, 1987].Contact stresses evidently play an important role in the failure of brittle materials, as well as in the friction and wear characterization of the components. However, one important aspect of regarding the fatigue life of ductile materials subjected to contact conditions is the occurrence of the maximum shear stress below the contact surface. Figure 6.14 shows the plots of the maximum shear stress (τ) normalized by the contact stress (p_0) along the depth of the semi-infinite solid (z/a) pressed by the cylinder.

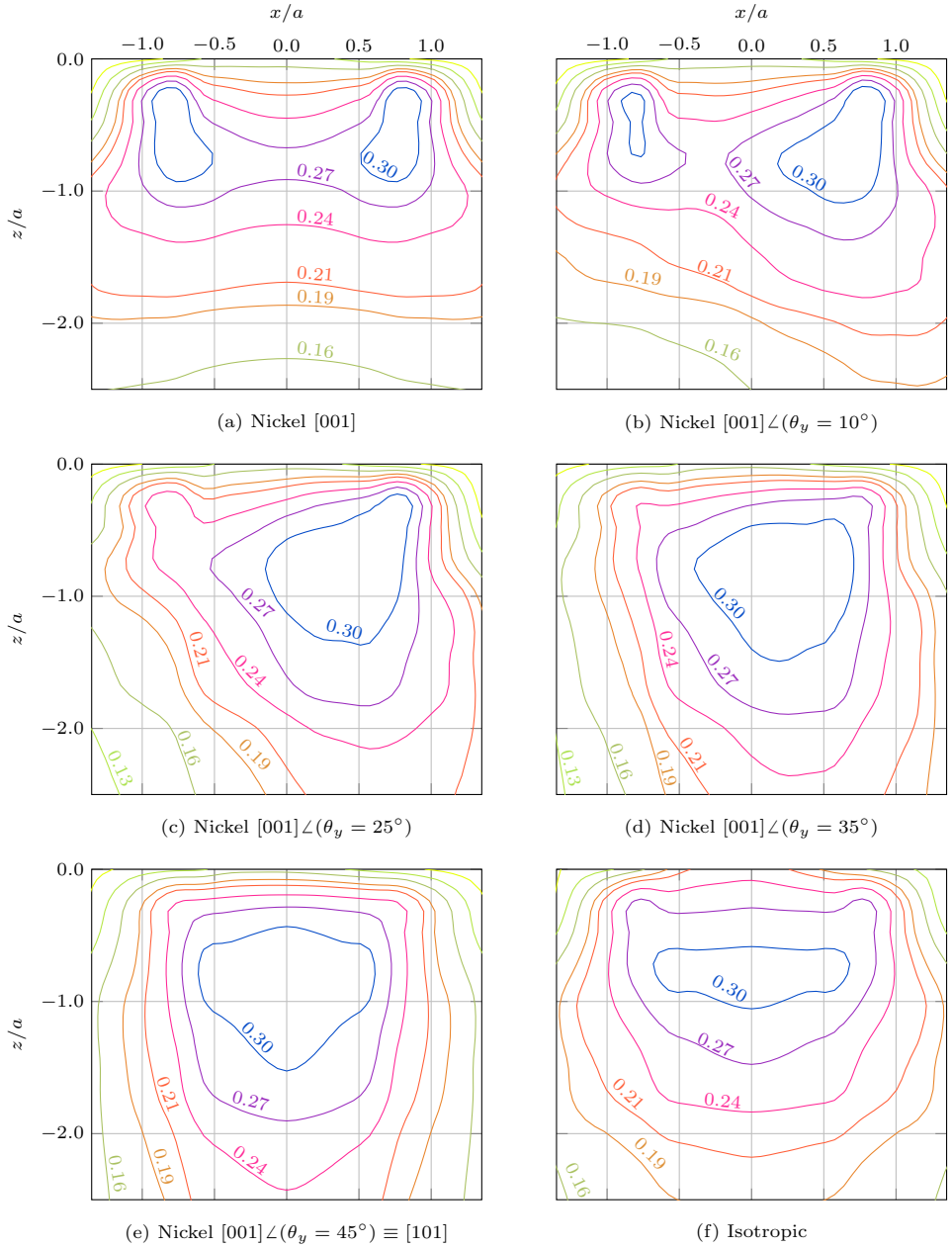

(a) Nickel [001]

(b) Nickel [001]$\angle(\theta_y = 10°)$

(c) Nickel [001]$\angle(\theta_y = 25°)$

(d) Nickel [001]$\angle(\theta_y = 35°)$

(e) Nickel [001]$\angle(\theta_y = 45°) \equiv$ [101]

(f) Isotropic

Figure 6.13 – Distribution of maximum shear stress normalized with the maximum contact pressure τ_{max}/p_0 at the x, z plane, below the contact area on the flat specimen. Material rotation in degrees around the y-axis.

Figure 6.15 shows the resultant shape derivative at the same lateral position as Figure 6.14. This represents $\partial\tau_1/\partial R$, the maximum shear stress τ_1 sensitivity to the variation of the indenter radius R. As the design variable which was already incremented for the previous shape derivative example, obtained from the same computational results from the ones which generated Figures 6.11 and 6.12, i.e., only one analysis was performed for

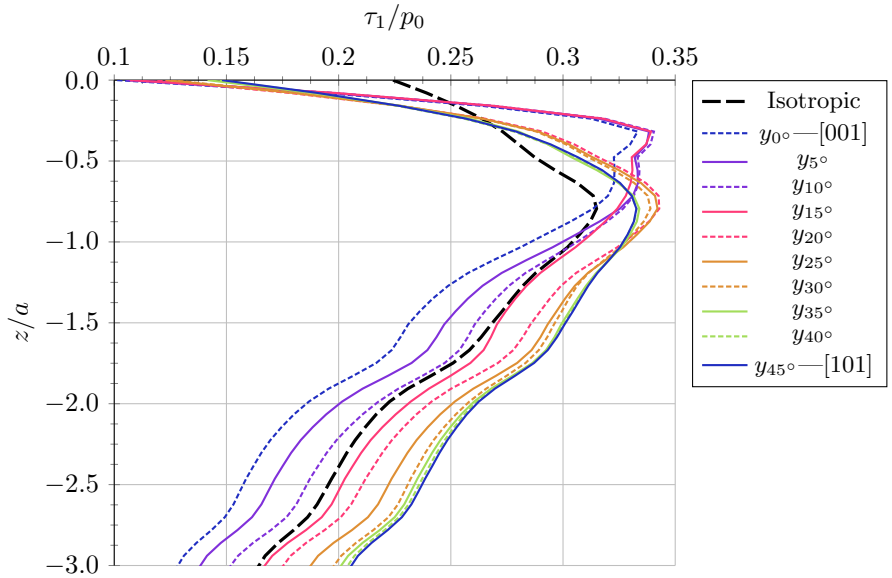

Figure 6.14 – Maximum shear stress along the depth of the flat specimen.

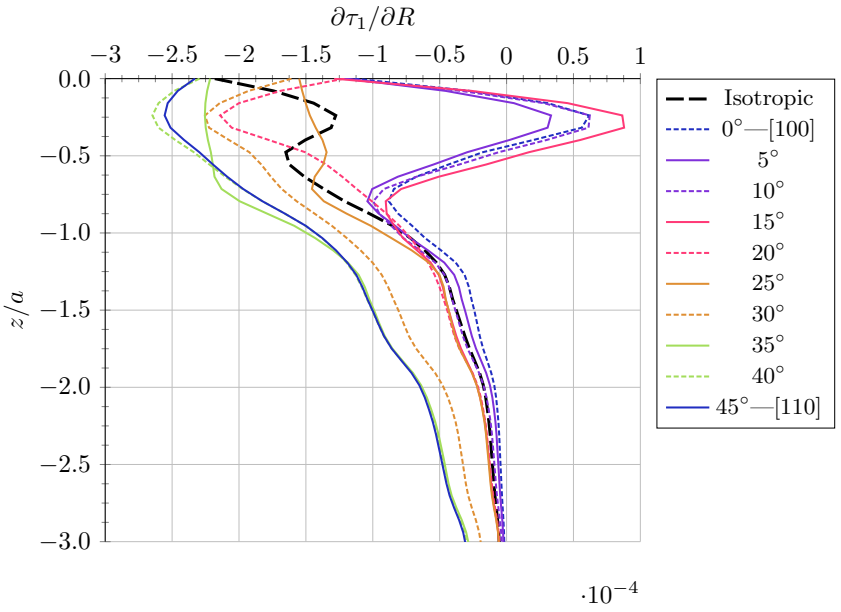

Figure 6.15 – Shape sensitivity to the indenter radius, for the maximum shear stress τ_1 throughout the depth z of the flat specimen, at the x position where it is maximum.

each material configuration. This study shows that the maximum shear stress sensitivity on the indenter shape shows variations for different rotations of the cubic material. More importantly, none of them behave equal or close to the isotropic material, emphasizing the differences between these materials and their application.

6.4 Indentation of a half-space with an orthotropic coating

In the industry, one very often finds problems involving thin layered materials. Their analysis can be troublesome with the FEM, due to the possible high aspect ratio found in these problems, which means that the size of the problem can build up exponentially [Hou et al., 2018]. Although common sense is that the BEM is interesting for problems where the volume is considerably greater than the surface area, the opposite also holds. In thin domains the BEM is also an interesting method; Usually, a 3D FEM discretization of the problem needs a high number of elements along the thickness to converge. The only drawbacks appearing at thin regions in the context of the 3D BEM formulation resides at the integration. Especially if the element size is beyond an order of magnitude larger than the thickness, this indeed triggers near-singularities in some integrals. This theme was subject of extensive research in this field. Quadrature to cancel near-singularities are found in Hayami and Matsumoto, 1994. Special formulations which allow near zero thickness also were also studied, e.g., Liu, 1998, Liu, 2000, Luo et al., 2000, and Zhang et al., 2011.

To provide another comparison case, which can evaluate many aspects of the proposed framework, let us consider a half-space coated by a thin layer, indented by a rigid spherical tip, Figure 6.16a. The mesh for this setting is found in Figure 6.16b. This mesh configuration, using 4×4 elements along the possible contact area, and 2 elements along the outer direction, resulted in $1{,}152 \times 10^3$, 2.688, and $7{,}68 \times 10^2$ DOF for the substrate, coating, and indenter regions, respectively. After the contact assembly with additional equations resulted in 5.376 unknowns.

Table 6.5 lists the geometric properties for this example problem. Firstly, we can assess the performance of a considerably thin layer under contact conditions. Also, in this same case, we can evaluate the correctness of the half-space consideration under the BEM framework.

In this analysis we consider both half space and coating anisotropic with properties listed in Table 6.6. The spherical indenter is isotropic with elastic stiffness $E^{\text{ind}} = 10^7 E_3^{(\text{c})}$, i.e., several orders of magnitude stiffer than the coating.

Although the indenter material is unrealistic, this example serves as an application example and for validation purposes. In this problem, we need to employ both contact and subregion formulations, i.e., the indenter-coating interface is modeled using the contact

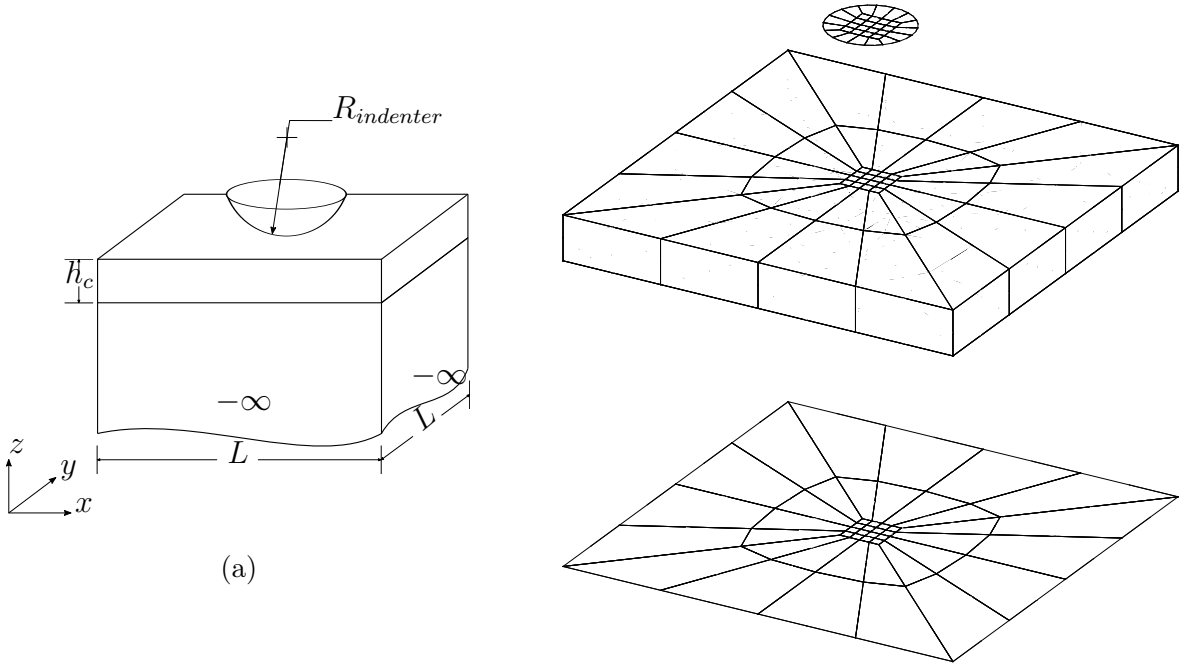

(a)

(b)

Figure 6.16 – (a) Setting for the coating indentation. (b) BEM Mesh used in this problem.

system, Equation 5.49 and the compatibility between coating and half-space is enforced as described in Equation 5.35.

This problem has been thoroughly studied in many works in the literature, but the solution is not straightforward, and many alternatives exist to overcome the singularities existent. Very recently, Hou et al., 2018, proposed a closed form solution for the special case of a transversely isotropic coated material, which could have been used as reference, but the authors did not provide sufficient data to translate the non-dimensional plots in their work, which makes impossible to reproduce the results therein. The comparison case is provided by the work Bagault et al., 2013. Figure 6.17, depicts a FEM mesh used by Bagault, 2013, to validate this problem.

Figure 6.18 shows the results for the normal traction at the indentation area. Unfortunately, the reference does not present the traction acting at the interface, which is

Table 6.5 – Geometric properties of the coating problem.

Coating thickness [μm]	h_c	1.5
Indenter tip radius [μm]	$R_i = 10h_c$	15
Mesh contact area size (Hertz) [μm]	a_{M}	0.5
Mesh specimen [μm]	$L = 10a_c$	6.675
Anisotropic contact area radius	a_c	$0.89a_H$
Indentation depth [μm]	d_{H}	0.0132
Reference contact area radius (Hertz) [μm]	a_{H}	0.5
Reference max. contact pressure [MPa]	p_0	$2{,}7983 \times 10^{-3}$
Reference indentation force [N]	P_z	$1{,}4652 \times 10^{-3}$
Coulomb friction coefficient	μ	0.00

Table 6.6 – Orthotropic material properties used in the coating problem.

	Coating	Substrate
$E_1 = E_2$	120 GPa	60 GPa
E_3	240 GPa	120 GPa
$\nu_{23} = \nu_{32}E_3/E_2$	0.3	0.3
$\nu_{13} = \nu_{31}E_3/E_1$	0.3	0.3
$\nu_{12} = \nu_{21}E_2/E_1$	0.3	0.3
$G_1 = G_2 = G_3$	46GPa	23.25GPa

of utmost importance for this example. The total solution times for our coating problem was around 240 seconds for the boundary element method with complex step (CS-BEM) approach. The total solution time with the FD scheme took 300 seconds. Also, notice that the times reported in Bagault et al., 2013, are relatively high to obtain one converged solution (more than 6 hours for the layered anisotropic model). For a semi-analytic solution, which is more restrictive, and demands considerable programming effort, as opposed to the general numerical model presented here, which can represent very complex geometries; shows that the BEM can be a fast and essential alternative to these methods.

As the intent of our methodology is to provide a shape sensitivity tool, which can be used not only in optimization procedures, we propose to evaluate the interfacial tractions shape sensitivity to the coating thickness variation.

In this case the parameter sensitivity chosen was the coating thickness, more specifically, the distance to the outer surface of the interface. This parameter is important as

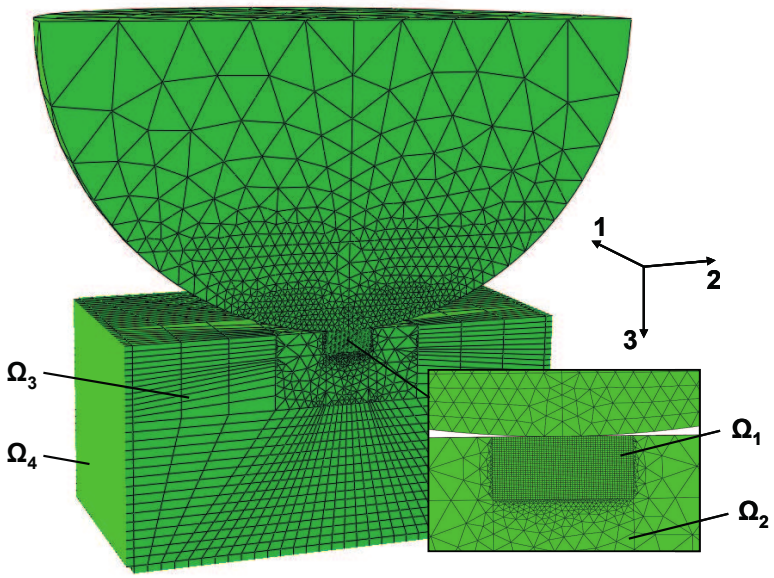

Figure 6.17 – Finite element mesh found in literature dealing with same problem [Source: Bagault, 2013].

wear can occur in the coating, and this can lead to debonding or tear of the coating. This parameter serve as an application example for problems involving coated structures under contact, which usually suffer from friction and wear, it is not uncommon to have a large variation of the coating thickness through the lifespan of industrial components. Such analysis can serve as an end-of-life assessment as well as a failure predictive one, provided it is used in combination with well-known failure criteria. The CS and FD increments the coating in the negative z axis direction, simulating an increase in the coating thickness.

Figure 6.20 shows the sensitivities of the interfacial tractions to the variation of the coating thickness. It is possible to observe that both methodologies provide visually the same result. In general, an increase in thickness results in a reduction of the normal traction at the interface, as is seen in the plot. For the case of tangential traction, which depend directly on the relative stiffness of the materials and on the thickness of the coating, there is no way to empirically determine the result for this problem, it is only possible to interpret the resulting sensitivity. At the center region, below the contact zone, the sensitivity is null, and it increases to a maximum value at around 1.0 and 1.5 times the contact area. In contrast with Figure 6.19, the tangential traction sensitivity has a similar behavior to the traction itself, but with opposite sign, which means that they are being reduced with the increase in the coating thickness. This traction is one

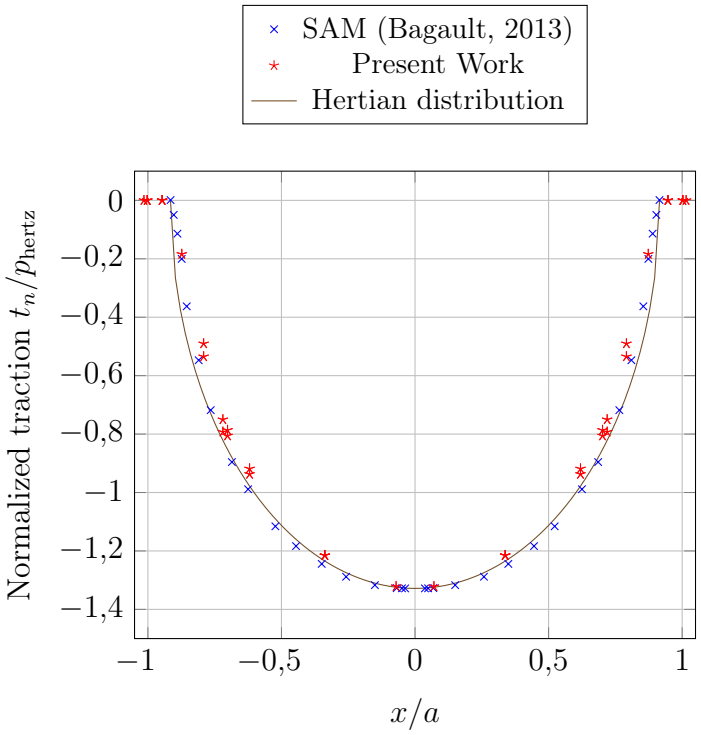

Figure 6.18 – Normal contact traction at the surface of the coating $z = 0$.

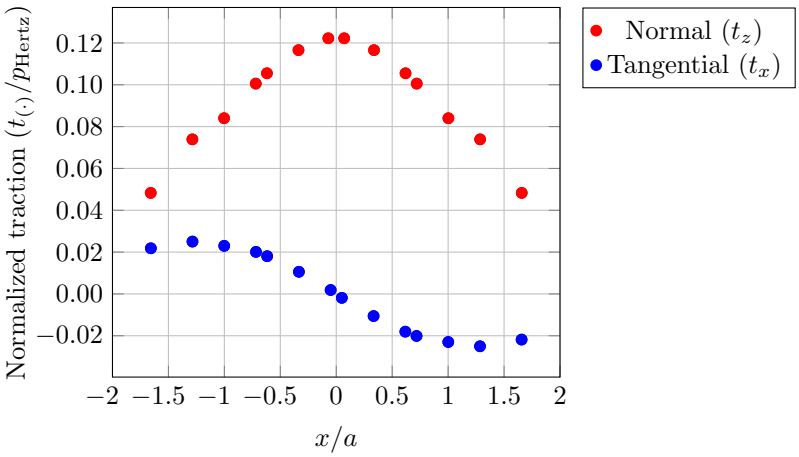

Figure 6.19 – Normal and tangential traction at the interface between the coating and substrate, i.e., $z = -h$.

of the components of the shear stress tensor, which typically increases below the contact surface, and reach a maximum value at some distance from it. The negative sensitivity indicates that the maximum shear stress is located above the interface.

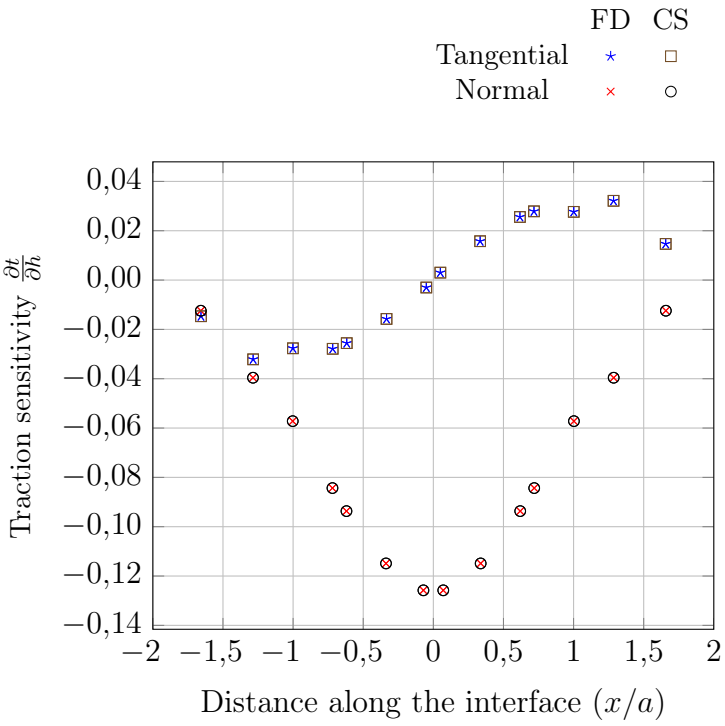

Figure 6.20 – Shape sensitivities for the interface tractions at $z = -h$.

6.5 Sensitivity analysis of a Dovetail type contact assembly

In the case of turbo-jet and turbo-fan type engines, it is necessary to use nickel-based superalloys with a solidification technique which provides a monolithic crystal, excluding the inter-granular slip at high temperatures [Langston, 2015]. This characteristic effectively reduces creep phenomena, increasing the fatigue life of the components, and is the reason for the use of single-crystal blades. On the other hand, as we showed later, it is known that the stress in cubic materials is highly dependent on the indentation direction in relation to the crystallographic planes. Therefore, we propose to perform a shape sensitivity study on a dovetail joint commonly found in turbine blades, providing an industrial application example for the proposed methodology, which has contact and anisotropic material. Notice that, although the single crystal blades commonly employ a different geometric connection style, the problem geometry used is the one depicted in Figure 6.21, the same as found in the works of Papanikos et al., 1998 and of Vale et al., 2012, which provide a comparison case. We analyze contact stress distribution and the design sensitivity of isotropic and anisotropic materials under the same geometry.

Rotor and blade thickness in direction y is 10mm, while the rotor section angle

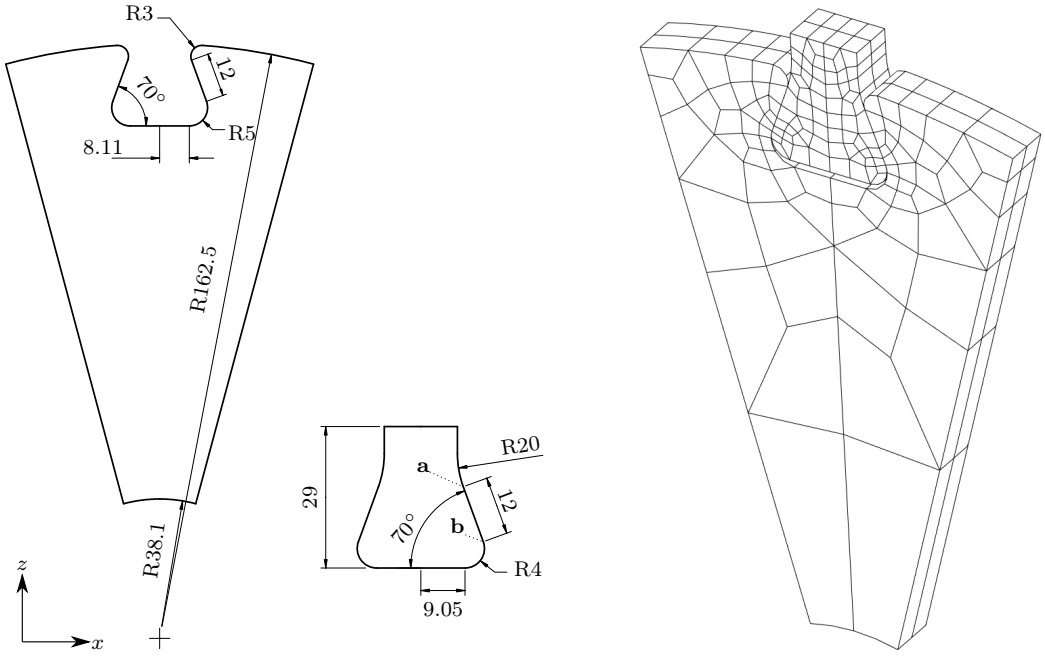

Figure 6.21 – (a) Rotor and Blade geometry and interest points at contact patch (dimensions in mm), and (b) Quadratic element mesh for the problem.

is of 30 degrees, as the number of blades is 12. To ensure the rotational symmetry we apply a displacement restriction at the normal direction of the element coordinate axis, using a rotation matrix similarly to the ones employed in the contact traction matrices. The rotor and blade y displacement was constrained to provide enough constraints in this direction. To simplify this study, we apply a concentrated force at the blade center of mass, avoiding domain mesh generation. The employed formulation for concentrated domain forces is due to Beer et al., 2008. This force was calculated considering the blade volume $v = 5663\text{mm}^3$, its center of mass position $\mathbf{x} = [0, 0, 12.86]$ plus the distance to the rotor center of rotation $\mathbf{x}_{\text{blade}} = [0, 0, 141.4]$, which results in $\mathbf{x} = [0, 0, 154.26]$. The angular speed is equal to 1000rpm.

The material densities are $\rho_{\text{Ti—}_6\text{Al—}_4\text{V}} = 4429\text{kg/m}^3$, $\rho_{\text{Ni}} = 8900\text{kg/m}^3$. The elastic properties for the isotropic analysis is the same as found in Papanikos et al., 1998, whose elastic constants are $E = 114$ GPa, $\nu = 0.33$. In the case of cubic Nickel stiffness tensor, the non-zero elastic constants in Voigt notation are $C_{11} = C_{22} = C_{33} = 252$ GPa, $C_{23} = C_{13} = C_{12} = 152$ GPa, $C_{44} = C_{55} = C_{66} = 123$ GPa.

Figure 6.22 depicts the equivalent Von Mises stress along the contact line $\{\mathbf{a}, \mathbf{b}\}$ at the blade edge. The considered contact length is $r = \|\mathbf{x} - \mathbf{a}\|$, the distance from the start of the plane contact region, i.e., from the end of the top rounding radius in the direction of the blade bottom. Results from Vale et al., 2012 are included as a validation standpoint for this problem configuration. In this figure, it is possible to observe an excellent agreement of the BEM results with the reference ones in most of the contact patch.

Also, notice that although the cubic Ni presents similar results, the stress rises toward point **b**, and is 24% higher near this point.

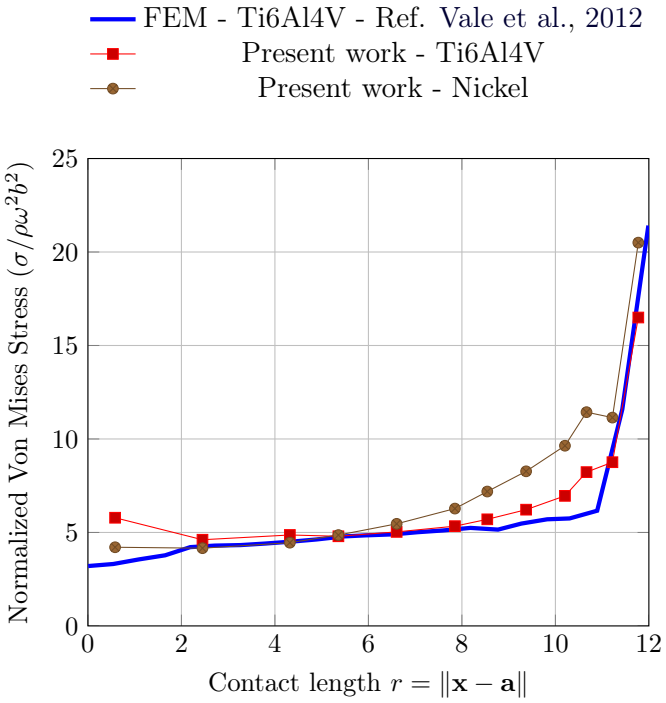

Figure 6.22 – Von Mises Stress along the dovetail conatct interface, line $\{\mathbf{a}, \mathbf{b}\}$.

Shape sensitivity was analyzed in a design velocity approach, i.e., a continuous function which modifies the boundary position along the width (x direction), starting at the blade height $h = 16.6$mm which is the height of point **a** relative to the bottom of the blade. The following velocity function was devised,

$$v(x, z) = -\frac{x}{w}\left(\frac{z_0 - z}{h}\right)^3 \Delta w \tag{6.9}$$

where x and z are the position of the mesh nodes being incremented, $w = 13.05$mm is the blade semi-width, $z_0 = 16.6$mm, and Δw is the step size. Figure 6.23a depicts the

resulting mesh increment scheme.

Figure 6.23b compares the shape sensitivity obtained with CS method and by FD of the Von-Mises stress along the contact patch. It also shows the sensitivity results for the isotropic blade case, in which one can observe that the cubic blade material is nearly three times more sensitive to the shape modification velocity function employed.

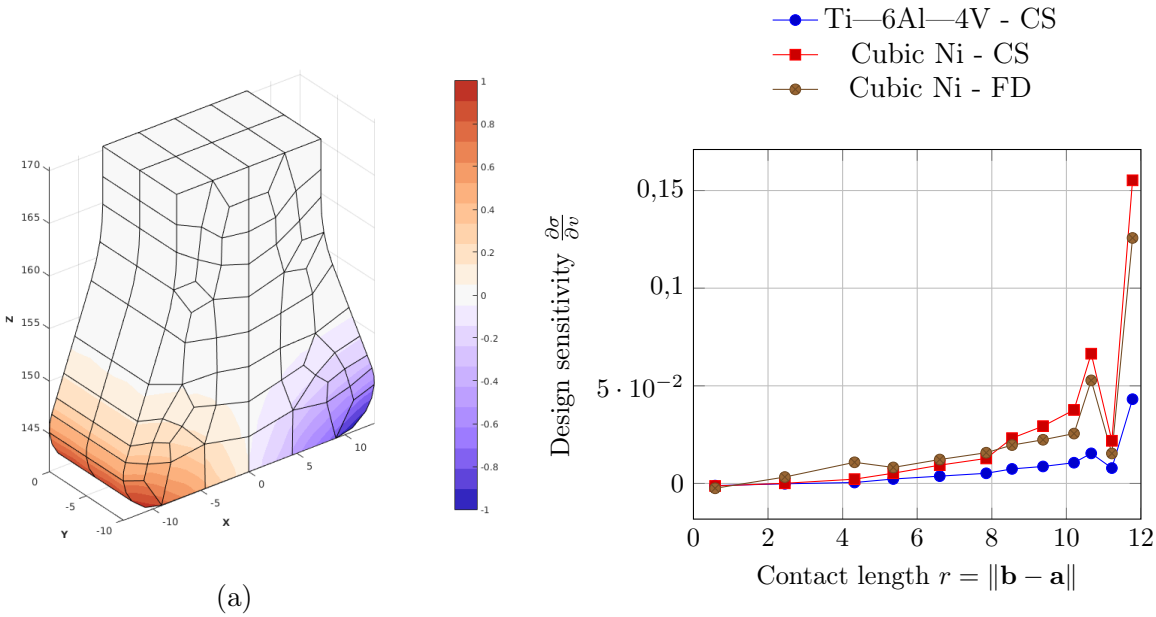

(a) (b)

Figure 6.23 – (a) Relative increment along the blade shape performed by the design variation function, Equation 6.9. (b) Sensitivity to the Design variation function, Equation 6.9.

Finally, in order to show the reliability of the CS method, we perform a convergence test similar to Figure 6.9, depicted in Figure 6.24, whose values are listed in Table 6.7. For a Δw around 1×10^{-3} the CS results stabilizes and maintains the same value. The FD scheme does not result in the same sensitivity for any of the step sizes tested, which shows the method suffers drastically from a mix of truncation and cancellation error. A similar convergence behavior has been found by Martins et al., 2001, on a different application example comparing these two methodologies.

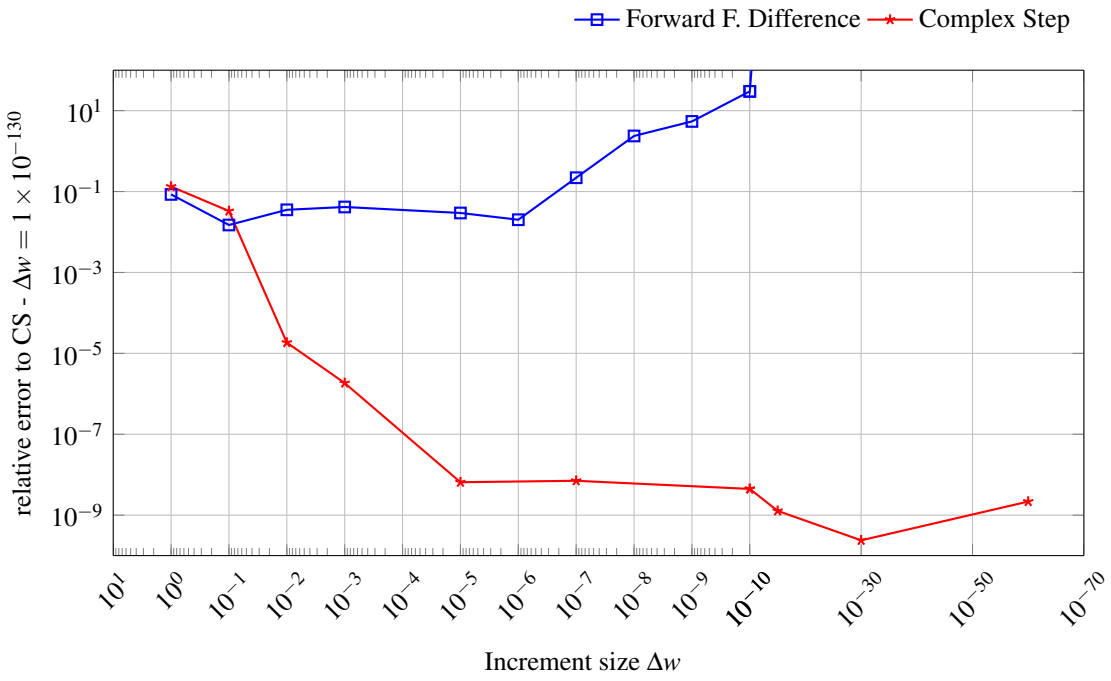

Figure 6.24 – Sensitivity at $r = 11.77$mm, as function of the increment size for FD and CS.

Table 6.7 – Sensitivity at $r = 11.77$mm for FD and CS.

Δw	Real increment	Complex Increment
10^{0}	0,240 195 6	0,288 047 4
10^{-1}	0,140 336 8	0,122 226 5
10^{-2}	0,119 859 7	0,155 260 0
10^{-3}	0,113 702 6	0,155 239 7
10^{-5}	0,125 716 9	0,155 241 5
10^{-6}	0,175 360 9	0,155 241 5
10^{-7}	−0,064 407 2	0,155 241 5
10^{-8}	2,523 026 5	0,155 241 5
10^{-9}	5,572 664 6	0,155 241 5
10^{-10}	30,166 487 1	0,155 241 5
10^{-11}	−1835,777 174 7	0,155 241 5
10^{-15}	—	0,155 241 5
10^{-30}	—	0,155 241 5
10^{-60}	—	0,155 241 5
10^{-130}	—	0,155 241 5

7 CONCLUSION AND DISCUSSION

This work has presented the following topics, namely contributions, in which we achieve the main objectives of this work successfully:

1. A general Fourier series representation of the Green's function for Magneto Electro Elastic materials, based on a newly developed non-degenerate MEE Green's function as a collaboration of this work. This representation is general as it can also represent the Piezo Electric, Piezo Magnetic, or the purely Elastic, Electric or Magnetic cases, because it is directly based on the Fourier series coefficients, and uses a non-degenerate Green's function, which works for any anisotropic symmetry.

2. A numerical shape sensitivity framework for elastic anisotropic materials, based on an anisotropic BEM formulation and the complex step (CS) method, also capable of analyzing contact shape sensitivity on these problems. The application of the CS method is only possible due to the real-valued Green's function presented in the first topic.

Relative to the first topic, one can perform the following closure comments:

- The presented results for the non-degenerate anisotropic magneto electro elastic (MEE) Green's function allow us to conclude that the proposed approach is stable and free of degeneracies, providing an excellent framework for the computation of Fourier coefficients.

- The newly proposed Fourier series approach takes full advantage of the intrinsic characteristics of the Green's function and needs fewer terms to obtain the same relative error when compared with the original reference, providing a two-fold reduction. This reduction provides a faster algorithm with an optimum convergence rate for the Green's function and its derivatives on boundary element method (BEM).

- It was presented an analysis of the Fourier series coefficients integration, not seen before in the literature. The previously cited number of Gauss quadratures in previous works was found not sufficiently converged in the present study, which raises a question about the influence of the numerical integration of the high order terms in the solution convergence, which is discussed in the next topic.

- In the *solution convergence* analysis presented, it was noticed that if the high order terms are not correctly integrated, their later use in the solution can degrade the solution quality. Also, it was noticed that the Fourier series is limited in precision, which can be directly related to the difficulty in the integration of higher-order terms. Nonetheless, the results found indicate that the Fourier series can represent the solutions with errors in the same order as found between the degenerate and non-degenerate solution. These errors are also many orders less than the accuracy in material stiffness provided by experimental data, which should be taken into consideration whenever possible.

- The convergence presented for the Green's function and its derivatives provides more insight on the approximation of these functions by the present approach. This analysis has never been performed in the literature, and therefore, provides quantitative data for future application of this methodology.

- A study regarding the anisotropic index was also carried out, to verify if the variation of this material characteristic can negatively influence the approximation of the Green's function. In that sense, we found no direct influence, and the least accurate case found at intermediate values of the anisotropic index range.

In the second part of this work, the conclusions can be summarized into the following topics:

- In Chapter 4, the shape sensitivity analysis using the CS was validated through a cantilever beam bending problem, which has an analytical solution. A convergence study was performed for this purpose, considering isotropic and anisotropic elastic materials, in this case, a cubic configuration. As was already mentioned, the cubic symmetry has no closed-form Green's function for a Zener index different from 1. This problem is useful to assess anisotropy influence the final BEM solution, in which similar behavior was found for this problem.

- Our Green's function implementation based on Fourier series yields accurate enough results with less computational cost than the Stroh's formalism approach from Buroni et al., 2011, which, allied with our proposed improvements, has provided an efficient BEM implementation for the analysis of anisotropic elasticity. These

performance improvements should be more significant for the case of piezo electric (PE), piezo magnetic (PM), and MEE materials, in which our approach will avoid even larger eigenvalue problem solutions.

- In Chapter 6, we solved Hertzian and Non-Hertzian contact problems, and both material and shape sensitivities were analyzed. The anisotropic material sensitivities are not possible to be directly evaluated the using the CS method, because the Green's functions are dependent on complex algebra, so we evaluated an example considering isotropic material, whose results were in excellent agreement with the analytical solution. For that matter, the authors have developed a framework that should result in a forthcoming article.

- In the cylinder-flat case, we showed that the subsurface shear stress sensitivity for anisotropic materials is extremely dependent on the indentation direction relative to the crystallographic planes, and analyzed the position at which maximum values occur as well as its variation. As this problem solution exists, we were able to validate the results on the contact area, in which the CS-BEM approach agreed with the analytical solution not only for sensitivity but also for the contact traction, which is also a key aspect in its further application on optimization problems.

- The anisotropic coating case provides another application example for which analytical solutions are still emerging with limitations. This case also shows considerably less meshing effort with the BEM. Even the semi-analytical method reported in the literature is of limited use, and its implementation is of high complication. In this case, shape sensitivity was evaluated at the interface of the coating, where debonding can occur in severe conditions. The sensitivity results for the CS method were in good agreement with finite differentiation (FD).

- In the last case analyzed, the dovetail connection, we showed one of the BEM advantages, which is the capability of reproducing stress concentrations and discontinuities, without resorting to extreme mesh refinement. Although the boundary conditions applied are not the same, the results agreed with the literature in an equivalent loading scenario. After this validation example, a configuration using monolithic cubic crystal was considered for the blade, and the resulting stress distribution for this anisotropic material was found considerably different from the

isotropic configuration. This study reveals an important contribution and continuation path for this work. In the case of sensitivity, the results are even more different, with the maximum value being than three times higher than that found on the isotropic material. Also, the results shown for the CS and FD convergence showed that FD cannot achieve the same sensitivity values — this points out the CS method is indeed an excellent analysis tool, and their advantages fully compensate its computational cost.

We also conclude in this work that indeed, the CS method is an extremely robust and accurate numerical method to approximate sensitivities in conjunction with the BEM. Its application in contact problems has been validated in several examples, which also provided excellent results.

The CS-BEM approach developed in this work is a robust method for contact shape optimization and other related problems requiring the analysis of sensitivities within the contact region with high accuracy and reliability.

7.1 Continuation of this work

The accomplishment of this work provide sensitivity analysis procedures with a variety of engineering applications, such as shape optimization. Also, this serves as a base program for further developments as a general numerical analysis tool.

The so-called analytic methods (implicit differentiation (ID) and material derivative-adjoint variable (MADV)), also have not been employed for sensitivity analysis on 3D contact *involving anisotropic materials* with the BEM. Therefore, this kind of analysis has never been performed. In that sense, the semi-analytic and analytic methods leave a field of research to the continuation of this work.

The continuation of this work has many other possible applications and improvements, related to the Green's function and development of BEM software, and on engineering application.

- Final implementation and validation of the BEM code for the MEE case, and perform shape and material sensitivity analysis also for these problems.
- Implementation of internal results for displacement and stress, as well as their sensitivities to change in geometry.

- Development of a semi-analytic sensitivity scheme based on the CS for fast optimization procedures.
- Implementation of domain forces to reproduce the centrifugal load conditions more correctly.
- Shape optimization of the dovetail connection for isotropic and cubic configurations.
- Study of fretting fatigue-related problems, including optimization, using the current implementation.
- Inclusion of adhesion law on the contact algorithm such as Talon and Curnier, 2003.
- Inclusion of large displacements, large deformations, and hyper-elastic material behavior.

7.2 Publications related to this work

During the development of this work, the following articles were published in Journals:

Ubessi, C. J. B. and Marczak, R. J. On the solution of 3D frictional contact problems with Boundary Element Method and discontinuous elements using a Generalized Newton Method with line search, **Revista Interdisciplinar de Pesquisa em Engenharia-RIPE**, vol. 2(7), p. 186–198, 2017

Ubessi, C. J. B. and Marczak, R. J. Sensitivity analysis of 3D frictional contact with BEM using complex-step differentiation, **Latin American Journal of Solids and Structures**, vol. 15(10), 2018

Buroni, F. C., Ubessi, C. J. B., Hattori, G., Saez, A., and Marczak, R. J. A fast and non-degenerate scheme for the evaluation of the 3D fundamental solution and its derivatives for fully anisotropic magneto-electro-elastic materials, **Engineering Analysis with Boundary Elements**, vol. 105, p. 94–103, 2019

BIBLIOGRAPHY

Abreu, R., Stich, D., and Morales, J. On the generalization of the complex step method, **Journal of Computational and Applied Mathematics**, vol. 241, p. 84–102, 2013.

Aithal, R., Saigal, S., and Mukherjee, S. Three dimensional boundary element implicit differentiation formulation for design sensitivity analysis, **Mathematical and Computer Modelling**, vol. 15(3), p. 1 – 10, 1991.

Alart, P. and Curnier, A. A Mixed Formulation for Frictional Contact Problems Prone to Newton Like Solution Methods, **Comput. Methods Appl. Mech. Eng.**, vol. 92(3), p. 353–375, 1991.

Alart, P. and Lebon, F. Numerical study of a stratified composite coupling homogenization and frictional contact, **Mathematical and Computer Modelling**, vol. 28(4), p. 273 – 286, 1998.

Alshits, V. I. Darinskii, A. N. and Lothe, J. On the existence of surface waves in half-infinite anisotropic elastic media with piezoelectric and piezomagnetic properties, **Wave Motion**, vol. 16, p. 265–283, 1992.

Andersson, T. **The boundary element method applied to two-dimensional contact problems with friction**. In *Boundary element methods*, pages 239–258. Springer, 1981.

Arakere, N. K., Knudsen, E., Swanson, G. R., Duke, G., and Ham-Battista, G. Subsurface stress fields in face-centered-cubic single-crystal anisotropic contacts, **Journal of engineering for gas turbines and power**, vol. 128(4), p. 879–888, 2006.

Arakere, N. K. and Swanson, G. Fretting Stresses in Single Crystal Superalloy Turbine Blade Attachments , **Journal of Tribology**, vol. 123(2), p. 413–423, 2000.

Ayorinde, E. and Gibson, R. Elastic constants of orthotropic composite materials using plate resonance frequencies, classical lamination theory and an optimized three-mode Rayleigh formulation, **Composites Engineering**, vol. 3(5), p. 395–407, 1993.

Bagault, C. **Mechanical contact for layered anisotropic materials using a semi-analytical method**. PhD thesis, INSA de Lyon, 2013.

Bagault, C., Nélias, D., Baietto, M., and Ovaert, T. Contact analyses for anisotropic half-space coated with an anisotropic layer: Effect of the anisotropy on the pressure distribution and contact area, **International Journal of Solids and Structures**, vol. 50(5), p. 743 – 754, 2013.

Banerjee, P. K. and Butterfield, R. **Boundary element methods in engineering science**. volume 17. McGraw-Hill London, 1981.

Barella, S., Boniardi, M., Cincera, S., Pellin, P., Degive, X., and Gijbels, S. Failure analysis of a third stage gas turbine blade, **Engineering Failure Analysis**, vol. 18(1), p. 386 – 393, 2011.

Barnett, D. M. The precise evaluation of derivatives of the anisotropic elastic Green's functions, **physica status solidi (b)**, vol. 49(2), p. 741–748, 1972.

Barnett, D. M. and Lothe, J. Dislocations and Line Charges in Anisotropic Piezoelectric Insulators, **Phys. Stat. Sol. (b)**, vol. 67, p. 051–018, 1975.

Barone, M. and Yang, R. Boundary integral equations for recovery of design sensitivities in shape optimization, **AIAA journal**, vol. 26(5), p. 589–594, 1988.

Barone, M. and Yang, R. A boundary element approach for recovery of share sensitivities in three-dimensional elastic solids, **Computer Methods in Applied Mechanics and Engineering**, vol. 74(1), p. 69 – 82, 1989.

Batra, R. and Jiang, W. Analytical solution of the contact problem of a rigid indenter and an anisotropic linear elastic layer, **International Journal of Solids and Structures**, vol. 45(22-23), p. 5814–5830, 2008.

Bebendorf, M. and Rjasanow, S. Adaptive Low-rank Approximation of Collocation Matrices, **Computing**, vol. 70(1), p. 1–24, 2003.

Beer, G., Smith, I., and Duenser, C. **The Boundary Element Method with Programming**. Springer Wien, New York, 2008.

Benedetti, I., Milazzo, A., and Aliabadi, M. A fast dual boundary element method for 3D anisotropic crack problems, **International journal for numerical methods in engineering**, vol. 80(10), p. 1356–1378, 2009.

Bharatish, A., Srihari, P. V., Panchal, A., and Narasimhamurthy, H. N. Analysis of Fir Tree Root of Aero-engine Disc Assembly for Simultaneous Optimization of Fretting Characteristics, **Journal of The Institution of Engineers (India): Series C**, vol. , 2018.

Blázquez, A., Mantič, V., and París, F. Application of BEM to generalized plane problems for anisotropic elastic materials in presence of contact, **Engineering Analysis with Boundary Elements**, vol. 30(6), p. 489 – 502, 2006.

Blázquez, A., París, F., and Mantič, V. BEM solution of two-dimensional contact problems by weak application of contact conditions with non-conforming discretizations, **International Journal of Solids and Structures**, vol. 35(24), p. 3259 – 3278, 1998.

Bonnet, M. Differentiability of strongly singular and hypersingular boundary integral formulations with respect to boundary perturbations, **Computational Mechanics**, vol. 19(3), p. 240–246, 1997.

Bonnet, M. Boundary element based formulations for crack shape sensitivity analysis, **Engineering Analysis with Boundary Elements**, vol. 25(4-5), p. 347–362, 2001.

Brandão, P., Infante, V., and Deus, A. Thermo-mechanical modeling of a high pressure turbine blade of an airplane gas turbine engine, **Procedia Structural Integrity**, vol. 1, p. 189 – 196, 2016.

Brebbia, C. A., Telles, J. C. F., and Wrobel, L. C. **Boundary element techniques: theory and applications in engineering**. Springer Science & Business Media, 2012.

Burczyński, T., Kane, J., and Balakrishna, C. Shape design sensitivity analysis via material derivative-adjoint variable technique for 3-D and 2-D curved boundary elements, **International Journal for Numerical Methods in Engineering**, vol. 38(17), p. 2839–2866, 1995.

Burczyński, T., Kane, J., and Balakrishna, C. Comparison of shape design sensitivity analysis formulations via material derivative-adjoint variable and implicit differentiation techniques for 3-D and 2-D curved boundary element, **Computer Methods in Applied Mechanics and Engineering**, vol. 142(1), p. 89 – 109, 1997.

Buroni, F. C., Ortiz, J. E., and Sáez, A. Multiple pole residue approach for 3D BEM analysis of mathematical degenerate and non-degenerate materials, **International Journal for Numerical Methods in Engineering**, vol. 86(9), p. 1125–1143, 2011.

Buroni, F. C. and Sáez, A. Unique and explicit formulas for Green's function in three-dimensional anisotropic linear elasticity, **Journal of Applied Mechanics**, vol. 80(5), p. 051–018, 2013.

Buroni, F. C. and Sáez, A. Three-dimensional Green's function and its derivative for materials with general anisotropic magneto-electro-elastic coupling, **Proceedings of the Royal Society A: Mathematical, Physical and Engineering Sciences**, vol. 466(2114), p. 515–537, 2010.

Buroni, F. C., Ubessi, C. J. B., Hattori, G., Saez, A., and Marczak, R. J. A fast and non-degenerate scheme for the evaluation of the 3D fundamental solution and its derivatives for fully anisotropic magneto-electro-elastic materials, **Engineering Analysis with Boundary Elements**, vol. 105, p. 94–103, 2019.

Bussetta, P., Marceau, D., and Ponthot, J.-P. The adapted augmented Lagrangian method: a new method for the resolution of the mechanical frictional contact problem, **Computational Mechanics**, vol. 49(2), p. 259–275, 2012.

Calvo, E. and Gracia, L. Shape design sensitivity analysis in elasticity using the boundary element method, **Engineering Analysis with Boundary Elements**, vol. 25(10), p. 887–896, 2001.

Camanho, P. and Matthews, F. Bonded metallic inserts for bolted joints in composite laminates, **Proceedings of the Institution of Mechanical Engineers, Part L: Journal of Materials: Design and Applications**, vol. 214(1), p. 33–40, 2000.

Camanho, P. P. and Matthews, F. A progressive damage model for mechanically fastened joints in composite laminates, **Journal of composite materials**, vol. 33(24), p. 2248–2280, 1999.

Campos, L. S., de Albuquerque, É. L., and Wrobel, L. C. An ACA accelerated isogeometric boundary element analysis of potential problems with non-uniform boundary conditions, **Engineering Analysis with Boundary Elements**, vol. 80, p. 108–115, 2017.

Carter, T. J. Common failures in gas turbine blades, **Engineering Failure Analysis**, vol. 12(2), p. 237 – 247, 2005.

Cavalcante, B., Shaterzadeh-Yazdi, M., Sollero, P., Albuquerque, E., and Doca, T. Analysis of a Cattaneo-Mindlin problem using the boundary element method, **Tribology International**, vol. 108, p. 194 – 201, 2017.

Chadwick, P., Vianello, M., and Cowin, S. C. A new proof that the number of linear elastic symmetries is eight, **Journal of the Mechanics and Physics of Solids**, vol. 49(11), p. 2471 – 2492, 2001.

Chen, W. Stresses in some anisotropic materials due to indentation and sliding, **International Journal of Solids and Structures**, vol. 5(3), p. 191 – 214, 1969.

Chen, Z., Xiao, H., Yang, X., and Su, C. Taylor series multipole boundary element-mathematical programming method for 3D multi-bodies elastic contact problems, **International Journal for Numerical Methods in Engineering**, vol. 83(2), p. 135–173, 2010.

Choi, J. H. and Kwak, B. M. Boundary integral equation method for shape optimization of elastic structures, **International Journal for Numerical Methods in Engineering**, vol. 26(7), p. 1579–1595, 1988.

Choi, K. K. **Shape Design Sensitivity Analysis and Optimal Design of Structural Systems**. In Mota Soares, C. A., editor, *Computer Aided Optimal Design: Structural and Mechanical Systems*, pages 439–492, Berlin, Heidelberg. Springer Berlin Heidelberg, 1987.

Chung, D. H. and Buessem, W. R. The Elastic Anisotropy of Crystals, **Journal of Applied Physics**, vol. 38(5), p. 2010–2012, 1967.

Collins, J. A. and Dooner, D. B. **Mechanical design of machine elements and machines: a failure prevention perspective**, 2003.

Cruse, T. A. Numerical Solutions in Three dimensional elastostatics, **International Journal Solids Structures**, vol. 5, p. 1259–1274, 1969.

Davis, T. A. Algorithm 832: UMFPACK V4.3—an Unsymmetric-pattern Multifrontal Method, **ACM Trans. Math. Softw.**, vol. 30(2), p. 196–199, 2004.

Dostál, Z., Friedlander, A., Santos, S., and Malík, J. Analysis of semicoercive contact problems using symmetric BEM and augmented Lagrangians, **Engineering Analysis with Boundary Elements**, vol. 18(3), p. 195 – 201, 1996.

Eberwien, U., Dünser, C., and Moser, W. Efficient calculation of internal results in 2D elasticity BEM, **Engineering analysis with boundary elements**, vol. 29(5), p. 447–453, 2005.

Erman, Z. and Fenner, R. T. Three-dimensional design sensitivity analysis using a boundary integral approach, **International Journal for Numerical Methods in Engineering**, vol. 40(4), p. 637–654, 1997.

Eshelby, J., Read, W., and Shockley, W. Anisotropic elasticity with applications to dislocation theory, **Acta metallurgica**, vol. 1(3), p. 251–259, 1953.

Espinosa, J. V. and Mediavilla, A. F. Boundary element method applied to three dimensional thermoelastic contact, **Engineering Analysis with Boundary Elements**, vol. 36(6), p. 928 – 933, 2012.

Espinosa-Almeyda, Y., López-Realpozo, J., Rodríguez-Ramos, R., Bravo-Castillero, J., Guinovart-Díaz, R., Camacho-Montes, H., and J. Sabina, F. Effects of interface contacts on magneto electro-elastic coupling for fiber reinforced composites, **International Journal of Solids and Structures - INT J SOLIDS STRUCT**, vol. 48, p. 1525–1533, 2011.

Fan, H. **Special Topics in the Theory of Piezoelectricity**. Springer, 2009.

Fancello, E., Haslinger, J., and Feijoo, R. Numerical comparison between two cost functions in contact shape optimization, **Structural Optimization**, vol. 9(1), p. 57–68, 1995.

Fancello, E. A. Topology optimization for minimum mass design considering local failure constraints and contact boundary conditions, **Structural and Multidisciplinary Optimization**, vol. 32, p. 229–240, 2006.

Frederiksen, P. S. Experimental procedure and results for the identification of elastic constants of thick orthotropic plates, **Journal of Composite Materials**, vol. 31(4), p. 360–382, 1997.

Gao, X., Liu, D., and Chen, P. Internal stresses in inelastic BEM using complex-variable differentiation, **Computational Mechanics**, vol. 28(1), p. 40–46, 2002.

Gao, X.-W. and He, M.-C. A new inverse analysis approach for multi-region heat conduction BEM using complex-variable-differentiation method, **Engineering Analysis with Boundary Elements**, vol. 29(8), p. 788 – 795, 2005.

Gaul, L., Kögl, M., and Wagner, M. **Boundary element methods for engineers and scientists: an introductory course with advanced topics**. Springer Science & Business Media, 2013.

Ghaderi-Panah, A. and Fenner, R. A general boundary element method approach to the solution of three-dimensional frictionless contact problems, **Engineering Analysis with Boundary Elements**, vol. 21(4), p. 305 – 316, 1998.

Goldberg, D. What every computer scientist should know about floating-point arithmetic, **ACM Computing Surveys (CSUR)**, vol. 23(1), p. 5–48, 1991.

González, J. A., Park, K., Felippa, C. A., and Abascal, R. A formulation based on localized Lagrange multipliers for BEM–FEM coupling in contact problems, **Computer Methods in Applied Mechanics and Engineering**, vol. 197(6), p. 623–640, 2008.

Guiggiani, M., Krishnasamy, G., Rudolphi, T. J., and Rizzo, F. J. A General Algorithm for the Numerical Solution of Hypersingular Boundary Integral Equations, **Transactions of ASME**, vol. 59, p. 604–614, 1992.

Haslinger, J. **Shape optimization in unilateral boundary value problems**. In *Unilateral Problems in Structural Analysis IV*, pages 51–55. Springer, 1991.

Haslinger, J. Contact shape optimization based on the reciprocal variational formulation, **Applications of Mathematics**, vol. 44(5), p. 321–358, 1999.

Haslinger, J. and Klarbring, A. Shape optimization in unilateral contact problems using generalized reciprocal energy as objective functional, **Nonlinear Analysis: Theory, Methods & Applications**, vol. 21(11), p. 815–834, 1993.

Haslinger, J., Neittaanmäki, P., Tiihonen, T., and Kaarna, A. Optimal shape design and unilateral boundary value problems: Part II, **OPTIMAL CONTROL APPLICATIONS & METHODS**, vol. 9, p. 145–163, 1988.

Hayami, K. and Matsumoto, H. Improvement of quadrature for nearly Singular Integrals in 3D-BEM, **Boundary Element Method**, vol. XIV, p. 201–210, 1994.

Head, A. K. The Galois unsolvability of the sextic equation of anisotropic elasticity, **Journal of Elasticity**, vol. 9(9), p. 9–20, 1979.

Heyliger, P., Ledbetter, H., and Kim, S. Elastic constants of natural quartz, **The Journal of the Acoustical Society of America**, vol. 114(2), p. 644–650, 2003.

Hou, P., Zhang, W., and Chen, J.-Y. Three-dimensional exact solutions of homogeneous transversely isotropic coated structures under spherical contact, **International Journal of Solids and Structures**, vol. 161, p. 136–173, 2018.

Huang, J. H. and Kuo, W.-S. The analysis of piezoelectric/piezomagnetic composite materials containing ellipsoidal inclusions, **Journal of Applied Physics**, vol. 81(3), p. 1378–1386, 1997.

Hwu, C. **Anisotropic elastic plates**. Springer Science & Business Media, 2010.

Hwu, C. and Fan, C. Sliding punches with or without friction along the surface of an anisotropic elastic half-plane, **Quarterly Journal of Mechanics and Applied Mathematics**, vol. 51(1), p. 159–177, 1998.

Jawson, M. A. Integral Equation Methods in Potential Theory. I, **Proceedings Royal Society London**, vol. 275, p. 23–32, 1963.

Jeong, G.-E., Youn, S.-K., and Park, K. Topology optimization of deformable bodies with dissimilar interfaces, **Computers & Structures**, vol. 198, p. 1 – 11, 2018.

John, F. **Plane Waves and Spherical Means Applied to Partial Differential Equations**, 1955.

Johnson, K. L. **Contact mechanics**. Cambridge university press, 1987.

Johnson, K. L., Kendall, K., and Roberts, A. Surface energy and the contact of elastic solids, **Proceedings of the royal society of London. A. mathematical and physical sciences**, vol. 324(1558), p. 301–313, 1971.

Jones, R. M. **Mechanics of Composite Materials**. Scripta Book Company, Washington, 2nd edition, 1999.

Katsikadelis, J. and Kokkinos, F. Analysis of composite shear walls with interface separation, friction and slip using BEM, **International Journal of Solids and Structures**, vol. 30(13), p. 1825 – 1848, 1993.

Kita, E. and Tanie, H. Shape optimization of continuum structures by genetic algorithm and boundary element method, **Engineering Analysis with Boundary Elements**, vol. 19(2), p. 129 – 136, 1997.

Klarbring, A. and Haslinger, J. On almost constant contact stress distributions by shape optimization, **Structural Optimization**, vol. 5, p. 213–216, 1993.

Koff, B. F100-PW-229 higher thrust in same frame size, **Journal of engineering for gas turbines and power**, vol. 111(2), p. 187–192, 1989.

Kočandrle, P. and Koška, P. Three-Dimensional shape optimization approach based on natural design variables and the boundary element method, **The Journal of Strain Analysis for Engineering Design**, vol. 31(5), p. 377–387, 1996.

Langston, L. Technologue Each Blade a Single Crystal, **American Scientist**, vol. 103, p. 30–33, 2015.

Lawry, M. and Maute, K. Level set shape and topology optimization of finite strain bilateral contact problems, **International Journal for Numerical Methods in Engineering**, vol. 113(8), p. 1340–1369, 2018.

Leahy, J. G. and Becker, A. A. A quadratic boundary element formulation for three-dimensional contact problems with friction, **The Journal of Strain Analysis for Engineering Design**, vol. 34(4), p. 235–251, 1999.

Ledbetter, H. and Migliori, A. A general elastic-anisotropy measure, **Journal of Applied Physics**, vol. 100(6), p. 063516, 2006.

Lee, J. J., Kang, D. W., and Kim, T. S. Development of a gas turbine performance analysis program and its application, **Energy**, vol. 36(8), p. 5274 – 5285, 2011.

Lempriere, B. Poisson's ratio in orthotropic materials., **AIAA Journal**, vol. 6(11), p. 2226–2227, 1968.

Li, K. and Qian, X. Isogeometric analysis and shape optimization via boundary integral, **Computer-Aided Design**, vol. 43, p. 1427–1437, 2011.

Lian, H., Kerfriden, P., and Bordas, S. Implementation of regularized isogeometric boundary element methods for gradient-based shape optimization in two-dimensional linear elasticity, **International Journal for Numerical Methods in Engineering**, vol. 106(12), p. 972–1017, 2016.

Lifshitz, I. and Rozentsveig, L. Construction of the Green tensor for the fundamental equation of elasticity theory in the case of unbounded elastically anisotropic medium, **Zh. Eksp. Teor. Fiz**, vol. 17(9), p. 783–791, 1947.

Liu, P., Luo, Y., and Kang, Z. Multi-material topology optimization considering interface behavior via XFEM and level set method, **Computer methods in applied mechanics and engineering**, vol. 308, p. 113–133, 2016.

Liu, Y. Analysis of shell-like structures by the boundary element method based on 3-D elasticity: Formulation and verification, **International Journal for Numerical Methods in Engineering**, vol. 41(3), p. 541–558, 1998.

Liu, Y. On the simple-solution method and non-singular nature of the BIE/BEM - a review and some new results, **Engineering Analysis with Boundary Elements**, vol. 24(10), p. 789–795, 2000.

Liu, Y. **Fast multipole boundary element method: theory and applications in engineering**. Cambridge university press, 2009.

Lovell, M. Analysis of contact between transversely isotropic coated surfaces: development of stress and displacement relationships using FEM, **Wear**, vol. 214(2), p. 165 – 174, 1998.

Luo, J. F., Liu, Y. J., and Berger, E. J. Interfacial stress analysis for multi-coating systems using an advanced boundary element method, **Computational Mechanics**, vol. 24(6), p. 448–455, 2000.

Luo, Y., Li, M., and Kang, Z. Topology optimization of hyperelastic structures with frictionless contact supports, **International Journal of Solids and Structures**, vol. 81, p. 373 – 382, 2016.

Lyness, J. N. and Moler, C. B. Numerical Differentiation of Analytic Functions, **SIAM Journal on Numerical Analysis**, vol. 4(2), p. 202–210, 1967.

Macmillan, P. **Human Development Report 2009: Overcoming Barriers: Hu- man Mobility and Development**, 2010.

Man, K., Aliabadi, M., and Rooke, D. BEM frictional contact analysis: load incremental technique, **Computers & structures**, vol. 47(6), p. 893–905, 1993.

Mantic, V. A new formula for the C-matrix in the Somigliana identity, **Journal of Elasticity**, vol. 33(3), p. 191–201, 1993.

Marczak, R. Optimization of elastic structures using boundary elements and a topological-shape sensitivity formulation, **Latin American Journal of Solids and Structures**, vol. 5(2), p. 99–117, 2008.

Martins, J., Sturdza, P., and Alonso, J. **The connection between the complex-step derivative approximation and algorithmic differentiation**. In *39th Aerospace Sciences Meeting and Exhibit*, page 921, 2001.

Martins, J. R., Sturdza, P., and Alonso, J. J. The complex-step derivative approximation, **ACM Transactions on Mathematical Software (TOMS)**, vol. 29(3), p. 245–262, 2003.

Matsumto, T., Tanaka, M., and Obara, R. Computation of stress intensity factors of interface cracks based on interaction energy release rates and BEM sensitivity analysis, **Engineering Fracture Mechanics**, vol. 65(6), p. 683 – 702, 2000.

Maury, A., Allaire, G., and Jouve, F. Shape optimisation with the level set method for contact problems in linearised elasticity, 2017.

Mijar, A. and Arora, J. An augmented Lagrangian optimization method for contact analysis problems, 1: formulation and algorithm, **Structural and Multidisciplinary Optimization**, vol. 28(2), p. 99–112, 2004.

Moharamian, A., Soltani, S., Rosen, M., Mahmoudi, S., and Morozyuk, T. A comparative thermoeconomic evaluation of three biomass and biomass-natural gas fired combined cycles using organic Rankine cycles, **Journal of Cleaner Production**, vol. 161, 2017.

Morse, L., Khodaei, Z. S., and Aliabadi, M. A multi-fidelity boundary element method for structural reliability analysis with higher-order sensitivities, **Engineering Analysis with Boundary Elements**, vol. 104, p. 183 – 196, 2019.

Mota Soares, C. A., Rodrigues, H. C., and Choi, K. K. Shape Optimal Structural Design Using Boundary Elements and Minimum Compliance Techniques, **Journal of Mechanical Design**, vol. 106(4), p. 518–523, 1984.

Mundstock, D. C. and Marczak, R. J. Boundary element sensitivity evaluation for elasticity problems using complex variable method, **Structural and Multidisciplinary Optimization**, vol. 38(4), p. 423–428, 2009.

Myśliński, A. Level set method for optimization of contact problems, **Engineering Analysis with Boundary Elements**, vol. 32(11), p. 986 – 994, 2008.

Nan, C.-W., Bichurin, M. I., Dong, S., Viehland, D., and Srinivasan, G. Multiferroic magnetoelectric composites: Historical perspective, status, and future directions, **Journal of Applied Physics**, vol. 103(3), p. 031101, 2008.

Niu, C., Zhang, W., and Gao, T. Topology Optimization of Continuum Structures for the Uniformity of Contact Pressures, **Struct. Multidiscip. Optim.**, vol. 60(1), p. 185–210, 2019.

Ostanin, I., Tsybulin, I., Litsarev, M., Oseledets, I., and Zorin, D. Scalable topology optimization with the kernel-independent fast multipole method, **Engineering Analysis with Boundary Elements**, vol. 83, p. 123 – 132, 2017.

Pan, E. Three-dimensional Green's functions in anisotropic magneto-electro-elastic bimaterials, **Zeitschrift für angewandte Mathematik und Physik ZAMP**, vol. 53(5), p. 815–838, 2002.

Pan, E. and Tonon, F. Three-dimensional Green's functions in anisotropic piezoelectric solids, **International Journal of Solids and Structures**, vol. 37(6), p. 943 – 958, 2000.

Pan, E. and Yuan, F. Three-dimensional Green's functions in anisotropic piezoelectric bimaterials, **International Journal of Engineering Science**, vol. 38(17), p. 1939–1960, 2000a.

Pan, E. and Yuan, F. G. Boundary element analysis of three-dimensional cracks in anisotropic solids, **International Journal for Numerical Methods in Engineering**, vol. 48(2), p. 211–237, 2000b.

Pan, Y. and Chou, T. Point force solution for an infinite transversely isotropic solid, **ASME, Transactions, Series E-Journal of Applied Mechanics**, vol. 43, p. 608–612, 1976.

Pang, J.-S. Newton's method for B-differentiable equations, **Mathematics of Operations Research**, vol. 15(2), p. 311–341, 1990.

Papanikos, P., Meguid, S. A., and Stjepanovic, Z. Three-dimensional Nonlinear Finite Element Analysis of Dovetail Joints in Aeroengine Discs, **Finite Elem. Anal. Des.**, vol. 29(3-4), p. 173–186, 1998.

París, F., Foces, A., and Garrido, J. Application of boundary element method to solve three-dimensional elastic contact problems without friction, **Computers & Structures**, vol. 43(1), p. 19 – 30, 1992.

Patterson, C. and Sheikh, M. **Non-Conforming Boundary Elements for Stress Analysis**. In Brebbia, C., editor, *Boundary Element Methods*, volume 3 of *Boundary Elements*, pages 137–152. Springer Berlin Heidelberg, 1981.

Patterson, C. and Sheikh, M. **Interelement Continuity in the Boundary Element Method**. In Brebbia, C., editor, *Basic Principles and Applications*, volume 1 of *Topics in Boundary Element Research*, pages 123–141. Springer Berlin Heidelberg, 1984.

Peillex, G., Baillet, L., and Berthier, Y. Homogenization in non-linear dynamics due to frictional contact, **International Journal of Solids and Structures**, vol. 45(9), p. 2451 – 2469, 2008.

Phan, A. V., Gray, L. J., and Kaplan, T. Residue approach for evaluating the 3D anisotropic elastic Green's function: multiple roots, **Engineering analysis with boundary elements**, vol. 29(6), p. 570–576, 2005.

Ranganathan, S. I. and Ostoja-Starzewski, M. Universal elastic anisotropy index, **Physical Review Letters**, vol. 101(5), p. 055504, 2008.

Rani, S., Agrawal, A. K., and Rastogi, V. Failure analysis of a first stage IN738 gas turbine blade tip cracking in a thermal power plant, **Case Studies in Engineering Failure Analysis**, vol. 8, p. 1 – 10, 2017.

Reyhani, M. R., Alizadeh, M., Fathi, A., and Khaledi, H. Turbine blade temperature calculation and life estimation - a sensitivity analysis, **Propulsion and Power Research**, vol. 2(2), p. 148 – 161, 2013.

Rizzo, F. J. An Integral Equation Approach to Boundary Value Problems of Classical Elastostatics, **Quarterly of applied Mathematics**, vol. 25, p. 83–95, 1967.

Rodríguez, R. Q., Tan, C. L., Sollero, P., and Albuquerque, E. L. Analysis of 3D Anisotropic Solids Using Fundamental Solutions Based on Fourier Series and the Adaptive Cross Approximation Method, **CMES: Computer Modeling in Engineering & Sciences**, vol. 102(5), p. 359–372, 2014.

Rodríguez-Tembleque, L. and Abascal, R. A FEM-BEM Fast Methodology for 3D Frictional Contact Problems, **Comput. Struct.**, vol. 88(15-16), p. 924–937, 2010.

Rodríguez-Tembleque, L. and Abascal, R. Fast FE–BEM algorithms for orthotropic frictional contact, **International Journal for Numerical Methods in Engineering**, vol. 94(7), p. 687–707, 2013.

Rodríguez-Tembleque, L., Abascal, R., Sáez, A., and Buroni, F. C. Numerical study of polymer composites in contact, **Comput. Model. Eng. Sci**, vol. 96(2), p. 131–158, 2013a.

Rodríguez-Tembleque, L., Buroni, F., Sáez, A., and Aliabadi, M. 3D coupled multi-field magneto-electro-elastic contact modelling, **International Journal of Mechanical Sciences**, vol. 114, p. 35–51, 2016.

Rodríguez-Tembleque, L., Buroni, F. C., Abascal, R., and Sáez, A. 3D frictional contact of anisotropic solids using BEM, **European Journal of Mechanics-A/Solids**, vol. 30(2), p. 95–104, 2011.

Rodríguez-Tembleque, L., Buroni, F. C., Abascal, R., and Sáez, A. Analysis of FRP composites under frictional contact conditions, **International Journal of Solids and Structures**, vol. 50(24), p. 3947 – 3959, 2013b.

Rodríguez-Tembleque, L., González, J. Á., and Abascal, R. **A formulation based on the localized Lagrange multipliers for solving 3D frictional contact problems using the BEM** . In Arriaga, M. C. S., Bundschuh, J., and Dominguez-Mota, F. J., editors, *Numerical Modeling of Coupled Phenomena in Science and Engineering: Practical Use and Examples*, chapter 29, pages 359–370. CRC Press, Oxford, 2008.

Rodríguez-Tembleque, L. and Abascal, R. A 3D FEM–BEM rolling contact formulation for unstructured meshes, **International Journal of Solids and Structures**, vol. 47(2), p. 330 – 353, 2010.

Rodríguez-Tembleque, L., Abascal, R., and Aliabadi, M. A boundary element formulation for wear modeling on 3D contact and rolling-contact problems, **International Journal of Solids and Structures**, vol. 47(18), p. 2600 – 2612, 2010.

Rodríguez-Tembleque, L., García-Sánchez, F., and Sáez, A. Crack Surface Frictional Contact Modeling in Fractured Fiber-Reinforced Composites, **Journal of Multiscale Modelling**, vol. 10(01), p. 1841005, 2019.

Rokhlin, V. Rapid solution of integral equations of classical potential theory, **Journal of Computational Physics**, vol. 60(2), p. 187–207, 1985.

Ruiz, C. and Nowell, D. **Designing against fretting fatigue in aeroengines**. In Fuentes, M., Elices, M., Martín-Meizoso, A., and Martínez-Esnaola, J., editors, *Fracture Mechanics: Applications and Challenges*, volume 26 of *European Structural Integrity Society*, pages 73 – 95. Elsevier, 2000.

Rus, G. and Gallego, R. Boundary integral equation for inclusion and cavity shape sensitivity in harmonic elastodynamics, **Engineering analysis with boundary elements**, vol. 29(1), p. 77–91, 2005.

Rus, G. and Gallego, R. Solution of identification inverse problems in elastodynamics using semi-analytical sensitivity computation, **Engineering Analysis with Boundary Elements**, vol. 31(4), p. 343 – 360, 2007.

Rüberg, T. and Schanz, M. An alternative collocation boundary element method for static and dynamic problems, **Computational Mechanics**, vol. 44(2), p. 247–261, 2009.

Sahli, A., Guemmour, M., Kebdani, S., Boutchicha, D., and Rahmani, O. Independent meshing of contact surfaces in 3D boundary element method contact analysis, **Journal of Applied Mechanics**, vol. 75(4), p. 041021, 2008.

Saigal, S., Aithal, R., and Kane, J. Semianalytical structural sensitivity formulation in boundary elements, **AIAA journal**, vol. 27(11), p. 1615–1621, 1989.

Sales, M. A. and Gray, L. Evaluation of the anisotropic Green's function and its derivatives, **Computers & Structures**, vol. 69(2), p. 247 – 254, 1998.

Segond, D. and Tafreshi, A. Stress analysis of three-dimensional contact problems using the boundary element method, **Engineering Analysis with Boundary Elements**, vol. 22(3), p. 199 – 214, 1998.

Sfantos, G. and Aliabadi, M. A boundary element sensitivity formulation for contact problems using the implicit differentiation method, **Engineering Analysis with Boundary Elements**, vol. 30(1), p. 22 – 30, 2006.

Sfantos, G. and Aliabadi, M. A boundary element formulation for three-dimensional sliding wear simulation, **Wear**, vol. 262(5), p. 672 – 683, 2007.

Shi, L., Wei, D.-s., Wang, Y.-r., Tian, A.-m., and Li, D. An investigation of fretting fatigue in a circular arc dovetail assembly, **International Journal of Fatigue**, vol. 82, p. 226–237, 2016.

Shiah, Y., Tan, C., and Wang, C. Efficient computation of the Green's function and its derivatives for three-dimensional anisotropic elasticity in BEM analysis, **Engineering Analysis with Boundary Elements**, vol. 36(12), p. 1746–1755, 2012.

Shiah, Y. C., Hematiyan, M. R., and Chen, Y. H. Regularization of the Boundary Integrals in the Bem Analysis of 3D Potential Problems, **Journal of Mechanics**, vol. 29, p. 385–401, 2013.

Simo, J. and Laursen, T. An augmented Lagrangian treatment of contact problems involving friction, **Computers & Structures**, vol. 42(1), p. 97–116, 1992.

Soares, C., Rodrigues, H., Faria, L., and Haug, E. Optimization of the Geometry of Shafts Using Boundary Elements, **Journal of Mechanisms Transmissions and Automation in Design**, vol. 106, 1984.

Soh, A. K., , and Liu, J. On the Constitutive Equations of Magnetoelectroelastic Solids, **Journal of Intelligent Material Systems and Structures**, vol. 16(7-8), p. 597–602, 2005.

Squire, W. and Trapp, G. Using Complex Variables to Estimate Derivatives of Real Functions, **SIAM Review**, vol. 40(1), p. 110–112, 1998.

Stroh, A. Dislocations and cracks in anisotropic elasticity, **Philosophical magazine**, vol. 3(30), p. 625–646, 1958.

Stroh, A. N. Steady State Problems in Anisotropic Elasticity, **Journal of Mathematics and Physics**, vol. 41(1-4), p. 77–103, 1962.

Strömberg, N. An augmented Lagrangian method for fretting problems, **European Journal of Mechanics-A/Solids**, vol. 16, p. 573–593, 1997.

Strömberg, N. **Topology Optimization of Orthotropic Elastic Design Domains with Mortar Contact Conditions**. In Schumacher, A., Vietor, T., Fiebig, S., Bletzinger, K.-U., and Maute, K., editors, *Advances in Structural and Multidisciplinary Optimization*, pages 1427–1438, Cham. Springer International Publishing, 2018.

Strömberg, N. and Klarbring, A. Topology optimization of structures in unilateral contact, **Structural and Multidisciplinary Optimization**, vol. 41(1), p. 57–64, 2010.

Sveshnikov, A. G. and Tikhonov, A. N. **The theory of functions of a complex variable**. Mir Publishers, 1971.

Symm, G. T. Iintegral Equation Methods in Potential Theory. II, **Proceedings Royal Society London**, vol. 275, p. 33–46, 1963.

Synge, J. L. and Rheinboldt, W. The hypercircle in mathematical physics, **Physics Today**, vol. 10, p. 45, 1957.

Tafreshi, A. Optimum Shape Design of Composite Structures Using Boundary-Element Method, **Aiaa Journal - AIAA J**, vol. 43, p. 1349–1359, 2005.

Tafreshi, A. Shape design sensitivity analysis with respect to the positioning of features in composite structures using the boundary element method, **Engineering Analysis with Boundary Elements**, vol. 30(1), p. 1 – 13, 2006.

Tafreshi, A. Shape sensitivity analysis of composites in contact using the boundary element method, **Engineering Analysis with Boundary Elements**, vol. 33(2), p. 215 – 224, 2009.

Tafreshi, A. Efficient evaluation of the J2-integral using the boundary element crack shape sensitivities, **Theoretical and Applied Fracture Mechanics**, vol. 76, p. 9 – 16, 2015.

Tafreshi, A. Computation of the Jk-integrals for bimaterial interface cracks using boundary element crack shape sensitivities, **Theoretical and Applied Fracture Mechanics**, vol. 82, p. 77–87, 2016.

Tai, K. and Fenner, R. T. Optimum shape design and positioning of features using the boundary integral equation method, **International Journal for Numerical Methods in Engineering**, vol. 39(12), p. 1985–2003, 1996.

Talon, C. and Curnier, A. A model of adhesion coupled to contact and friction, **European Journal of Mechanics - A/Solids**, vol. 22(4), p. 545 – 565, 2003.

Tan, C., Shiah, Y., and Wang, C. Boundary element elastic stress analysis of 3D generally anisotropic solids using fundamental solutions based on Fourier series, **International Journal of Solids and Structures**, vol. 50(16), p. 2701–2711, 2013.

Telles, J. and Oliveira, R. Third degree polynomial transformation for boundary element integrals: Further improvements, **Engineering Analysis with Boundary Elements**, vol. 13(2), p. 135 – 141, 1994.

Ting, T. C. T. **Anisotropic elasticity: theory and applications**. Number 45. Oxford University Press, 1996.

Ting, T. C. T. and Lee, V.-G. The three-dimensional elastostatic Green's function for general anisotropic linear elastic solids, **The Quarterly Journal of Mechanics and Applied Mathematics**, vol. 50(3), p. 407–426, 1997.

Tonon, F., Pan, E., and Amadei, B. Green's functions and boundary element method formulation for 3D anisotropic media, **Computers & Structures**, vol. 79(5), p. 469 – 482, 2001.

Tserpes, K., Labeas, G., Papanikos, P., and Kermanidis, T. Strength prediction of bolted joints in graphite/epoxy composite laminates, **Composites Part B: Engineering**, vol. 33(7), p. 521 – 529, 2002.

Távara, L., Mantič, V., Ortiz, J., and París, F. Unique real-variable expressions of the integral kernels in the Somigliana stress identity covering all transversely isotropic elastic materials for 3D BEM, **Computer Methods in Applied Mechanics and Engineering**, vol. 225, p. 128 – 141, 2012.

Távara, L., Ortiz, J. E., Mantič, V., and París, F. Unique real-variable expressions of displacement and traction fundamental solutions covering all transversely isotropic elastic materials for 3D BEM, **International Journal for Numerical Methods in Engineering**, vol. 74(5), p. 776–798, 2008.

Ubessi, C. J. B. **Método dos elementos de contorno para elasticidade linear 3D com avaliação direta das integrais singulares**. Master's thesis, Universidade Federal do Rio Grande do Sul, 2014.

Ubessi, C. J. B. and Marczak, R. J. On the solution of 3D frictional contact problems with Boundary Element Method and discontinuous elements using a Generalized Newton Method with line search, **Revista Interdisciplinar de Pesquisa em Engenharia-RIPE**, vol. 2(7), p. 186–198, 2017.

Ubessi, C. J. B. and Marczak, R. J. Sensitivity analysis of 3D frictional contact with BEM using complex-step differentiation, **Latin American Journal of Solids and Structures**, vol. 15(10), 2018.

Ullah, B. and Trevelyan, J. A boundary element and level set based topology optimisation using sensitivity analysis, **Engineering Analysis with Boundary Elements**, vol. 70, p. 80 – 98, 2016.

Ullah, B., Trevelyan, J., and Ivrissimtzis, I. A three-dimensional implementation of the boundary element and level set based structural optimisation, **Engineering Analysis with Boundary Elements**, vol. 58, p. 176 – 194, 2015.

Vale, T. d. O., Villar, G. d. C., and Menezes, J. C. Methodology for structural integrity analysis of gas turbine blades, **Journal of Aerospace Technology and Management**, vol. 4(1), p. 51–59, 2012.

Vandervort, C., Leach, D., and Scholz, M. **Advancements in H Class Gas Turbines for Combined Cycle Power Plants for High Efficiency, Enhanced Operational Capability and Broad Fuel Flexibility**. In *The Future of Gas Turbine Technology, 8th International Gas Turbine Congress*, 2016.

Vogel, S. and Rizzo, F. An integral equation formulation of three dimensional anisotropic elastostatic boundary value problems, **Journal of Elasticity**, vol. 3(3), p. 203–216, 1973.

Vondrák, V., Kozubek, T., Markopoulos, A., and Dostál, Z. Parallel solution of contact shape optimization problems based on Total FETI domain decomposition method, **Structural and Multidisciplinary Optimization**, vol. 42(6), p. 955–964, 2010.

Walston, S., Cetel, A., MacKay, R., OHara, K., Duhl, D., and Dreshfield, R. Joint Development of a Fourth Generation Single Crystal Superalloy, **Proceedings of the International Symposium on Superalloys**, vol. , 2005.

Wang, C. Elastic fields produced by a point source in solids of general anisotropy, **Journal of Engineering Mathematics**, vol. 32(1), p. 41–52, 1997.

Wang, C. and Achenbach, J. D. Three-dimensional time-harmonic elastodynamic Green's functions for anisotropic solids, **Proceedings of the Royal Society of London. Series A: Mathematical and Physical Sciences**, vol. 449(1937), p. 441–458, 1995.

Wang, C.-Y. and Denda, M. 3D BEM for general anisotropic elasticity, **International Journal of Solids and Structures**, vol. 44(22), p. 7073 – 7091, 2007.

Warren, K. C., Lopez-Anido, R. A., Vel, S. S., and Bayraktar, H. H. Progressive failure analysis of three-dimensional woven carbon composites in single-bolt, double-shear bearing, **Composites Part B: Engineering**, vol. 84, p. 266 – 276, 2016.

Weber, W., Kolk, K., Willner, K., and Kuhn, G. **On the Solution of the 3D Crack Surface Contact Problem Using the Boundary Element Method**. In *Key Engineering Materials*, volume 454, pages 11–29. Trans Tech Publ, 2011.

Wei, Y., Zhao, C., Yao, Z., Hauret, P., Li, X., and Kaliske, M. Adjoint design sensitivity analysis and optimization of nonlinear structures using geometrical mapping approach, **Computers & Structures**, vol. 183, p. 1 – 13, 2017.

Wilson, R. and Cruse, T. Efficient implementation of anisotropic three dimensional boundary-integral equation stress analysis, **International Journal for Numerical Methods in Engineering**, vol. 12(9), p. 1383–1397, 1978.

Xie, L., Hwu, C., and Zhang, C. Advanced methods for calculating Green's function and its derivatives for three-dimensional anisotropic elastic solids, **International Journal of Solids and Structures**, vol. 80, p. 261 – 273, 2016.

Xie, L., Zhang, C., and Wang, J. Unified and explicit expressions of three-dimensional Green's functions and their first derivatives for piezoelectric solids with general anisotropy, **International Journal of Solids and Structures**, vol. 155, p. 1 – 14, 2018.

Xue, F., Wang, Z.-X., Zhao, W.-S., Zhang, X.-L., Qu, B.-P., and Wei, L. Fretting fatigue crack analysis of the turbine blade from nuclear power plant, **Engineering Failure Analysis**, vol. 44, p. 299 – 305, 2014.

Yamazaki, K. and Mori, M. Analysis of an Elastic Contact Problem by the Boundary Element Method:(An Approach by the Penalty Function Method), **JSME international journal. Ser. 1, Solid mechanics, strength of materials**, vol. 32(4), p. 508–513, 1989.

Yamazaki, K., Sakamoto, J., and Kitano, M. Three-dimensional shape optimization using the boundary element method, **AIAA Journal**, vol. 32(6), p. 1295–1301, 1994a.

Yamazaki, K., Sakamoto, J., and Takumi, S. Penalty method for three-dimensional elastic contact problems by boundary element method, **Computers & structures**, vol. 52(5), p. 895–903, 1994b.

Yang, Q., Zhou, W., Gai, P., Zhang, X., Fu, X., Chen, G., and Li, Z. Investigation on the fretting fatigue behaviors of Ti-6Al-4V dovetail joint specimens treated with shot-peening, **Wear**, vol. 372-373, p. 81 – 90, 2017.

Yu, C., Shen, G., and Liu, D. Mathematical programming solution for the frictional contact multipole BEM, **Tsinghua Science & Technology**, vol. 10(1), p. 51–56, 2005.

Zener, C. M. and Siegel, S. Elasticity and Anelasticity of Metals., **The Journal of Physical Chemistry**, vol. 53(9), p. 1468–1468, 1949.

Zhang, W. and Niu, C. A linear relaxation model for shape optimization of constrained contact force problem, **Computers & Structures**, vol. 200, p. 53 – 67, 2018.

Zhang, Y.-M., Gu, Y., and Chen, J.-T. Stress analysis for multilayered coating systems using semi-analytical BEM with geometric non-linearities, **Computational Mechanics**, vol. 47(5), p. 493–504, 2011.

APPENDIX A – Derivation of real-valued Fourier series terms

$$H_{jk} = \sum_{m,n=-a}^{a} \lambda_{ij}^{m,n} e^{\mathrm{i}(m\theta+n\phi)} \tag{A.1}$$

$$= \lambda_{ij}^{m,n}(\cos(m\theta+n\phi) + \mathfrak{i}\sin(m\theta+n\phi)) \tag{A.2}$$

$$= (R_{ij}^{m,n} + \mathfrak{i}I_{ij}^{m,n})(\cos(m\theta+n\phi) + \mathfrak{i}\sin(m\theta+n\phi)) \tag{A.3}$$

$$\tag{A.4}$$

It is known that the tensor is real valued, so the imaginary part must vanish,

$$H_{jk} = \mathrm{Re}(+\mathfrak{i}\begin{bmatrix} R_{ij}^{m,n}\cos(m\theta+n\phi) \\ I_{ij}^{m,n}\cos(m\theta+n\phi) \\ R_{ij}^{m,n}\sin(m\theta+n\phi) \end{bmatrix}) \\ +\mathfrak{i}^2 I_{ij}^{m,n}\sin(m\theta+n\phi) \tag{A.5}$$

$$= (R_{ij}^{m,n}\cos(m\theta+n\phi) - I_{ij}^{m,n}\sin(m\theta+n\phi)) \tag{A.6}$$

$$= \begin{array}{l} \mathbf{R}^{(m,n)}\ \cos(m\theta)\ \cos(n\phi) - \\ \mathbf{R}^{(m,n)}\ \sin(m\theta)\ \sin(n\phi) - \\ \mathbf{I}^{(m,n)}\ \cos(m\theta)\ \sin(n\phi) - \\ \mathbf{I}^{(m,n)}\ \sin(m\theta)\ \cos(n\phi) \end{array} \tag{A.7}$$

By $\lambda_{m,n} = \bar{\lambda}_{-m,-n}$, and $\sin(n) = -\sin(-n)$, also, $\cos(m) = \cos(-m)$, is possible to write as

$$H_{jk} = \sum_{m=0}^{\alpha} \begin{bmatrix} 2(\mathbf{R}^{(m,n)} + \mathbf{R}^{(m,-n)})\cos(m\theta)\ \cos(n\phi) - \\ 2(\mathbf{R}^{(m,n)} - \mathbf{R}^{(m,-n)})\sin(m\theta)\ \sin(n\phi) - \\ 2(\mathbf{I}^{(m,n)} - \mathbf{I}^{(m,-n)})\ \cos(m\theta)\ \sin(n\phi) - \\ 2(\mathbf{I}^{(m,n)} + \mathbf{I}^{(m,-n)})\ \sin(m\theta)\ \cos(n\phi) \end{bmatrix} \tag{A.8}$$

By similarity, it is demonstrated by the use of Equations 2.158 and 2.159, the

following equivalence is obtained on the constants for $m, n \neq 0$,

$$4\boldsymbol{\lambda}_{\mathbf{R1}}{}^{(m,n)} = \mathbf{R}^{(m,n)} + \mathbf{R}^{(m,-n)} \tag{A.9}$$

$$4\boldsymbol{\lambda}_{\mathbf{R2}}{}^{(m,n)} = \mathbf{R}^{(m,n)} - \mathbf{R}^{(m,-n)} \tag{A.10}$$

$$4\boldsymbol{\lambda}_{\mathbf{I1}}{}^{(m,n)} = \mathbf{I}^{(m,n)} - \mathbf{I}^{(m,-n)} \tag{A.11}$$

$$4\boldsymbol{\lambda}_{\mathbf{I2}}{}^{(m,n)} = \mathbf{I}^{(m,n)} + \mathbf{I}^{(m,-n)} \tag{A.12}$$

which is sintethically the same as presented in Shiah et al., 2013, apart from the new period in ϕ.

In order to provide a equivalence with the Shiah et al., 2013 formulation, the following relations are brought

$$\tilde{R}^{(m,n)} = 0.5\boldsymbol{\lambda}_{\mathbf{R1}}{}^{(m,n)} \tag{A.13}$$

$$\hat{R}^{(m,n)} = 0.5\boldsymbol{\lambda}_{\mathbf{R2}}{}^{(m,n)} \tag{A.14}$$

$$\hat{I}^{(m,n)} = 0.5\boldsymbol{\lambda}_{\mathbf{I1}}{}^{(m,n)} \tag{A.15}$$

$$\tilde{I}^{(m,n)} = 0.5\boldsymbol{\lambda}_{\mathbf{I2}}{}^{(m,n)} \tag{A.16}$$

APPENDIX B – Period graphs for the Barnett-Lothe tensor for the remaining components of *Material C - MEE*

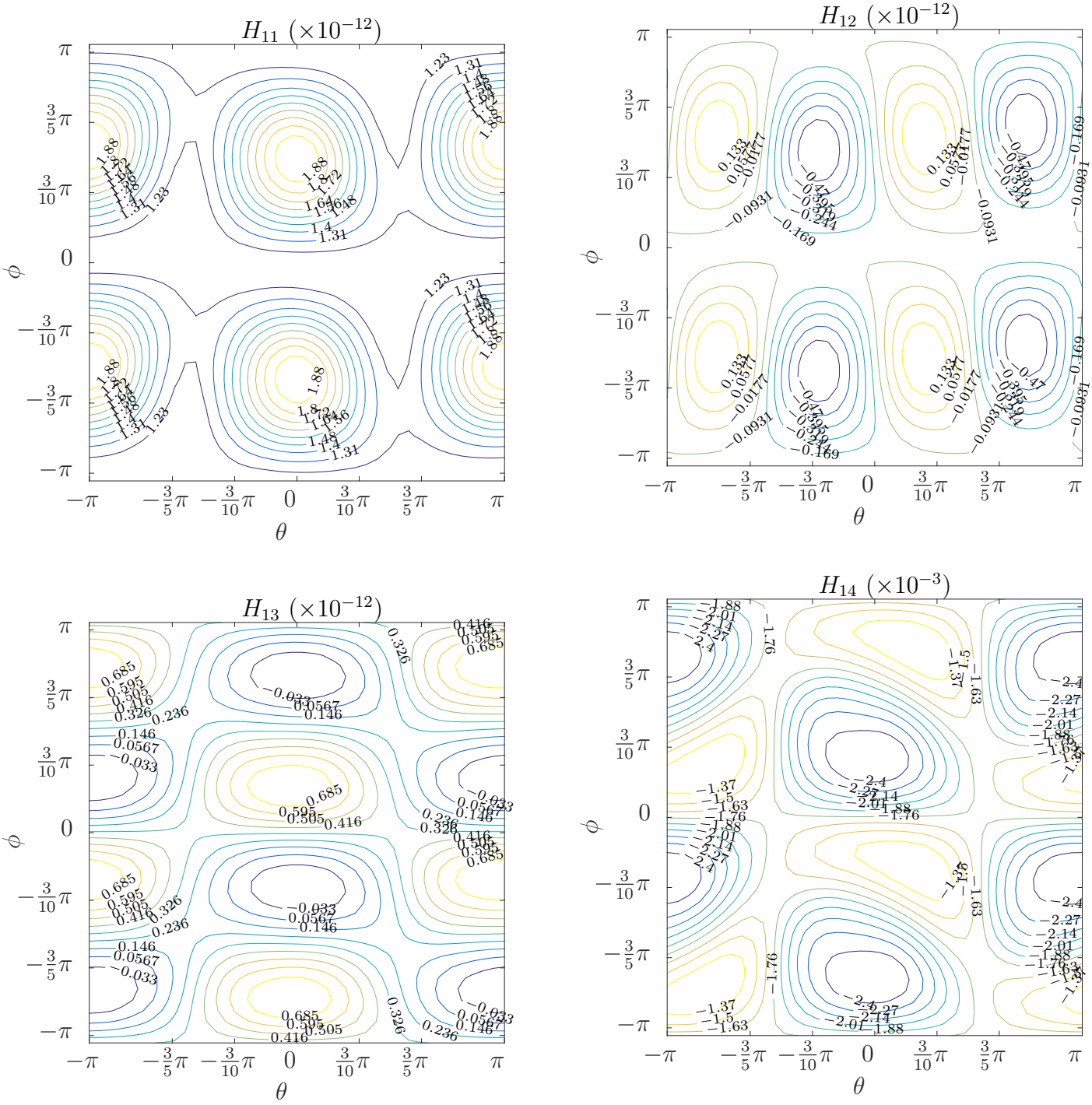

Figure B.1 – The Barnett-Lothe tensor, H_{ij}, $i, j = [1, ..., 5]$, for the *Material C - MEE*, in spherical coordinates.

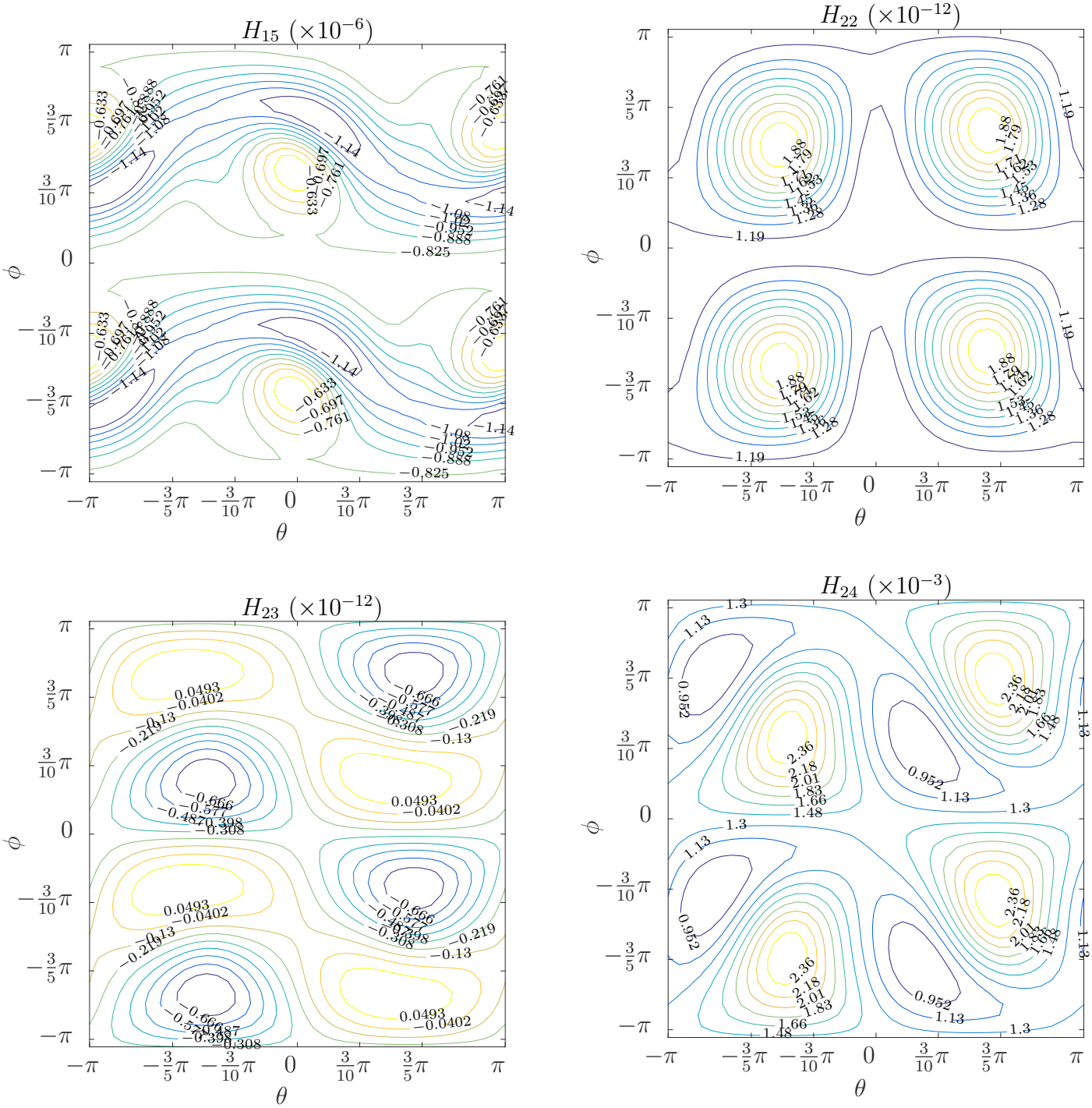

Figure B.2 – The Barnett-Lothe tensor, H_{ij}, $i, j = [1, ..., 5]$, for the *Material C - MEE*, in spherical coordinates.

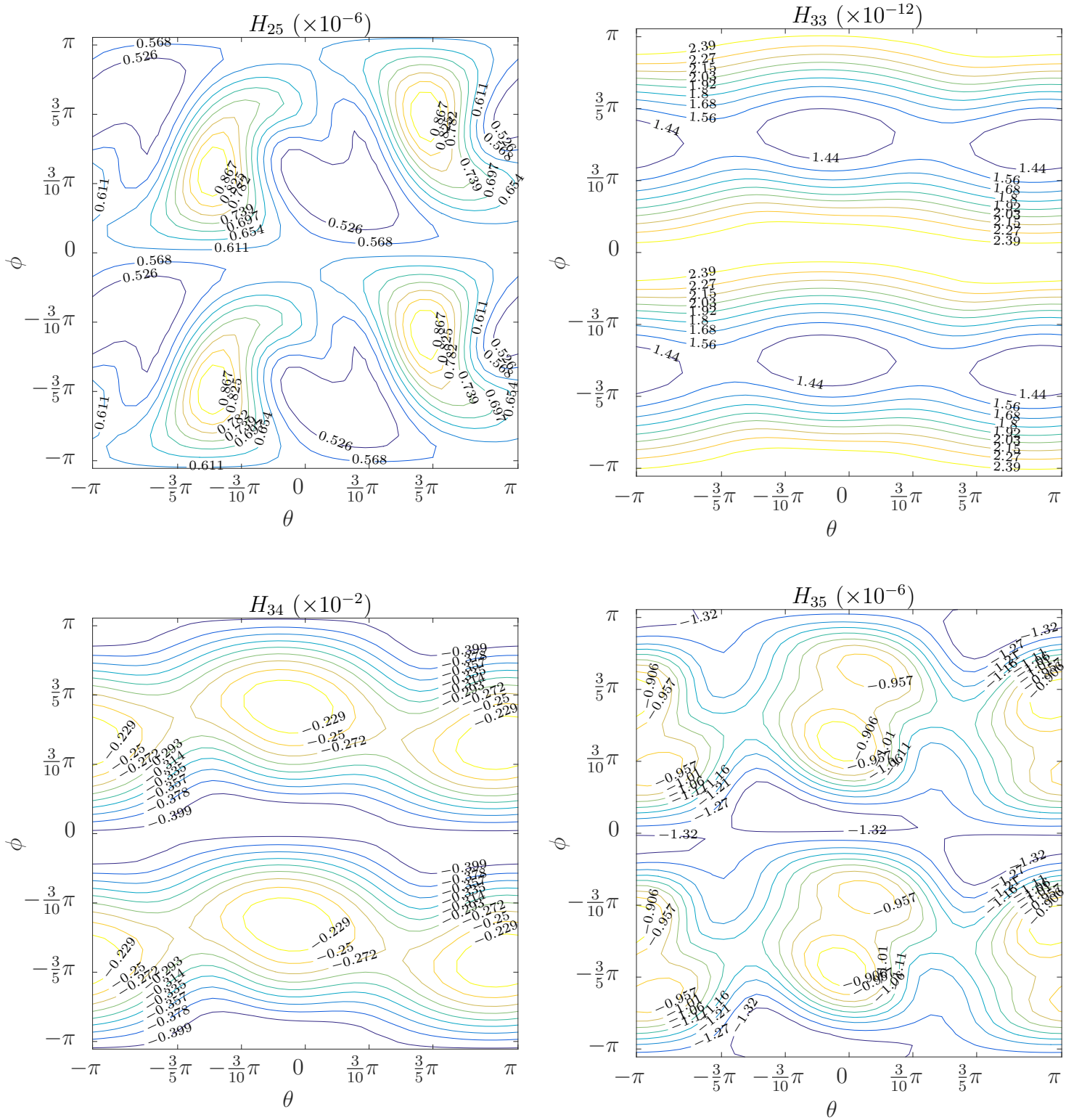

Figure B.3 – The Barnett-Lothe tensor, H_{ij}, $i, j = [1, ..., 5]$, for the *Material C - MEE*, in spherical coordinates.

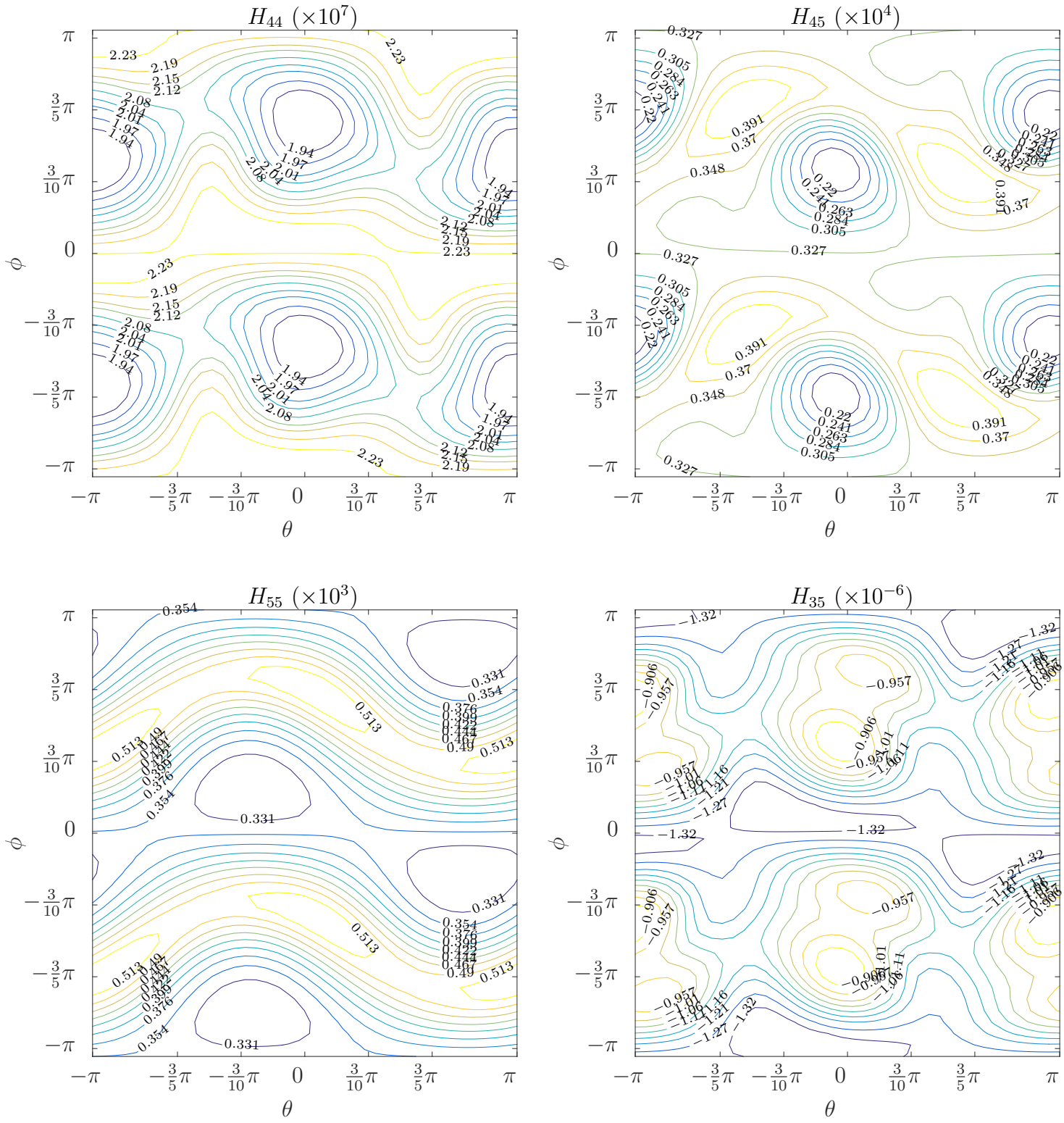

Figure B.4 – The Barnett-Lothe tensor, H_{ij}, $i, j = [1, ..., 5]$, for the *Material C - MEE*, in spherical coordinates.

ANNEX I – Elastic, Piezoeletric and MEE constants for the example materials

Table I.1 – Piezoeletric properties for Material A

Elastic Constants $\left[10^9 \frac{N}{m^2}\right]$	c_{1111}	139
	c_{3333}	115
	c_{1122}	77.8
	c_{1133}	74.3
	c_{2323}	25.6
Piezoeletric Constants $\left[\frac{C}{m^2}\right]$	e_{113}	12.7
	e_{333}	15.1
	e_{322}	-5.1
Dielectric permeability coefficients $\left[10^{-9} \frac{C}{Vm}\right]$	ε_{11}	6.461
	ε_{33}	5.62

Table I.2 – Piezoeletric properties for Material B

Elastic constants $\left[10^9 \frac{N}{m^2}\right]$	c_{1111}	166
	c_{3333}	77
	c_{1122}	78
	c_{1133}	162
	c_{2323}	43
Piezoeletric Constants $\left[\frac{C}{m^2}\right]$	e_{113}	11.6
	e_{333}	18.6
	e_{322}	-4.4
Piezomagnetic Constants $\left[\frac{N}{A\,m}\right]$	q_{113}	550
	q_{333}	699.7
	q_{322}	580.3
Magneto-electric coefficients $\left[\frac{N\,s}{A\,m}\right]$	λ_{11}	0
	λ_{33}	0
Dielectric permeability coefficients $\left[10^{-9} \frac{C}{Vm}\right]$	ε_{11}	11.2
	ε_{33}	12.6
Magnetic permeability coefficients $\left[10^{-6} \frac{Ns^2}{C^2}\right]$	μ_{11}	5
	μ_{33}	10

Table I.3 – Magneto-electro-elastic constants for Material C ($BaTiO_3$−$CoFe_2O_4$)

Elastic Constants $\left[10^9 \frac{N}{m^2}\right]$	c_{1111}	220.12	c_{1212}	46.651	c_{1323}	-0.217
	c_{1112}	2.090	c_{1213}	0.552	c_{2223}	1.516
	c_{1113}	-2.196	c_{1222}	0.991	c_{2233}	126.24
	c_{1122}	124.285	c_{1223}	-0.968	c_{2333}	0.401
	c_{1123}	-0.853	c_{1233}	-1.317	c_{3333}	215.586
	c_{1133}	125.807	c_{1333}	-0.505	c_{2323}	45.753
	c_{2222}	218.338	c_{1322}	1.115	c_{1313}	46.258
Piezoeletric Constants $\left[\frac{C}{m^2}\right]$	e_{111}	9.374	e_{211}	1.241	e_{311}	-2.354
	e_{112}	-4.666	e_{212}	4.857	e_{312}	-0.504
	e_{113}	8.847	e_{213}	-0.821	e_{313}	5.379
	e_{122}	-1.767	e_{222}	-5.721	e_{322}	-1.395
	e_{123}	-0.820	e_{223}	7.441	e_{323}	-4.346
	e_{133}	-0.643	e_{233}	0.519	e_{333}	13.214
Piezomagnetic Constants $\left[\frac{N}{A\,m}\right]$	q_{111}	358.82	q_{211}	-99.692	q_{311}	189.018
	q_{112}	-61.593	q_{212}	44.217	q_{312}	11.224
	q_{113}	116.775	q_{213}	26.881	q_{313}	37.090
	q_{122}	130.939	q_{222}	-200.163	q_{322}	135.735
	q_{123}	26.878	q_{223}	67.743	q_{323}	-29.976
	q_{133}	94.107	q_{233}	-76.044	q_{333}	291.03
Magneto-electric coefficients $\left[10^{-9} \frac{N\,s}{A\,m}\right]$	λ_{11}	-0.688	λ_{13}	-0.784	λ_{23}	0.634
	λ_{12}	0.413	λ_{22}	-1.022	λ_{33}	-1.890
Dielectric permeability coefficients $\left[10^{-9} \frac{C}{V\,m}\right]$	ϵ_{11}	-5.817	ϵ_{13}	-0.203	ϵ_{23}	0.165
	ϵ_{12}	0.107	ϵ_{22}	-5.905	ϵ_{33}	-6.129
Magnetic permeability coefficients $\left[10^{-6} \frac{Ns^2}{C^2}\right]$	μ_{11}	-243.62	μ_{13}	61.326	μ_{23}	-49.543
	μ_{12}	-32.341	μ_{22}	-217.516	μ_{33}	-149.639